Oxygen-Regulating MEMS Devices for Cell Transplantation to Cure Type 1 Diabetes

Thesis by

Kuang-Ming Shang

In Partial Fulfillment of the Requirements for

the Degree of

Doctor of Philosophy

CALIFORNIA INSTITUTE OF TECHNOLOGY

Pasadena, California

2024

(Defended May 17, 2024)

by Kuang-Ming Shang
ORCID: 0000-0001-5065-7607

To my parents, Chun and Hui

ACKNOWLEDGMENTS

First and foremost, I would like to extend my heartfelt thanks to my advisor, Dr. Yu-Chong Tai, who has been an exceptional mentor and true inspiration throughout my PhD journey. His enthusiasm for developing new technologies to address clinical challenges is palpable in every conversation. His profound understanding of fundamental knowledge and his ability to simplify complex ideas have made our intellectual discussions incredibly rewarding. More than an academic guide, Dr. Tai has shown genuine care for my personal growth, and for this, I am deeply grateful.

I would also like to express my profound gratitude to Dr. Hirotake Komatsu, my co-advisor, who introduced me to the field of transplantation. His relentless support and commitment to excellence have been indispensable. Whether at City of Hope, Caltech, or over Zoom, our rigorous and extended discussions on scientific data interpretation have been incredibly stimulating. The trust and mutual respect we have developed are deeply valued, and I am grateful for Dr. Komatsu's influence in my PhD journey.

My sincere appreciation goes to Dr. Morteza Gharib, Dr. Changhuei Yang, Dr. Mikhail Shapiro, and Dr. Wei Gao, members of my thesis and/or candidacy committee, for their invaluable insights and feedback during the development of my research project.

During my time at Caltech, I had the privilege to work with many collaborators on a variety of exciting projects. I would like to acknowledge their support and contributions. Dr. Taro Toyoda from Kyoto University and Mr. Hiroyuki Kato from City of Hope, thank you for your dedication and commitment to our islet and stem cell projects. Dr. John Hsiai at UCLA, your willingness to share your knowledge and insights has been invaluable. Dr. Sunghoon Kim at UCSF, your contagious enthusiasm and continuous support for our implantable pressure sensor project are greatly appreciated. Dr. Yuman Fong at City of Hope, your insights have been

enlightening in our development of magnet-assisted robotic surgical tools. Dr. Nai-Chang Yeh and Dr. Chen-Hsuan Lu at Caltech, your collaborative spirit has not only made our graphene project successful but also enjoyable. I am also grateful to Mr. Mark Mathison for all the legal guidance in patenting our works.

To all the talented members of the MEMS lab: Nick, Aubrey, Colin, May, Jake, and Yuan, who were the first cohort when I joined. Each of you has generously taught me everything I needed to learn to thrive in this lab. Shane, Suhash, David, Haixu, Akhila, Ting-Wei, Ningxuan, I have thoroughly enjoyed working with you and will miss our many conversations, both related and unrelated to our projects. Thanks to Trevor for the support in the cleanroom. Learning how to fix and modify machines from you is both enjoyable and invaluable. I also thank Christine and Tanya for their indispensable administrative support and guidance. Despite our small group size, I cherish the friendships we have fostered both inside and outside the lab.

To my high school teacher, Dr. Tsui-Hua Liu, you sparked my initial interest in science and engineering. You have consistently motivated me to push and extend my boundaries. To Dr. Hsu-An Chu and Dr. Lie-Fen Shyur, thank you for allowing a high school student to experiment in your fantastical research labs at Academia Sinica. The time I spent there was both enriching and memorable. Thank you, Dr. Jung-Yaw Lin, Dr. Yi-Fang Tsay, and many other professors who encouraged and advised me to participate in ISEF in the United States, a truly eye-opening experience. To my undergraduate advisor, Dr. Huei Wang, your guidance has been instrumental in shaping my development as an engineer.

To the friends I made during my time at Caltech—Zhiyang, Xinhong, Shumao, William, Yu-Wei, Peiwei, and the rest of the first cohort I connected with upon arriving at Caltech. To the members of the Taiwanese community—Yen-Yung, Tina, Yung-Ting, Yu-Li, Chien-Han, Hsiao-Yi, Chien-Yi, Che-Chin, Evan, Min-Feng, Sophia, Yu-Hung, Shih-Hao, Yu-An, Xavier, Po-Hsuan, Howard, Kenny, Ernie, Benjamin, Chung-Yi, I-Hui, Hao-Hsuan, Albert, Debbie, Chien-Ying, Sean, Sean, Richard, and many others—I deeply value your support and the time we spent

together. Special thanks to my roommates, Steve, Meng-Jhang, and Wen, for their companionship, especially during the challenging times of the pandemic.

To my buddies, Charlie and Peter, your unwavering support has been my anchor throughout this journey. From joking around to late-night pep talks, your presence has made all the difference when times were tough. To all my friends out there, I am deeply grateful for the encouragement, wisdom, and humor you have shared with me.

To my cherished family—my grandparents, aunties, uncles, and cousins—your curiosity about my research and your steadfast support have been constant sources of encouragement. Thank you for always believing in me.

To my beloved parents, Hui Wang and Chun Shang, who I love wholeheartedly and who have always supported me unconditionally. Mom and Dad, you not only gave me the gift of life but also gave me the strength to face the world with confidence, the liberty to explore without restraint, and the comfort I find in times of need. Every step I take is imbued with the values you've lovingly instilled in me. I am immensely proud to be your son. This accomplishment is as much yours as it is mine. From the depths of my heart, thank you for everything.

ABSTRACT

Type 1 diabetes is an autoimmune disease in which immune cells specifically attack and destroy the insulin-producing beta cells in the pancreatic islets that regulate blood glucose levels. Traditionally managed with frequent injections of exogenous insulin, beta cell replacement therapy—also known as islet transplantation—has emerged as an alternative clinical option. Recently, the focus has shifted toward subcutaneous islet transplantation, offering a promising and minimally invasive therapy. However, the survival of transplanted islets has been shown to be significantly challenged by hypoxia-induced graft loss stemming from inadequate oxygen supply.

To address this issue, we have developed innovative hollow mesh devices that regulate oxygen. These devices can either bring oxygen from the adjacent oxygen-rich tissue or draw additional oxygen from ambient air to improve oxygen delivery to the hypoxic microenvironment of islet grafts. Fabricated using MEMS techniques and biocompatible materials, these devices feature a network of unobstructed air-containing microchannels. Utilizing the property that oxygen diffuses 10,000 times faster in air than in interstitial fluids, these devices effectively overcome oxygen supply barriers when co-transplanted with islet grafts. By integrating these hollow meshes with the islet grafts, oxygen can be rapidly redistributed throughout the graft, establishing local oxygen balance and regulation. This approach significantly reduces hypoxia-induced graft loss and improves the efficacy of post-transplant blood glucose regulation in recipients.

In this thesis, we first delved into the physiology of oxygen transport within an islet, establishing the critical oxygen threshold necessary for islet cell survival. We developed equivalent circuit models for oxygen diffusion and constructed oxygen-regulating hollow mesh MEMS devices based on these models. We investigated the effects of oxygenation through both computational models and benchtop experiments. Finally, using our device, we demonstrated enhanced survival of islet grafts in diabetic rodent models, successfully achieving a long-term cure for diabetes.

With the preclinical success of this oxygen-regulating hollow mesh in mitigating cellular oxygen deficiency, we also explored and proposed future pathways toward clinical effectiveness. Our device holds significant therapeutic potential to revolutionize clinical outcomes in islet transplantation with the ultimate goal of curing type 1 diabetes.

PUBLISHED CONTENT AND CONTRIBUTIONS

[1] **K.-M. Shang**, H. Kato, N. Gonzalez, F. Kandeel, Y.-C. Tai, and H. Komatsu, "A novel approach to determine the critical survival threshold of cellular oxygen within spheroids via integrating live/dead cell imaging with oxygen modeling," *American Journal of Physiology-Cell Physiology*, vol. 326, no. 4, pp. C1262–C1271, Apr. 2024, doi: 10.1152/ajpcell.00024.2024
K.-M. Shang initiated, designed, and conducted most of the experiments, analyzed the data, and prepared and revised the manuscript.

[2] R. J. Myrick*, **K.-M. Shang*,** J. F. Betts, N. Gonzalez, J. Rawson, K. Izumi, N. Koba, T. Tsuchiya, H. Kato, K. Omori, F. Kandeel, Y. Mullen, Y.-C. Tai, E. Botvinick, and H. Komatsu, "Micropyramid-patterned, oxygen-permeable bottomed dish for high density culture of pancreatic islets," *Biofabrication*, vol. 15, no. 1, p. 015018, Dec. 2022, doi: 10.1088/1758-5090/aca79a
K.-M. Shang initiated, designed, and conducted part of the experiments, analyzed the data, and prepared and revised the manuscript.

[3] **K.-M. Shang**, H. Komatsu, and Y.-C. Tai, "Oxygen-transporting parylene-HT mesh for cell transplantation to reduce hypoxia," in *2021 IEEE 34th International Conference on Micro Electro Mechanical Systems (MEMS)*, Jan. 2021, pp. 458–461. doi: 10.1109/MEMS51782.2021.9375215
K.-M. Shang initiated, designed, and conducted most of the experiments, analyzed the data, and prepared and revised the manuscript.

TABLE OF CONTENTS

LIST OF FIGURES AND TABLES

Number *Page*

Chapter 1

Introduction

Diabetes shortens life expectancy [1], [2]. Discovering a long-term cure for diabetes would have a transformative effect on patient lives. This introduction chapter discusses the fundamentals of diabetes, focusing specifically on type 1 diabetes, and explores the current management strategies for type 1 diabetes. It then delves into cell transplantation therapy as a potential promising cure. An emphasis is placed on the challenge of oxygen deficiency, a critical and clinical obstacle in cell transplantation to achieving the long-term cure of type 1 diabetes. We will explore the latest approaches and limitations aimed at resolving the issue of oxygen supply in cell therapy.

1.1 DIABETES AND TYPE 1 DIABETES

Diabetes is a chronic disease in which the body has an *elevated level of blood sugar*. This occurs when insulin, a hormone typically produced by the beta cells in the pancreas, is unable to regulate the blood glucose. Elevated and unregulated glucose levels can lead to severe health complications over time, including heart disease, vision loss, stroke, kidney failure, and lower limb amputation [3].

Diabetes is a global burden on public health. According to the International Diabetes Federation (IDF), approximately 463 million individuals were living with diabetes in 2019, constituting nearly one-tenth of the global population [4]. The prevalence of diabetes has been steadily increasing over the past several decades, and projections indicate that the incidence of diabetes will continue to rise [5].

Diabetes is primarily classified into two types: type 1 diabetes (T1D) and type 2 diabetes (T2D) [6]. As illustrated in **Figure 1-1**, T1D is characterized by insufficient insulin production in the pancreas, whereas T2D occurs when the body cannot

effectively use the insulin it produces—a condition known as insulin resistance. Insulin resistance is often a result of obesity and sedentariness, leading to increased insulin demand and inadequate production to maintain normal glucose levels. This could culminate in the progressive loss of beta-cell function. Although T2D is more common, it can usually be managed initially with lifestyle modifications and oral medications, and there are effective strategies available to prevent its onset. In contrast, T1D cannot be prevented and requires immediate and careful management due to the quick emergence of severe and potentially life-threatening complications from the halt in insulin production.

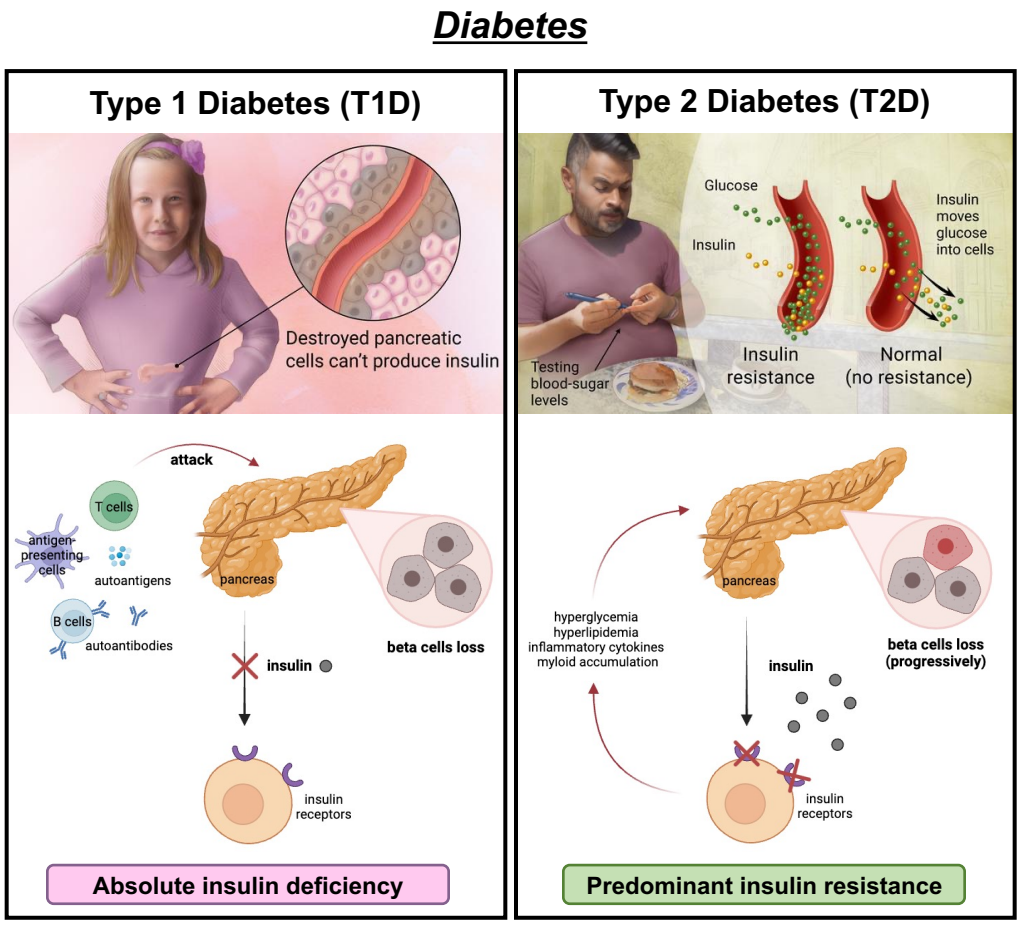

Figure 1-1. Pathophysiology difference between type 1 diabetes and type 2 diabetes. Images are adapted from health drawings from Google.

The pathophysiology of T1D is rooted in its nature as an *autoimmune disease*, wherein the innate immune system of the body mistakenly initiates a cascade of processes that leads to the destruction of pancreatic beta cells (or β-cells). As shown in **Figure 1-2**, these beta cells are responsible for insulin production. The excess loss of beta cells leads to the hallmark deficiency of insulin production. While the precise trigger for T1D remains elusive, it is understood to emerge from an interplay of genetic predispositions and environmental influences. Commonly diagnosed in children and young adults, T1D can also occur in older adults. The clinical presentation of T1D includes symptoms such as frequent urination, excessive thirst, unexplained weight loss, fatigue, and blurred vision.

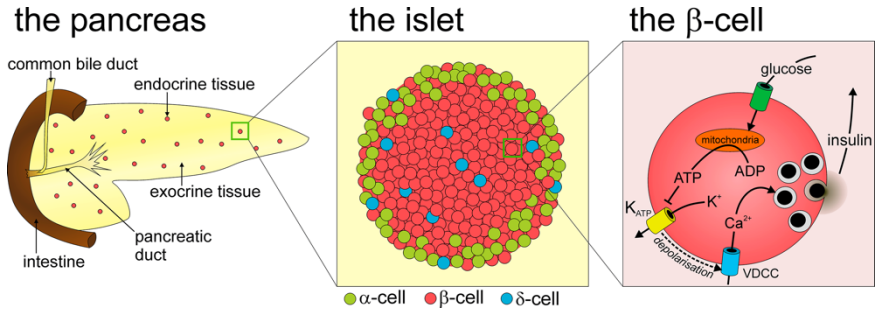

Figure 1-2. Physiology of pancreatic beta cells within the islet of the pancreas. Image is adapted from [7] under open access license.

The diagnosis of diabetes in general incorporates not only the identification of characteristic symptoms but also the verification of elevated blood glucose levels (hyperglycemia). A conclusive diagnosis of diabetes, and diabetes in general, can be determined through the measurement of plasma glucose concentrations. A random plasma glucose reading exceeding 200 mg/dL (11.1 mmol/L) or a fasting plasma glucose level above 126 mg/dL (7.0 mmol/L) is indicative of diabetes [8], [9], [10], [11], [12]. Hemoglobin A1c (HbA1c) levels exceeding 6.5% may indicate diabetes [13]. HbA1c is glycated hemoglobin, a form of hemoglobin that is covalently bonded to glucose, reflecting elevated blood sugar levels over time. In addition, various type of glucose tolerance tests are also utilized to diagnose diabetes.

The complications of T1D can be divided into two categories: microvascular and macrovascular [14], [15]. Microvascular complications include diabetic retinopathy (damage to the blood vessels in the eye), diabetic neuropathy (nerve damage), and diabetic nephropathy (kidney disease). Macrovascular complications include cardiovascular disease, such as coronary artery disease and stroke.

1.2 TREATMENT OPTIONS FOR TYPE 1 DIABETES

The primary approach to managing T1D involves administering biosynthetic recombinant insulin exogenously. Since the breakthrough of insulin discovery a century ago [16], it has remained the standard option of T1D treatment [17]. To maintain normoglycemia throughout the day, patients typically require multiple injections. These injections, usually delivered via syringe or insulin pump, are administered subcutaneously into the fat tissue under the skin. The type of insulin prescribed or required varies according to lifestyle, dietary intake, and blood sugar levels, with bolus and basal insulin being common variants. Common sites for insulin administration include the abdomen, upper arms, thighs, or hips.

Despite the efficacy of insulin injection in managing T1D, the manual monitoring of blood glucose levels and the maintenance of insulin storage can be burdensome, potentially leading to erratic and inaccurate dosing. Such challenges may compromise glycemic control, increasing the risk of long-term complications [18]. Moreover, insufficient insulin can lead to hyperglycemia, whereas excessive insulin intake can result in hypoglycemia. In severe cases, patients may experience life-threatening hyperglycemic or hypoglycemic episodes.

To alleviate the burden of manual monitoring and management of blood sugar levels in patients with T1D, insulin pumps integrated with Continuous Glucose Monitoring (CGM) systems have been developed (**Figure 1-3**). These insulin pumps deliver insulin continuously, thereby mimicking the natural insulin release of the native pancreas and promoting more stable blood glucose levels than those achieved

through multiple daily injections. When combined with CGM systems, which automatically measure blood glucose, the insulin pump can autonomously adjust insulin dosages based on real-time CGM readings. With dedicated algorithms, the prediction of blood glucose fluctuations enables a more precise determination of both the optimal timing and duration for insulin administration. This integration, with the clinical trial (ClinicalTrials.gov Identifier: NCT02463097) results using the Medtronic MiniMed 670G system, has demonstrated reductions in HbA1c levels, as well as decreased incidents of both hypoglycemia and hyperglycemia [19]. The MiniMed 670G hybrid closed-loop CGM system, which was FDA-approved in September 2016 [20], represents a significant advancement in T1D care technology.

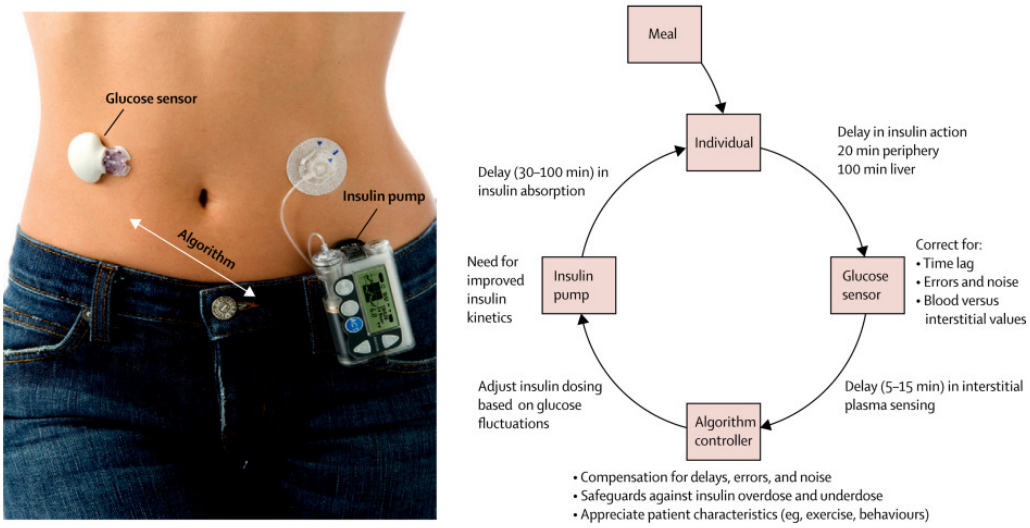

Figure 1-3. Closed-loop system integrated with insulin pump and continuous glucose monitoring for type 1 diabetes. Image is adapted from [14] with permission from the copyright holder, Elsevier.

While CGM systems with integrated insulin delivery represent a substantial advancement in T1D management, it is crucial to understand that these systems do not equate to a cure. They improve glucose regulation by administering exogenous insulin, but do not reinstate the insulin production from the innate pancreas. The fundamental issue of pancreatic beta-cell destruction remains unaddressed. As a result, even with the remarkable improvements these systems provide in enhancing life quality for those with T1D, the pursuit of a long-term T1D cure continues.

1.3 ISLET CELL TRANSPLANTATION

Beyond the reliance on exogenous insulin injections for managing T1D, pancreatic islet cell transplantation has been proposed clinically to restore the endogenous insulin-producing capabilities of patients. This approach is to avoid lethal hypoglycemia and could achieve insulin independence and presents a potential pathway to a complete cure for T1D.

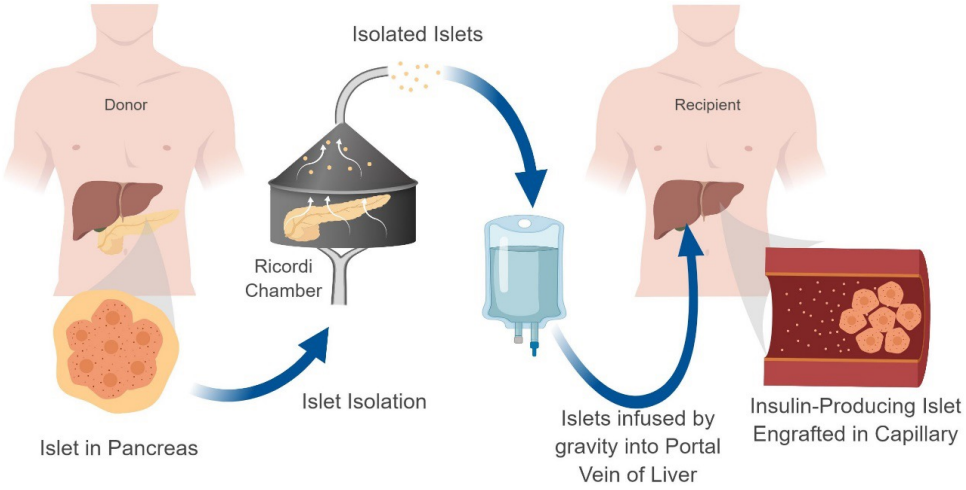

Figure 1-4. Islet transplantation procedure for type 1 diabetes. Image is adapted from [21] under open access license.

The Edmonton protocol, established in 2000, is a landmark procedure for islet transplantation, as illustrated in **Figure 1-14**. Islets are isolated from the pancreas of deceased donors utilizing specialized enzymes. Following isolation, these islets undergo a purification process and are quantified. Typically, around 400,000 islets are transplanted during each procedure. These islets are then carefully infused into the portal vein in the liver site of a recipient through a minimally invasive percutaneous procedure. This allotransplantation, combined with glucocorticoid-free immunosuppressive medicine, has enabled insulin independence in all seven human subjects in the initial trial studies, marking a significant milestone in T1D treatment [22].

Subsequent to its establishment, the Edmonton protocol underwent an international, multicenter clinical trial (ClinicalTrials.gov Identifier: NCT00014911) to further investigate islet transplantation from deceased donors [23]. In this trial, 36 subjects were enrolled, and after one year, 44% maintained insulin independence with satisfactory glycemic control. However, 28% experienced a complete islet graft loss within the same period.

As of 2020, the Collaborative Islet Transplant Registry (CITR) reported 1,399 recipients of allogeneic islet transplants, who received a total of 2,832 infusions from 3,326 deceased donors [24]. According to CITR data, the unadjusted prevalence of insulin independence post-last islet infusion stands at about 50% one year after transplantation, and around 35% at three years post-transplant. Fortunately, even without achieving complete insulin independence, an islet transplant can significantly protect T1D patients from severe hypoglycemic episodes, provided some residual function of the islet graft is maintained. While recent data indicates improvements in rates of insulin independence [25], sustaining this state post-pancreatic islet transplantation remains challenging [23], [26].

The decline in insulin independence observed in recipients following the Edmonton protocol can be attributed to various factors. Notably, the liver can present a hostile environment for transplanted islets with the acute reduction of islet mass, as well as their gradual loss over time [27], [28], [29]. Additionally, while immunosuppressants are necessary to prevent islet graft rejection in allotransplantation settings, they can pose risks to the recipient and have been shown to potentially exert toxic effects on the transplanted islets [30]. Because of this low engraftment efficacy in the liver site, as well as the chronic reduction of the mass over the time course after the transplantation, a patient requires more than two transplantations for the stable glycemic controls in the current clinical strategy. Due to low engraftment efficacy in the liver and the gradual reduction in mass over time following transplantation, patients currently require more than two transplantations to achieve stable glycemic control in clinical strategies.

A fundamental challenge in the current islet transplantation strategy is the shortage of donor islets [31]. The need for multiple transplantations exacerbates the donor shortage issue. This scarcity of cadaveric islets has spurred researchers to investigate alternative sources, such as stem-cell-derived insulin-producing cells [32]. Due to the neoplastic potential of stem-cell-derived cells [33], the liver is no longer a suitable site because of the potential need for surgical intervention. This has propelled the clinical trial investigation in extrahepatic transplantation sites like intramuscular (ClinicalTrials.gov Identifier: NCT01967186, NCT03977662), omentum (ClinicalTrials.gov Identifier: NCT02213003, NCT02803905, NCT02821026), or subcutaneous (ClinicalTrials.gov Identifier: NCT01652911, NCT05073302) spaces.

1.4 OXYGEN DEFICIENCY IS THE LIMITING FACTOR IN ISLET TRANSPLANTATION

Among the issues previously mentioned, one of the major challenges in islet transplantation is inadequate oxygen supply in all the transplantation sites. Native islets, composed of roughly 2000 cells and typically large in volume, require microvascular perfusion for oxygen delivery. Within their natural environment in the pancreatic parenchyma, oxygen levels have been measured at approximately 40 mmHg [29], and it is possible that islets experience even higher levels of oxygen due to their well-vascularized nature, facilitated by the micro-arteries.

However, once islets are isolated from a pancreas from diseased donors, the perfusion of blood—and thus oxygen—through the endothelial vessels ceases (**Figure 1-15**) [34]. In the absence of active blood flow, oxygen can only be supplied through diffusion, a much slower process [35]. Given the significant size of islets, ranging from 50 to 300 μm in diameter, diffusion alone is insufficient for the oxygenation of the entire islet [36]. Consequently, the isolated islets rapidly suffer from severe hypoxia, leading to central necrosis, if the oxygen microenvironment is not properly designed and regulated.

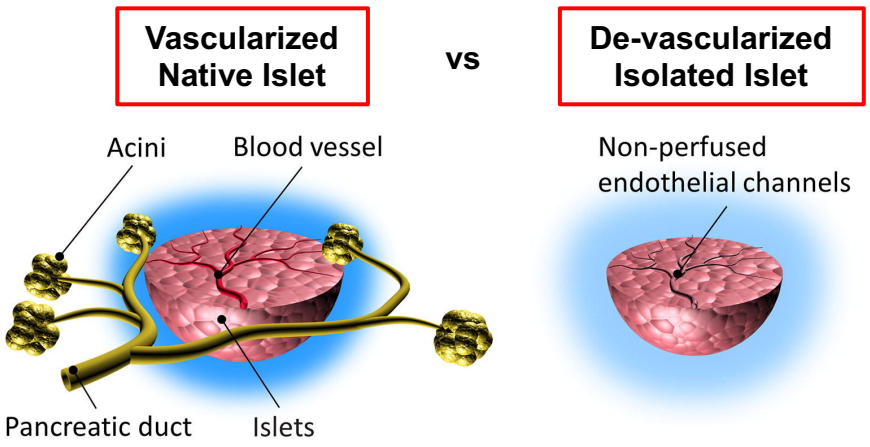

Figure 1-5. Comparison between a vascularized native islet and a de-vascularized isolated islet. Image is adapted from [34] with permission from the copyright holder, Elsevier.

The challenge of oxygenating the islet is not only due to its larger size but is also significantly compounded by its high rate of oxygen consumption. For a typical human cell, with an average size of 2000 μm^3 [37], the oxygen consumption rate is approximately 1.25×10^{-3} $mol/m^3/s$ [38]. Islet cells, however, have an average oxygen consumption rate of 2.5×10^{-2} $mol/m^3/s$ [39], 20 times higher than that of average cells. This increased consumption is attributed to the high metabolic activity required for maintaining proper endocrine function [40]. This high oxygen consumption rate hinders the full oxygenation of the entire isolated islet, a situation that is further exacerbated by the lack of pre-formed blood vessels.

At the hepatic site, inadequate oxygen supply for islet transplant has been documented [27]. The oxygen tension within an islet transplanted in the liver capsule is measured to be approximately 5 mmHg [29]. In short, mild hypoxia is a condition present at the hepatic site (**Figure 1-6A**). Following the Edmonton protocol, which involves the engraftment of islets in the portal vein, these hepatically transplanted islets often face severe immune responses [28]. Should thrombosis occur, it can significantly exacerbate the oxygen tension within the islet. This is due to the increased distance from the islet's core to the nearest external oxygen source, impeding the already limited oxygen supply [41].

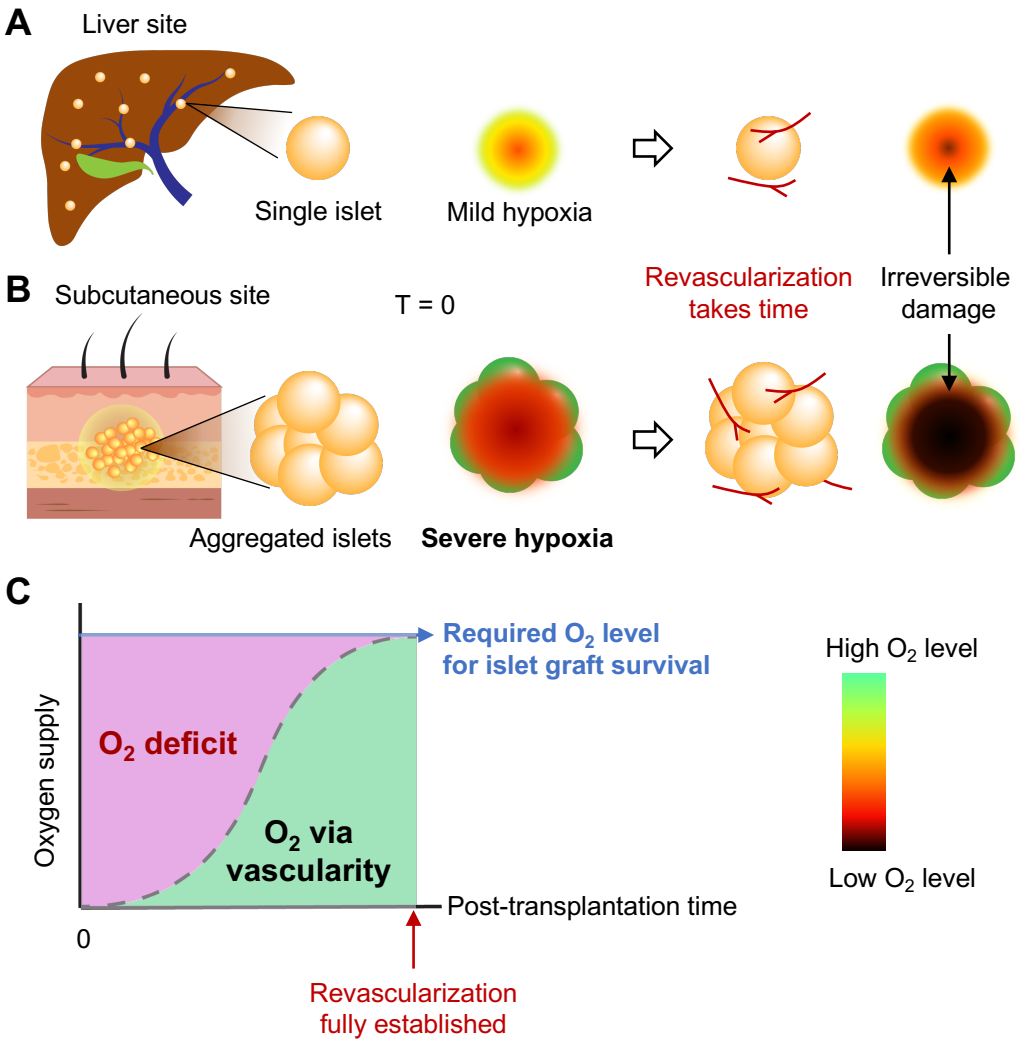

Figure 1-6. Schematic of insufficient oxygen supply to transplanted islets. (A) Single islet settled in the liver site shows mild hypoxia. Some irreversible damage occurs even if revascularization is established. (B) High-density islet graft aggregated in an extrahepatic site shows a huge hypoxic core. Severe irreversible damage occurs even if revascularization is established. (C) Oxygen deficit and supply after transplantation and until revascularization for islet transplantation.

Moreover, when islets are transplanted into an extrahepatic location, the problem of hypoxia becomes even more pronounced. Firstly, the tendency for islet grafts to aggregate poses an additional obstacle. When islets aggregate together, the cells in the center of these aggregates are placed even further from the oxygen supply provided by existing blood vessels in the adjacent tissue (**Figure 1-6B**). This results

in a gradient of oxygenation, with cells on the periphery having access to more oxygen than those in the core of the aggregation [42]. Secondly, the extrahepatic sites typically have lower levels of blood vessel density. This scarcity of vasculature means that the transplanted islets cannot receive an adequate oxygen supply immediately after transplantation, leading to severe irreversible damage. The oxygen deprivation persists until new blood vessels form, a process known as revascularization, which could take at least a few days to weeks as shown in **Figure 1-6C** [43], [44], [45].

In addition to the challenges of ensuring an adequate oxygen supply, another factor that can complicate the oxygenation of islet cells is immunoisolation, a technique used in islet transplantation [34], [46]. These processes are deployed as they create a protective barrier around the transplanted islet cells, safeguarding them from the immune response from the recipient. This protection eliminates the necessity for a continuous immunosuppressive regimen.

Immunoisolation encompasses methods like microencapsulation and microencapsulation [47]. Microencapsulation involves enveloping individual or small clusters of islet cells in a semi-permeable membrane, while macroencapsulation contains larger groups of islet cells within a single and larger encapsulating device. Both methods prevent immune cells from making contact and destroying the transplanted islet cells. Unfortunately, a significant downside is that oxygen then needs to diffuse through the encapsulating material into the transplanted islet, making the diffusion distance from the encapsulated cells farther away from the blood vessel networks. Without an immediate and adequate blood supply, the effectiveness of the islet transplant may be significantly reduced due to the hampered oxygen delivery.

In conclusion, the crux of the challenge in islet transplantation lies in ensuring an adequate oxygen supply. This pivotal issue is compounded by several interrelated factors, such as the islet seeding density, the chosen site for transplantation, and the applied immunoisolation strategies. Particularly in the initial phase post-

transplantation, these elements can collectively precipitate severe hypoxia, leading to an irreversible loss of islet graft mass, hindering the efficacy of islet cell therapy. Consequently, delving into innovative strategies that guarantee sufficient oxygenation to the transplanted islets is paramount. Such advancements are the foundation of transforming islet transplantation into a sustainable and successful long-tern cure for T1D.

1.5 STATE-OF-THE-ART OXYGENATION DEVICES FOR ISLET TRANSPLANTATION

Implantable medical devices for type 1 diabetes have seen significant advancements through clinical trials. Among them, based on oxygenation strategies, there are two major types: direct vascularization and concentrated oxygen injection.

DIRECT VASCULARIZATION

Effective engraftment of islet grafts relies heavily on direct vascularization because of oxygen and nutrient supply. This concept is central to the evolution of ViaCyte's two generation of devices (**Figure 1-7**). Their first device, the VC-01 or PEC-Encap, utilizes macroencapsulation technology so no direct vascularization to the islet graft. With the VC-02 device, pancreatic progenitor cells, derived from human pluripotent stem cells (hPSCs), are encapsulated and the entire devices are implanted subcutaneously. Unfortunately, clinical trials conducted between 2014-2017 (ClinicalTrials.gov Identifier: NCT02239354) and 2019-2021 (ClinicalTrials.gov Identifier: NCT04678557) were terminated due to inadequate functional engraftment. Preliminary findings indicated that fibrotic tissue enveloped the retrieved devices [48], which obstructed the integration into the host tissue and disrupted oxygen and nutrient delivery to the cells inside the device [49].

In response to these challenges, ViaCyte developed a second-generation device, the VC-02 or PEC-Direct. This device builds upon the VC-01's design but includes opening ports that allow the blood vessels to infiltrate and directly supply the

engrafted cells with oxygen, thus enhancing their survival. However, this direct vascularization comes at the cost of immunoprotection, necessitating immunosuppressive drugs for the patient. Currently, the VC-02, loaded with pluripotent stem cell-derived pancreatic endoderm cells, is undergoing clinical trials (ClinicalTrials.gov Identifier: NCT03162926, NCT03163511). Preliminary interim reports show that 63% of VC-02 units extracted from patients demonstrated engraftment and insulin expression 3-12 months post-implantation [49].

The development of ViaCyte's two generations of devices underscores the critical role of oxygenation through vascularization. Insufficient oxygenation can complicate islet engraftment, thereby impeding the therapeutic outcomes of such treatments. It's noteworthy that ViaCyte's devices were inspired by the TheraCyte device [50].

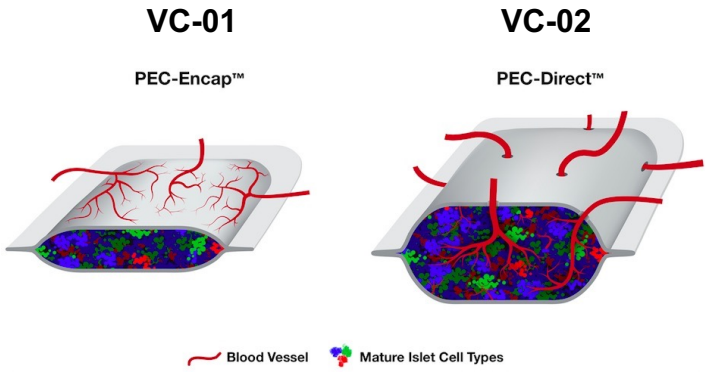

Figure 1-7. ViaCyte devices for islet transplantation. VC-01 (also known as PEC-Encap™) is a macroencaspulation device. VC-02 (also known as PEC-Direct™) is an open device that based on VC-01 but has opening ports allowing direct vascularization into the islet graft. Images are adapted and sourced from ViaCyte.

CONCENTRATED OXYGEN INJECTION

In an effort to overcome the limitations of oxygen supply while maintaining immunoisolation through encapsulation, an innovative device known as ß-Air, developed by Beta-O2, has been proposed (**Figure 1-8**).

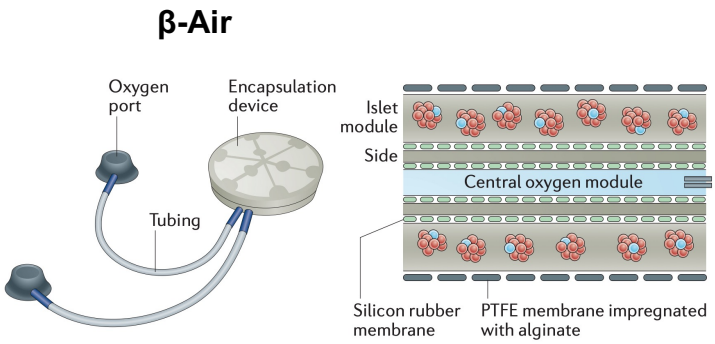

Figure 1-8. ß-Air encapsulation device from Beta-O2 for islet transplantation. Image is adapted from [47] with permission from the copyright holder, Springer Nature.

This encapsulation device is equipped with two ports for oxygenation and is implanted subcutaneously. The ports facilitate the daily administration of concentrated oxygen (up to 40%) directly to the islet graft, ensuring it receives ample oxygenation. Unlike vascularized grafts, the islet graft within the ß-Air device relies heavily on this externally supplied oxygen. Pilot studies have demonstrated that the device's functionality is critically dependent on this oxygen supply, as grafts fail if the oxygen is discontinued [51], [52]. During the clinical trial (ClinicalTrials.gov Identifier: NCT02064309), while the islet cells survived within the ß-Air device, only trace levels of C-peptide—an indicator of insulin secretion—have been detected, and the device does not significantly influence metabolic control. This could be attributed to two potential factors: the hyperoxic conditions created by oxygen injection may inhibit islet function, or the lack of integration with the recipient's vascular network could limit glucose sensing and insulin secretion capabilities. Furthermore, the requirement for daily oxygen injections with precise dosing, which parallels daily insulin injections, still presents additional management challenges for patients.

OTHER INVESTIGATIONAL DEVICES

Researchers around the world are investigating many innovative devices. In this brief review, we aim to briefly examine the proposed functions of these devices. Emphasizing the significance of local vascularity as in VC-02, researchers have

suggested increasing localized prevascularization using a pre-implantation method involving a catheter and synergetic material. This catheter is subsequently removed, creating a highly vascular pocket in a device-less approach [53]. This pocket is also transplanted with islet cells and the device-like synergetic material [54]. Additionally, the co-transplantation of materials that generate oxygen is being explored. For instance, islet cells are co-transplanted with PDMS-encapsulated calcium peroxide, which upon hydration, hydrolytically releases oxygen [55]. Another approach under investigation involves wirelessly delivering power to the transplant site to induce hydrolysis of surrounding water vapor, generating gaseous-phase oxygen at the cathode facing the encapsulated islet cells [56]. The potential of co-transplantation with materials that have high oxygen solubility, such as nanoscale pores in fluoropolymers, is also being researched [57].

A primary concern with some investigational devices conducted in the academic setting is their safety, as some materials lack long-term biocompatibility and certain approaches could pose greater risks than benefits if a malfunction occurs.

Nevertheless, analyses of the VC-01, VC-02, ß-Air, and other investigational devices reaffirm the importance of adequate oxygenation for successful islet engraftment and functionality. However, oxygen delivery methods must not interfere with the critical integration of the islet graft with the native vascular system. This integration is essential for proper not only for function and sustainable oxygenation through micro-vessel perfusion. This suggests that the oxygen supply is particularly vital in the early stages post-transplant, when the graft lacks vascular oxygen support and is most susceptible to hypoxia. *Since islet graft revascularization takes time and hypoxia occurs rapidly, identifying solutions to this early-stage oxygenation challenge is pivotal for the success of islet transplantation therapy.*

Chapter 2

Oxygen Transport in Pancreatic Islets

2.1 OXYGEN DIFFUSION IN ISLETS

Oxygen diffusion in liquid is a fundamental process by which dissolved oxygen moves from regions of higher concentration to regions of lower concentration, driven by the random motion of oxygen molecules. Oxygen diffusion from the microcapillary to the surrounding tissue is essential for the survival of all the cells inside our body. The diffusion of dissolved oxygen in fluid is governed by Fick's law of diffusion (**2.1**), which states that the rate of diffusion is proportional to the concentration gradient:

$$\boldsymbol{J} = -\boldsymbol{D}\nabla c \tag{2.1}$$

where $\boldsymbol{J}$ is the diffusion flux with the dimension of the number of oxygen molecules per unit area per unit time, $\boldsymbol{D}$ is the diffusion coefficient (or diffusivity) with the dimension of area per unit time, and c is the concentration of oxygen molecules. Typically, for small molecules like oxygen in an aqueous solution within the temperature range from ambient to body temperature, the diffusivity value $\boldsymbol{D}$ is on the order of $10^{-5}\ cm^2/s$.

The Stokes-Einstein-Sutherland equation is commonly employed to estimate the diffusivity of spherical particles in a liquid with low Reynolds number:

$$\boldsymbol{D} = \frac{k_B \boldsymbol{T}}{6\pi\eta r} \tag{2.2}$$

where k_B is the Boltzmann constant, $\boldsymbol{T}$ is the absolute temperature, η is the dynamic viscosity of solvent, and r is the stoke radius of the spherical particle (solute). For

oxygen dissolved in pure water at 310 K, the diffusivity can be estimated at $5.45 \times 10^{-5}\ cm^2/s$.

It is also important to understand how oxygen concentration changes in a timely manner. By mass conservation (**2.3**) and the assumption of constant diffusivity, we can derive Fick's second law of diffusion (**2.4**):

$$\frac{\partial}{\partial t}c + \nabla \boldsymbol{J} = 0 \tag{2.3}$$

$$\frac{\partial}{\partial t}c = \boldsymbol{D}\nabla^2 c \tag{2.4}$$

where the dimensionality of this equation pertains to the concentration change per unit time. Fick's second law provides the foundation for understanding how diffusion evolves over time and space.

While the specific solution to Fick's second law hinges on initial and boundary conditions, dimensional analysis can be utilized to ascertain a characteristic diffusion length (x) for rough estimates:

$$x \sim \sqrt{Dt} \tag{2.5}$$

where this characteristic length is a useful metric for preliminary calculations, giving an estimate of how far oxygen molecules diffuse over a given period. Understanding this diffusion length is particularly valuable for designing oxygenation medical devices for biological organisms where oxygen diffusion is limited.

2.2 OXYGEN DIFFUSION AND CONSUMPTION IN ISLETS

When considering the dynamics of dissolved oxygen that is concurrently being consumed within a medium, we must introduce an additional bulk consumption term to the mass conservation equation:

$$\frac{\partial}{\partial t}c + \nabla \boldsymbol{J} + R = 0 \tag{2.6}$$

where R is the bulk consumption term. Consequently, the comprehensive transport equation governing oxygen becomes:

$$\frac{\partial}{\partial t}c = D\nabla^2 c - R \tag{2.7}$$

when substituting (**2.1**) into (**2.6**). In (**2.7**), the consumption term is initially assumed to be constant. However, in biological systems, the consumption rate typically varies with the concentration of oxygen, often conforming to a hyperbolic relationship as defined by the Michaelis-Menten model for metabolic kinetics:

$$R = OCR_{max}\frac{c}{c + K_m} \tag{2.8}$$

where OCR_{max} represents the maximal oxygen consumption rate of biological tissue, and K_m is the Michaelis constant where the consumption rate is halved.

Noticed that the Michaelis-Menten mode (**2.8**) is a special case of a general four-parameter Hill equation [58]:

$$R = R_0 + \frac{c^{\alpha}}{c^{\alpha} + K_D{}^{\alpha}} \tag{2.9}$$

where R_0 is the consumption effect at zero concentration, K_D is the dissociation constant (analogous to Michaelis constant), and α is the Hill coefficient, signifying the cooperativity among binding sites. A high Hill coefficient ($\alpha > 1$) indicates

positive cooperativity, meaning that the binding of one oxygen molecule increases the affinity of the enzyme for the next oxygen molecule. Setting $R_0 = 0$ and $\alpha = 1$ reduces the hill equation (**2.9**) back to the Michaelis-Menten form (**2.8**).

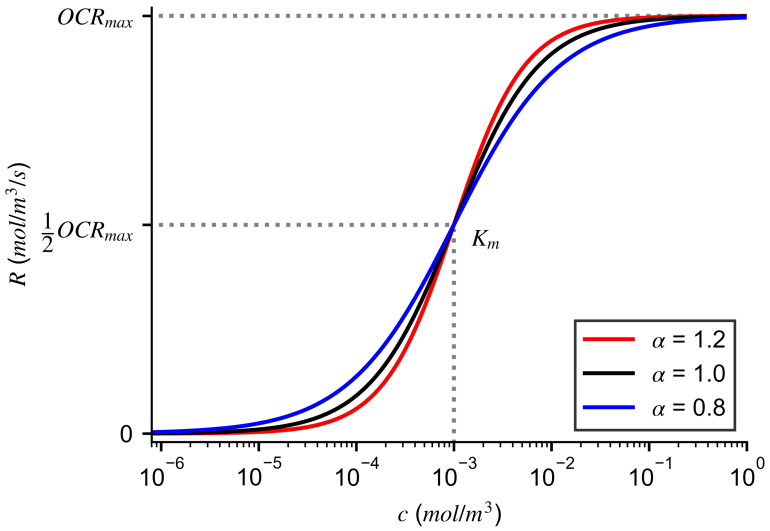

Figure 2-1. Hill equation plot of oxygen consumption rate (R) as a function of oxygen concentration at different hill coefficients (α = 0.8, 1.0, and 1.2).

In **Figure 2-1**, we visualize the curve for Hill equation depicting the rate of oxygen consumption (R) as a function of oxygen concentration for three different values of the Hill coefficient ($\alpha = 0.8, 1.0, 1.2$), with the assumption that $R_0 = 0$.

The OCR_{max} value can be influenced by various factors, such as the number and activity of mitochondrial electron transport chain (ETC) enzymes, the availability of co-factors and substrates, and the level of oxidative stress in cells. On the other hand, K_m represents the affinity of the ETC enzyme for oxygen and is a measure of the enzyme's ability to bind to the oxygen. A low K_m value indicates a high affinity of the ETC enzymes for oxygen, meaning that they are able to efficiently bind and consume oxygen at low concentrations. In contrast, a high K_m value indicates a low affinity for oxygen, meaning that the enzymes require higher oxygen concentrations to reach their maximum activity.

2.3 PARTIAL PRESSURE OF OXYGEN (OXYGEN TENSION)

Another concept in studying oxygen transport is partial pressure of oxygen (pO_2). The term is sometimes used interchangeably with oxygen tension. To relate the partial pressure of oxygen to the concentration of dissolved oxygen in a liquid, Henry's law (**2.10**) is used with the assumption that the gas does not react with the solvent and does not bind to molecules in the solution:

$$c = H\ pO_2 \tag{2.10}$$

where H is the Henry's law solubility constant (or solubility S), c is the oxygen concentration and pO_2 is the partial pressure of oxygen.

Note here the solubility has a dimension of molar concentration over pressure (M/Pa) rather than the commonly used solubility of solid solute in liquid solvent with the dimension of weight per volume (g/dL).

One insight that Henry's law shows is that it is the partial pressure of oxygen are equal at the gas-liquid interface, not the concentration of oxygen. It is also applicable to liquid-liquid or liquid-solid interfaces when the solubility of oxygen is different in those materials. In other words, the continuity of oxygen tension needs to be hold across the interfaces.

It is also important to highlight the resemblance between the Henry's law constant and the partition coefficient. The partition coefficient (P) is defined as the ratio of concentrations of a solute in a mixture of two immiscible solvents. Both of these constants lie in their common role in describing equilibrium between phases [59].

2.4 OXYGEN PERMEABILITY

Once we understand oxygen diffusivity and solubility, we can then introduce the concept of oxygen permeability:

$$P = DS \tag{2.11}$$

where P is permeability, D is diffusivity, and S is solubility of oxygen. Noted that the solubility (S) here is the same as Henry's constant (H).

2.5 NON-DIMENSIONAL EQUATIONS OF OXYGEN TRANSPORT IN PANCREATIC ISLETS

Knowing all the fundamentals and governing equations, we can perform a non-dimensional analysis of oxygen diffusion and consumption within a spherical pancreatic islet. Illustrated in **Figure 2-2** is a schematic representation of such an islet.

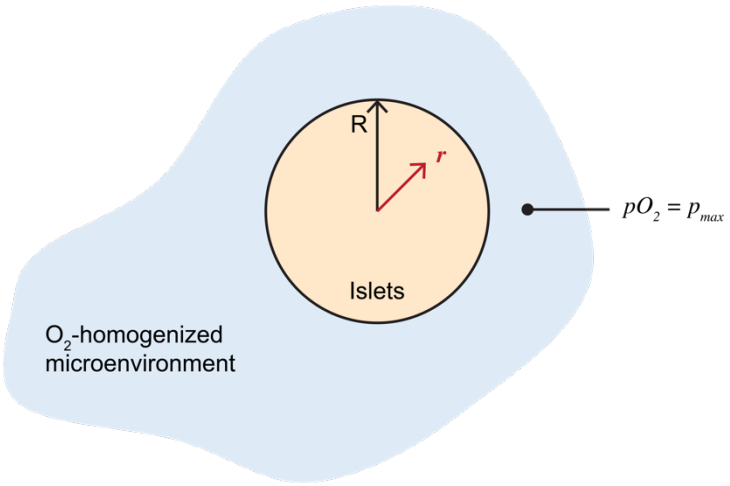

Figure 2-2. Schematic of oxygen transport model of a spherical pancreatic islet in an oxygen-homogenized microenvironment.

We use a spherical coordinate in this analysis. Since the pO_2 is homogenized in the microenvironment, the boundary condition and symmetric condition for the islets are described in (**2.12**) and (**2.13**).

$$pO_2(r = R) = p_{max} \tag{2.12}$$

$$\frac{\partial pO_2}{\partial r}(r = 0) = 0 \tag{2.13}$$

The governing equation can be derived from (**2.7**), (**2.8**), and (**2.10**) under the assumption of steady-state conditions.

$$D \cdot \frac{1}{r^2}\frac{\partial}{\partial r}\left(r^2 \frac{\partial}{\partial r}\left(S \cdot pO_2(r)\right)\right) = OCR_{max}\frac{S \cdot pO_2(r)}{S \cdot pO_2(r) + K_m} \tag{2.14}$$

We introduce the following non-dimensional variables and parameters in (**2.15**) and (**2.16**).

$$x = \frac{r}{R} \tag{2.15}$$

$$q(x) = \frac{pO_2(r)}{p_{max}} \tag{2.16}$$

As such, we can rewrite the equations into:

$$\frac{\partial^2 q(x)}{\partial x^2} + \frac{2}{x}\frac{\partial q(x)}{\partial x} = N\frac{q(x)}{q(x) + O} \tag{2.17}$$

where N and O are described in (**2.18**) and (**2.19**).

$$N = \frac{OCR_{max} \cdot R^2}{D \cdot S \cdot p_{max}} \tag{2.18}$$

$$O = \frac{K_m}{S \cdot p_{max}} \tag{2.19}$$

The dimensionless number (N) can be regarded as the effective ratio of the oxygen consumption to oxygen diffusion for the islets, indicating the severity of oxygen depletion within the islets. For a single isolated primary islet ($R = 150\ \mu m$) being transplanted at the subcutaneous cite ($p_{max} = 40\ mmHg$), with the typical oxygen

parameters, OCR_{max} being 0.02 mol/m^3, D being 1.3×10^{-9} m^2/s, S being 7.6×10^{-6} $mol/(kg \cdot m^2)$, N is approximately 2.

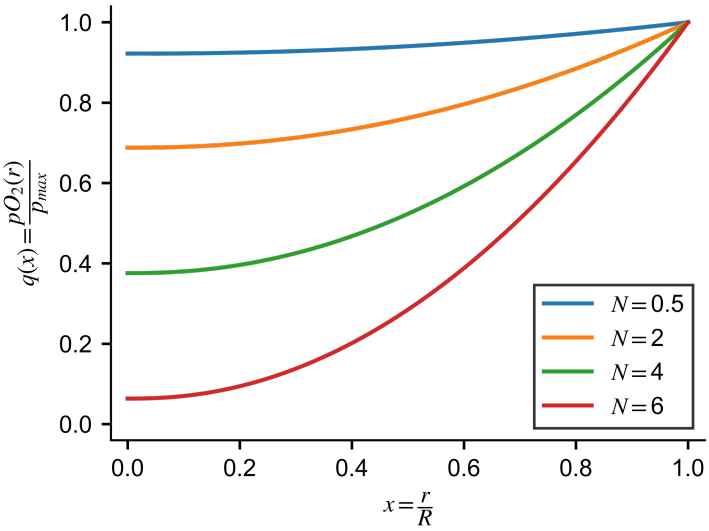

Figure 2-3. Normalized oxygen profile of an isolated islet for different *N* values.

Figure 2-3 illustrates the normalized oxygen profiles within islets for different N values, indicating that a single islet with N equal to 2, when implanted in subcutaneous sites, still maintains a relatively high pO_2 across the islet, exceeding 25 mmHg. This observation contrasts with literature reports of significant hypoxia in islets transplanted into subcutaneous locations, suggesting a need to revisit previous assumptions.

The presence of a boundary layer at the islet surface impedes oxygen diffusion. This layer is necessary to balance a flux from the micro-vessels (oxygen source) to the islet (oxygen drain). The diffusive boundary layer increases the diffusion distance and consequently reduces oxygen availability. In addition, when multiple islets are transplanted together, their crowded aggregation depletes the local pO_2 in the microenvironment, challenging the maintenance of 40 mmHg as the boundary condition in the previous model.

These phenomena indicate that individual cells within the pancreatic islet could experience fatal hypoxia, struggling to survive at extremely low oxygen tensions. That is, a critical survival threshold ($pO_2{}^c$) exists for these cells, oxygen tensions below this threshold lead to progressive cellular death and cessation of oxygen consumption. Hence, the oxygen consumption rate equation (**2.8**) requires modification to incorporate a delta function as described in (**2.20**).

$$R = OCR_{max}\frac{c}{c + K_m} \cdot \delta\left(pO_2 - pO_2{}^c\right) \tag{2.20}$$

In light of these insights, the model for the isolated pancreatic islet cell needs an update on the geometry to include a total of three layers: the innermost dead islet core ($0 \le r < Rt$), the middle oxygen-consuming layer of living islet ($Rt \le r < R$), and the outer diffusive boundary layer ($R \le r < \alpha R$). Here, Rt denotes the radius of necrotic core within the pancreatic islet and αR denotes the radius of outer diffusive boundary layer, assuming a fixed pO_2 boundary conditions provided by micro-vessels at $r = \alpha R$, with varying α (**Figure 2-4**).

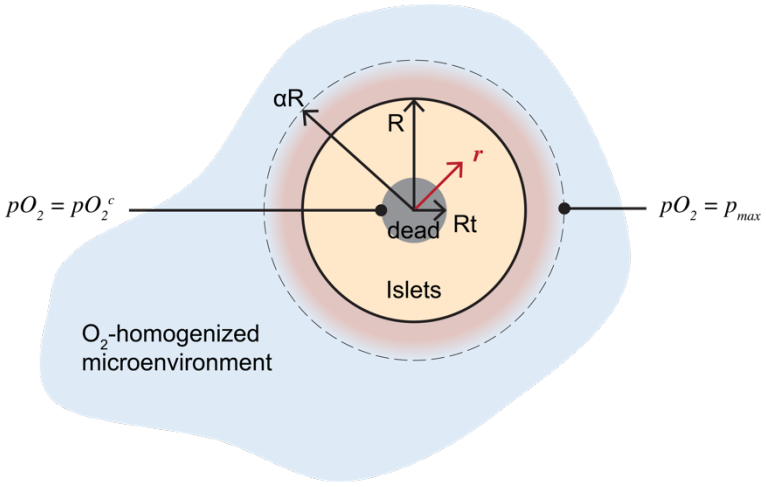

Figure 2-4. Revised schematic of oxygen transport model of a spherical pancreatic islet in an oxygen-homogenized microenvironment. The islet is with a necrotic core at the center and a diffusive boundary layer at the islet surface.

Then, the formalization of the steady-state oxygen transport equations in three regions can be articulated as follows:

$$D^{(1)} \cdot \frac{1}{r^2}\frac{\partial}{\partial r}\left(r^2 \frac{\partial}{\partial r}\left(S^{(1)} \cdot pO_2^{(1)}(r)\right)\right) = 0 \quad , 0 \le r < Rt \tag{2.21}$$

$$D^{(2)} \cdot \frac{1}{r^2}\frac{\partial}{\partial r}\left(r^2 \frac{\partial}{\partial r}\left(S^{(2)} \cdot pO_2^{(2)}(r)\right)\right) = OCR_{max}\frac{S^{(2)} \cdot pO_2^{(2)}(r)}{S^{(2)} \cdot pO_2^{(2)}(r) + K_m}$$

$$, Rt \le r < R \tag{2.22}$$

$$D^{(3)} \cdot \frac{1}{r^2}\frac{\partial}{\partial r}\left(r^2 \frac{\partial}{\partial r}\left(S^{(3)} \cdot pO_2^{(3)}(r)\right)\right) = 0 \quad , R \le r < \alpha R. \tag{2.23}$$

The boundary conditions are based on the continuities of pO_2 and diffusive flux:

$$D^{(1)} \cdot \frac{\partial}{\partial r}\left(S^{(1)} \cdot pO_2^{(1)}(r = 0)\right) = 0 \tag{2.24}$$

$$pO_2^{(1)}(r = Rt) = pO_2^{(2)}(r = Rt) = pO_2^{c} \tag{2.25}$$

$$D^{(1)} \cdot \frac{\partial}{\partial r}\left(S^{(1)} \cdot pO_2^{(1)}(r = Rt)\right) = D^{(2)} \cdot \frac{\partial}{\partial r}\left(S^{(2)} \cdot pO_2^{(2)}(r = Rt)\right) \tag{2.26}$$

$$pO_2^{(2)}(r = R) = pO_2^{(3)}(r = R) = \beta p_{max} \tag{2.27}$$

$$D^{(2)} \cdot \frac{\partial}{\partial r}\left(S^{(2)} \cdot pO_2^{(2)}(r = Rt)\right) = D^{(3)} \cdot \frac{\partial}{\partial r}\left(S^{(3)} \cdot pO_2^{(3)}(r = Rt)\right) \tag{2.28}$$

$$pO_2^{(3)}(r = \alpha R) = p_{max}. \tag{2.29}$$

Noticed that $\alpha > 1$ and $\beta < 1$. In fact, β can be determined based on an assumed α.

Region 2, the area containing living islet cells, represents the primary focus of interest (**2.22**). In essence, regions 1 and 3 serve as supplementary areas that aid in understanding the oxygen transport behavior within region 2.

Expanding on the previous non-dimensional analyses of (**2.15**) and (**2.16**), we establish the following non-dimensional variables and parameters specific to region 2, which is characterized by the presence of living islet cells:

$$x = \frac{r - Rt}{R - Rt} \tag{2.30}$$

$$q^{(i)}(x) = \frac{pO_2^{(i)}(r) - pO_2^c}{\beta p_{max} - pO_2^c} \quad , i = 2, 3. \tag{2.31}$$

Then, the non-dimensional equations are thus updated to:

$$\frac{\partial^2 q^{(2)}(x)}{\partial x^2} + \frac{2}{x + \widetilde{M}} \frac{\partial q^{(2)}(x)}{\partial x} = \widetilde{N} \frac{q^{(2)}(x) + \widetilde{O_1}}{q^{(2)}(x) + \widetilde{O_1} + \widetilde{O_2}} \tag{2.32}$$

where:

$$\widetilde{M} = \frac{Rt}{R - Rt} \tag{2.33}$$

$$\widetilde{N} = \frac{OCR_{max} \cdot (R - Rt)^2}{D^{(2)} \cdot S^{(2)} \cdot (\beta p_{max} - pO_2^c)} \tag{2.34}$$

$$\widetilde{O_1} = \frac{pO_2^c}{(\beta p_{max} - pO_2^c)} \tag{2.35}$$

$$\widetilde{O_2} = \frac{K_m / S^{(2)}}{(\beta p_{max} - pO_2^c)}. \tag{2.36}$$

It becomes particularly fascinating to compare the N values, representing the severity of oxygen depletion, between the prior model (**2.18**) and the revised model (**2.34**). In the denominators, (**2.18**) has the p_{max} term, while (**2.34**) has the $(\beta p_{max} - pO_2^c)$ term. Since $\beta < 1$ and $pO_2^c > 0$, the term $\beta p_{max} - pO_2^c$ is smaller than p_{max}. In the numerators, (**2.18**) has the R^2 term, while (**2.34**) has the $(R - R_t)^2$ term. Therefore, $(R - R_t)^2$ is smaller than R^2.

The value of β correlates with the thickness of the additional boundary layer, which, from a physiological perspective, is determined by the distance between the micro-vessels and the transplanted islet, as well as by the density of the micro-vessels.

Conversely, the value of Rt is linked to a range of geometric factors and oxygen parameters. Envision a fully oxygenated islet being transplanted into the subcutaneous site; Rt can only be determined once the system achieves equilibrium.

Generally, the goal is to sustain all islet cell viable. That is, $Rt = 0$ and $pO_2(r) > pO_2^c$ for all r. Then, $\widetilde{N}$ exceeds N. Consequently, the revised model reveals that indeed a more significant extent of oxygen depletion occurs within a typical islet.

To mitigate the severity of oxygen depletion within the islet, it's essential to position the oxygen source as close to the islet surface as feasible. This concept is encapsulated once again in equation (**2.34**), where an increase in β leads to a reduction in $\widetilde{N}$.

The terms α and β encapsulate the ratio crucial for understanding oxygen transport phenomena within a spherical islet model, establishing a baseline for swiftly grasping and designing oxygen transport systems.

However, for more intricate geometries and multisystem scenarios, we turn to finite element modeling to simulate oxygen transport behavior. See Chapter 2.6 for more information.

The last parameter to address in this model is the critical survival threshold ($pO_2{}^c$). Suprisley, $pO_2{}^c$ does not have a well-defined value in the existing literature. A frequently used value is 0.1 mmHg or 0.7 mmHg for various islet types [60], [61], [62], sourced from single-cell viability assays for liver cells [60]. To address this discrepancy, we introduce a novel methodology in Chapter 2.7 to determine this threshold more accurately, which will also involve employing the finite element method to profile oxygen transport.

2.6 FINITE ELEMENT METHODS FOR OXYGEN TRANSPORT

Oxygen diffusion and consumption can be properly modeled by the oxygen transport equations. It is the foundation of this study where we engineered devices to alter the oxygen microenvironment in the islets and in the tissue. Although a good understanding of the equation and the non-dimensional analysis certainly helps us project the device function with the islets, we rely on finite element method to obtain a holistic view of the device function and the information help improve further design iterations of device.

COMSOL Multiphysics is a finite element software commonly used for oxygen studies. There are typical steps to construct a simulation environment: (1) Create a 3D geometry based on the actual *in vitro* or *in vivo* configuration. (2) Define the physics. In COMSOL, we can use "Transport of Diluted Species" physics module. We can then define the properties of the oxygen such as diffusivity, solubility, concentration, consumption rate, and boundary conditions. (3) Mesh the geometry. (4) Set up the solver. (5) Run the simulation.

There are few tricks when it comes to contrast an efficient and accurate simulation: (1) Utilize the symmetry. In almost all the configurations, we are able to find one or more symmetry planes. Setting up symmetry planes in the geometry greatly reduces the computation power. (2) Homogenized the geometry. The aim of simulation is often not to get the exact results but to gain a holistic view of the device function. In some cases where the geometry is complex, we can homogenize the structure by simple law of physics. Herein, the equivalent circuit models become a powerful tool. Nonetheless, it is critical to make sure the assumption is correct. (3) Perform a subset of the simulation and then combine it. To be efficient, it is always a good idea to break down the entire geometry into a number of individual configurations and perform separate simulations. Although this might require educated guesses on the boundary conditions and may lead to incorrect results, doing iterations of separate simulations and then combining to get the final results is oftentimes proved to be

more efficient than doing everything altogether right from the beginning. (4) Vary a few critical parameters to make sure the results are robust. Oftentimes, if the initial conditions, boundary conditions, and other parameters are not set properly, the simulation results may not converge. As such, it is essential to vary those values to a plus and minus ten percent to see if the results are sill valid. Meanwhile, we can learn if the deviation is still within the margin of errors of our design.

Leveraging the robust capabilities of finite element analysis, we propose to employ this computational method to determine the critical survival threshold of oxygen tension in diverse types of pancreatic islet cells. The critical survival threshold is a pivotal parameter that delineates the boundary between cellular viability and central necrosis due to hypoxia. It is imperative to quantify this threshold accurately for the development of islet transplantation therapies and to understand the physiological resilience of islet cells under hypoxic conditions.

2.7 DETERMINING CRITICAL SURVIVAL PO2 FOR ISLET SPHEROIDS

This section is adapted from: **K.-M. Shang**, H. Kato, N. Gonzalez, F. Kandeel, Y.-C. Tai, and H. Komatsu, "A novel approach to determine the critical survival threshold of cellular oxygen within spheroids via integrating live/dead cell imaging with oxygen modeling," *American Journal of Physiology-Cell Physiology*, vol. 326, no. 4, pp. C1262–C1271, Apr. 2024 [63]. Permission for the reuse of the licensed material within this thesis/dissertation has been granted by the copyright holder, the American Physiological Society.

INTRODUCTION

Hypoxia, characterized by insufficient oxygen availability at the cellular, tissue, or systemic level, plays a pivotal role in both physiological adaptation and pathological processes within the human body. At the molecular level, the response to hypoxia is intricately regulated by the hypoxia-inducible factor 1 alpha (HIF-1α), a key transcription factor that orchestrates downstream molecular functions [64], [65]. Hypoxia represents multifaceted adaptive responses that are crucial for survival, with both beneficial and detrimental consequences dictated by the HIF-1α downstream molecular functions. HIF-1α activation triggers essential responses for oxygen delivery including increased erythropoietin to produce red blood cells [66], [67], secretion of vascular endothelial growth factor to facilitate angiogenesis [68], as well as for CD18-mediated inflammation [69]. In addition, the duality of hypoxia is evident in its role in normal tissues and cancer cells. Cancer cells exploit hypoxia-inducible factors to thrive in the hostile microenvironment by promoting angiogenesis, metabolic reprogramming, and resistance to cell death [70], [71] which contributes to disease progression.

Although hypoxia is widely acknowledged as a crucial phenomenon in biology and physiology, establishing a universal threshold between normoxia and hypoxia proves challenging. The diversity among cells and tissue types, exemplified by variations between normal and cancer cells, complicates the standardization of cut-off values. Consequently, defining specific critical survival pO_2 values for distinct cell types and

tissues is essential, offering insights into their hypoxia resistance in physiological assessments. While theoretically feasible to determine critical survival pO_2 for inducing single-cell death in vitro under precisely controlled hypoxia culture conditions, the ideal scenario involves identifying such thresholds within in vivo-mimicking 3D tissues where physiological cell-cell contact is maintained.

Defining critical survival pO_2 is essential not only for understanding cellular and tissue biology but also for developing cell therapies, particularly evident in pancreatic islet transplantations for patients with type 1 diabetes [35], [72], [73], [74]. Isolated islet spheroid, a micro-organ consisting of thousands of insulin-secreting cells from the donor pancreas, faces challenges due to the loss of native microvessels during isolation. Relying on interstitial oxygen, cells within the spheroid compete for oxygen, and cells in the spheroid center with increased diffusion distances (average size of 150 μm in diameter) are susceptible to hypoxic stress [36], [75]. Thus, islet spheroids are at risk of hypoxia-induced central necrosis, reducing total islet cell mass in culture and transplantation engraftment in islet cell therapy. Several oxygenation approaches have been introduced to prevent hypoxia-induced islet graft loss. Concentrated oxygen was injected into a compartment encasing the transplanted islets [76], [77], [78], and co-transplantation techniques incorporating oxygen-containing or oxygen-generating materials improved the viability of transplanted islets [55], [57], [79]. Although these approaches were experimentally demonstrated to be effective, understanding the critical survival pO_2 of islet cells is crucial for developing improved oxygenation strategies, particularly in estimating exogenous oxygen requirements that ensure the viability of grafts.

While understanding the critical survival pO_2 for cells and tissues is crucial, accurately measuring this pO_2 value within 3D tissues and spheroids presents significant challenges. Direct measurements, such as needle-like Clark electrode [80], [81] and optical fiber methods [82], necessitate the insertion of a sensor tip into the tissues to access the necrotic core; this process intrinsically alters the original oxygen gradient and, thus, compromises the accuracy of the measurement. Silicone microbeads incorporated into a 3D cell culture and electron paramagnetic resonance

imaging (EPR) are potential non-invasive approaches. However, the large size of the beads and the low resolution of EPR are critical barriers to measuring pO_2 in small 3D tissues at the μm level [83], [84], [85].

In this study, we present a novel and comprehensive methodology for determining the critical survival pO_2 for 3D cell spheroids; this method integrates three key techniques: 1) inducing cell death within spheroids under precisely regulated oxygen concentrations and geometric parameters [86]; 2) employing semi-automated imaging to distinguish live and dead cells within spheroids [87]; and 3) utilizing computational modeling to assess oxygen distribution within spheroids [61]. Our approach effectively addresses current challenges in defining the critical survival pO_2 within tiny 3D spheroids, offering a non-invasive technique with high spatial resolution data.

MATERIALS AND METHODS

Rat Islet Isolation Procedures

Rat islets were isolated from rat pancreata using our standard procedure [88]. Male Lewis rats (Charles River, Wilmington, MA) aged between 16 and 20 weeks and weighing between 400 and 500 grams, were used as islet donors. Under general anesthesia, 9 mL of collagenase solution (2.5 mg/mL, [Sigma-Aldrich, MO], HEPES at 100 mM [Irvine Scientific, Santa Ana, CA] in ice-cold Hanks' balanced salt solution [HBSS; Sigma-Aldrich]) was injected into the pancreatic duct through the common bile duct. The distended pancreas was dissected, followed by enzymatic digestion at 37°C for 10 minutes. The digested pancreas was centrifuged at 300×g for 3 minutes. Pellets were washed and subjected to density gradient centrifugation in HBSS solution and Histopaque-1077 (density: 1.077 g/mL, Sigma-Aldrich) for 25 minutes at 300×g and 24°C. Islets were hand-picked for purity. The use of animals and animal procedures in this project was approved by City of Hope/Beckman Research Institute Institutional Animal Care and Use Committee. Following isolation, all islets from a single donor were cultured in a 10 cm petri dish (Corning

Life Sciences) containing 8 mL of CMRL 1066 culture medium (Corning Life Sciences, Tewksbury, MA) and incubated overnight at 27°C in a CO2 incubator for recovery. Due to the heterogeneous size of the isolated islets, the standardized unit of Islet Equivalent (IEQ) was used to count the volume-based, normalized islet number, in which the islet with 150 μm in diameter is defined as 1 IEQ [89]. Islet yield per donor ranged from 750 to 1200 IEQ, assessed after overnight recovery. Islet purity was assessed before initiating hypoxia experiments and confirmed to be > 90% using our standard procedure with Dithizone staining (iDTZ, Gemini Bio-products, CA) [90].

Production of Pseudo-islets (PsIs)

A rat beta cell line (INS-1 832/13 Rat Insulinoma Cells, Sigma-Aldrich) was used to produce 3D Pseudo-islets (PsIs). After the expansion of the cells in the 2D conventional tissue culture-treated dishes with RPMI1640 medium (Life Technologies, Carlsbad, CA) supplemented with 10% heat-inactivated fetal bovine serum (FBS, Atlanta Biologicals, Lawrenceville, GA), 50 mM of 2-Mercaptoethanol (Sigma-Aldrich), 10 mM of HEPES (Sigma-Aldrich), 1 mM of sodium pyruvate (Sigma-Aldrich), 2 mM of L-glutamine (Sigma-Aldrich), cells were trypsinized into single cells. Dissociated single cells were seeded on a 35 mm-microwell plate (EZSPHERE 900SP; 500 μm-microwell diameters; AGC Techno Glass, Yoshida, Japan) at the seeding density of 1.25 × 106 cells / dish. After the two-day culture of the cells to form the PsIs in a CO2 incubator at 37°C, PsIs were retrieved for the subsequent experiments. The standardized unit of IEQ was used to count the volume-based, normalized PsIs number [89].

Culture Conditions of Islet Spheroids

One hundred IEQ per well of either isolated rat primary islets or PsIs were seeded onto the micropyramid-patterned, oxygen-permeable bottomed dish (24-well platform) [86], using 1 mL of their specific culture medium described above. The culture dish bottom had the inverse topography of Aggrewell 400 microwell array

(Aggrewell 400, STEMCELL Technologies, Vancouver, Canada) made of polydimethylsiloxane (PDMS), which allows for the separation of seeded islets in a uniform oxygen environment throughout the well bottom. The plate was placed within the air-tight modular incubator chambers (Billups-Rothenberg, San Diego, CA), and the designated mixed gas (1% O_2, 5% CO_2, and 94% N_2) was filled using the gas mixer (GB3000, MCQ Instruments, Rome, Italy). The distilled water added to the chamber to provide a humidified culture condition (6.2% $H_2O(g)$). Once the oxygen was reached to the designated partial pressure, the chamber was tightly sealed and placed into the incubator at 37°C. To monitor the partial oxygen pressure within the chamber during the subsequent culture period, the RedEye patch was attached to the inner surface of the modular incubator chamber to non-invasively measure the pO_2 in the chamber from the outside using the optical oxygen sensor (NeoFox, Ocean Optics, Dunedin, FL). The spheroids were cultured for 2 days with no culture medium changes. During the culture period, the pO_2 within the chamber was maintained at the designated value ± 10% deviation (i.e., 0.9 – 1.1% O_2), measured with RedEye patch. At the end of the culture period, the chamber was opened, and the actual pO_2 in the culture medium at the bottom level of the dish, where islets or PsIs were placed, was directly measured by inserting the flexible needle-type optical oxygen sensor (NeoFox, Ocean Optics) that reconfirmed the pO_2 within the 10% deviation to the designated values.

Viability Assessment of Islet Spheroids Using Image Analysis

Viability of islet spheroids (both primary islets and PsIs) was analyzed using live/dead staining by a semi-automated method previously reported [91], [92]. Cultured islet spheroids (100 IEQ per group) were incubated in 0.48 μM of fluorescein diacetate (FDA; Sigma-Aldrich) and 15 μM of propidium iodide (PI; Sigma-Aldrich) solution in phosphate-buffered saline for 5 min in the dark at room temperature. Subsequently, they were washed with phosphate-buffered saline and transferred to a 96-well plate to capture the fluorescent images (IX50, Olympus, Tokyo, Japan). By setting thresholds for green (FDA; live cells) and red (PI; dead cells), FDA-positive or PI-positive areas were automatically calculated by the

imaging software (cellSens, Olympus). FDA-positive area and PI-positive area were mutually exclusive within the islet spheroids for the analysis (sky blue for FDA-positive areas and magenta for PI-positive areas), and the islet area was defined as the sum of FDA-positive and PI-positive areas. The volumetric viability of an islet sample was calculated as follows: viability (%) = 100 – [(PI-positive area/islet area)3 × 100]. Shape factor, which numerically describes the shape of a particle under two-dimensional images in a microscope [93] was calculated for all spheroids by the software, and spheroids with shape factor < 0.7 (regarded as non-spherical) were excluded from the analyses. A total of 262 primary islets and 107 PsIs were analyzed.

Oxygen Consumption Rate Measurement

The oxygen consumption rate (OCR) assay was performed for the metabolism assessments of islet spheroids as previously described [94]. Approximately 100 IEQ of primary islets or PsIs were plated on a Seahorse XFe islet capture plates (Seahorse Bioscience, North Billerica, MA) and pre-incubated at 37°C in a non-CO_2-incubator for 3 hours. Measurement of the OCR was performed using a Seahorse XFe analyzer (Seahorse Bioscience North Billerica, MA) every 7.5 minutes at 3 mM glucose for 7 measurements. OCR data was normalized by the IEQ applied. OCRs of primary islets from 5 rats and 7 preparations of PsIs were individually measured. The OCR measurement was conducted in an environment with oxygen levels (pO_2) exceeding 120 mmHg to minimize the oxygen gradient between the plastic cell plate and the microchamber containing spheroids. This approach reduced the potential for oxygen diffusion through the plastic cell plate, which could otherwise result in inaccurate OCR readings. Given that the measurements took place in a well-oxygenated setting, the observed OCR was utilized to estimate the maximal OCR values for the following simulations.

Computational Model of Oxygen Diffusion and Consumption

We employed the finite element method (COMSOL Multiphysics 5.3, MA) to derive the complete pO_2 profile within each islet spheroid and its surrounding

microenvironment. The governing equations for oxygen transport are delineated in eq. 2-10 and 2-11. The relationship of pO_2 profile between each boundary are tracked using eq. 2-13.

Statistical Analysis

Statistical analyses were conducted utilizing the SciPy library [95]. Sample sizes were calculated based on the estimated population variance obtained from a preliminary study. This calculation incorporated a z-score of 2.58 to achieve 99% confidence intervals. Data were presented as the mean ± the standard error of the mean (SEM) with relevant percentiles. For the statistical analysis, outliers were excluded if the data points were beyond the 75th percentile plus 1.5 times the interquartile range or below the 25th percentile minus 1.5 times the interquartile range. We employed Pearson's correlation coefficient (r) to quantify the linear relationship between variables. We employed Welch's t-test to address unequal sample sizes and variances. The results reported the P-value and an alpha level of 0.01 to interpret the statistical significance.

RESULTS

The method to determine the survival threshold of cellular oxygen within a spheroid was developed by integrating live/dead cell imaging with oxygen modeling.

We employed three techniques: 1) inducing cell death within spheroids under the precisely controlled oxygen and geometric parameters; 2) semi-automated live/dead cell imaging of spheroids; and 3) oxygen computational modeling of spheroids to determine the critical survival pO_2 within spheroids.

We used the air-tight chamber to apply the 1% oxygen at 37°C under atmospheric conditions to induce the initial step—hypoxic cell death within a controlled oxygen microenvironment (**Figure 2-5A**). Subsequently, we seeded spheroids ranging 70–300 μm in diameter at approximately 0.5 spheroids / mm2 on the micropyramid arrays (which equates to 100 spheroids per well of a 24-well plate) on the oxygen-

permeable, micro-pyramid patterned culture plates [86], with 1200 micropyramids per well. This configuration ensured the separation of each islet and prevented the interference of reduced oxygen by the oxygen-consuming neighboring spheroids. Moreover, oxygen-permeable PDMS micropyramids allowed for 1% oxygen air in the chamber to effectively diffuse from the bottom of the plate to the culture medium around the spheroids. We prepared two representative spheroids, primary rat pancreatic islets and pseudo pancreatic islets (PsIs) derived from a rat beta cell tumor. We cultured them for 2 days, inducing hypoxic cell death in the core of the spheroids. Our culture setup enables investigators to precisely control the pO_2 levels surrounding spheroids and minimize uncertainty and variation in the subsequent computational modeling of the pO_2 profile.

The second step was to acquire the two-color- live/dead fluorescent images of spheroids post 2-day hypoxic culture to extract the parameters required for the subsequent oxygen simulations. **Figure 2-5B** demonstrates the process to extract the radius of the spheroid ($r_{spheroid}$) and dead core (r_{dead}); the pancreatic islet, approximately 150 μm in diameter, consisting of thousands of endocrine cells, is presented. Typically, dead cells are concentrically present in the spheroid's core, which is characteristic of hypoxia-induced central necrosis due to the oxygen gradient within the spheroid. Subsequently, we used a software for semi-automated two-color recognition for live and dead areas to calculate the areas of the spheroid and the dead core. We introduced the concentric model that converts the actual shape traced into a completely circular shape for calculating the estimated radius of the spheroid ($r_{spheroid}$) and the dead core (r_{dead}).

We established a steady state pO_2 profile in the microenvironment within the spheroid by integrating the live/dead imaging parameters in the third step. **Figure 2-5C** illustrates the 3D geometry, boundary conditions, and a cross-sectional pO_2 profile, using a representative spheroid with $r_{spheroid}$ at 73 μm and r_{dead} at 39 μm. We designed the oxygen simulation geometry for the spheroids with the following parameters: each spheroid comprises a concentric inner dead core and an outer live shell; the central necrotic area does not consume oxygen (i.e., $R = 0$); oxygen

consumption rate in the outer live shell follows Michaelis-Menten metabolic kinetics; and spheroids were surrounded by culture medium, forming a tall cuboid geometry. We also constructed the oxygen simulation geometry for a micropyramid-shaped, oxygen-permeable PDMS. The height of the medium was 5.3 mm based on a medium volume of 1 mL in a 24-well plate. The cuboid's dimensions, both width and length, were 1.4 mm, which was triple the base side length of the micropyramid. The boundary conditions are established with a 1% oxygen concentration (equivalent to 7.6 mmHg) at both the top and bottom surfaces of the medium. We set the side faces as symmetrical planes under the assumption of negligible oxygen interference between spheroids. A comprehensive list of simulation parameters is presented in **Table 2-1**. The OCR data of primary islets and PsIs is available in **Figure 2-6**.

The final step was to define the critical survival pO_2 within the spheroid (**Figure 2-5D**). We calculated the critical survival pO_2 by averaging the pO_2 profiles at the boundary between the live shell and the dead core within the spheroid. Collectively, we developed a new method to define the survival threshold of cellular oxygen within a spheroid by integrating the three key techniques.

The method defined the critical survival threshold of cellular oxygen within pancreatic endocrine spheroids.

We applied our newly developed approach to determine the critical survival pO_2 in two types of spheroids for the proof of concept of this approach. We tested 1) primary pancreatic islets isolated from the native pancreas and 2) pseudo-islets derived from the insulin-secreting endocrine cell line. These spheroids secrete insulin; thus, when transplanted as beta cell replacement therapy, they can treat diabetes [22], [96]. However, spheroids are vulnerable to hypoxia, which has been one of the roadblocks to their wide-use beta cell replacement therapy; thousands of oxygen-consuming cells within the spheroids create a steep oxygen gradient and subsequent hypoxia-induced central necrosis. Our new method will determine the physiological oxygen sensitivity of these spheroids by defining the critical survival pO_2 of the cells within the spheroids.

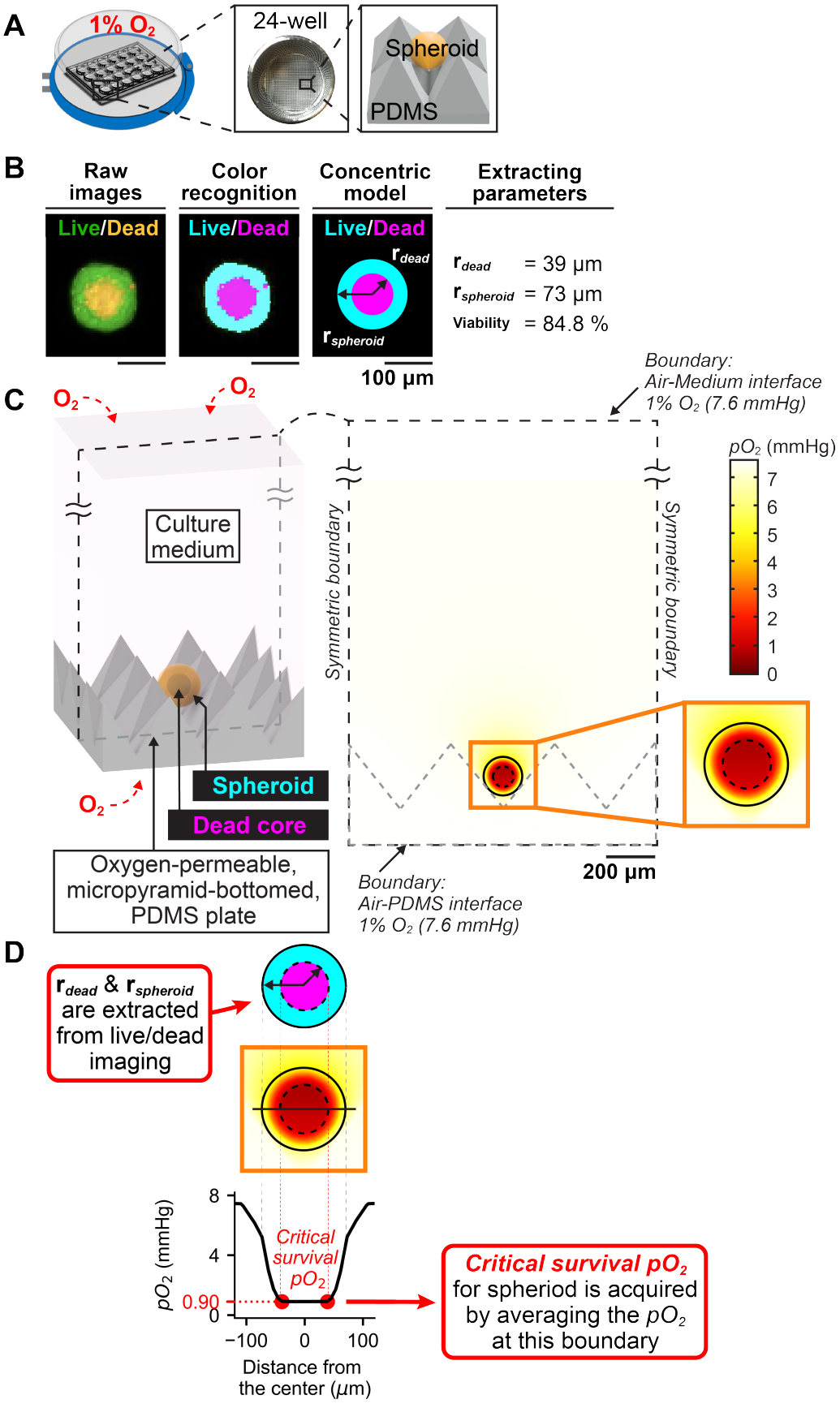
A
1% O2
24-well
Spheroid
PDMS
B
Raw images
Color recognition
Concentric model
Extracting parameters
Live/Dead
Live/Dead
Live/Dead
r dead
r spheroid
r dead = 39 μm
r spheroid = 73 μm
Viability = 84.8 %
100 μm
C
O2
O2
Culture medium
Spheroid
Dead core
O2
Oxygen-permeable, micropyramid-bottomed, PDMS plate
Boundary: Air-Medium interface 1% O2 (7.6 mmHg)
pO2 (mmHg)
7
6
5
4
3
2
1
0
Symmetric boundary
Symmetric boundary
200 μm
Boundary: Air-PDMS interface 1% O2 (7.6 mmHg)
D
r dead & r spheroid are extracted from live/dead imaging
8
4
0.90
0
pO2 (mmHg)
Critical survival pO2
−100
0
100
Distance from the center (μm)
Critical survival pO2 for spheriod is acquired by averaging the pO2 at this boundary

Figure 2-5. Workflow for determining the critical survival pO_2 in spheroids. (A) Spheroids are cultured in a controlled hypoxic environment with 1% oxygen (O_2). The structure and material of the culture dish, micropyramid shape and oxygen-permeable PDMS bottom plate, ensure individual islet separation and a uniform oxygen environment for each islet cultured. (B) An example of the parameter extraction process, which includes post-culture live/dead staining and imaging, semi-automated software-based color recognition of spheroids and dead cores, and conversion into a concentric geometry model to calculate the spheroid radius ($r_{spheroid}$) and dead core radius (r_{dead}). Sky-blue and magenta areas indicate the viable and dead cells, respectively. Scale bar: 100 μm. (C) A steady-state oxygen diffusion and consumption model for an individual spheroid requires parameters of the spheroid, the micropyramid-bottomed PDMS dish, and the culture medium. Schemas of the three-dimensional geometry (left panel), and the cross-sectional pO_2 profile (right panel) are shown. Scale bar: 200 μm. (D) Integration of live/dead images (a concentric geometry model, top panel) with oxygen simulations (middle panel) enables calculation of the critical survival pO_2, defined as the pO_2 at the live/dead boundary (bottom panel; a graph demonstrating the pO_2 in the mid-line cross-section of the spheroid). Simulation details and coefficients can be found in Table 2-1.

We cultured these spheroids in hypoxia culture at 1% oxygen for 2 days. **Figure 2-7A** demonstrates the representative live/dead stain images of primary islets at pre- and post-culture timepoints in the typical size at r = ~75 μm. We converted the post-culture image into the concentric model image to measure the $r_{spheroid}$, r_{dead}, and viability. Integrating cell imaging data with oxygen modeling identified the critical survival pO_2 of the primary islets at 2.39 mmHg (**Figure 2-7B**). Similarly, **Figure 2-7C** demonstrates the representative live/dead stain images of PsIs with the measured $r_{spheroid}$, r_{dead}, and viability data. The critical survival pO_2 of this specific PsIs was 0.89 mmHg (**Figure 2-7D**). Subsequently, we collected the data of $r_{spheroid}$, r_{dead}, viability, and critical survival pO_2 from individual spheroids of 262 primary islets and 107 PsIs. Live/dead images in various sizes of spheroids (r = 50, 75, and 100 μm) at pre- and post-hypoxic culture are available in **Figure. 2-8A** (primary islets) and **2-8B** (PsIs). Distribution of the spheroid size in primary islets and PsIs is presented in **Figure. 2-8C** and **2-8D**. **Figure 2-7E** displays all data plots of $r_{spheroid}$ and r_{dead} in primary islets and PsIs, demonstrating the positive linear correlations between $r_{spheroid}$

and r_{dead}. Overall viability of primary islets and PsIs on day 2 were 75.8 ± 1.1 % and 78.2 ± 1.1 %, respectively (**Figure 2-7F**, P = 0.116). The viability of all individual spheroids is available in **Figure. 2-8E** (primary islets) and **2-8F** (PsIs).

Table 2-1. Simulation coefficients of oxygen of primary islet, pseudo-islets (PsIs), culture medium, and polydimethylsiloxane (PDMS).

Materials	P	D	S	OCR_{max}	K_m	Ref
Primary Islets	0.99	1.3	0.76	0.0174*	0.001	[61], [97]
Pseudo-islets (PsIs)	0.99	1.3	0.76	0.0200*	0.001	[61], [97]
Culture Medium	3.05	2.8	1.09	-	-	[98], [99]
PDMS	104	7.9	13.2	-	-	[99], [100]

P, Oxygen permeability $(10^{-14}\ s \cdot mol/kg)$; D, Oxygen diffusivity $(10^{-9}\ m^2/s)$; S, Oxygen solubility coefficient $(10^{-5}\ s^2 \cdot mol/(kg \cdot m^2))$; OCR_{max}, Maximal oxygen consumption rate $(mol/(m^3 \cdot s))$; K_m, Michaelis oxygen constant (mol/m^3); Permeability equals diffusivity times solubility (P = D × S). *See **Figure 2-6**.

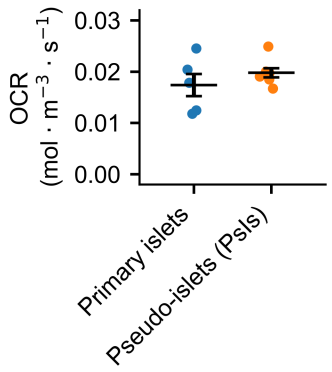

Figure 2-6. Oxygen consumption rate (OCR) of the spheroids. OCRs of primary pancreatic islets and pseudo-islets (PsIs) derived from the insulin-secreting cell line were measured under the well-oxygenated condition. Primary pancreatic islets were collected from five individual rats (n = 5). OCRs of PsIs were measured from the individual preparations (n = 7). The data was normalized by the volume of the spheroids applied for the measurements. The data were presented as mean ± standard error of the mean (SEM).

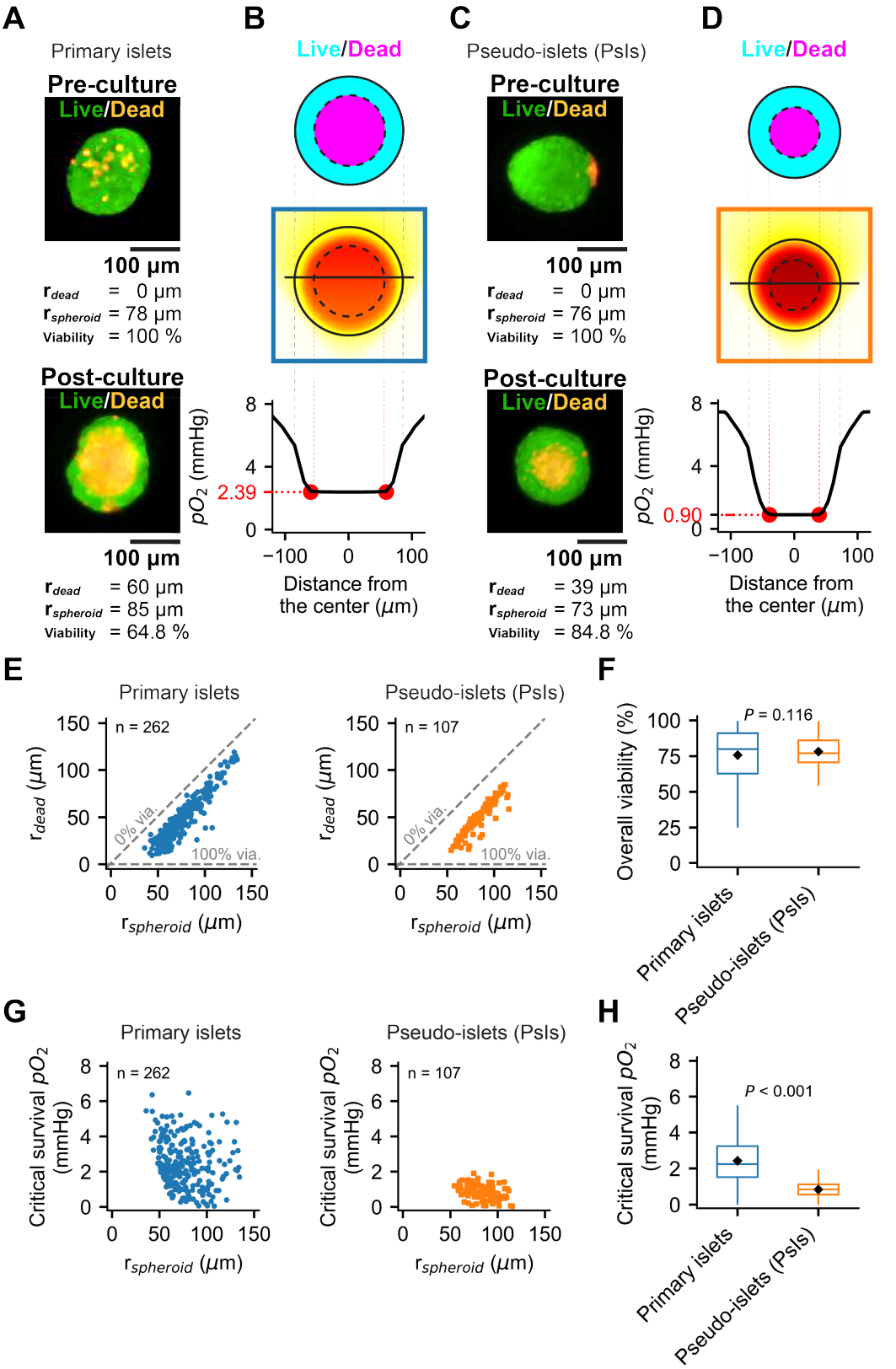
A
Primary islets
Pre-culture
Live/Dead
100 µm
r_dead = 0 µm
r_spheroid = 78 µm
Viability = 100 %
Post-culture
Live/Dead
100 µm
r_dead = 60 µm
r_spheroid = 85 µm
Viability = 64.8 %
B
Live/Dead
pO2 (mmHg)
2.39
Distance from the center (µm)
C
Pseudo-islets (PsIs)
Pre-culture
Live/Dead
100 µm
r_dead = 0 µm
r_spheroid = 76 µm
Viability = 100 %
Post-culture
Live/Dead
100 µm
r_dead = 39 µm
r_spheroid = 73 µm
Viability = 84.8 %
D
Live/Dead
pO2 (mmHg)
0.90
Distance from the center (µm)
E
Primary islets
n = 262
0% via.
100% via.
r_dead (µm)
r_spheroid (µm)
Pseudo-islets (PsIs)
n = 107
F
Overall viability (%)
P = 0.116
Primary islets
Pseudo-islets (PsIs)
G
Primary islets
n = 262
Critical survival pO2 (mmHg)
r_spheroid (µm)
Pseudo-islets (PsIs)
n = 107
H
Critical survival pO2 (mmHg)
P < 0.001
Primary islets
Pseudo-islets (PsIs)

Figure 2-7. Critical survival pO_2 within spheroids. The approach was applied to two types of pancreatic endocrine spheroids: primary pancreatic islets and pseudo-islets (PsIs) derived from the insulin-secreting cell line. (A) Representative live/dead images of primary islets. A primary islet in the pre-culture (top) and post-culture (bottom), with the extracted parameters demonstrated. Scale bar: 100 μm. (B) The calculation of the critical survival pO_2, using live/dead images (concentric geometry model, top panel), oxygen simulations (middle panel), and the pO_2 calculation (bottom graph). The data was retrieved from the specific spheroid shown in Figure 2-7A (post-culture image). Sky-blue and magenta areas indicate the viable and dead cells, respectively. (C) Representative live/dead images of PsIs. A PsIs in the pre-culture (top) and post-culture (bottom), with the extracted parameters demonstrated. Scale bar: 100 μm. (D) The calculation of the critical survival pO_2, using live/dead images (concentric geometry model, top panel), oxygen simulations (middle panel), and the pO_2 calculation (bottom graph). The data was retrieved from the specific spheroid shown in Figure 2-7C (post-culture image). (E) Scatter plots showing the correlation between $r_{spheroid}$ and r_{dead} in primary islets (left panel, n = 262 spheroids) and in PsIs (right panel, n = 107 spheroids). (F) Analysis of the overall viability of spheroids. Box plots demonstrate the interquartile range, median, and the data range. Black diamond plots indicate the average. $P = 0.116$ (Welch's t test). (G) Scatter plots of individual spheroids with the information of $r_{spheroid}$ and critical survival pO_2 in primary islets (left panel) and in PsIs (right panel). (H) Analysis of the critical survival pO_2 of spheroids. Box plots demonstrate the interquartile range, median, and the data range. Black diamond plots indicate the average. $P < 0.001$ (Welch's t test).

Lastly, we determined the critical survival pO_2 of individual spheroids and plotted all data according to the spheroid size ($r_{spheroid}$, **Figure 2-7G**). The average critical survival pO_2 values of primary islets and PsIs were 2.43 ± 0.08 mmHg and 0.84 ± 0.04 mmHg, respectively (**Figure 2-7H**); the median and interquartile range (IQR) value of critical survival pO_2 values of primary islets and PsIs were 2.24 (IQR 1.52 – 3.24) mmHg and 0.84 (IQR 0.56 – 1.12) mmHg, respectively. The critical survival pO_2 was lower in PsIs than in primary islets, indicating greater hypoxia resistance in PsIs ($P < 0.001$). PsIs are derived from beta cell malignant tumor cell line, and malignant cells typically exhibit more hypoxia resistance than the primary non-malignant cells [70], [71]. Interestingly, the **Figure 2-7G** showed the negative correlation between the critical survival pO_2 and the radius of spheroids for both primary islets and PsIs ($r = -0.15$ ($P = 0.010$) for primary islets; $r = -0.33$ ($P = 0.005$)

for PsIs). This may suggest that larger spheroids could provide a more favorable microenvironment at the individual cell level due to a more interconnected organoid structure, despite becoming more vulnerable to hypoxia at the whole spheroid level.

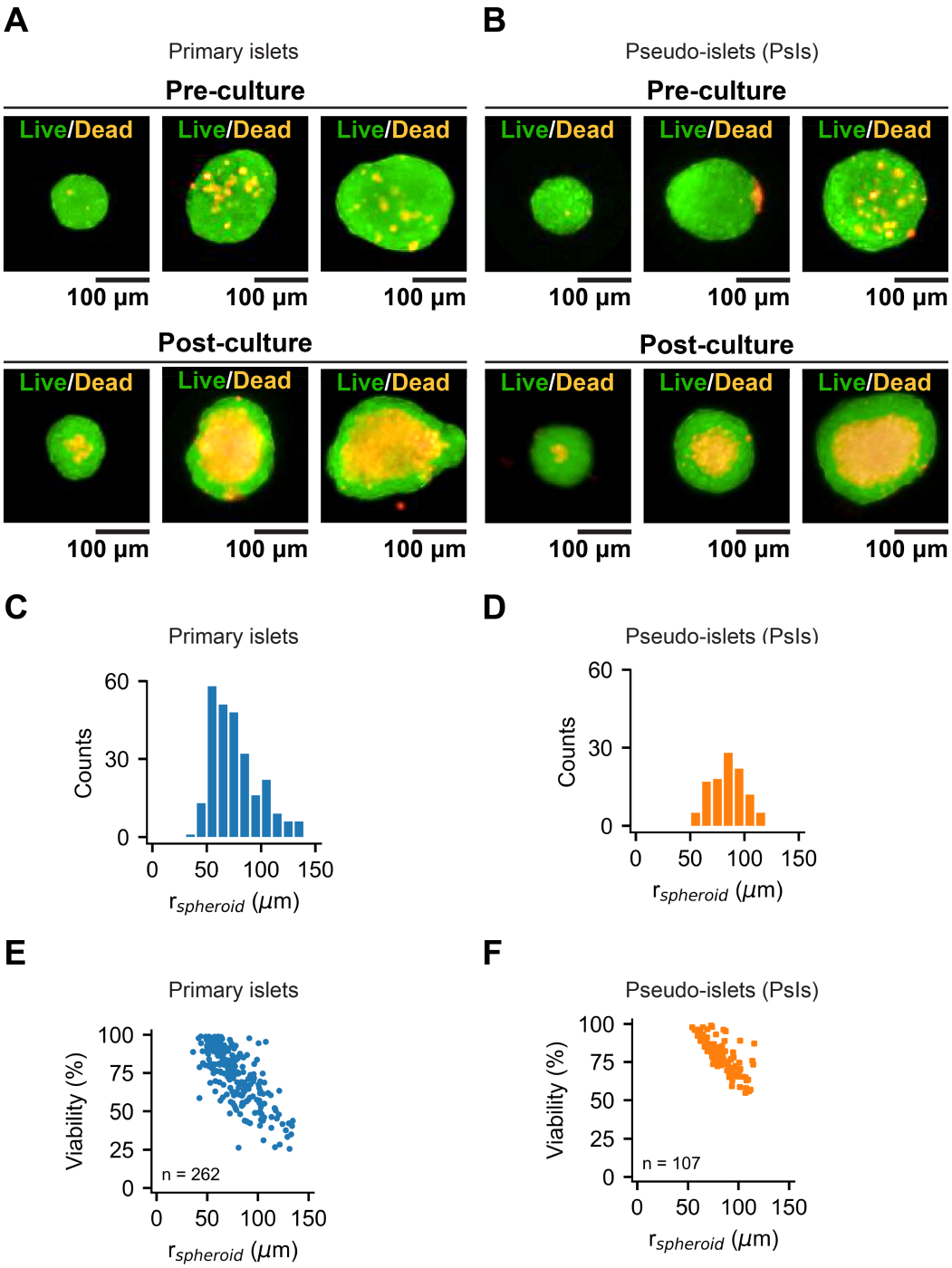

Figure 2-8. Live/dead images in various sizes of spheroids and distribution of the spheroid size analyzed in the study. (A) Representative live/dead images of primary islets in various sizes, approximately radius at 50, 100 and 150 μm. Pre-culture (top) and post-culture (bottom). Scale bar: 100 μm. (B) Representative live/dead images of pseudo-islets (PsIs) in various sizes, approximately radius at 50, 100 and 150 μm. Pre-culture (top) and post-culture (bottom). Scale bar: 100 μm. (C) Size distribution of the primary islets analyzed in this study, categorized by the radius in 10 μm pitch. (D) Size distribution of the PsIs analyzed in this study, categorized by the radius in 10 μm pitch. (E) Scatter plots of individual primary islets in their viability versus size (n = 262). (F) Scatter plots of individual PsIs in their viability versus size (n = 107).

Collectively, our novel method not only calculated critical survival pO_2 values of different spheroid types but also elucidated physiological characteristics of the cells and spheroids including the differences in physiological hypoxia resistance of primary vs. malignant cell spheroids.

The critical survival pO_2 contributes to the prediction of the islet graft viability in various oxygen environment.

As demonstrated, elucidating the hypoxia resistance with the critical survival pO_2 values has significance in characterizing the distinct cells. Another potential application using this approach is predicting spheroid survival in various oxygen conditions; this insight is particularly valuable in cell transplantations, including pancreatic islets. Since the hypoxia of the graft site is one of the leading causes of reducing graft survival in islet transplantations, several oxygenation strategies to improve the transplanted islet graft have been developed [55], [77], [101], [102], [103]. The critical survival pO_2 values enabled us to accurately simulate graft viability under various oxygen conditions. With the peri-spheroidal pO_2 defined as the oxygen on the surface of the spheroid (**Figure 2-9A**), we employed simulations of the spheroid viability (**Figure 2-9B**). The simulation data estimated the viability for primary islets and PsIs, according to the peri-spheroidal pO_2 and spheroid size ($r_{spheroid}$). This approach provides critical information for designing the oxygenation strategy. For instance, transplant site environment at 5 mmHg (peri-spheroidal pO_2)

for a typical-sized rat primary islet with a $r_{spheroid}$ of 75 µm calculates the estimated viability at 70% with the critical survival pO_2 value at 2.43 mmHg. Conversely, to achieve 100% viability for the rat islet, a peri-spheroidal environment of pO_2 > 15 mmHg is required.

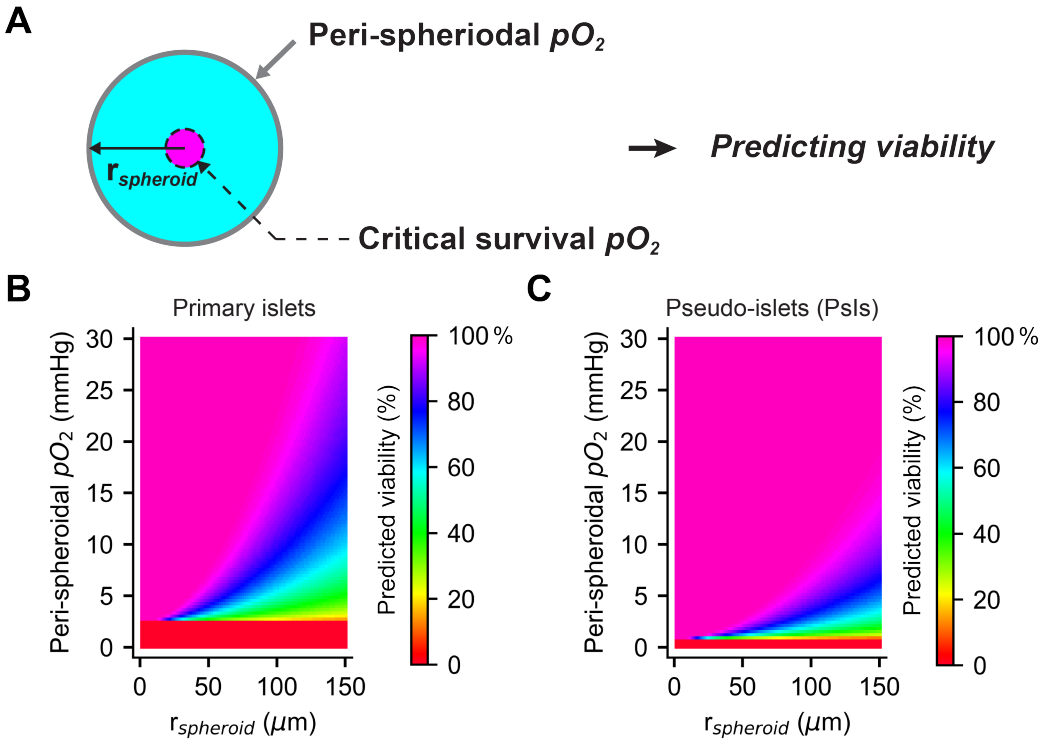

Figure 2-9. Prediction of the spheroid viability based on the critical survival pO_2 values. (A) A schema demonstrating the concept. By providing the three values, peri-spheroidal pO_2, radius of spheroid and critical survival pO_2 defined, the viability of the spheroid can be estimated. Sky-blue and magenta areas indicate the viable and dead cells, respectively. (B) The predicted viability of primary islets. (C) The predicted viability of pseudo-islets (PsIs).

DISCUSSION

In this study, we introduced an innovative method for determining critical survival pO_2 within islet spheroids. Integrating imaging techniques with computational simulations of 3D spheroids, we identified the pO_2 at live/dead cell boundary with high spatial resolution to define the critical survival pO_2. Cells remain viable above

this threshold while they succumb to death below it. Utilizing this model, we uncovered the oxygen sensitivity of pancreatic islet spheroids during acute phases. Importantly, the values identified a difference in physiological characteristics of critical survival pO_2 between primary islets and tumor-derived islet spheroids, confirming higher hypoxia resistance in tumor cells compared to primary cells. Non-malignant primary cells predominantly rely on oxidative phosphorylation for energy production in the presence of oxygen; in contrast, tumor cells generally display aerobic glycolysis for energy production, known as the Warburg effect, contributing to their hypoxia resistance [104]. The critical survival pO_2 accurately reflects such physiological processes, underlining the significance of our method in the physiological characterization of cells within spheroids.

Our study demonstrated another potential application of the critical survival pO_2 value for improving cell transplantation outcomes. The hypoxic environment limits the success of pancreatic islet transplantations due to their oxygen-diffusion-limiting spheroidal structure. Correlations among three critical factors in islet transplantations—namely, islet spheroid size ($r_{spheroid}$), surrounding oxygen microenvironment (peri-spheroidal pO_2), and viability of the spheroids—can be determined when the critical survival pO_2 of the spheroids is defined. Calculating the essential peri-transplantation oxygen levels to achieve a desired graft survival rate is a key aspect in developing cell transplantation strategies. In addition to the simple examples in the Results section, it is particularly important when encapsulation techniques are employed to protect islet graft from host immunity [39], [47], [105], [106]. Macro- and micro-encapsulation, coating islet spheroids with hydrogels or microporous membranes, have shown promise in allogeneic or xenogeneic islet transplantations. Although effective with respect to immunoisolation, oxygen supply for their survival should be carefully considered because the additional layer of hydrogel could restrict oxygen diffusion to the grafts. Understanding the critical survival pO_2 value of the graft cells could provide the estimated graft viability depending on the dimensions and properties of encapsulation materials and devices. In scenarios of severe oxygen deprivation, such as when a large number of islets are

encapsulated within a confined space [77], designing the oxygenation strategies is especially important in which the critical survival pO_2 value will serve as a key element to estimate the viability of transplanted cells under varying oxygen conditions.

While previous studies demonstrated methods to determine the critical survival pO_2 value of the cells, critical survival pO_2 values of various cell types and tissues have not been well established. The spearheading work demonstrated the critical survival pO_2 value of the rat-isolated hepatocyte cells at 0.1 mmHg [60]. A second study introduced technical advancement by utilizing a fine-tuned, feedback-controlled oxystat system, maintaining steady-state pO_2 between 0.01 mmHg and 150 mmHg in the culture setting [107] but relied on conventional trypan blue staining for single cell viability. The critical survival pO_2 value obtained from these studies was applied to islet cells for the oxygen simulation models [61]; however, the approximation deviated from the actual threshold of islet cells, as the values could be cell-type-specific, as demonstrated by others [108], as well as our current study. Advantages of the previous approach include the straightforward methods applicable to any cell type. However, the critical survival pO_2 value of the cell could be only measured in single cells, which could be a crucial limitation for several reasons: the critical survival pO_2 value is likely different in the single cell state vs. actual tissue environment with cell-cell interactions, and the manipulation of the tissue dissociation into single cells itself would damage cells to reduce viability [60]. Our method enables the calculation of the pO_2 within the cell spheroids, which mimics the 3D tissue environment. Furthermore, our approach has the following advantageous features: broad applicability across various cell types using non-cell-type-specific viability assessment by live/dead staining, high throughput analytic capability for large quantities of cells, and indirect measurement or the maintenance of a low oxygen tension environment, which eliminates the technical challenges of direct measurements that are prone to drift and susceptible to inaccuracies.

Some limitations in our approach are as follows: First, it does not provide cell type-specific critical survival pO_2 values, particularly when the spheroids are composed

of multiple cell types. For example, the primary islets consist of predominantly insulin-secreting beta cells but contain multiple endocrine cells and other cell types. Second, the model operates under the assumption that hypoxia is the primary factor influencing cell survival in the short term within hours – days [36], [60]. Multiple molecules, including nutrients, create concentration gradients and contribute to cell death in the longer observation period. Therefore, the method may not be accurate in defining critical survival pO_2 in chronic hypoxic conditions. Third, our method does not define the oxygen threshold of cell function. The cell function may be reduced in the oxygen condition above the critical survival pO_2; therefore, our approach requires other methods, especially for functional analyses. Fourth, the biological variation and fluctuations in the OCR of cells must be carefully considered. For instance, our study utilized primary islets isolated from young male rats. It is well-documented that OCR and insulin-secreting functions vary by sex and age, reflecting mitochondrial functionality [94]. Additionally, the OCR is influenced by the microenvironment, such as glucose conditions; high glucose conditions have been shown to increase cell metabolism including OCR [94], [109]. Given that OCR is a critical factor in oxygen simulations, employing accurate OCR values and accounting for these variations will contribute to more precise results of the critical survival pO_2. Lastly, we identified a negative correlation between the critical survival pO_2 and spheroid size, which may require thorough interpretation. Our results suggest novel physiological environmental differences between large and small spheroids—the interconnected 3D organoid structure in large spheroids likely creates a favorable microenvironment, despite the occurrence of hypoxia. However, potential technical biases that could influence this size-dependency of the critical survival pO_2 should be carefully considered, although we did not detect such flaws in our methodology.

In summary, we have developed a new method to determine the critical survival pO_2 within 3D cell spheroids, offering a high throughput non-invasive technique with high spatial resolution data.

2.8 SURVEY OF OXYGEN PARAMETERS IN PANCREATIC ISLETS AND CULTURE MEDIUM

OXYGEN CONSUMPTION RATE

The oxygen consumption rate (OCR) serves as an indicator of metabolic activity within islets and is an important parameter for assessing islet quality and for establishing computational models of islet function.

The OCR is often normalized to the weight of DNA present in the islets, given that each cell within an islet typically contains 2–28 pg of DNA, with an average of 6 pg per cell [110]. Considering there are approximately 1500 cells in an islet equivalent (IEQ) [111], this translates to roughly 10.4 ng DNA per IEQ [39]. An IEQ is defined as an islet spheroid measuring 150 micrometers in diameter [112], correlating to a volume of 1.77 nL.

Literature on the subject reveals varied OCR values. In [97], ranges approximately from 100–300 nmol/min/mg DNA. Reference [61] cites an OCR of 0.034 mol/m^3/s.

According to [113] clinical islets have an OCR of 138 ± 54 nmol/min/mg-DNA, while research islets have an OCR of 202 ± 87 nmol/min/mg-DNA. [114] reports the OCR of adult islets as 130 pM/min/µg-DNA, with a range of 40–300 pM/min/µg-DNA; it also records the OCR of stem-cell derived islets at 120 pM/min/µg-DNA, within a range of 40–200 pM/min/µg-DNA, based on a volume corresponding to approximately 20-25 islets.

Additionally, [39] presents the OCR for different species: 0.0294, 0.0340, 0.0172, 0.134, and 0.0222 mol/m^3/s in mouse, rat, juvenile porcine, human, and NN SC-beta cells, respectively, showcasing the diversity in metabolic rates across species and cell types.

Our own research aligns with these findings, indicating an OCR range of approximately 0.010–0.025 mol/m^3/s (**Figure 2-6**).

OXYGEN SOLUBILITY

The solubility of oxygen in cells can be approximated based on the volumetric water content within the cells, which is typically around 70%. This estimation relies on the known solubility of oxygen in water or saline. Some sources also suggest that this water content may be as high as 80% [54].

It is documented that the solubility of oxygen in cells is 1.02×10^{-3} mol/m^3/mmHg [39] and another value of 1.45×10^{-3} mol/m^3/mmHg [61].

Additionally, the solubility of oxygen in culture media is reported to be 1.27×10^{-3} mol/m^3/mmHg [54], while reference [99] indicates an oxygen solubility of 1.049 mM/atm in cells. Moreover, the solubility of oxygen in water at a temperature of 313 K is 1.04×10^{-3} mol/dm^3/atm [98].

OXYGEN DIFFUSIVITY

The diffusivity of oxygen in islet tissue is reported as 1.30×10^{-9} m^2/s [97], 2.00×10^{-9} m^2/s [39], [61], and 2.10×10^{-9} m^2/s [36].

In addition, the diffusivity of oxygen in culture medium is recorded at 2.78×10^{-9} m^2/s [54], [61], 3.1×10^{-9} m^2/s [61], and with another source noting a value of 2.8×10^{-9} m^2/s [99].

Chapter 3

Oxygen Transport in Parylene Materials

Oxygen diffusion in materials also follows Fick's first law of diffusion (2.1) and Fick's second law of diffusion (**2.4**). It is important to understand oxygen transport properties in materials when designing devices for biological systems that require oxygen. The permeability of a material to oxygen serves as a key indicator of its potential role as either a barrier or facilitator of oxygen transport. Poly(dimethylsiloxane) (PDMS) is a notable example of a material with high oxygen (and gas) permeability, making it a popular choice for various applications. Oxygen transport properties of PDMS have been extensively studied in [100], [115], [116], [117], [118].

However, fabricating a reliable PDMS layer thinner than 10 μm presents significant challenges due to its inherent properties. The porous nature of PDMS elastomer, utilizing crosslinker to crosslink the PDMS siloxane chains resembling that of a sponge, allows for the absorption of small molecules, which can influence its oxygen permeability and alter its surface properties [119].

Consequently, we would like to explore *parylene* as an alternative material for oxygen transport, owing to its favorable permeability attributes. Despite parylene's denser composition, which results in lower permeability compared to PDMS, its ability to be conformally coated in very thin layers potentially allows for comparable oxygen flux rates. Moreover, thinner films thus less bulky devices are beneficial in reducing foreign body reactions when materials are used in biomedical implants [120]. Additionally, parylene's inert surface and low surface energy minimize the risk of small molecule absorption and swelling, further establishing its suitability for applications requiring precise oxygen transport.

We now provide a concise overview of parylene, focusing on its characteristics relevant to the transport of dissolved gases, especially oxygen.

3.1 PARYLENE

Parylene refers to a class of polymer compounds originating from para-xylylene, renowned for its superior coating qualities, particularly in the fields of electronics, aerospace components, and medical devices due to its exceptional chemical and physical properties. In the realm of medical applications, parylene is classified as a USP Class VI material, which denotes the pinnacle of biocompatibility for plastic materials utilized within the human body. Furthermore, the biocompatibility of Parylene-coated medical devices has been rigorously evaluated in accordance with ISO 10993 protocols, an extensive suite of standards dedicated to the assessment of medical device biocompatibility [121], [122], [123], [124].

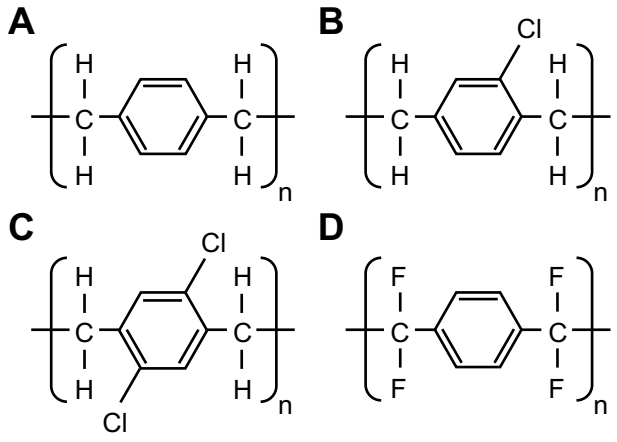

Figure 3-1. Repeating chemical unit structures of four types of commonly used Parylene. (A) Parylene N. (B) Parylene C. (C) Parylene D. (D) Parylene HT.

Parylene can be categorized by the presence of distinctive functional groups on the benzene ring or the polymer backbone. The four commonly utilized variants of parylene—Parylene N, Parylene C, Parylene D, and Parylene HT—each possess unique chemical structures that confer specific properties and uses. The distinctive molecular configurations of these parylene types are detailed in **Figure 3-1**.

Parylene's molecular architecture features a benzene ring backbone, which imparts remarkable stability and inertness to the material. Its resistance to chemical aggression (i.e., acids, bases, oxidizers) is central to its function as a superior barrier material, ensuring isolation of the coated substrates from moisture, corrosive chemicals, and other detrimental contaminants to a certain extend. The efficacy of parylene as a barrier is enhanced by its ability to form a uniform and defect-free layer, which maintains the integrity of sensitive components by preventing exposure to potentially harmful agents. This inertness, combined with parylene's uniform coating capability, positions it as an optimal solution for applications where protective coatings are critical to reliability and longevity.

These significant advantages originate from parylene's unique deposition process. Utilizing a chemical vapor deposition (CVD) approach that requires no solvents or catalysts, parylene is deposited in a vapor phase, ensuring a conformal coat over even the most complex surfaces. The result is a pinhole-free layer that attaches to the underlying material without the introduction of impurities or solvent-related defects.

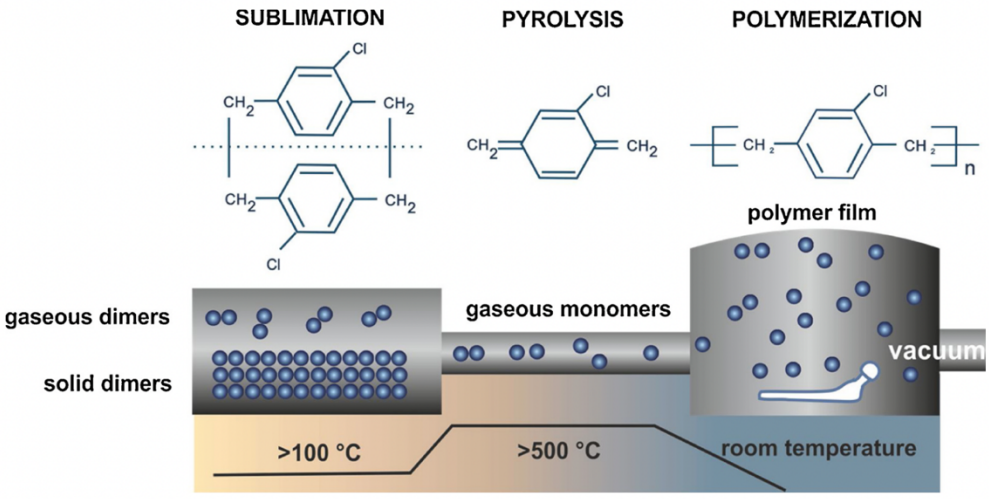

Figure 3-2. Key steps of parylene chemical vapor deposition (CVD) process. Image is adapted from [125] with permission from the copyright holder, Elsevier.

The CVD technique was pioneered by William F. Gorham in the 1950s [126]. It unfolds in three major steps within a vacuum [125], [127]. Initially, the parylene dimer (di-p-xylylene) is vaporized at temperatures between 120°C and 170°C. Following this, the dimer is cleaved into reactive monomer radicals in a pyrolysis furnace, with temperatures ranging from 550°C to 750°C depending on the dimer type. These monomers are then transported into the deposition chamber, where they collide and adhere to all surfaces exposed within the chamber. The deposited monomers undergo a migration process that leads to chain polymerization, including initiation, propagation, and termination, resulting in the formation of a conformal parylene coating. **Figure 3-2** demonstrates the parylene CVD process.

Parylene coatings, as deposited, exhibit two distinct morphological forms, amorphous parylene and crystalline parylene. The crystallinity can be defined as the volumetric percentages of the crystalline regions. Crystallinity significantly influences key characteristics such as thermal stability, mechanical strength, and barrier efficacy. The crystalline structure in parylene can develop under a range of conditions, including those related to deposition pressure, substrate temperature, and post-deposition processing methods [128], [129], [130], [131]. A prevalent method to enhance crystallinity in parylene is through low-temperature annealing at temperatures exceeding its glass transition range [132], [133]. This thermal treatment, conducted under vacuum conditions, provides sufficient energy for polymer chains to mobilize and form crystalline structures, thereby increasing the overall crystallinity. While higher crystallinity can enhance the durability of barrier properties, it may reduce the polymer film's flexibility, leading to a more brittle material that is prone to rupture. By tailoring the crystallinity, one can optimize the film's properties to suit specific applications.

On the contrary, in the amorphous region of parylene, molecules are arranged neither densely nor periodically, creating free volumes (V_f) amidst the atomic structures [134]. This, along with the occupied volume (V_o), allows us to quantify the porosity of the parylene film using the formula (**3.1**).

$$porosity\ (\%) = \frac{V_f}{V_f + V_o} \times\ 100\ \% \tag{3.1}$$

Estimations of parylene's free volume and intermolecular distances have been conducted via molecular dynamics (MD) simulations [135], [136], [137], [138]. The absorption and diffusion of physical gases within these free volumes are crucial for inferring the apparent solubility and diffusivity of gases in the parylene film.

Here, we aim to obtain oxygen coefficients of Parylene C and Parylene HT. We start with calculating the solubility of Parylene C and Parylene HT. Molecular dynamics (MD) simulations, referenced in [134], [135], indicate that parylene C and parylene HT possess free volumes of 0.91 nm^3 and 4 nm^3 in the amorphous region within defined lattice dimensions of 1.78 $nm \times 1.87\ nm\ \times 1.97\ nm$ and 2.46 $nm \times 2.72\ nm \times 1.88\ nm$, respectively. Utilizing equation (**3.1**), we calculate that the amorphous porosities of parylene C and parylene HT are 13.88% and 31.80%, respectively. The crystallinity of the as-deposited films is approximately 45% for Parylene C [139] and 60% for Parylene HT [140]. We can then estimate the gas solubility (S_{est}) in parylene by utilizing the air solubility (S_{air}) as a benchmark:

$$S_{est} = S_{air} \times porosity \times (1 - crystallinity). \tag{3.2}$$

Assuming that air behaves as an ideal gas, we can also derive the solubility of air (S_{air}) using the ideal gas law:

$$S_{air} = \frac{c}{P} = \frac{n}{VP} = \frac{1}{RT} \cong 3.872 \times 10^{-4} \left(\frac{s^2 \cdot mol}{kg \cdot m^2}\right) \text{ where } T = 310K. \tag{3.3}$$

Applying the above equation (3.2), we determine the estimated gas solubility in Parylene C to be $2.955 \times 10^{-5} \left(\frac{s^2 \cdot mol}{kg \cdot m^2}\right)$ and in Parylene HT to be $4.186 \times 10^{-5} \left(\frac{s^2 \cdot mol}{kg \cdot m^2}\right)$. The oxygen solubility in parylene C has been previously reported in [141] as $3.492\ [2.495 - 4.488] \times 10^{-5} \left(\frac{s^2 \cdot mol}{kg \cdot m^2}\right)$. This similarity further validates our method for estimating the apparent solubility in parylene films.

Understanding solubility enables one to measure permeability and thereby calculate the diffusivity of gas in parylene film. Permeability is typically reported in Barrers, a non-SI unit, due to the testing method. One Barrer is defined as (**3.4**). By applying the ideal gas law (**3.2**), moles per volume can be calculated (**3.5**) and permeability can be converted to an SI unit (**3.6**).

$$1 \text{ Barrer} = 10^{-10} \frac{cm^3_{(STP)} \cdot cm}{cm^2 \cdot s \cdot cmHg} \tag{3.4}$$

$$1\ cm^3_{(STP)} \cong 4.4 \times 10^{-5}\ mol \tag{3.5}$$

$$1 \text{ Barrer} = 3.35 \times 10^{-16} \left(\frac{mol \cdot m}{m^2 \cdot s \cdot Pa} = \frac{mol \cdot s}{kg} \right) \tag{3.6}$$

The oxygen permeability of Parylene C and Parylene HT at 25°C is documented in a data sheet from Specialty Coating Systems (SCS). According to this source [142], Parylene C exhibits an oxygen permeability of 2.8 $\frac{cc \cdot mm}{m^2 \cdot day \cdot atm}$, and Parylene HT has a value of 23.5 $\frac{cc \cdot mm}{m^2 \cdot day \cdot atm}$, as measured under the ASTM D 1343 standard. To express these values in SI units, Parylene C has an oxygen permeability of 1.33×10^{-17} $\frac{mol \cdot s}{kg}$, and for Parylene HT, the oxygen permeability is 1.12×10^{-16} $\frac{mol \cdot s}{kg}$.

Using the provided permeability data, we can calculate the oxygen diffusivity for Parylene C as 4.03×10^{-13} $\frac{m^2}{s}$ and for Parylene HT as 2.67×10^{-12} $\frac{m^2}{s}$. These calculations are corroborated by some diffusivity data from [141], which show that the oxygen diffusivity for Parylene C is measured at 3.51×10^{-13} $\frac{m^2}{s}$.

It is evident from the data that Parylene HT exhibits a notably higher oxygen permeability compared to Parylene C, precisely 8.4 times greater. Similarly, when considering diffusivity, Parylene HT is 6.6 times more permeable than Parylene C. This substantiates the rationale for selecting Parylene HT over Parylene C in our devices, given its superior oxygen permeability and diffusivity.

In addition to permeability, the contact angle and surface energy of parylene coatings are also key properties. Smooth Parylene C typically presents a water contact angle of approximately 90º [121], [143], [144]. Parylene HT, on the other hand, exhibits a water contact angle of approximately 120º [145], [146]. The presence of fluorine in Parylene HT generally makes it more hydrophobic compared to Parylene C.

3.2 OXYGEN DIFFUSION MODEL OF A SINGLE LAYER FILM

The diffusion through a single layer film can be shown as **Figure 3-3**. Typical boundary conditions can be with one open end with a fix concentration (or pressure) and with the other end with no flux (closed end).

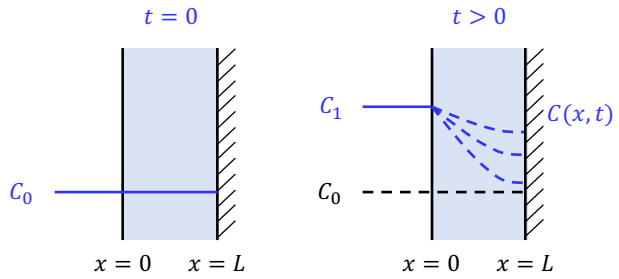

Figure 3-3. Schematic of oxygen diffusion through a thin film with thickness L. The left-hand side ($x = 0$) is an open end with a fixed concentration, whereas the right-hand side ($x = L$) is an impermeable end with no flux condition.

Here is the formulation of oxygen diffusion through a single layer:

$$\frac{\partial}{\partial t}C(x,t) = D\frac{\partial^2}{\partial^2 x}C(x,t), \qquad x \in [0, \mathrm{L}]. \tag{3.7}$$

The initial condition can be generalized as (**3.8**).

$$C(x, t = 0) = C_0 \tag{3.8}$$

Boundary conditions can be formulated as (**3.9**) and (**3.10**).

$$C(x = 0, t) = C_1 \tag{3.9}$$

$$\frac{\partial}{\partial x} C(x = \mathrm{L}, t) = 0 \tag{3.10}$$

Using the separation of variables, we could obtain to the general solution of Equation (**3.7**):

$$C(x,t) = X(x)T(t) = \frac{1}{2}a_0 + \sum_{n=0}^{\infty}\left[a_n(\lambda_n x) + b_n(\lambda_n x)\right]\exp\left[-(\lambda_n)^2 DSt\right] \tag{3.11}$$

where a_0, a_n, and b_n are constant and λ_n are the eigenvalues to be obtained from the initial and boundary conditions.

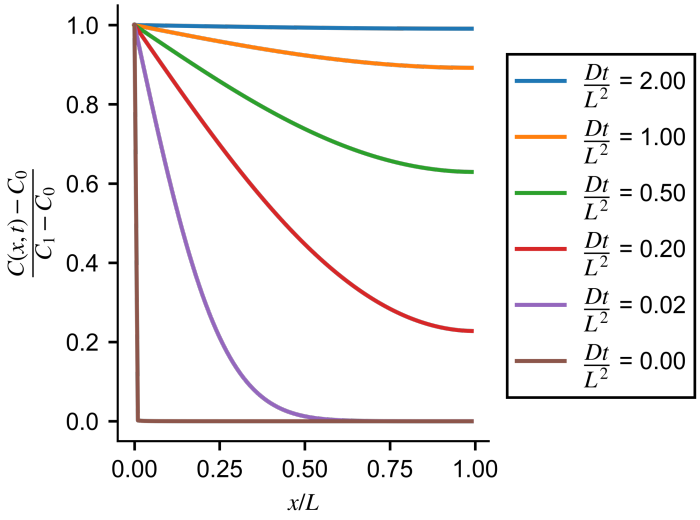

Figure 3-4. Solution plots of equation (3.12). Different values of Dt/L^2 are used to indicate the transient effects.

In this single layer model, with the boundary conditions (**3.9**) and (**3.10**) and initial condition (**3.8**), we can obtain the solution as described in (**3.12**) [118]:

$$\frac{C(x,t)-C_0}{C_1-C_0}$$
$$= 1-\frac{4}{\pi}\sum_{n=0}^{\infty}\left(\frac{1}{2n+1}\right)\sin\left[\left(\frac{2n+1}{2}\pi\right)\left(\frac{x}{L}\right)\right]\exp\left[-\left(\frac{2n+1}{2}\pi\right)^2\left(\frac{D}{L^2}\right)t\right] \quad (3.12)$$

The normalization plot in **Figure 3-4** visualizes the transient oxygen profile.

Another parameter of interest is the total uptake of the dissolved oxygen in the film after a time t, which can be calculated by the volume integration over the entire film (e.g., $M(t)=\int_0^L C(x,t)dx$). The analytical form is derived and described in (**3.13**).

$$\frac{M(t)}{M_\infty}=1-\frac{8}{\pi^2}\sum_{n=0}^{\infty}\left(\frac{1}{2n+1}\right)^2\exp\left[-\left(\frac{2n+1}{2}\pi\right)^2\left(\frac{D}{L^2}\right)t\right] \quad (3.13)$$

Figure 3-5 visualizes the transient volumetric oxygen uptake profile (**3.13**).

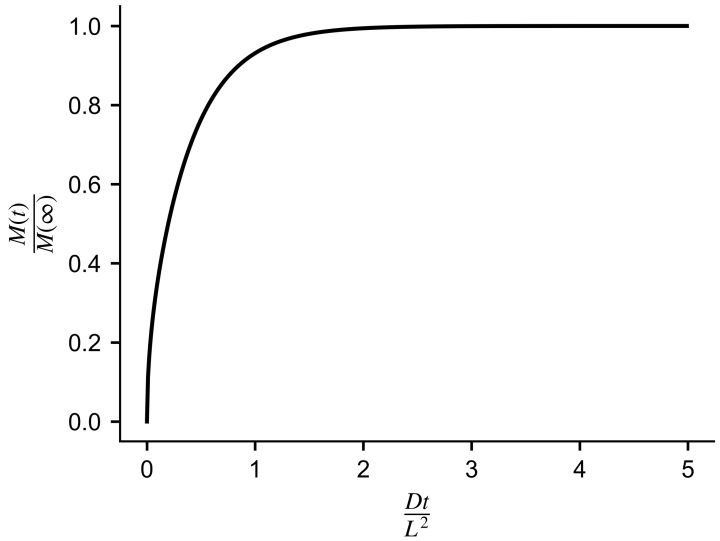

Figure 3-5. Total update of dissolved oxygen in a film with thickness L with respect to Dt/L^2.

3.3 OXYGEN DIFFUSION MODEL OF A BI-LAYER FILM

Oftentimes, the bi-layer oxygen diffusion model could be more useful and be generalized to many situations. For example, the boundary condition in the single layer model that one end is with a fixed concentration is often time not realistic because the flux it takes to remain at the concentration could be too large. As such, an additional boundary layer is sometime included to remedy the situation. Here, we derive the bilayer oxygen diffusion model with an open boundary at one end and with a wall (e.g., no flux) at the other end. **Figure 3-6** shows the general schematic. This model is also particularly useful to inform the oxygen transport properties of films with one end being the oxygen-sensing film, which we will discuss in the later chapter. The boundary at $x = -L_1$ is the open end, whereas the boundary at $x = L_2$ is the wall. The interface of these bilayer structures is set at $x = 0$.

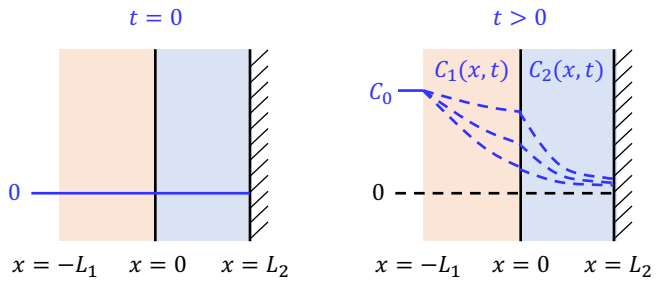

Figure 3-6. Schematic of oxygen diffusion through a bilayer film with the total thickness $L_1 + L_2$. The film on the left has a thickness of L_1. The film on the right has a thickness of L_2. The interface is set at $x = 0$. The bilayer film has an open end with fixed concentration at $x = -L_1$. The film is impermeable at the other end $x = L_2$.

We first write down Fick's second law of diffusion for both layers:

$$\frac{\partial}{\partial t}C_1(x,t) = D_1\frac{\partial^2}{\partial^2 x}C_1(x,t), \qquad x \in [-L_1, 0] \tag{3.14}$$

$$\frac{\partial}{\partial t}C_2(x,t) = D_2\frac{\partial^2}{\partial^2 x}C_2(x,t), \qquad x \in [0,\ L_2] \tag{3.15}$$

where $C_{1,2}$ is the concentration and $D_{1.2}$ is the diffusivity of solute in the films.

The initial and boundary conditions are expressed as follow. Notice that we set the open end to have a concentration of C_0. And at the interface, the continuity of pressure (**3.17**) and diffusive flux (**3.18**) needs to be conserved. The pressure can be expressed as the concentration divided by the solubility. On the end of the wall ($x = L_2$), there is no flux condition.

Initial condition:

$$C_{1,2}(x, t = 0) = 0. \tag{3.16}$$

Boundary conditions:

$$\frac{C_1(x = 0, t)}{S_1} = \frac{C_2(x = 0, t)}{S_2} \tag{3.17}$$

$$D_1 \frac{\partial}{\partial x} C_1(x = 0, t) = D_2 \frac{\partial}{\partial x} C_2(x = 0, t) \tag{3.18}$$

$$C_1(x = -L_1, t) = C_0 \tag{3.19}$$

$$\frac{\partial}{\partial x} C_2(x = L_2, t) = 0. \tag{3.20}$$

Then, we perform non-dimensional analyses:

$$p_1(y_1, \tau) = \frac{C_1(x, t)}{S_1 C_0} \tag{3.21}$$

$$y_1 = \frac{x_1}{L_1} \tag{3.22}$$

$$p_2(y_2, \tau) = \frac{C_2(x, t)}{S_2 C_0} \tag{3.23}$$

$$y_2 = \frac{x_2}{L_2} \tag{3.24}$$

$$\tau = \frac{D_1 t}{L_1^2} \tag{3.25}$$

$$\kappa = \frac{S_2}{S_1}\frac{L_1}{L_2}\frac{D_2}{D_1} \tag{3.26}$$

$$\rho = \sqrt{\frac{D_1}{D_2}}\frac{L_2}{L_1}. \tag{3.27}$$

Finally, we can utilize the Laplace transform to solve for the non-dimensional solution.

$p_1(y_1, \tau) =$

$$1 - \sum_{n=1}^{\infty} \frac{2\left(\cos(\rho\lambda_n)\cos(y_1\lambda_n) + \kappa\rho\sin(\rho\lambda_n)\sin\left(y_1\lambda_n\right)\right)\cdot e^{-\lambda_n^2\tau}}{\begin{bmatrix}\lambda\left(\kappa\rho^2+1\right)\sin(\lambda_n)\cos(\rho\lambda_n) + \rho(\kappa+1)\lambda_n\sin(\rho\lambda_n)\cos(\rho\lambda_n) \\ -\kappa\rho\sin(\lambda_n)\sin(\rho\lambda_n) + \cos(\lambda_n)\cos(\rho\lambda_n)\end{bmatrix}} \tag{3.28}$$

$p_2(y_2, \tau) =$

$$1 - \sum_{n=1}^{\infty} \frac{2\left(\cos(\rho\lambda_n(1-y_2))\right)\cdot e^{-\lambda_n^2\tau}}{\begin{bmatrix}\lambda\left(\kappa\rho^2+1\right)\sin(\lambda_n)\cos(\rho\lambda_n) + \rho(\kappa+1)\lambda_n\sin(\rho\lambda_n)\cos(\rho\lambda_n) \\ -\kappa\rho\sin(\lambda_n)\sin(\rho\lambda_n) + \cos(\lambda_n)\cos(\rho\lambda_n)\end{bmatrix}} \tag{3.29}$$

where the eigenvalues (λ_n) are solved for:

$$-\kappa\rho\sin(\lambda_n)\sin(\rho\lambda_n) + \cos(\lambda_n)\cos(\rho\lambda_n) = 0. \tag{3.30}$$

Figure 3-7 visualizes the normalized partial oxygen pressure profile with varying values of κ.

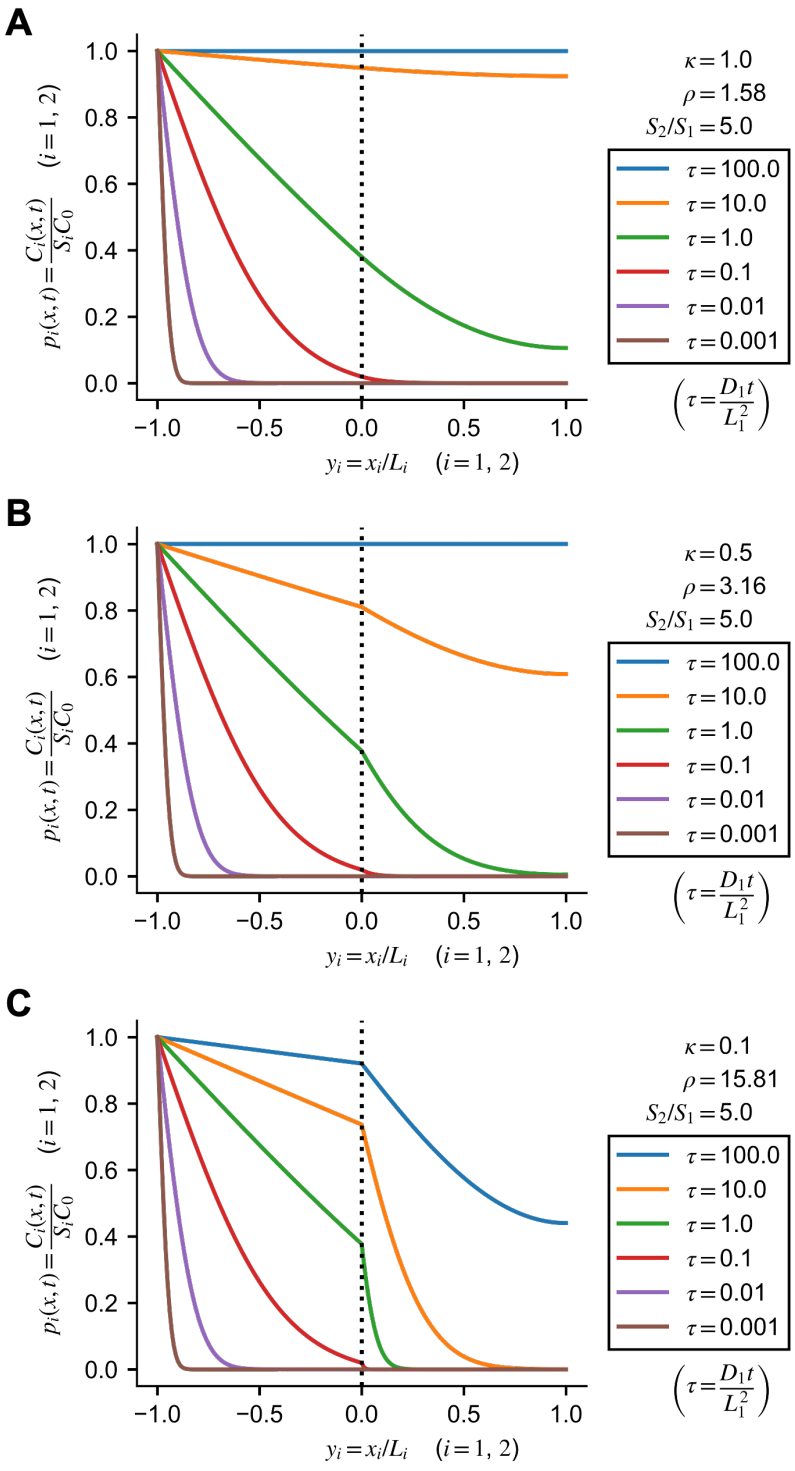

Figure 3-7. Normalized oxygen profile in the bilayer model with varying values of κ. (A) $\kappa = 5$. (B) $\kappa = 1$. (C) $\kappa = 0.1$.

3.4 EQUIVALENT CIRCUIT MODEL FOR OXYGEN DIFFUSION AND PERMEATION

If we draw an analogy of Fick's law of diffusion (**2.1**) to the generalized Ohm's law (**3.31**), we can characterize the diffusion coefficient (D) as a function of an effective diffusive resistivity (ρ_d) (**3.32**) by comparing the linear coefficients of the two equations. As such, an equivalent circuit model for diffusion can be developed. The driving forces for the two equations are chemical gradient ($-\nabla c$) and electric potential gradient ($-\nabla V$). The responses are the diffusive flux (J) and current density (J_c). The linear coefficients are diffusivity (D) and conductivity (σ).

$$J_c = \sigma E = -\left(\frac{1}{\rho}\right)\nabla V \tag{3.31}$$

$$D \sim \frac{1}{\rho_d} \tag{3.32}$$

Based on the diffusion resistivity (ρ_d), we can then calculate the diffusion resistance (R_d) with diffusion length (L) and cross-sectional area (A) as described in (**3.33**).

$$R_d = \frac{\rho_d L}{A} = \frac{L}{DA} \tag{3.33}$$

The diffusion resistances can therefore be applied using the circuit model, which will be useful when estimating the oxygen tension across different diffusion paths.

Based on (**2.10**) and (**2.11**), we can rewrite the Fick's first law (**2.1**) into (**3.34**).

$$J = -P\,\nabla pO_2 \tag{3.34}$$

Then the analogy of diffusion resistance (**3.33**) becomes permeation resistance:

$$R_p = \frac{L}{PA} \tag{3.35}$$

in which the circuit model can then also be applied to oxygen permeation.

3.5 EFFECTIVE THEOREM FOR OXYGEN COEFFICIENTS IN HETEROGENEOUS MATERIALS

When dealing with heterogeneous structures, composed of various materials, it's beneficial to homogenize the entire structure. This simplification facilitates back-of-the-envelope calculations and reduces the computational load during FEM simulations. Consider a one-dimensional diffusion problem involving multiple layers of different materials. The total thickness of the structure (L_{total}) is the sum of the thicknesses of each material (L_i), where *i* represents the i^{th} material.

$$L_{total} = \sum_i L_i \tag{3.36}$$

In this context, the effective permeation resistance is determined by aggregating the permeation resistance of each layer.

$$\frac{L_{total}}{P_{eff}A} = \sum_i \frac{L_i}{P_i A} \tag{3.37}$$

Here, P_{eff} denotes the effective permeability, and P_i represents the permeability of the ith material. It's then important to note that effective permeability can be expressed as a product of the effective diffusivity (D_{eff}) and the effective solubility (S_{eff}), as described in (**3.38**).

$$P_{eff} = D_{eff}\ S_{eff} \tag{3.38}$$

Furthermore, the effective solubility is derived from the cumulative volume fraction of each material's solubility as described in (**3.39**).

$$S_{eff} = \sum_i \left(\frac{L_i}{L_{total}}\right) S_i \tag{3.39}$$

By applying this approach, we can ascertain the effective diffusivity. Extending this technique to parallel configuration and three dimensions enables a comprehensive understanding of the transport properties within composite materials [147].

3.6 OXYGEN MEASUREMENT TECHNIQUES

Accurately measuring dissolved oxygen is critical throughout the course of this work. A comprehensive review can be found at [148], [149], [150]. The following offers a brief review of several established techniques used to measure dissolved oxygen.

The first approach is the iodometric titration, also known as the Winkler method, and established in ISO 5813:1983 [151]. The process involves a sequence of chemical reactions that produce a measurable change in color, which is then titrated to determine oxygen levels. This technique is notable for its precision; however, it is labor-intensive and less suitable for providing precise temporal or spatial information.

Another prevalent technique is the electrochemical method, which includes polarographic sensors. This involves recording the current potential curve or the potential-time curve of polarized electrodes during electrolysis. A prominent example of this technique is the Clark electrode [152]. It benefits from a gas-permeable polymeric membrane that houses a built-in electrolyte to encapsulate the electrodes, thereby safeguarding the working electrode from contaminants. One drawback is that the polarographic measurement of dissolved oxygen involves slow kinetic reactions and requires a significant potential, which can be sensitive to ionic concentrations. Moreover, these sensors consume oxygen during operation, potentially altering the local oxygen microenvironment.

Optical methods for measuring oxygen have risen to prominence due to their non-invasive, non-depletive attributes and their ability to deliver measurements with high spatial and temporal precision. These methods are founded on the principle of fluorescence quenching [153], [154]. The process commences with the introduction of a fluorescent dye to the area under examination. Subsequently, this substance is exposed to visible or ultraviolet light, triggering the excitation of electrons within the dye molecules. As these electrons revert to their stable state, they emit light—a phenomenon known as fluorescence. Oxygen molecules present in the environment

disrupt this fluorescent emission by quenching, which affects the fluorescence in a measurable way. This alteration allows for the deduction of oxygen levels either through quantifying the change in fluorescence intensity or by timing the fluorescence decay, with the latter adhering to the Stern-Volmer relationship. Practical implementation of optical detection involves utilizing optical fibers to detect shifts in fluorescence lifetimes [155] or deploying specialized cameras to capture changes in fluorescence intensity [156]. Both methods have been implemented throughout the course of this study. These non-destructive methods are highly valued for their precision and the minimal interference they pose to the system being studied [157].

Chapter 4

Oxygen-Regulating Hollow Mesh— Design, Fabrication, and Characterization

The critical challenge in islet cell transplant therapy is the initial lack of sufficient oxygen supply to the transplanted cells. This issue is most severe right after the transplantation because the islet cells are transplanted without any blood vessels to supply them with oxygen through blood flow. Instead, these de-vascularized islets must rely solely on diffusion from nearby tissues for oxygen. The denser core of the graft, being isolated, suffers from deadly hypoxia soon after the transplantation. Over time, the graft can undergo revascularization—a process where new blood vessels form, integrating the transplanted islets with the recipient's blood circulation system [158]. However, this revascularization process takes time, approximately 2 – 4 weeks, and the islet graft lose its mass because of hypoxia-induced islet death. Therefore, ensuring an adequate oxygen supply until revascularization is complete is crucial, as the viability and functionality of the islets are directly impacted by oxygen levels.

4.1 DESIGN AND WORKING PRINCIPLE

In response to this, we have designed and developed a MEMS device, termed **Oxygen-Regulating Hollow Mesh** (**Figure 4-1**). Our device leverages the fact that oxygen diffusivity in air is 10,000 times higher than in bodily fluids. Incorporating micron-sized hollow air channels within the mesh structure allows for efficient and effective regulation of local oxygen and supply of oxygen to the transplanted islet cells.

The diameter of these hollow microchannels is a mere 25 μm, akin to the dimensions of natural blood micro-vessels. The thin and flexible structures significantly reduce the potential for a foreign body reaction, a common complication arising from the

introduction of bulkier synthetic materials into the body [159]. These air-conveying hollow channels are enveloped in a thin coating of parylene, a material chosen for its excellent biocompatibility and its barrier properties to tissue fluids while still allowing oxygen to pass through. This dual functionality ensures that oxygen is delivered efficiently to the islets without the risk of fluid ingress blocking the micro-channels.

This device, when co-transplanted with islet cells, utilizes hollow channels that can harness oxygen from the microcapillaries in nearby tissue and redistribute it to the islet grafts. The diffusion of oxygen through the device's channels is almost instantaneous, promoting even oxygen tension throughout the adjacent tissue and forestalling local hypoxia with the islet graft.

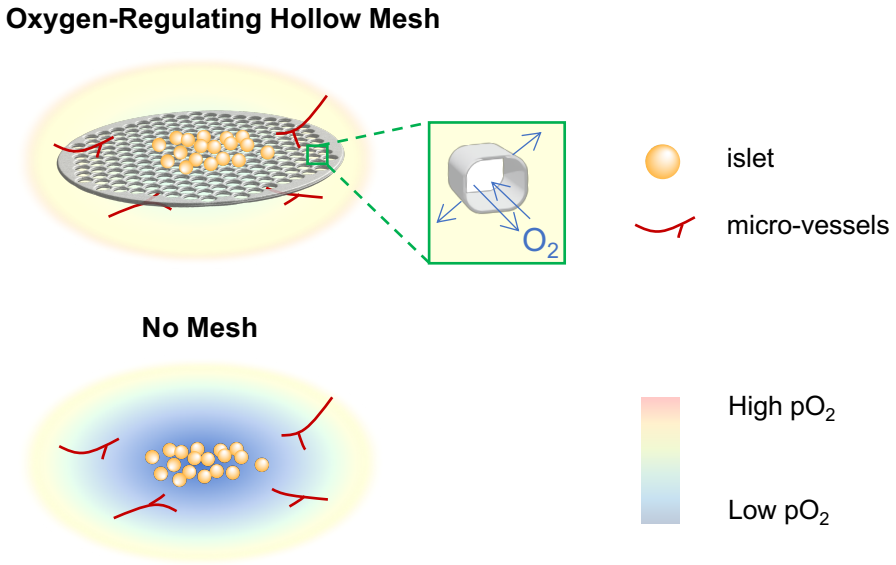

Figure 4-1. Schematic representation of the Oxygen-Regulating Hollow Mesh when being transplanted with islet graft. This illustration showcases the microscopic hollow channels and the oxygen-permeable membrane that encases them. It also contrasts the oxygen environment for transplantations between scenarios using hollow mesh and those without mesh.

Other than the oxygen-regulating functionality, the hexagonal lattice, punctuated with circular holes, forming a mesh shaped device, is designed with multifaceted intent. Firstly, in subcutaneous islet transplantation, graft aggregation impedes the diffusion of oxygen within the islets. A mesh-shaped device enhances graft layout by encapsulating the islets and thereby mitigating aggregation-induced lethal hypoxia [42]. Then, the openings are meticulously sized to be marginally smaller than a typical islet, providing structural support for the islets placed upon the mesh. This architecture not only facilitates vascularization by enabling micro-vessels to weave through the mesh, nourishing the transplanted cells, but it also ensures the unimpeded passage of insulin, which is crucial for the therapeutic efficacy of the transplanted islets. At the same time, essential hormones and nutrients can also be provided and waste products can be properly disposed.

DEVICE WORKING PRINCIPLE

The working principle of the Oxygen-Regulating Hollow Mesh is delineated in **Figure 4-2**. This figure contrasts the oxygen delivery to islet cells with and without the Oxygen-Regulating Hollow Mesh. In the absence of the mesh, oxygen must travel from the pre-existing micro-vessels through the interstitial fluid to reach the islet cells (**Figure 4-2A**). Especially at the initial stages before revascularization is complete, the islets are significantly distanced from the micro-vessels in the interstitial space. In this scenario, the oxygen supply is limited by the slower process of diffusion in the interstitial space.

In contrast, with the Oxygen-Regulating Hollow Mesh accompanying a transplanted islet, the islet not only sources oxygen from the existing diffusion pathway from adjacent micro-vessels, as well as an augmented oxygen supply through the mesh from more distant micro-vessels (**Figure 4-2A**). The mesh's hollow microchannels facilitate rapid oxygen diffusion in the gas phase, which is markedly faster than in liquid—a difference in diffusivity of 10,000 times. Thus, the Oxygen-Regulating Hollow Mesh essentially acts to 'shrink the distance' between remote micro-vessels

and the islet cells regarding oxygen diffusion, significantly enhancing the oxygen availability to the transplanted islets.

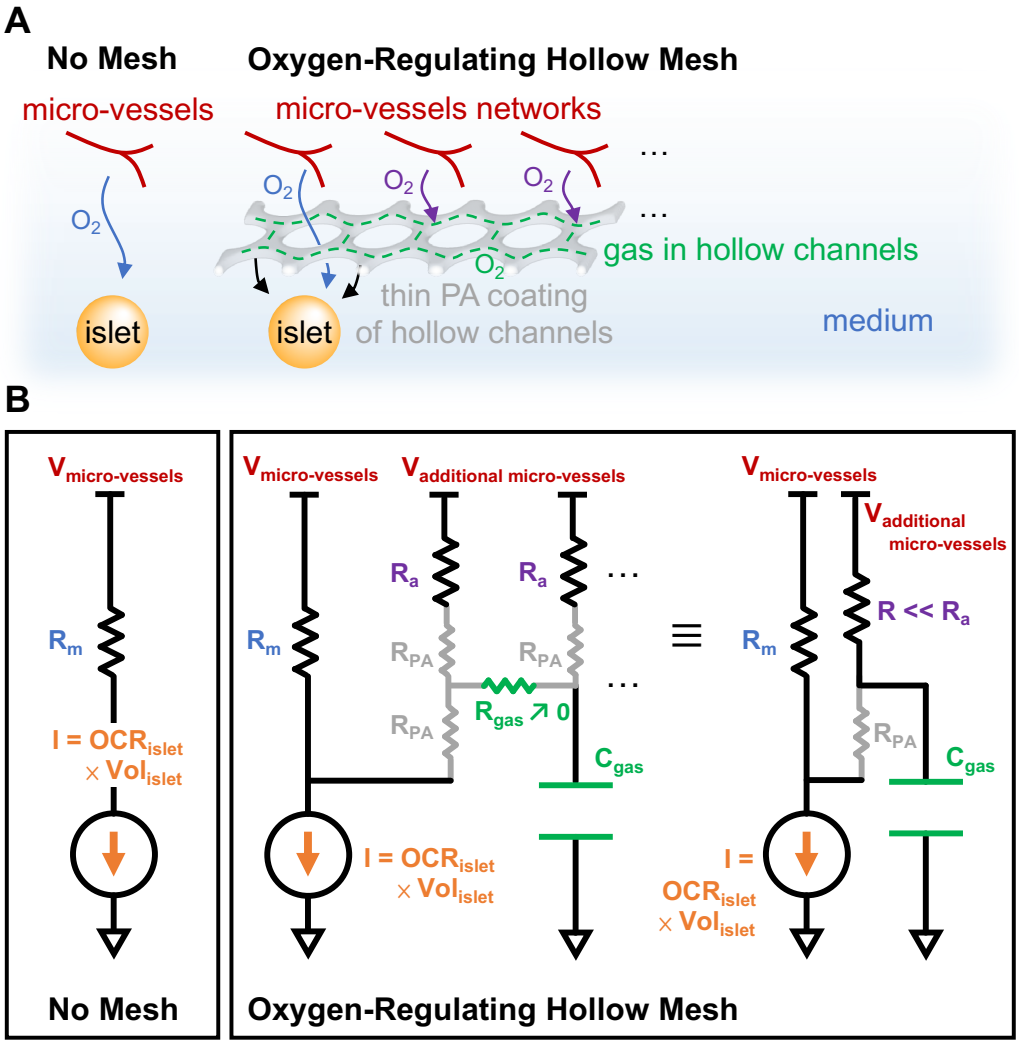

Figure 4-2. Working principles of the Oxygen-Regulating Hollow Mesh versus a No Mesh condition. (A) Comparative schematic representations of the oxygen diffusion mechanism. (B) Comparative permeation resistivity circuit models.

OXYGEN PERMEATION CIRCUIT MODEL

This functional aspect of the Oxygen-Regulating Hollow Mesh can be more quantitatively articulated by employing a permeation circuit model for oxygen diffusion. In this model, one may analogize partial oxygen pressure (pO_2 ($kg/m/s^2$))

to electrical voltage (V (V)) and the oxygen consumption rate times the islet volume ($OCR_{islet} \times Vol_{islet}$ (mol/s)) to electric current (I (A)). Furthermore, the distance across which diffusion occurs can be modeled to a form of permeation resistance ($R_{permeation}$ (kg/m/mol/s)). This approach allows for a precise, mathematical depiction of oxygen transport properties to the islet cells.

Utilizing the equivalent circuit model, we can quantitatively assess and juxtapose the characteristics of oxygen transport to the islet cells both with and without the use of the Oxygen-Regulating Hollow Mesh (**Figure 4-2B**). Without the mesh, the model presents a straightforward circuit consisting of a voltage source ($V_{micro\text{-}vessels}$) representing the micro-vessels, a resistor (R_m) symbolizing the impedance to oxygen diffusion through the interstitium, and a current drain (I) corresponding to the oxygen consumption by the islet.

From this model, it becomes clear that a high diffusion resistance correlates to a reduced voltage at the islet site, indicating that the pO_2 the islet experiences is diminished. This scenario can result in a localized hypoxic environment within the islet.

Conversely, when the Oxygen-Regulating Hollow Mesh is employed, it introduces additional components that enhance the "current" supply to the islet. This setup is reflected in the transition from the illustration in **Figure 4-2A** to the circuit model depicted in **Figure 4-2B**. Specifically, there is an extra voltage source ($V_{additional\ micro\text{-}vessels}$) originating from more distant micro-vessels. Accompanying this are the diffusion resistances (R_a) that arise from these farther micro-vessels to the Oxygen-Regulating Hollow Mesh. Within the Oxygen-Regulating Hollow Mesh itself, we encounter the resistance due to the thin parylene coating (R_{PA}) as well as the resistance (R_{gas}) associated with the gas hallow channel oxygen diffusion pathway.

Within this model, an intriguing addition is the conceptual inclusion of a capacitor that stores oxygen in the hollow channels within the Oxygen-Regulating Hollow Mesh, analogous to an electrical capacitor that stores charges. An electrical capacitor

holds energy in the form of electrical charges (Q) multiplied by the potential difference (V), quantified as coulombs times volts. In a similar vein, the Oxygen-Regulating Hollow Mesh's channels can be envisaged as storing “chemical energy”, represented by the total oxygen molecules (n) times the chemical potential (μ). In a simple system, the chemical potential is related to the system's temperature and pressure, whereas pressure is also related to the partial pressure of oxygen in our model. Thus, this metaphoric chemical capacitor in our model is introduced and symbolized by (C_{gas}).

Both the resistors and capacitor frameworks allow for a simplification of the oxygen diffusion model, as depicted on the rightmost panel of **Figure 4-2B**. It becomes apparent that the islet's oxygenation can be significantly improved by the additional oxygen transport routes supplied by distal micro-vessels through Oxygen-Regulating Hollow Mesh. Compared to scenarios lacking the Oxygen-Regulating Hollow Mesh, the inclusion of these hollow microchannels is instrumental in mitigating hypoxic conditions around the islet.

Moreover, with the “capacitive” features present, the oxygen partial pressure is evenly distributed across the Oxygen-Regulating Hollow Mesh—much like electrical potential remains consistent across the conductive material of a capacitor's electrode. This capacitive effect ensures a uniform oxygen distribution, preventing spatial variations in oxygenation levels. This uniformity is critical, given that islet distribution across the device is unlikely to be even, with some regions potentially having higher islet densities, hence a greater oxygen “current” demand. The constant oxygen redistribution properties of the Oxygen-Regulating Hollow Mesh ensure that each islet receives an equivalent oxygen tension, fostering an optimal oxygen environment for islet functionality.

The Oxygen-Regulating Hollow Mesh excels not only in oxygen distribution but also in its capacity for self-regulating oxygen delivery. This passively operated device allows the pO_2 within the hollow channels to naturally equilibrate with that of the surrounding tissue, thereby circumventing the risks associated with active

oxygenation devices, such as exogenous oxygen injections. These methods can inadvertently introduce hyper oxidative stress that may compromise the microenvironment of the islet. Moreover, an excess of oxygen is known to impede revascularization, thereby delaying islet engraftment, which is crucial for the islet cells to monitor blood glucose levels and release insulin into the vascular network for glycemic control. The Oxygen-Regulating Hollow Mesh is designed to avoid such complications by capping the maximum pO_2 at levels provided by the native vascular network, typically not surpassing 45 mmHg at subcutaneous sites. Additionally, Oxygen-Regulating Hollow Mesh leverages the native vascular network to modulate pO_2 in accordance with vascular density and blood flow rates.

SIMILARITIES TO HEMOGLOBIN

The topic of oxygen transport in the blood presents a rich area for exploration, particularly in the context of our device, which introduces oxygen into air-containing microchannels. Oxygen is primarily transported through the blood via hemoglobin in red blood cells. The hematocrit value, indicating the proportion of blood volume occupied by red blood cells, typically ranges from 40 to 50% in humans. The normal concentration of hemoglobin in human blood is approximately 12-18 grams per 100 mL of blood [160].

Hemoglobin molecules contain four binding sites for oxygen, associated with the iron atoms in the heme groups. The total molecular weight of hemoglobin is 64,548 g/mol. [161]. Applying the ideal gas law for oxygen, we calculate that approximately 1.39 mL of oxygen binds to each gram of hemoglobin. However, due to other type of hemoglobin presented in the blood that cannot bind to oxygen (e.g., methemoglobin and carboxyhemoglobin), it is experimentally determined that the actual oxygen-binding capacity of hemoglobin is about 1.34 mL of oxygen per gram of hemoglobin [162].

Given this data, we can deduce that 100 mL of blood can bind up to about 20 mL of oxygen. This measure, known as the oxygen-binding capacity of blood, remarkably mirrors the oxygen volume percentage in the atmosphere, which is 20.9%.

It is worth noting that the binding of oxygen to hemoglobin follows Hill's equation with a Hill coefficient of 2.7 [163], indicating that the actual oxygen content in the blood is dependent on the oxygen partial pressure, so the actual oxygen content typically falls below the oxygen-binding capacity. Nevertheless, by introducing air-containing microchannels into the tissue, we effectively create an additional microvascularized-mimetic network that aims to transport oxygen by oxygen diffusion in air, mimicking the oxygen transport by perfusion in blood.

4.2 FABRICATION PROCESSES

OXYGEN-REGULATING HOLLOW MESH

Constructing an Oxygen-Regulating Hollow Mesh involves fabricating the MEMS structures [164], [165]. This intricate process mandates the application of microfabrication techniques, designed to fabricate hollow mesh microchannels with dimensions measured in microns. The process starts with the creation of a sacrificial template made by copper. Parylene is then used for its conformal coating properties, ensuring an even layer over the template. After the coating is finalized, the sacrificial layer is meticulously removed, leaving behind the desired microchannel structures.

The comprehensive procedure for fabricating the Oxygen-Regulating Hollow Mesh is depicted in **Figure 4-3**. Initially, a copper film (CAS: 7440-50-8, Thermo Fisher) with a thickness of 25 μm is cut to match a 4-inch wafer size. The copper surface is meticulously cleaned through a sequential rinsing process using acetone, isopropyl alcohol (IPA), and deionized water, followed by drying with a nitrogen gun. It is imperative at this juncture to ensure that the copper film remains as planar as possible, and to carefully reduce the occurrence of creases to optimize the efficacy of subsequent etching stages. Thereafter, a photoresist layer (AZ1518,

MicroChemicals), 2 μm in thickness, is uniformly coated onto the copper substrate by spinning at 3,000 rpm for a duration of 45 seconds. Subsequently, the layer undergoes a 30-miunte soft bake in a convection oven set at 100°C. Once the copper foil wafer has been allowed to cool, it is subjected to a photolithographic patterning process using a custom-crafted mask on a Karl-Suss mask aligner. This is performed with an exposure power setting of approximately 150 mJ/cm^2 tailored for i-line. The patterned photoresist is then developed in a 1:3 solution of AZ340 developer (MicroChemicals) and deionized water for roughly one minute. After the application of a photoresist pattern, the copper wafer is subjected to air drying. Following a careful microscopic examination to verify the precision of the pattern transfer, a 120-μm thick dry-film photoresist (WBR2120, DuPont) is applied to the back side of the copper wafer to prevent backside etching subsequently. Then, the etching phase involves the removal of exposed copper regions using a wet aqueous solution, which consists of 0.3% v/v of 30% w/w hydrogen peroxide (P/N: 219003, Gallade Chemical) and 0.7% v/v of 18 M sulfuric acid (CAS: 7664-103-9, Fisher Scientific). Vigorous bubbling or agitation is maintained throughout this step. Both photoresist layers are then stripped away using a sonicated acetone bath, followed by rinses with IPA and deionized water. Subsequently, the copper template is subjected to an electropolishing process in an 85% w/w phosphoric acid solution (CAS: 7664-38-2, Fisher Scientific), with an anodic voltage of 20 V applied for thirty seconds to one minute. This step ensures that any sharp edges are significantly reduced. Post-electropolishing, the template undergoes thorough cleaning. The next stage involves suspending the copper template in a parylene coating chamber, where a 2-μm layer of Parylene HT is conformally deposited. The template with Parylene HT is then segmented at the junction connecting to the cannula. The template with Parylene HT is immersed in a 68 % v/v nitric acid (CAS: 7697-37-2, Macron Fine Chemicals) to dissolve and leach out the copper template. To eliminate any residual copper oxide potentially lingering within the microchannels, the entire structure is bathed in a dilute sulfuric acid solution. The final step entails a thorough rinse in deionized water, followed by a drying process in preparation for the subsequent assembly stages.

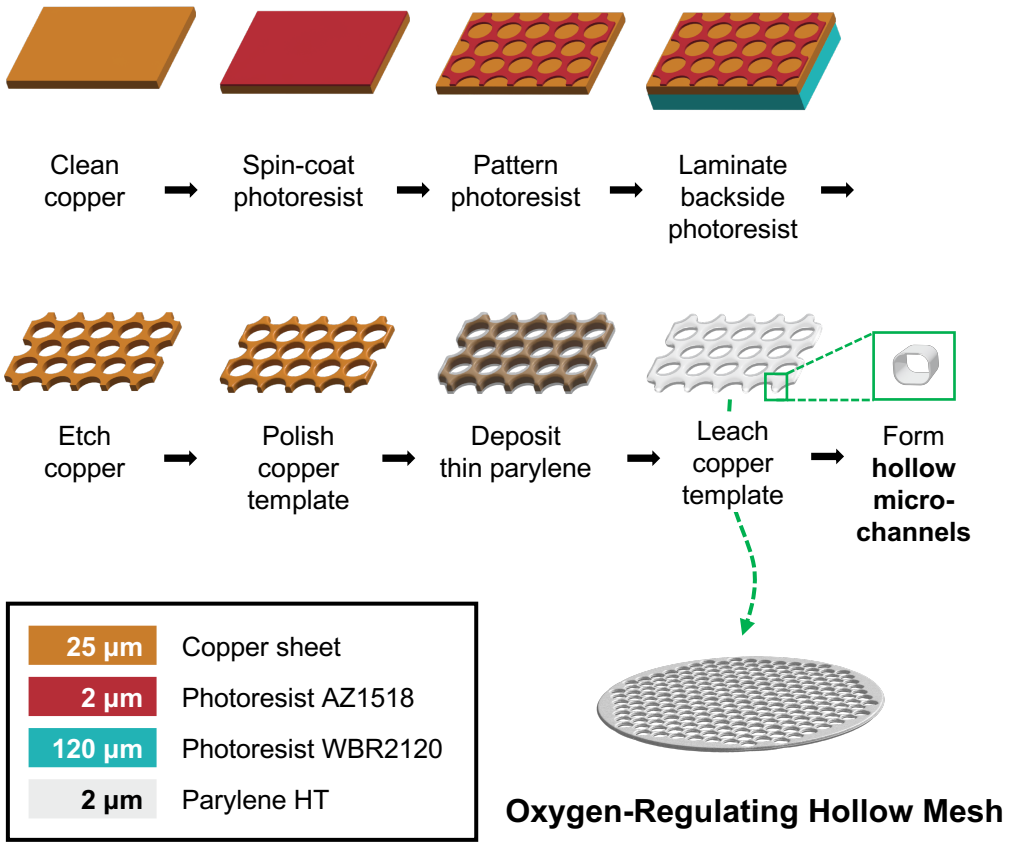

Figure 4-3. Fabrication processes of the Oxygen-Regulating Hollow Mesh. This figure details the photolithographic step-by-step processes and materials applied in its fabrication.

CONTROL NON-HOLLOW MESH

To rigorously evaluate the effectiveness of Oxygen-Regulating Hollow Mesh, a Control Non-Hollow Mesh is meticulously crafted for comparison. The mesh-shaped device is understood to enhance the oxygen microenvironment by preventing islet graft aggregation [42]. To isolate the impact of the oxygen-containing hollow channels from the mesh shape islet sandwiching effects—both features of the Oxygen-Regulating Hollow Mesh—a Control Non-Hollow Mesh is. The Control Non-Hollow Mesh also features a mesh design that can sandwich islets; however, its branches are formed using a solid and thick Parylene C film as opposed to hollow channels in the Oxygen-Regulating Hollow Mesh. Both devices are crafted with precisely the same dimensions, ensuring that any observed differences in outcomes

between the Oxygen-Regulating Hollow Mesh and Control Non-Hollow Mesh are directly attributable to the presence of the Oxygen-Regulating Hollow Mesh's distinctive hollow channels.

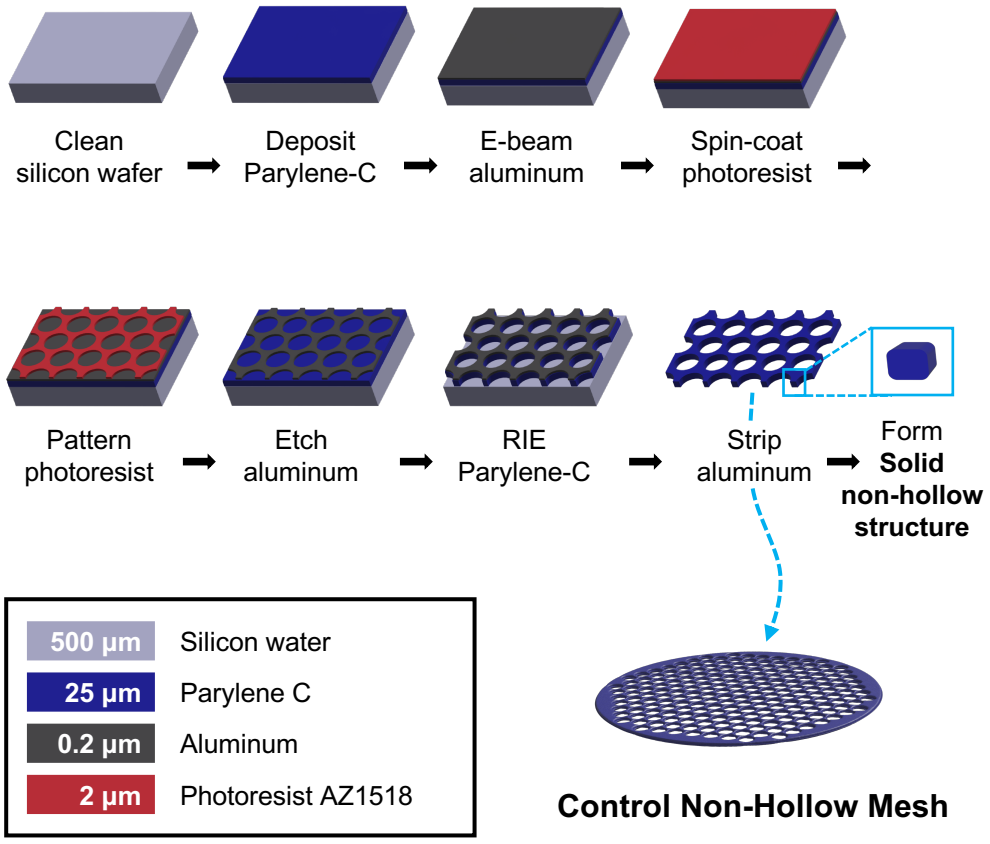

Figure 4-4. Fabrication processes of a single layer Control Non-Hollow Mesh.

Figure 4-4 outlines the detailed process for crafting the thin mesh structure. The procedure begins with the cleansing of a 4-inch silicon wafer (ID: 452, University Wafer, Inc.) using acetone, IPA, and deionized water. Preserving the wafer's native oxide layer is desired for moderate parylene film adhesion. Subsequently, a 25-µm layer of Parylene C is deposited atop the wafer. A mild oxygen plasma treatment (50 W, 200 mTorr, 30 seconds) is then applied to create a rough surface on the Parylene C film. This is immediately followed by the e-beam deposition of a 1-2 kÅ thick aluminum layer onto the parylene at a rate of 1 Å/s, serving as a hard mask for subsequent processes. The surface is then coated with a photoresist (AZ1518,

MicroChemicals) at a spin speed of 3,000 rpm, achieving a thickness of approximately 2 μm. This layer undergoes a soft bake in a convection oven at 100°C for 30 minutes. The photoresist is exposed to an i-line specific energy of about 150 mJ/cm², and the patterned photoresist is developed using a 1:4 mixture of AZ400K developer (MicroChemicals) and deionized water for roughly one minute. Following a thorough rinse and clean, an aluminum etchant etches the exposed aluminum layer. The wafer is rinsed again and air-dried, then subjected to an oxygen reactive ion etching (RIE) process at 400 W power and 200 mTorr partial pressure. The etching, recommended not to exceed 15 minutes continuously to prevent extensive heat, proceeds at a rate of approximately 0.2 μm/min until all exposed parylene layers are etched away. The aluminum mask is removed using an aluminum etchant. Finally, the entire structure is thoroughly rinsed and cleaned.

PHOTOMASK DESIGN

The photomasks utilized for creating intricate structures within both the Oxygen-Regulating Hollow Mesh and the Control Non-Hollow Mesh are meticulously crafted to specification. Patterns are designed using CAD software (AutoCAD, Autodesk) and transferred from a printed transparency onto a photoresist and chromium-coated soda lime mask (5x5x.090 SL LRC 10M 1518 5k, Nanofilm).

Detailed in **Figure 4-5A**, the diagram highlights the circles outlined in black, denoting the areas of transparency that will be exposed during the photolithography process. Due to the copper etching process in the Oxygen-Regulating Hollow Mesh, which results in undercut etching, the holes are intentionally designed to be smaller than the desired final shape. The undercut etching area is depicted with blue-checkboard shade. Since the copper template's thickness is approximately 25 μm, and accordingly, the undercut distance is designed to be around 25 μm, given that the etching process is largely isotropic. **Figure 4-5B** displays microscopic images of the hexagonally-arranged circular holes in the mesh structures of both devices. In the mesh branch area of the Oxygen-Regulating Hollow Mesh, the transparency

initiation point is visible. Conversely, the mesh branches in the Control Non-Hollow Mesh exhibit a solid appearance.

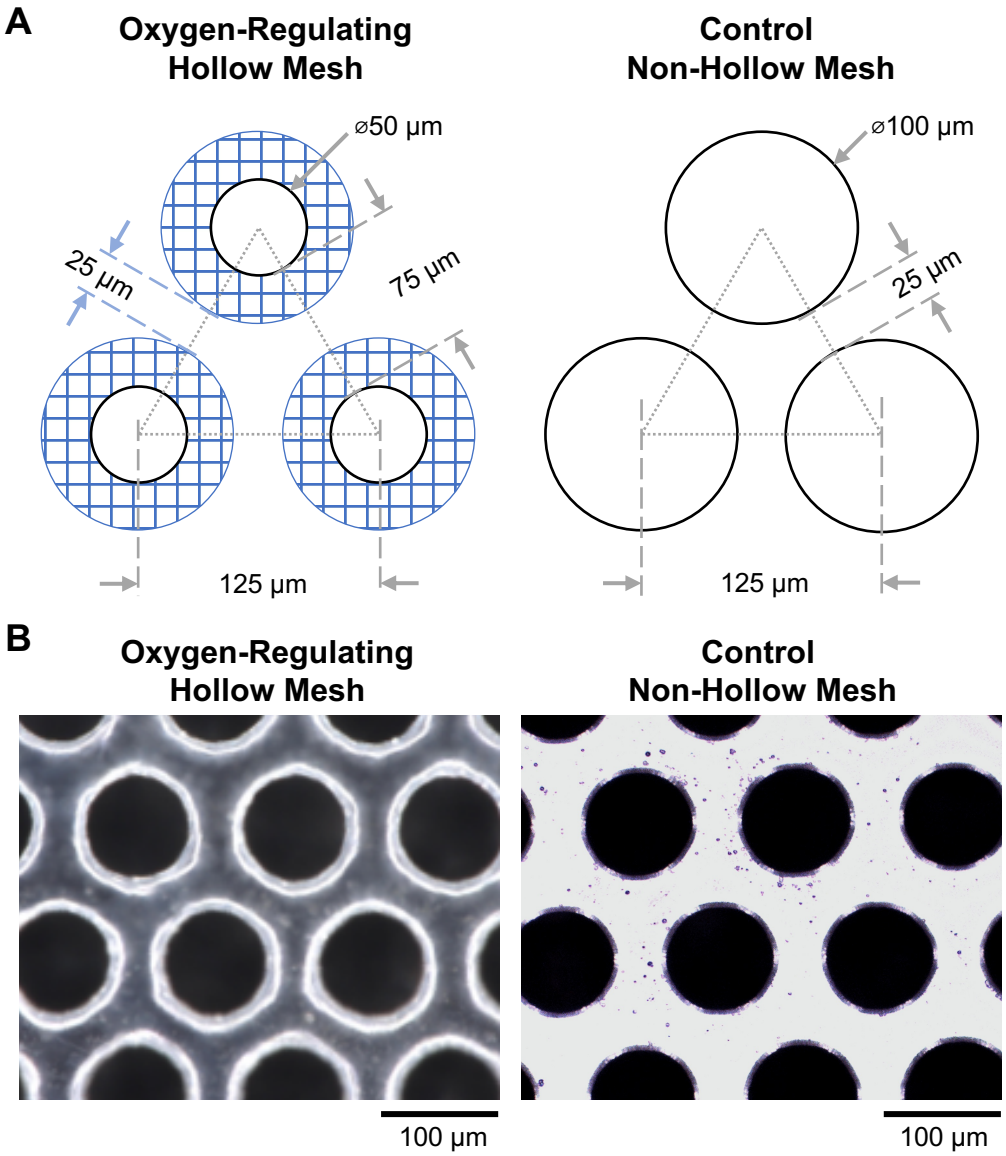

Figure 4-5. Geometric details and dimensions of the mesh structures in the Oxygen-Regulating Hollow Mesh and Control Non-Hollow Mesh. (A) The schematic layout of the hexagonally-arranged circular holes, with circles outlined in black denoting the open areas. The areas shaded in a checkerboard pattern in blue represent the regions subject to undercut etching in the fabrication process. (B) The visual appearance and detailed imagery of the fabricated Oxygen-Regulating Hollow Mesh and Control Non-Hollow Mesh.

The openings or holes have a diameter of 100 μm. The underlying concept is that a large percentage of islets are larger than 100 μm in size. Thus, when loading the islets, they will not fall through these openings. We can also calculate the porosity of the configurations presented in **Figure 4-5**. Porosity, defined as the percentage of openings relative to the total area, is approximately 58%. Consequently, this implies that the area occupied by the parylene constitutes about 42%. These numbers will be useful for simulations conducted later. It is also important to highlight that the circular shape is intentionally designed to minimize stress concentration. Furthermore, the mesh arrangement ensures that if any branch is damaged and water intrusion obstructs the air pathways, the surrounding pathways can still facilitate oxygen transport.

ELECTROPOLISHING OF COPPER TEMPLATE

Polishing the copper template, sacrificial material, is critical and essential before applying a conformal Parylene HT coating. The roughness of the copper template directly affects the inner surface of the air-containing microchannels. Despite Parylene HT being a hydrophobic material, which means it naturally repels water and does not thermodynamically favor water condensation, the smoother the Parylene-HT surface, the lower the surface energy, making it even less likely for water to condense on the inner surface, ensuring the oxygen transport pathways remain unobstructed. Moreover, electropolishing can smooth the sharp edges of the copper template because the electrical field concentrates at these sharp edges during polishing, resulting in a faster etch rate. If the parylene hollow channels have sharp edges, they are also prone to breaking, leading to subsequent water intrusion that could block oxygen transport. We demonstrate the effect of electropolishing on copper templates through various imaging techniques. Both microscopic images (**Figure 4-6A, B**), atomic force microscopic 2D images (**Figure 4-6C, D**), and atomic force microscopic 3D images (**Figure 4-6E, F**) are presented. Before polishing, the sharp edges at the boundary of the opening holes and the line-shaped morphologies resulting from the copper sheet machining process are clearly visible. After polishing, the machining stripes are reduced, and the boundaries of the hole openings appear

smooth. The root mean square roughness (Rq) is measured at 44.4 nm for the unpolished copper template and 6.61 nm for the polished template. The arithmetic average roughness (Ra) is 35.5 nm for the unpolished copper template and 5.53 nm for the polished template.

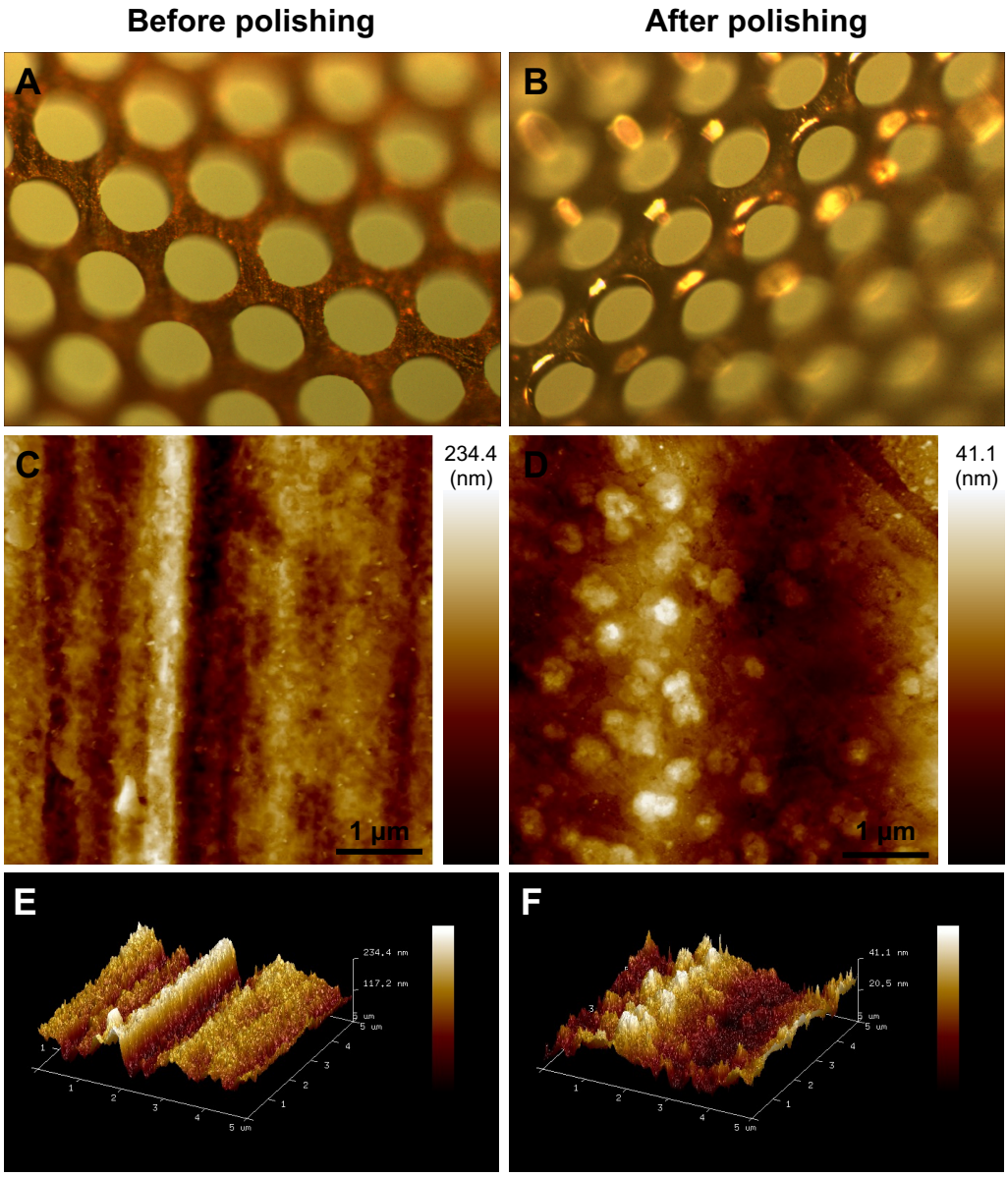

Figure 4-6. Comparison of the copper template used in Oxygen-Regulating Hollow Mesh fabrication before and after electropolishing. Micrographs of copper template before (A) and after (B) electropolishing. 2D AFM images of copper template before (C) and after (D) electropolishing. 3D AFM images of copper template before (E) and after (F) electropolishing.

IMAGE GALLERY

The constructed Oxygen-Regulating Hollow Mesh and Control Non-Hollow Mesh, both with and without the PDMS frame, are depicted in **Figure 4-7**. It should be noted that each device features a protrusion shaped like an ear on the right side, which is designed to facilitate the surgical procedure, allowing surgical tools to interact with this area without compromising the integrity of the mesh structure.

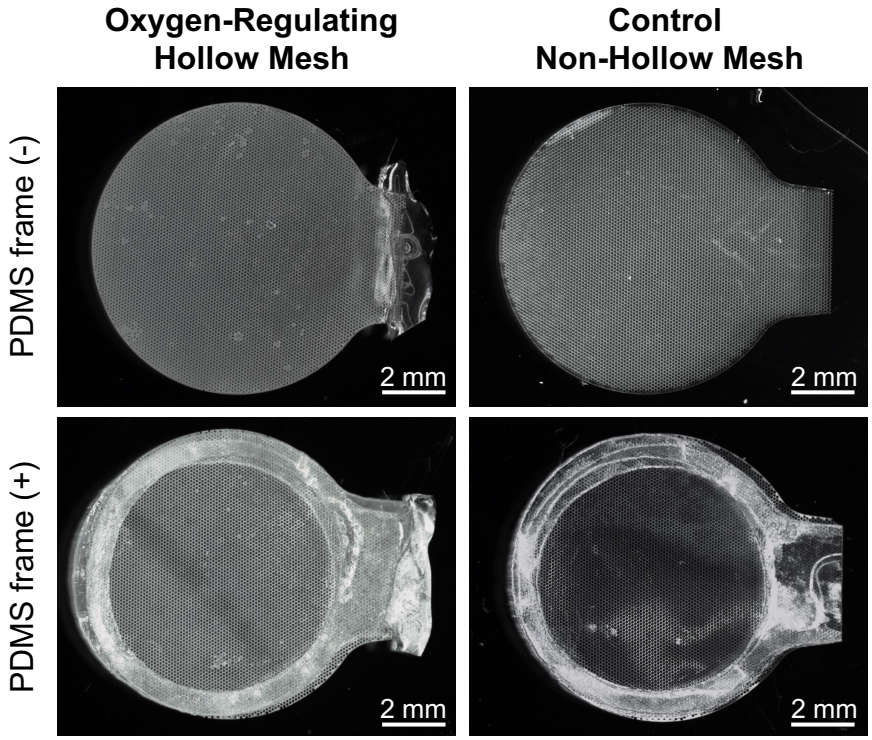

Figure 4-7. Images of single-layered Oxygen-Regulating Hollow Mesh and Control Non-Hollow Mesh with and without the supporting PDMS frame.

The additional and optional PDMS frame serves to bolster mechanical support. It is crafted to approximately 100 μm in thickness, with the mesh sandwiched between two PDMS layers. MED 6219, a NuSil medical-grade silicone, was chosen for the PDMS frame material. The fabrication process includes spinning a degassed silicone mixture onto the wafer, followed by a high-temperature cure. The PDMS film is then precision-cut using a CO_2 laser cutter (VLS3.50, Universal Laser System) under

specific conditions (5W, speed: 10%, 2 passes). Residues are carefully removed by brushing, after which the PDMS frame is separated from the wafer using an isopropyl alcohol (IPA) extraction method prior to the assembly stage. A medical-grade silicone adhesive is applied to affix the PDMS frame to the mesh.

Due to fabrication constraints, an area on the surgical handling part of the Oxygen-Regulating Hollow Mesh remains uncoated with parylene. To ensure a complete seal of the hollow mesh structures, a medical-grade silicone (MED 6219, NuSil) is utilized to prevent fluid penetration.

ASSEMBLY OF DEVICES

To integrate islet cells with the mesh devices, **Figure 4-8A** illustrates the layered construction method. In this process, a predetermined quantity of islets (for instance, 1000 IEQ) is divided into three portions and then interleaved with four mesh layers. For added structural integrity, one layer includes the PDMS-reinforced mesh. The same assembly protocol applies to both the Oxygen-Regulating Hollow Mesh and the Control Non-Hollow Mesh.

Displayed in **Figure 4-8B** are the images showcasing both the 1000 IEQ islets and the islets affixed to the device. The central graft area, where islets are densely situated, spans approximately 4 mm in diameter. Surrounding islet-free zones serve as interfaces for enhanced oxygen uptake from the more distant micro-vessels, ensuring a sufficient oxygen supply for the centrally located islet graft.

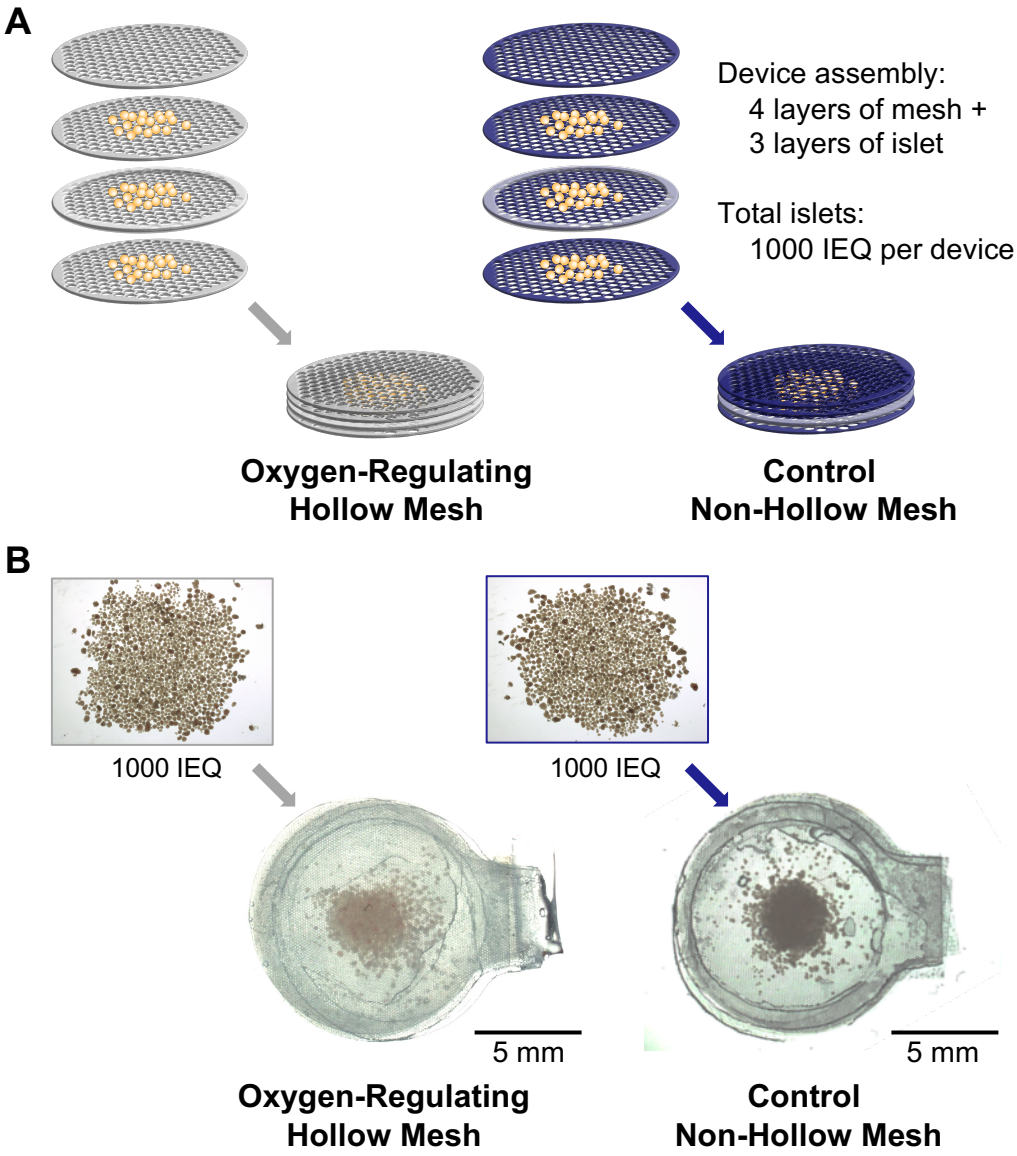

Figure 4-8. Assembly of islet cells with Oxygen-Regulating Hollow Mesh or Control Non-Hollow Mesh. (A) Depictions of exploded view of the meshes alongside its assembled state, comprising four layers of mesh sandwiching three layers of islet cells. (B) Visual representations of 1000 IEQ and the fully assembled device integrating four mesh layers with three layers of islet cells.

4.3 IN VITRO OXYGEN REDISTRIBUTION EFFECTS

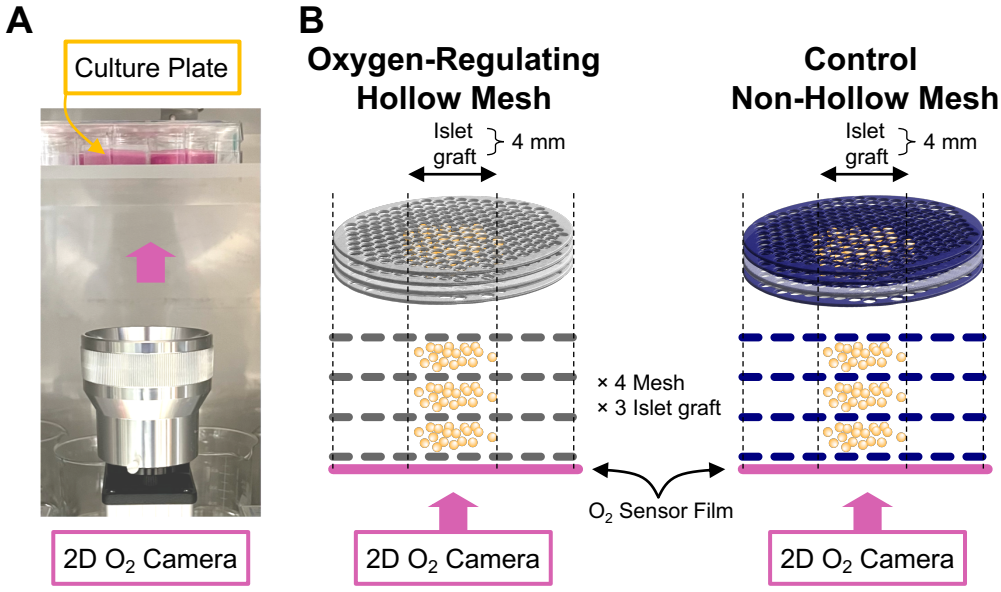

Figure 4-9. In vitro setup for 2D oxygen imaging of islet-integrated mesh devices. (A) Photograph depicting the 2D O2 camera aligned with the 6-well culture plate. (B) A cross-sectional schematic showing both the Oxygen-Regulating Hollow Mesh and Control Non-Hollow Mesh positioned over the oxygen-sensing film to capture time-dependent oxygen distribution profiles. N=3 for each group.

Figure 4-9A illustrates our imaging setup, where a 2D O_2 camera captures the pO_2 distribution from beneath the culture plate. This entire arrangement is housed within an incubator at 37°C with 5% CO_2. **Figure 4-9B** provides a cross-sectional view of the structural composition of islets, mesh devices, and O_2 sensing film.

The study was carried out over a 24-hour period for both the Oxygen-Regulating Hollow Mesh (n=3) and Control Non-Hollow Mesh (n=3). **Figure 4-10A** presents the pO_2 imaging at initial culture (t=0) and subsequent intervals of 2, 4, 8, 16, and 24 hours. The dotted line in these images demarcates the islet graft region, while the outer area of the image delineates the boundary of the mesh devices. For a more comprehensive understanding of the oxygen levels, **Figure 4-10B** maps the pO_2

values against the radial distance from the central point of the islet graft at the indicated time points.

From the data presented in **Figures 4-10A and B**, it's noticeable that the Oxygen-Regulating Hollow Mesh maintains a relatively uniform pO_2 throughout the device, even the islet graft region. This is because the air-containing microchannels could instantaneously redistribute the oxygen tension. Since pseudo islet cells remain viable and actively consume oxygen, there is an overall gradual decrease in pO_2 as time progresses.

Conversely, the Control Non-Hollow Mesh exhibits a severe depletion of oxygen in the central islet graft area. This significant gradient of oxygen tension is established within the first 2 hours and remains relatively stable over the 24-hour duration. Despite higher pO_2 in adjacent areas and larger pO_2 gradient of the Control Non-Hollow Mesh, this oxygen does not effectively support the islet graft as the diffusivity of oxygen in culture medium is low.

Throughout the experiments, the pO_2 within the islet graft in the Control Non-Hollow Mesh consistently registers lower than that of the Oxygen-Regulating Hollow Mesh. However, in areas of the mesh not covered by islets, the pO_2 associated with the Oxygen-Regulating Hollow Mesh begins to drop below that of the Control Non-Hollow Mesh. This supports the inference that the Oxygen-Regulating Hollow Mesh redistributes oxygen across the device, enabling regions adjacent to the oxygen-consuming islets to draw on surrounding oxygen resources. Consequently, the areas adjacent to the Oxygen-Regulating Hollow Mesh record a lower pO_2 compared to the Control Non-Hollow Mesh.

Even without micro-vessels in our in vitro model to provide oxygen, diffusion from the air and cell culture medium interface acts as a surrogate oxygen supply. The Oxygen-Regulating Hollow Mesh's design allows it to forestall and mitigate local hypoxia effectively.

We analyze the average pO_2 within the islet graft and track the temporal pO_2 changes for both Oxygen-Regulating Hollow Mesh and Control Non-Hollow Mesh (**Figure 4-11A**). It was observed that for the Control Non-Hollow Mesh, pO_2 levels dropped rapidly (within 4 hours) and remained low, stabilizing at around 60 mmHg throughout the experiment. In contrast, the islet graft utilizing the Oxygen-Regulating Hollow Mesh exhibited a delayed decline in pO_2, which stabilized later (around 16 hours) and at a higher level, approximately 90 mmHg.

To quantify the oxygen redistributing effect, we calculate the maximum pO_2 differential within the islet graft area (**Figure 4-11B**) and across the entire mesh device (**Figure 4-11C**). Within the islet graft, the delta pO_2 for the Control Non-Hollow Mesh plateaus at about 45 mmHg, whereas for the Oxygen-Regulating Hollow Mesh, the differential remained significantly lower, around 20 mmHg—less than half that of the control group. Across the entire device, the delta pO_2 for the Control Non-Hollow Mesh reaches approximately 95 mmHg, in contrast to the Oxygen-Regulating Hollow Mesh, which maintains a much smaller difference of about 35 mmHg, almost one-third of the control group's value.

In addition to pO_2 levels, we seek to evaluate cell viability and function during the experiments. For this purpose, we employ fluorescein diacetate (FDA) staining, which relies on esterase enzymes active in metabolically alive cells. These enzymes hydrolyze FDA into fluorescein and acetate, with the resultant green fluorescence signaling the presence of living cells. Images of the FDA-stained islet grafts are shown in **Figure 4-12A**. Four hours into the experiment, islet grafts in both the Oxygen-Regulating Hollow Mesh and Control Non-Hollow Mesh groups remain viable. However, by the 24-hour mark, while the islets in the Oxygen-Regulating Hollow Mesh predominantly sustain their viability, those in the Control Non-Hollow Mesh are largely nonviable, with only the peripheral cells of the graft remaining alive. This distinctive pattern suggests that cell death is primarily attributable to oxygen deprivation; oxygen supplied from the peripheral areas is insufficient for the graft's center due to limited diffusion, resulting in hypoxia-induced cell death.

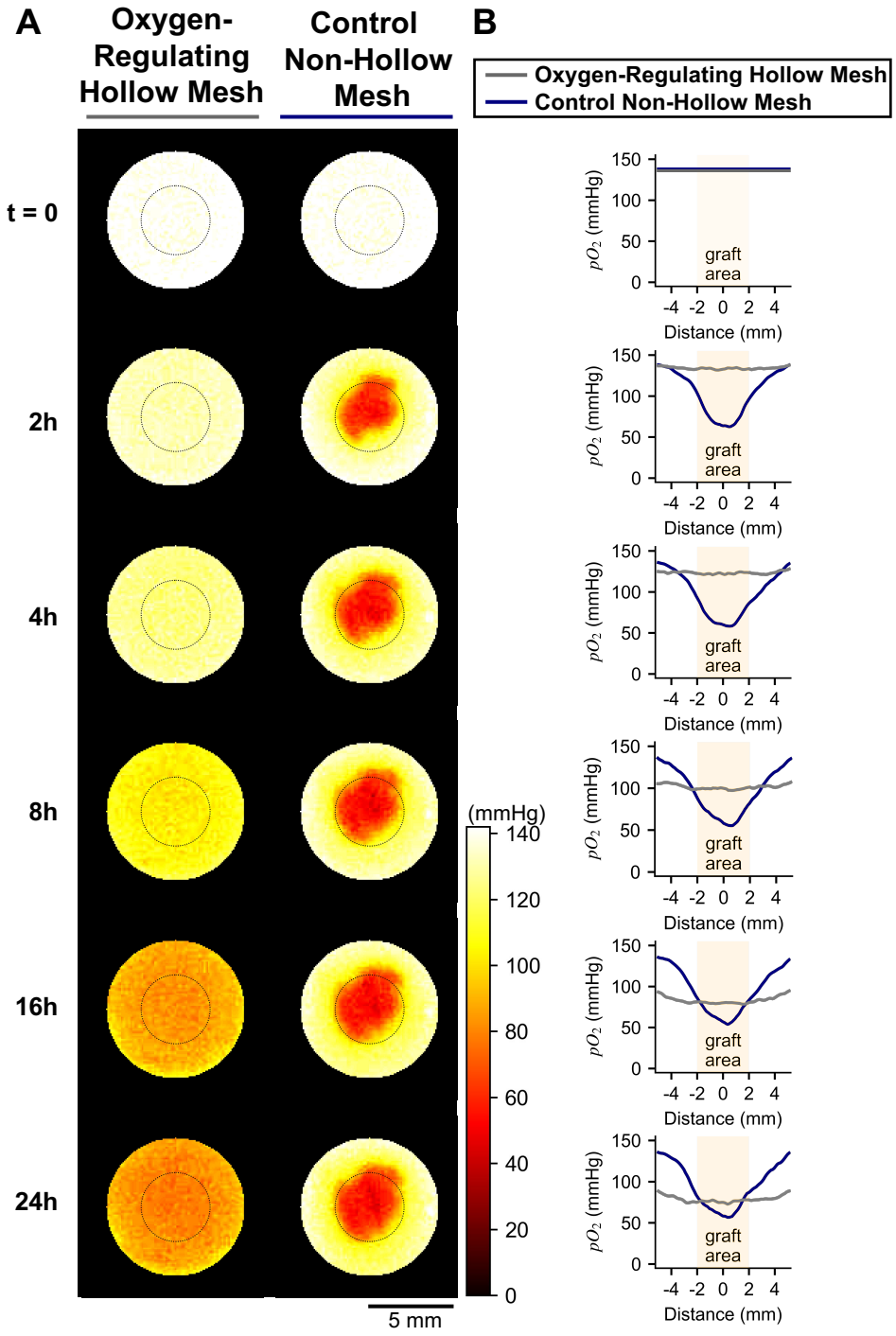

Figure 4-10. Temporal and spatial oxygen profiles for Oxygen-Regulating Hollow Mesh and Control Non-Hollow Mesh. (A) Sequential pO_2 images of Oxygen-Regulating Hollow Mesh and Control Non-Hollow Mesh. The dotted line delineates the designated islet graft area, while the outer boundary marks the extent of the mesh devices. (B) Graphical representation of pO_2 levels as a function of radial distance from the islet graft center over the same time intervals.

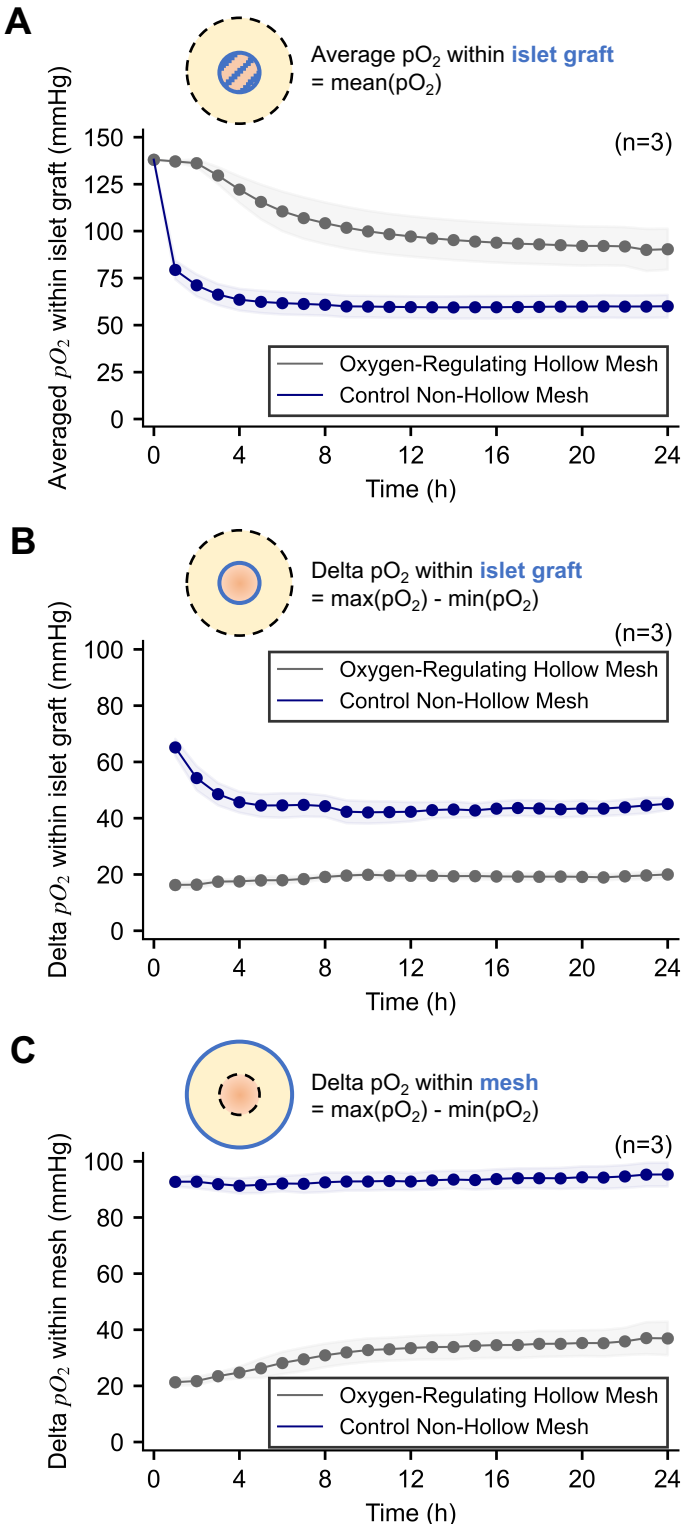

Figure 4-11. Temporal pO_2 plot in different regions of Oxygen-Regulating Hollow Mesh and Control Non-Hollow Mesh. Average pO_2 (A) within the islet graft area. Maximum pO_2 differences inside the graft region (B) or across the entire device (C). Error band: ±SEM.

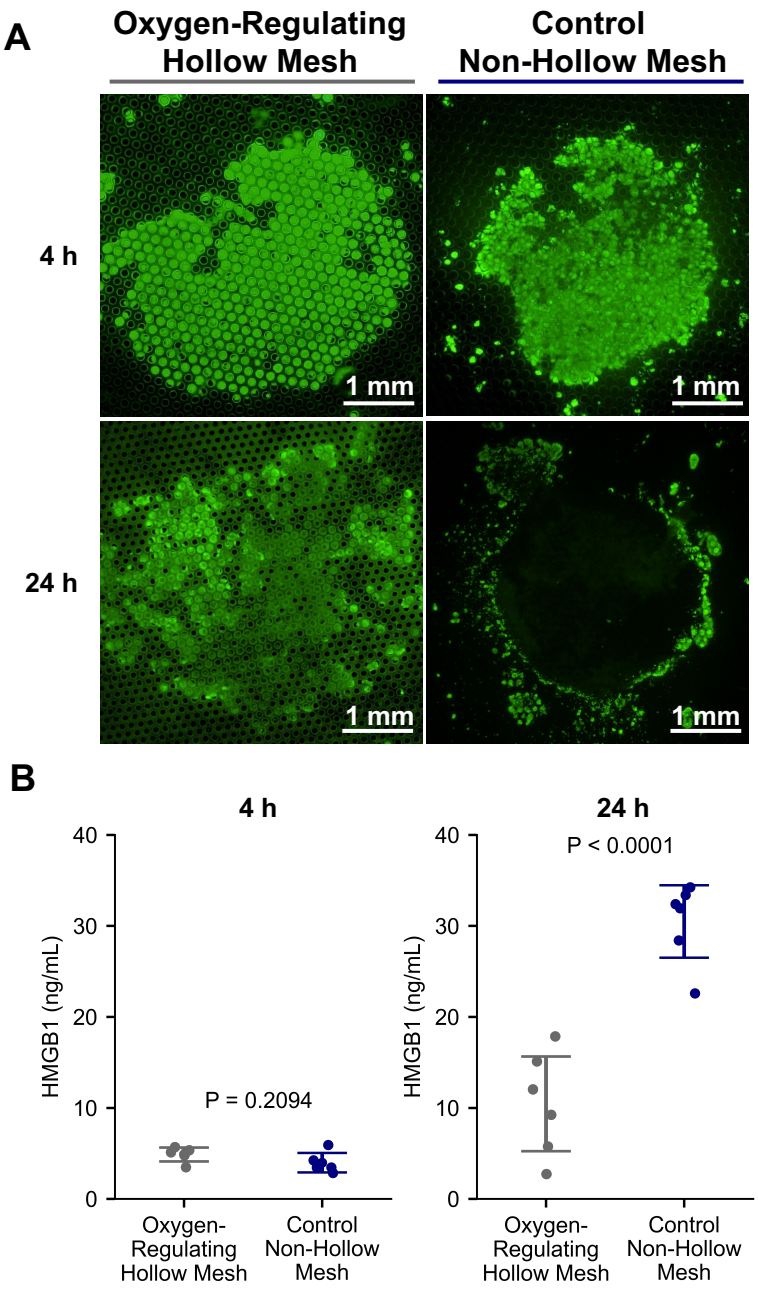

Figure 4-12. Assessment of biomarkers in pseudo islet cells within Oxygen-Regulating Hollow Mesh and Control Non-Hollow Mesh. (A) Fluorescence micrographs depicting cell viability, as indicated by fluorescein diacetate (FDA) staining; green fluorescence signifies live cells. (B) Quantification of High Mobility Group Box 1 (HMGB1) protein levels in the culture medium, serving as an indicator of cellular damage of the pseudo islet cells. We employed Welch's t-test to calculate the P-value for statistical significance. Error bars represent standard deviations. Error bars: ±SD.

High Mobility Group Box 1 (HMGB1), a non-histone chromosomal protein, serves as another biomarker of non-cell-type-specific cellular damage. The release of HMGB1 into the culture medium is typically induced by cell death [166]; we have shown HMGB1 is a sensitive biomarker for cell damage in cultured islets [86]. **Figure 4-12B** illustrates the HMGB1 concentration in the culture medium of both Oxygen-Regulating Hollow Mesh and Control Non-Hollow Mesh at the 4-hour and 24-hour marks. At 4 hours, HMGB1 levels are comparable between the two groups (~ 5 ng/mL). However, after 24 hours of culture time, there is a marked increase in HMGB1 concentration (~ 30 ng/mL) within the Control Non-Hollow Mesh group as opposed to the Oxygen-Regulating Hollow Mesh group (~10 ng/mL), suggesting that significant cell death has occurred in the islets associated with the Control Non-Hollow Mesh.

The findings presented in **Figure 4-12** highlight the rapid onset of hypoxia-induced cell death, which can occur in less than 24 hours. The use of Oxygen-Regulating Hollow Mesh can effectively delay and mitigate hypoxic cell death, even in an in vitro setting where the oxygen supply at the boundary is 142 mmHg, a level significantly higher than what is typically found at subcutaneous sites.

It is important to acknowledge that there are certain limitations in this experimental setup. Since the oxygen-sensing film is positioned at the bottom of the mesh, the oxygen environment within the islet graft could be lower than what our measurements indicate. Second, while the purpose of this experiment is to visually demonstrate the effect of oxygen redistribution, the experiment is performed in the conventional culture incubator containing higher oxygen level compared to the tissue environment. Additionally, the in vitro setup does not replicate the active oxygen-replenishing effect of the microvascular network in vivo. Therefore, the actual in vivo tissue environment may present a different oxygen profile, which will be tested in subsequent experiments. Nevertheless, the results from **Figures 4-10, 4-11 and 4-12** underline the Oxygen-Regulating Hollow Mesh's ability to improve oxygen supply within the islet graft by ensuring a more uniform distribution throughout the device, thus reducing both the severity and likelihood of local hypoxia.

4.4 IN SILICO CHARACTERIZATION OF OXYGEN REDISTRIBUTION EFFECTS

Having established the efficacy of Oxygen-Regulating Hollow Mesh in redistributing oxygen in vitro, we proceeded to utilize computational modeling to predict the behavior of the Oxygen-Regulating Hollow Mesh and islets following subcutaneous transplantation in silico. Both the three-dimensional (**Figure 4-13A**) and two-dimensional (**Figure 4-13B**) steady state pO_2 distributions of the mesh device post-implantation are illustrated. The simulation presupposes that the surrounding tissue is supported by a microvascular network, sustaining a pO_2 of 40 mmHg at the subcutaneous site; hence, the boundary condition for the computational domain is set at this value. In this model, 1000 IEQ are uniformly dispersed across the center islet graft area, structured into three interspersed layers. The islet graft area assumes an effective maximum oxygen consumption rate ($OCR_{max,eff}$), which is calculated based on the volumetric proportion of the 1000 IEQ volume relative to the islet graft seeding volume. The volume for the 1000 IEQ is derived from the formula $1000 \times \frac{4}{3}\pi \times (75\ \mu m)^3$ (IEQ is a sphere with a radius of 75 μm), and the islet graft seeding volume is calculated using $\pi \times (2\ mm)^2 \times 150\ \mu m \times 3$ (representing a cylindrical volume of the graft area with a diameter of 4 mm and a height accommodating 3 layers of islets). The resulting value is applied to the maximum oxygen consumption rate (OCR_{max}) for islet cells to obtain the effective rate.

The visualizations clearly indicate that the Oxygen-Regulating Hollow Mesh facilitates the redistribution of pO_2 throughout the device. The total oxygen flux, denoted by magenta arrows, suggests that oxygen from surrounding tissue can permeate into the islet graft area through the hollow micro-channels. In contrast, the Control Non-Hollow Mesh shows a profound oxygen deficit within the islet graft region. Based on the oxygen flux's directionality, it appears that oxygen diffusion to the islet graft is predominantly vertical, coming from either above or below within the tissue environment. The differences highlight the Oxygen-Regulating Hollow Mesh's advantage in enhancing oxygen availability from the adjacent micro-vessels.

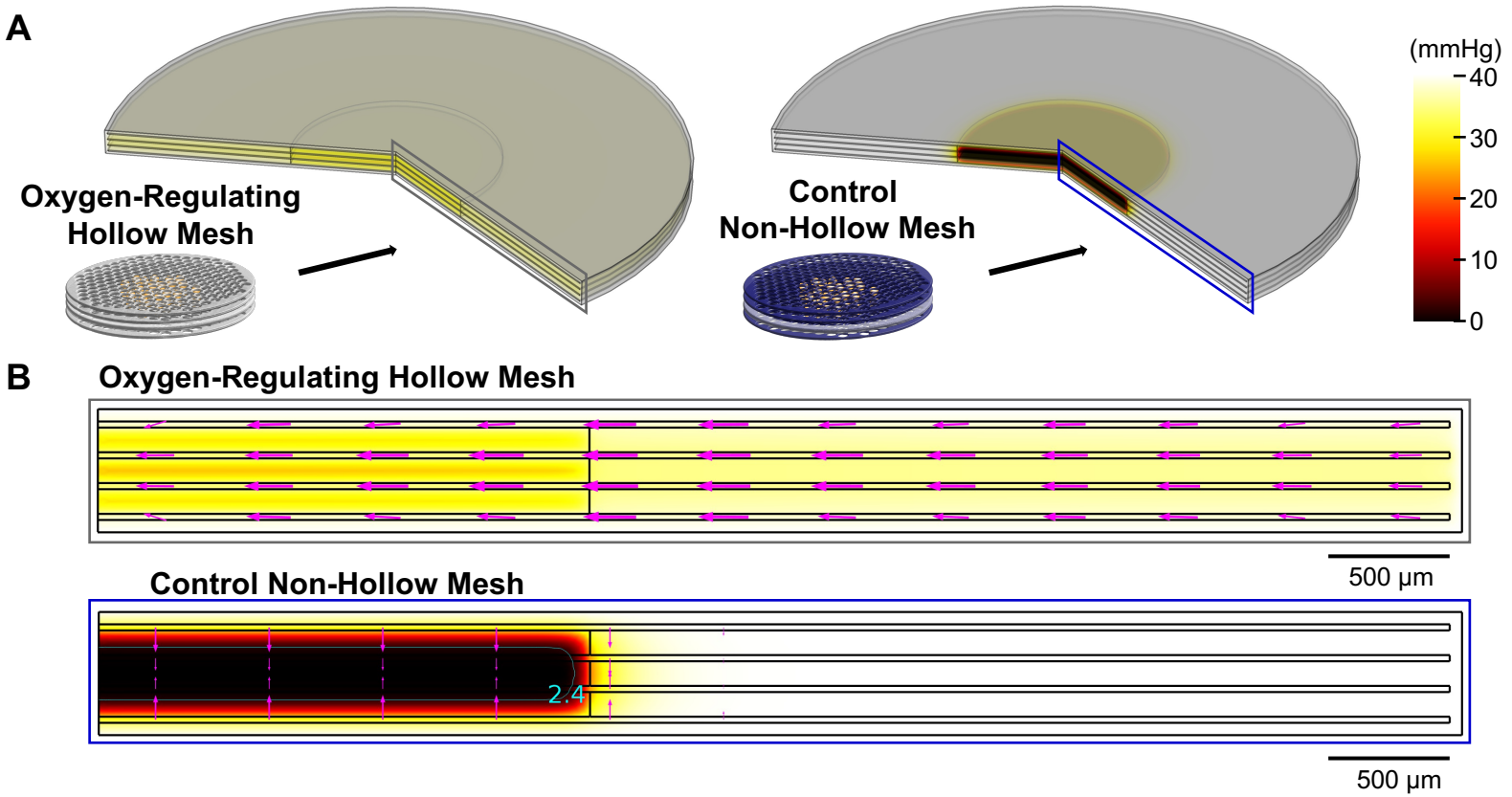

Figure 4-13. Simulated oxygen profiles for Oxygen-Regulating Hollow Mesh and Control Non-Hollow Mesh with 1000 IEQ islets transplanted subcutaneously. (A) 3D pO_2 profile. (B) 2D cross-sectional pO_2 profile. The magenta arrows indicate the normalized total oxygen diffusive flux. The cyan contour delineates the critical pO_2 threshold of 2.43 mmHg, below which primary islet cell death is induced.

OXYGEN COEFFICIENTS

To model the oxygen transport characteristics of the mesh devices and obtain the results in **Figure 4-13**, we apply the permeation (or diffusion) circuit model, which integrates the unique geometry of the devices to calculate their effective permeability (or diffusivity). The specific geometry of the mesh leads us to characterize its anisotropic permeability (or diffusivity), detailed as follows (**4.1**). The effective solubility (S_{eff}), a scalar quantity, can be determined using a volumetric-based homogenization method described in equation (**3.39**).

$$\begin{bmatrix} P_{eff,horizontal} & 0 & 0 \\ 0 & P_{eff,horizontal} & 0 \\ 0 & 0 & P_{eff,vertical} \end{bmatrix} = S_{eff} \cdot \begin{bmatrix} D_{eff,horizontal} & 0 & 0 \\ 0 & D_{eff,horizontal} & 0 \\ 0 & 0 & D_{eff,vertical} \end{bmatrix} \tag{4.1}$$

The initial step in modeling the Oxygen-Regulating Hollow Mesh device involves a layout of its geometry to determine the effective vertical permeability ($P_{eff,vertical}$). **Figure 4-14A** provides a bird's-eye view of the Oxygen-Regulating Hollow Mesh, displaying its hexagonally arranged holes. To simplify, we consider a triangular unit cell within this arrangement, which is highlighted in the figure. This unit cell contains regions corresponding to the open holes and the mesh branches. The open holes are expected to be filled with interstitial fluids; the branches consist of two layers of Parylene HT coating that encapsulate hollow air channels. By assessing the pore area relative to the unit cell's footprint, we find that the open area constitutes approximately 58% of the total, and the branch area constitutes approximately 42% of the total. With the geometric information, we construct a resistive network as depicted in **Figure 4-14B**. Effectively, the resistive network for modeling permeability can be simplified to a single equivalent resistor, as depicted in the right panel of the figure. Inputting the relevant values into the equations provided allows us to calculate the effective vertical permeability ($P_{eff,vertical}$) for the Oxygen-Regulating Hollow Mesh, which is determined to be 1.82×10^{-14} $(mol \cdot s/kg)$.

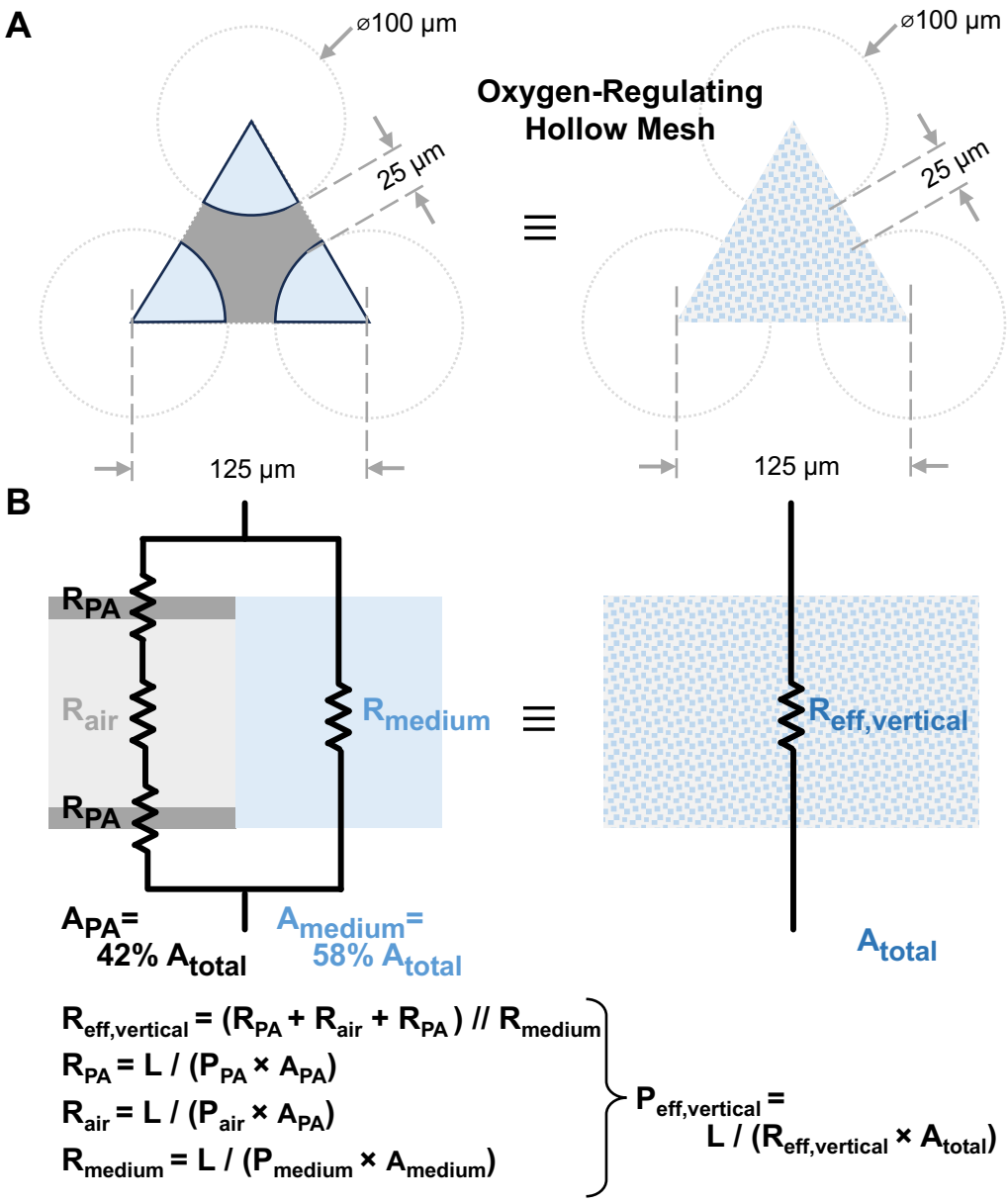

Figure 4-14. Visualization of effective vertical permeability calculation using the permeability circuit model for the Oxygen-Regulating Hollow Mesh, based on its geometry. The left panel showcases the geometry of the Oxygen-Regulating Hollow Mesh, consisting of open hole areas permeated by the medium (light blue), and air-containing mesh hollow branches structured with dual layers of parylene (PA) coating (dark gray) sandwiching a single layer of air (light gray). The right panel demonstrates the homogenized material with an effective permeability for computer simulation. (A) Top-down view of the Oxygen-Regulating Hollow Mesh. (B) Cross-sectional view of the Oxygen-Regulating Hollow Mesh with the permeability circuit model.

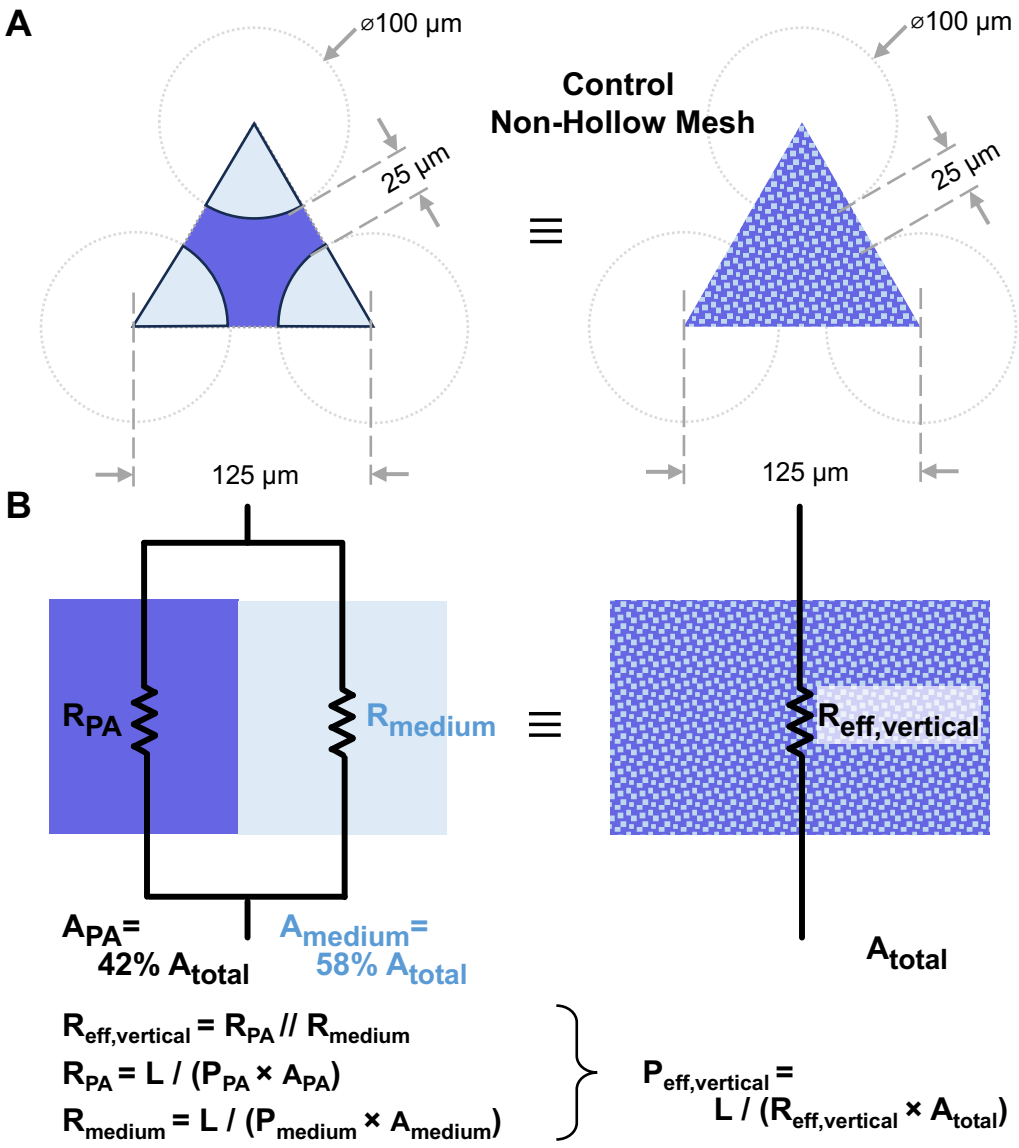

Figure 4-15. Visualization of effective vertical permeability calculation using the permeability circuit model for the Control Non-Hollow Mesh, based on its geometry. The left panel showcases the geometry of the Control Non-Hollow Mesh, consisting of open hole areas permeated by the medium (light blue), and mesh branches structured with a single layer of parylene (PA) coating (blue). The right panel demonstrates the homogenized material with an effective permeability for computer simulation. (A) Top-down view of the Control Non-Hollow Mesh. (B) Cross-sectional view of the Control Non-Hollow Mesh with the permeability circuit model.

The methodology utilized for the Oxygen-Regulating Hollow Mesh can similarly be applied to the Control Non-Hollow Mesh. **Figure 4-15A** illustrates a top-down view of the Control Non-Hollow Mesh, which features a hexagonal pattern of holes as well. The selected unit cell within this pattern includes both open holes and mesh branches. The key distinction between the Control Non-Hollow Mesh and the Oxygen-Regulating Hollow Mesh lies in the composition of the mesh branches; the Control Non-Hollow Mesh is constructed from a single solid layer of Parylene C. Utilizing this geometric information, we construct the permeation resistive network as presented in **Figure 4-15B**. Subsequently, the effective vertical permeability ($P_{eff,vertical}$) for the Control Non-Hollow Mesh is calculated to be 1.76×10^{-14} $(mol \cdot s/kg)$.

Note that the effective vertical permeabilities of both the Oxygen-Regulating Hollow Mesh and the Control Non-Hollow Mesh are quite comparable. The interstitial medium possesses a permeability of 3.05×10^{-14} $(mol \cdot s/kg)$. Thus, the presence of the mesh branches reduces the approximately 40% of overall oxygen permeability, similar to the area they occupy.

To ascertain the effective horizontal permeability ($D_{eff,horizontal}$) of the mesh devices, we diverge from the effective circuit model due to the horizontal complexity of the mesh's geometry. Instead, a segment of the mesh device is extracted for simulation that follows the precise geometry of the mesh. One boundary of the simulation domain is set as a constant volume source (pO_2 = 40 mmHg), and the opposite boundary is a no-flux wall. We track the temporal evolution of pO_2 at the domain's wall end. The simulation outcomes are then juxtaposed against theoretical expectations for a homogeneous material under uniform diffusivity across an equivalent length (**3.12**). Through this comparison, the effective horizontal diffusivity for the mesh devices can be deduced.

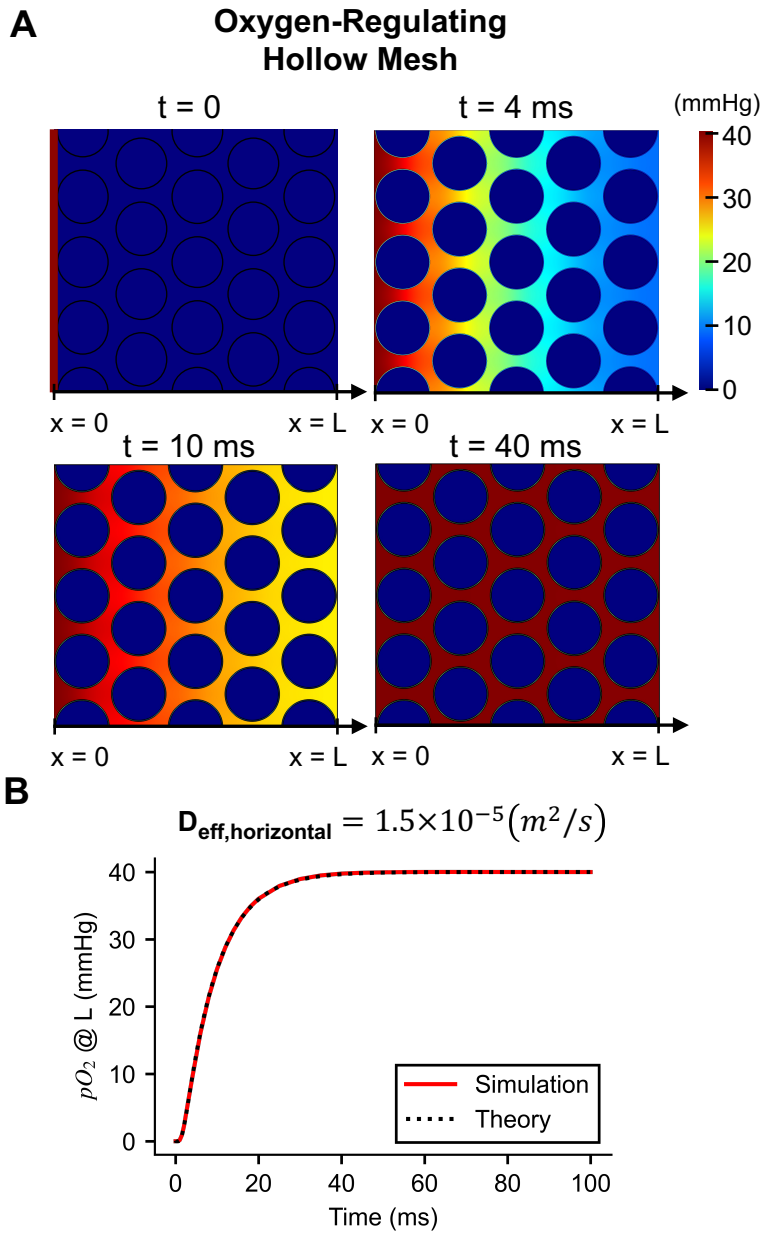

Figure 4-16. Simulation setup for assessing effective horizontal diffusivity of the Oxygen-Regulating Hollow Mesh using its geometrical configuration. (A) 2D layout of Oxygen-Regulating Hollow Mesh with the pO_2 profile snapshots at 0, 4, 10, and 40 ms. (B) Time-series plot of average pO_2 values along the length (x=L) of Oxygen-Regulating Hollow Mesh. The red line indicates the simulation results from part A; the black dotted line plots the theoretical calculation assuming a uniform diffusivity throughout a homogenous material with the length (L = 541 μm).

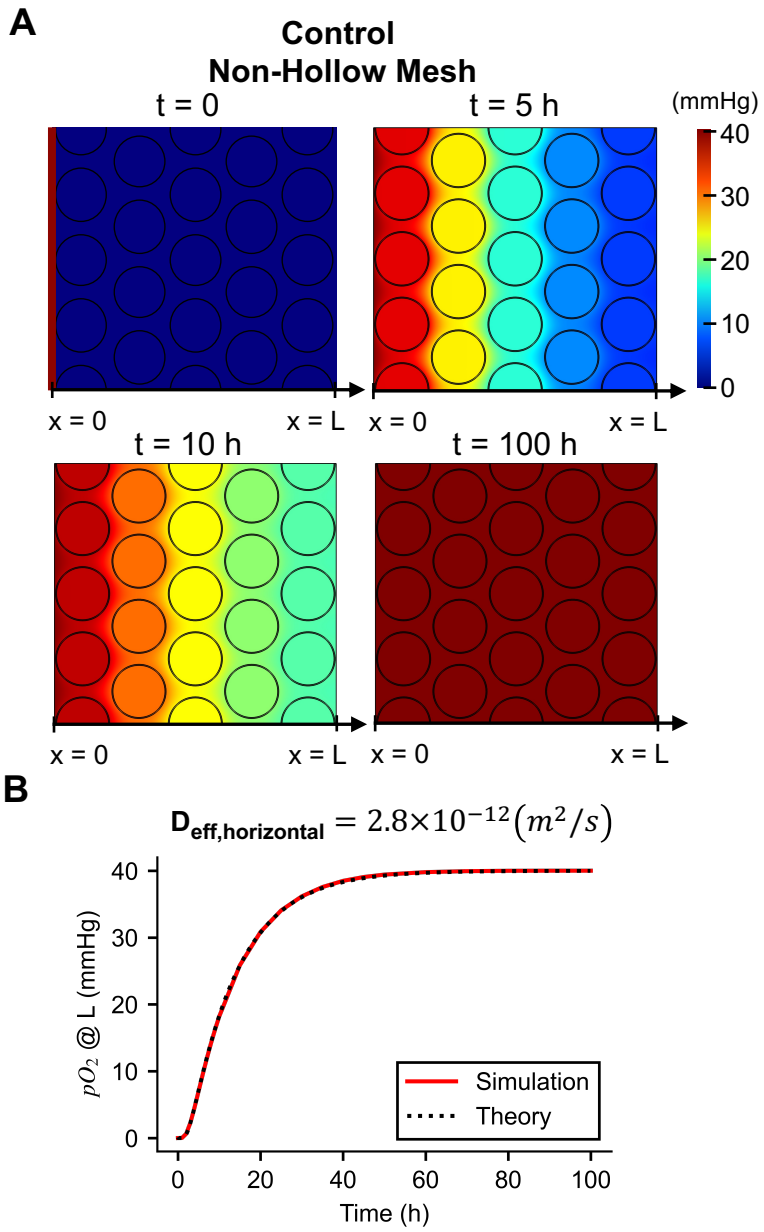

Figure 4-17. Simulation setup for assessing effective horizontal diffusivity of the Control Non-Hollow Mesh using its geometrical configuration. (A) 2D layout of Control Non-Hollow Mesh with the pO_2 profile snapshots at 0, 5, 10, and 100 h. (B) Time-series plot of average pO_2 values along the length (x=L) of Oxygen-Regulating Hollow Mesh. The red line indicates the simulation results from part A; the black dotted line plots the theoretical calculation assuming a uniform diffusivity throughout a homogenous material with the length (L = 541 μm).

Figure 4-16A visualizes the process used to calculate the effective horizontal permeability ($D_{eff,horizontal}$) for the Oxygen-Regulating Hollow Mesh. Notably pO_2 has progressed significantly through the hollow channels at 4 ms, whereas the regions filled with medium remain mostly unchanged. **Figure 4-16B** compares the time-series simulation of pO_2 based on the setup in **Figure 4-16A** with the theoretical calculation of oxygen diffusion through a homogenous single-layer material (**3.12**). These results indicate that the effective horizontal diffusivity ($D_{eff,horizontal}$) of the Oxygen-Regulating Hollow Mesh device is 1.5×10^{-5} (m^2/s).

In parallel, **Figure 4-17A** provides a visualization for determining the effective horizontal permeability ($D_{eff,horizontal}$) for the Control Non-Hollow Mesh. In contrast to the Oxygen-Regulating Hollow Mesh, oxygen transport within the Control Non-Hollow Mesh is significantly slower. It takes up to 5 hours from the start of the measurement for a pO_2 gradient to become apparent across the material. From the analysis presented in **Figure 4-17B**, we conclude that the effective horizontal diffusivity ($D_{eff,horizontal}$ of the Control Non-Hollow Mesh device is 2.8×10^{-12} (m^2/s), which is almost seven orders of magnitude lower than that observed for the Oxygen-Regulating Hollow Mesh group.

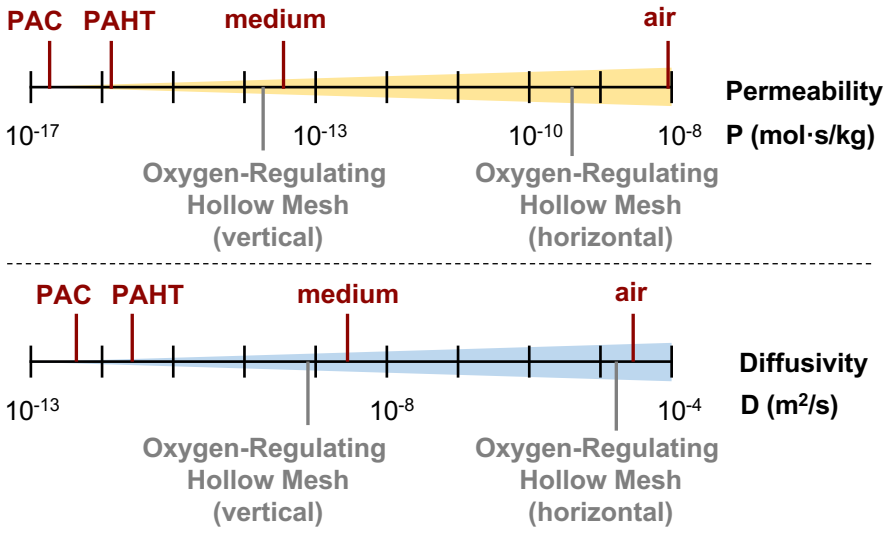

Figure 4-18. Visualization of log-scaled oxygen permeability and diffusivity in key materials applied in this work.

Table 4-1 and **Figure 4-18** provide a comprehensive summary of oxygen transport coefficients, encompassing values for both the constituent materials and those computed for the mesh devices, including Oxygen-Regulating Hollow Mesh and Control Non-Hollow Mesh.

Table 4-1. Simulated and computed oxygen transport coefficients for various materials and mesh devices. The order of the material is arranged in descending sequence according to permeability.

Materials	P (mol·s/kg)	D (m^2/s)	S (mol·s^2/m^2/kg)
Air	9.48×10^{-9}	2.45×10^{-5}	3.87×10^{-4}
Hollow Mesh (horizontal)	3.36×10^{-10}	1.50×10^{-5}	2.24×10^{-5}
Medium	3.05×10^{-14}	2.80×10^{-9}	1.09×10^{-5}
Hollow Mesh (vertical)	1.82×10^{-14}	8.13×10^{-10}	2.24×10^{-5}
Non-Hollow Mesh (vertical)	1.76×10^{-14}	1.68×10^{-9}	1.05×10^{-5}
Parylene-HT (PAHT)	1.12×10^{-16}	2.67×10^{-12}	4.20×10^{-5}
Non-Hollow Mesh (horizontal)	2.94×10^{-17}	2.80×10^{-12}	1.05×10^{-5}
Parylene-C (PAC)	1.33×10^{-17}	4.03×10^{-13}	3.30×10^{-5}

P, Oxygen permeability; D, Oxygen diffusivity; S, Oxygen solubility. $P = D \times S$.

Chapter 5

Oxygen-Regulating Hollow Mesh— Preclinical Studies

5.1 EX VIVO OXYGEN-REGULATING EFFECTS ON SHORT-TERM ISLET GRAFT SURVIVAL

The first preclinical study aims to show that the Oxygen-Regulating Hollow Mesh significantly improves islet graft viability, particularly during the early post-transplantation phase, a period when hypoxia is the major challenge to islet survival.

Figure 5-1 details the experimental methodology. Essentially, luciferase-transgenic (Luc-Tg) rat islets are chosen for their ability to emit bioluminescence as an indicator for islet graft survival [103], [167], [168]. Islets are isolated from the pancreases of Luc-Tg LEW rats using an established method [88]. Luc-Tg islets (1000 IEQ/subject), integrated with either Oxygen-Regulating Hollow Mesh or Control Non-Hollow Mesh, are transplanted into the dorsal subcutaneous site of nonobese diabetic/severe combined immunodeficiency (NOD scid) mouse recipients. Streptozotocin (STZ) at a dosage of 50 mg/kg body weight is administered intraperitoneally three days in a row three weeks prior to the graft transplantation to induce diabetes.

As illustrated in **Figure 5-1**, the chosen site for transplantation is subcutaneous. To improve vascularity, prevascularization has been significantly validated in experimental models and is currently being evaluated in a clinical trial for its ability to enhance islet engraftment [53], [103], [169]. In our protocol, a disc with basic fibroblast growth factor (bFGF) is pre-transplanted two weeks prior to the islet transplantation (T = -2 weeks). This bFGF disc is prepared from a lyophilized 4.5% agarose disc, measuring 15 mm in diameter and 1.5 mm in thickness, which is then infused with a solution of bFGF (75 µl at 500 µg/ml) and heparin sodium (75 µl at 250 µg/ml).

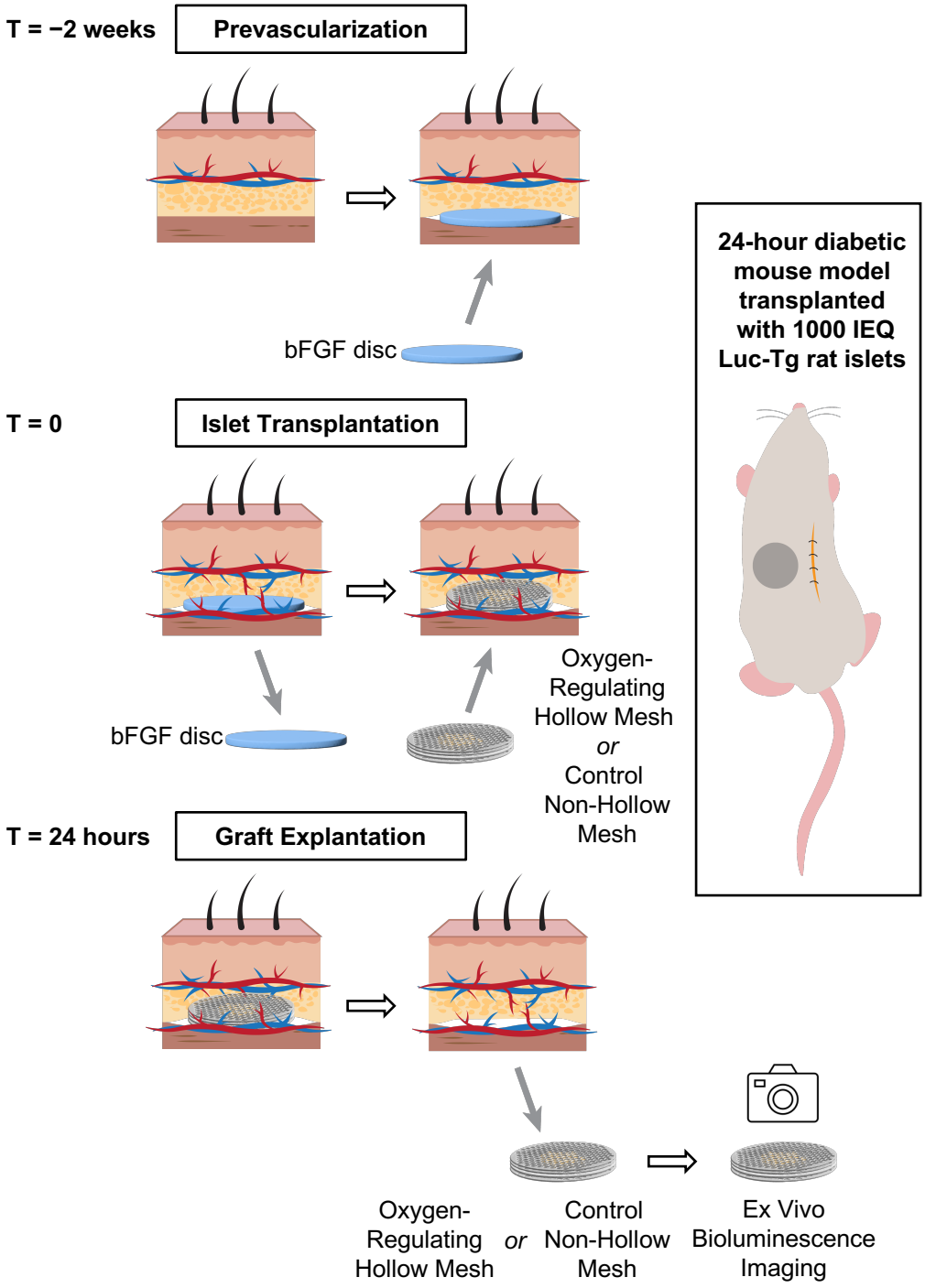

Figure 5-1. Illustration of the experimental protocol employing Oxygen-Regulating Hollow Mesh and Control Non-Hollow Mesh to evaluate oxygen-regulating effects on short-term islet survival using ex vivo bioluminescence imaging.

At the time of transplantation (T = 0), the bFGF discs are first surgically removed. Subsequently, either the Oxygen-Regulating Hollow Mesh or the Control Non-Hollow Mesh, each loaded with 1000 IEQ Luc-Tg islets, is transplanted. Twenty-four hours after transplantation (T = 24 hours) into the subcutaneous space, the islet grafts, along with the devices, are explanted. **Figure 5-2** presents the critical surgical steps undertaken on the mouse subjects for extracting the Oxygen-Regulating Hollow Mesh with islet graft 24 hours after the transplantation. The revascularization of the graft does not occur within 24 hours and the tissue adhesion to the device has not been established; therefore, the devices containing islet graft are retrieved without the dissociation of the tissue. This also indicates that the oxygen supply for the graft survival solely relied on diffusion. All animal procedures were conducted under general anesthesia.

Figure 5-2. Photographs of surgical procedures on a mouse subject. Wound clips have been applied to secure skin closure for a period of 24 hours. Mesh devices integrated with luciferase-transgenic rat islets are explanted for ex vivo bioluminescence imaging.

Ex vivo bioluminescence imaging is performed 10 minutes after luciferin is introduced to the explanted islet grafts [170]. The rationale for explanting the islet grafts is to mitigate the bias produced by the absorption of emitted bioluminescence by the skin layer, which would occur if the experiment were conducted in vivo. The

intensity of the bioluminescent signal serves as an indicator of the viability of the transplanted islets.

Figure 5-3 displays the bioluminescence-based assessment of islet graft viability. **Figure 5-3A** presents representative bioluminescent images across four experimental conditions. In **Figure 5-3B**, the total bioluminescent flux is quantified with measurements indicating $1.24\pm0.24 \times 10^7$ photons/s for Oxygen-Regulating Hollow Mesh and $0.63\pm0.22 \times 10^7$ photons/s for Control Non-Hollow Mesh. A notable observation is that the Oxygen-Regulating Hollow Mesh exhibits an approximately two-fold increase in total bioluminescent flux compared to the Control Non-Hollow Mesh with P = 0.0059. This underscores the efficacy of the Oxygen-Regulating Hollow Mesh in mitigating the decrease in viability due to hypoxia. The experiment also indicates that oxygen deficiency can rapidly affect islet graft viability; significant reductions can occur within the first 24 hours if the oxygen microenvironment is not effectively engineered to support the transplanted islets.

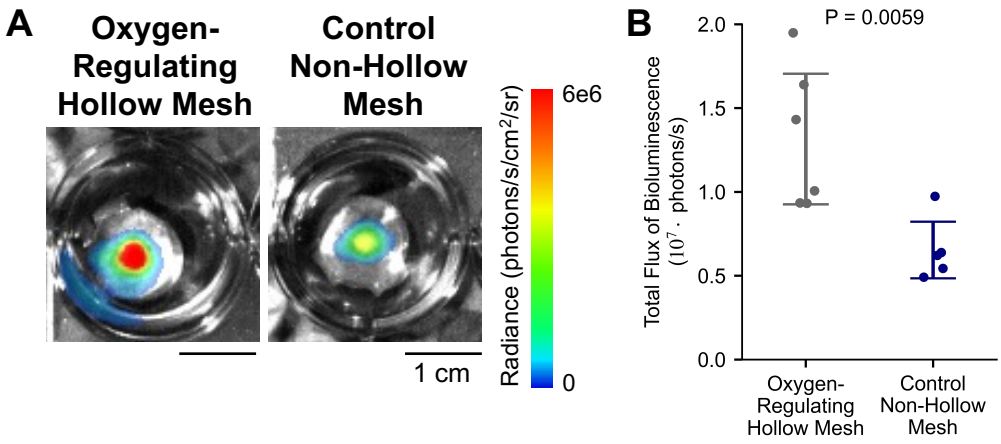

Figure 5-3. Bioluminescence imaging outcomes from the ex vivo experiment. (A) Representative bioluminescence images showcasing luciferase-transgenic rat islets integrated within Oxygen-Regulating Hollow Mesh or Control Non-Hollow Mesh. Images are taken 10 minutes after the introduction of luciferin in the PBS solution. (B) Quantification the total flux of bioluminescence with sample sizes of five in Oxygen-Regulating Hollow Mesh and six in Control Non-Hollow Mesh. Error bars: ±SD.

5.2 IN VIVO OXYGEN REGULATING EFFECTS ON LONG-TERM ISLET GRAFT SURVIVAL AND DIABETIC REVERSAL

In this second section, we aim to illustrate that the Oxygen-Regulating Hollow Mesh is capable of significantly enhancing the long-term survival of islet grafts as well as sustaining diabetic reversal. Extending beyond 16 weeks post-transplantation, the in vivo experiments are conducted with a diabetic mouse model.

Figure 5-4 outlines the methodology of our extended study, paralleling the approach of the short-term experiment by selecting the subcutaneous site for islet transplantation. To enhance vascularity, a bFGF-releasing disc is implanted two weeks prior to islet transplantation (T = -2 weeks), prepared as delineated in Chapter 4.5. To induce diabetes, STZ is administered intraperitoneally at a dose of 50 mg/kg body weight for three consecutive days, three weeks before graft transplantation.

At the time of transplantation (T = 0), the bFGF discs are surgically removed. Next, either the Oxygen-Regulating Hollow Mesh or the Control Non-Hollow Mesh, each loaded with 1200 IEQ of LEW rat islets, is transplanted into the dorsal subcutaneous space of immunodeficient NOD scid diabetic mice. The rat islets are harvested from the pancreases of LEW rats using the established method [88]. There are 7 mice recipients in the Oxygen-Regulating Hollow Mesh group and 6 in the Control Non-Hollow Mesh group. All procedures are carried out under general anesthesia to ensure the well-being of the animal subjects.

During the 20-week study, the non-fasting blood glucose levels and body weight of mice are recorded weekly, with the data detailed in **Figure 5-5A and B**. In the group of Oxygen-Regulating Hollow Mesh, six out of seven mice achieve blood glucose regulation below 200 mg/dL within two weeks following transplantation. A subsequent graftectomy for Oxygen-Regulating Hollow Mesh at 16 weeks result in an increase in blood glucose levels, verifying that the improved glycemic control is a direct result of the transplanted graft, not the mice's native islets.

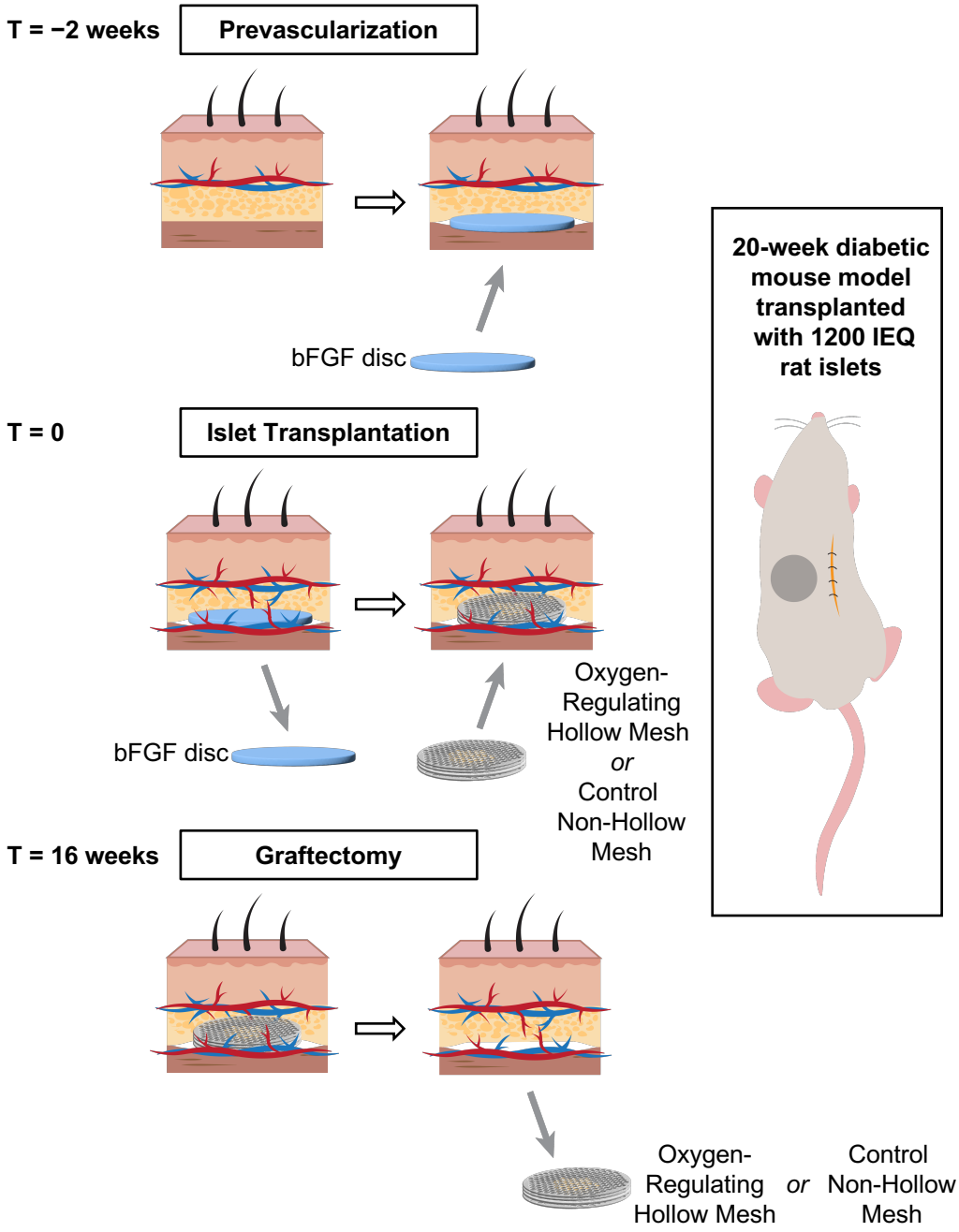

Figure 5-4. Illustration of the experimental protocol employing Oxygen-Regulating Hollow Mesh and Control Non-Hollow Mesh to evaluate oxygen-regulating effects on long-term islet graft survival by monitoring the blood glucose concentration and diabetic reversal rate. Graftectomy is performed only for Oxygen-Regulating Hollow Mesh.

Conversely, in the Control Non-Hollow Mesh group, only half of the subjects, three out of six, show a reversal of diabetes three weeks after transplantation. The

remaining three subjects do not achieve this reversal during the 20-week period. Furthermore, two subjects from the group that initially show diabetic reversal experienced fluctuations in blood glucose levels after six or nine weeks, eventually returning to levels above 200 mg/dL, suggesting insufficient engraftment at the initial stage.

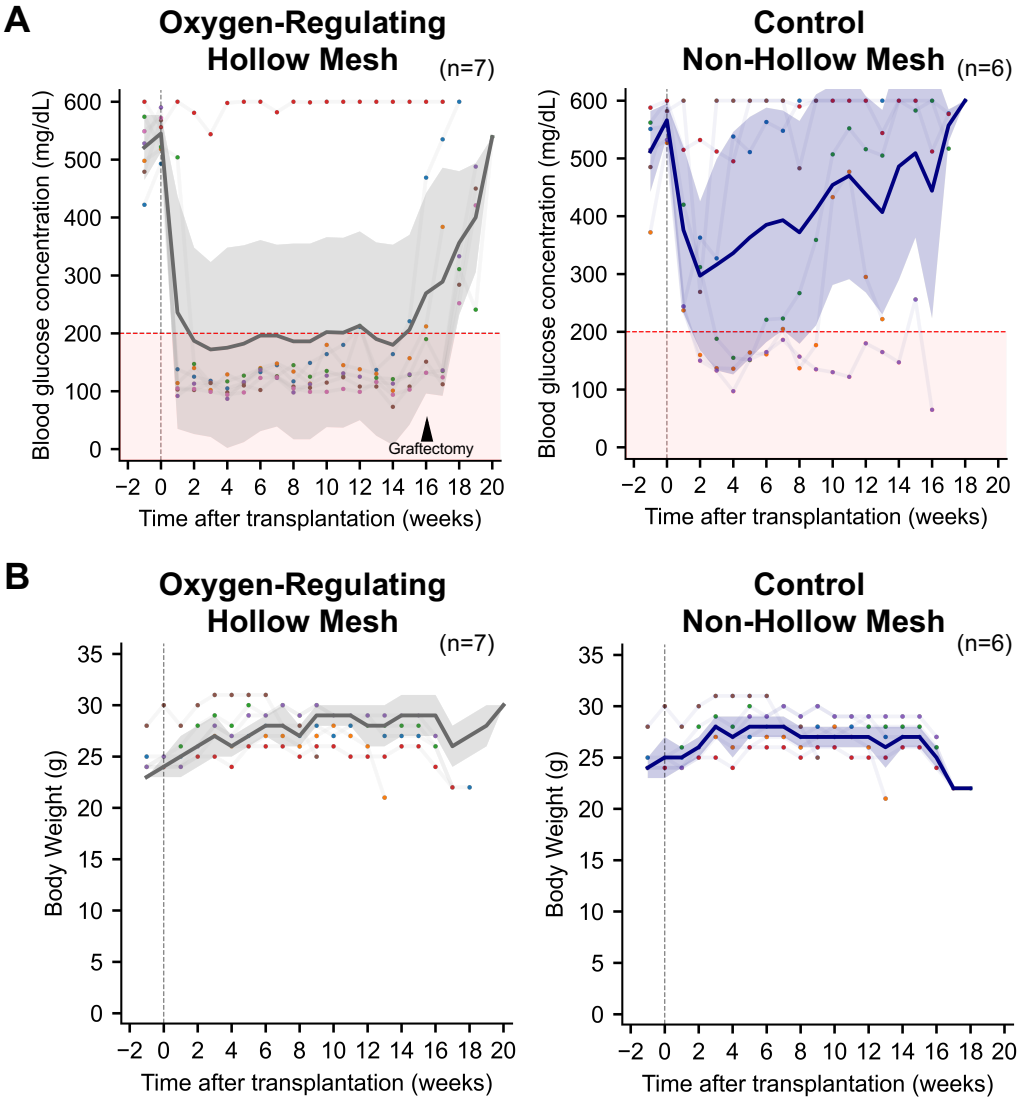

Figure 5-5. Blood glucose concentration (A) and body weight (B) measurements of STZ-induced diabetic male NODscid rat after 1200 IEQ islet transplantation into the Oxygen-Regulating Hollow Mesh and Control Non-Hollow Mesh. Graftectomy is performed 16 weeks after the islet transplantation. Error band: ±SD.

On average, the blood glucose levels for the Oxygen-Regulating Hollow Mesh group remain around or below 200 mg/dL during the study. In contrast, the Control Non-Hollow Mesh group's islet grafts does not maintain blood glucose regulation effectively. A Mann-Whitney U test with a Chi-square distribution is used to rigorously compare the blood glucose results, obtaining P-values to deduce statistical significance from week 2 to week 15. The P-values are summarized in **Table 5-1**, indicating that week 4, 10, 11, and 12 are not statistically significant, whereas all other weeks show statistical significance, emphasizing the effectiveness of the Oxygen-Regulating Hollow Mesh over Control Non-Hollow Mesh in managing long-term glycemia.

Table 5-1. The statistical analysis of body glucose between the Oxygen-Regulating Hollow Mesh and Control Non-Hollow Mesh. Mann-Whitney U test is used with Chi square distribution to obtain the P value. A P value less than 0.05 denotes statistical significance; numbers are highlighted in bold.

Week	2	3	4	5	6	7	8
P value	**0.032**	**0.022**	0.085	**0.022**	**0.022**	**0.015**	**0.038**
Week	9	10	11	12	13	14	15
P value	**0.015**	0.088	0.167	0.062	**0.035**	**0.047**	**0.038**

Further analysis of the blood glucose data is also carried out, with the results depict in **Figure 5-6A** revealing an AUC of blood glucose from 0 to 4 weeks of 959.79±568.33 mg/dL·week for the Oxygen-Regulating Hollow Mesh group compared to 1442.00±506.43 mg/dL·week for the Control Non-Hollow Mesh group. The P-value between these two groups is 0.063. For the period from 0 to 12 weeks, shown in **Figure 5-6B**, the AUC for the Oxygen-Regulating Hollow Mesh group is 2503.36±1881.25 mg/dL·week, and for the Control Non-Hollow Mesh group, it is 4338.20±1847.55 mg/dL·week, with a P-value of 0.062. Despite the P-values for both the 4-week and 12-week data not reaching the conventional threshold of statistical significance ($P < 0.05$), it can be noted that there is an outlier in the Oxygen-Regulating Hollow Mesh group contributing to higher blood glucose levels, while

the remaining subjects maintain comparatively low levels. This distribution skewness contributes to the marginally non-significant P-value.

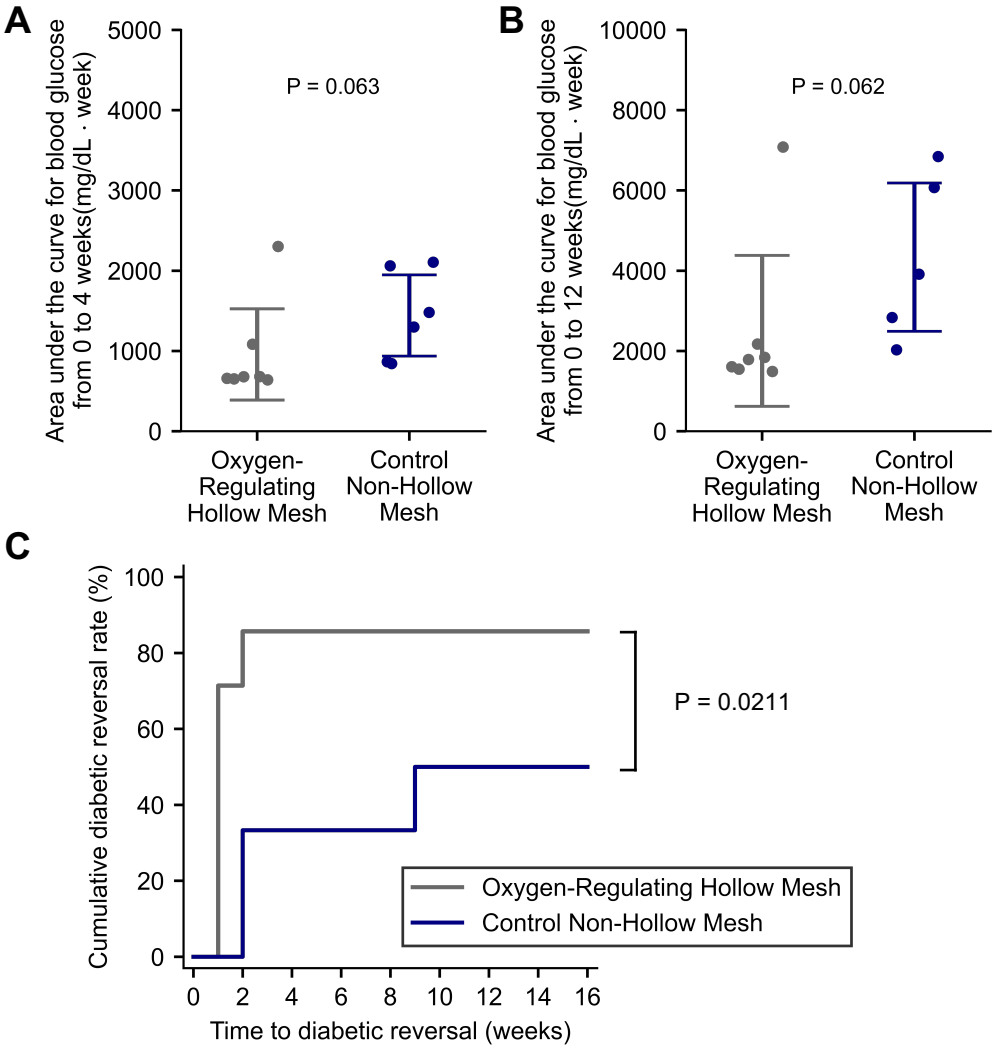

Figure 5-6. Detailed analysis of blood glucose measurements from long-term in vivo transplantation experiments using Oxygen-Regulating Hollow Mesh and Control Non-Hollow Mesh. (A) Area under the curve (AUC) of blood glucose levels recorded from week 0 to week 4. Mann-Whitney U test with Chi square distribution is used to determine the P-value. Error bar: ±SD. (B) Area under the curve (AUC) of blood glucose levels recorded from week 0 to week 12. Mann-Whitney U test with Chi square distribution is used to determine the P-value. Error bar: ±SD. (C) Cumulative diabetes reversal rate in the diabetic mouse model treated with Oxygen-Regulating Hollow Mesh and Control Non-Hollow Mesh groups over a 16-week period. The log-rank test is used for statistical analysis to calculate the P-value.

When considering the criterion for diabetes reversal—a blood glucose level below 200 mg/dL—the cumulative diabetes reversal rate is calculated (**Figure 5-6C**). The final diabetes reversal rate is 85.7% for the Oxygen-Regulating Hollow Mesh group and 50% for the Control Non-Hollow Mesh group. The P-value from the log-rank test is 0.021, indicating a statistically significant difference in reversal rates between the two mesh groups, with the Oxygen-Regulating Hollow Mesh group showing a higher success rate in reversing diabetes. Once again, the results reflect the superiority of oxygen-regulating effects of Oxygen-Regulating Hollow Mesh in the successfulness of islet transplantation therapy.

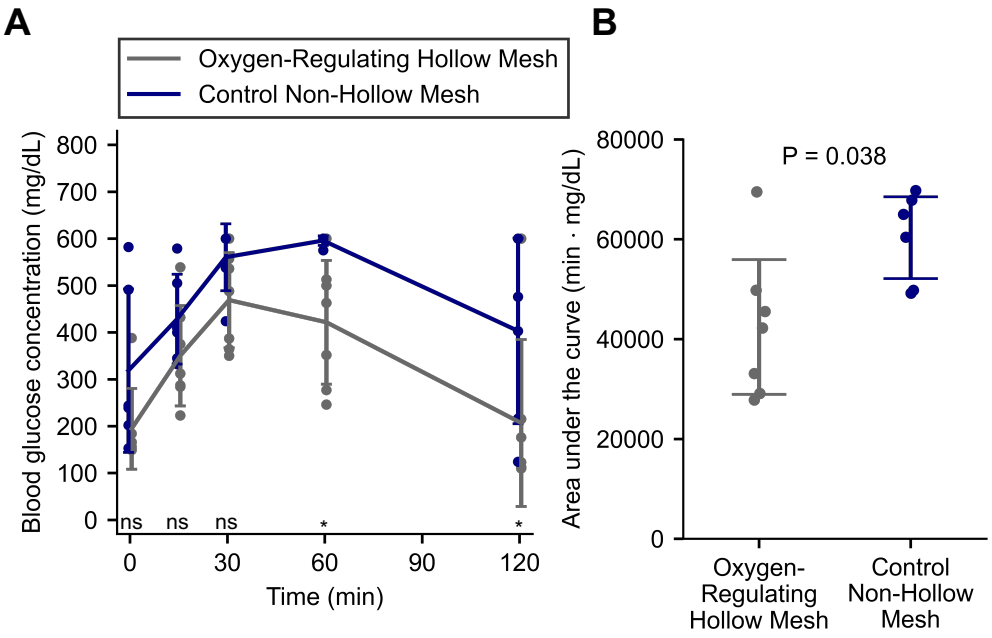

Figure 5-7. Blood glucose responses using the intraperitoneal glucose tolerance test (IPGTT) six weeks post-transplantation to assess the in vivo function of islets with the Oxygen-Regulating Hollow Mesh and Control Non-Hollow Mesh. (A) The IPGTT blood glucose concentration at time points 0, 15, and 30 minutes. Error bar: ±SD. (B) The area under the curve (AUC) analysis between Oxygen-Regulating Hollow Mesh and Control Non-Hollow Mesh. Mann-Whitney U test with Chi square distribution is used to determine the P-value (*, P < 0.05; ns, non-significant). Error bar: ±SD.

The IPGTT evaluates islet graft function by monitoring blood glucose concentrations over time, with results shown in **Figure 5-7**. Glucose measurements taken at 60 minutes post-glucose administration, the Oxygen-Regulating Hollow Mesh group shows a statistically significant improvement in glucose handling compared to the Control Non-Hollow Mesh group, with a P-value of 0.013. This trend continues at 120 minutes, with a P-value of 0.046, reinforcing the benefit of the Oxygen-Regulating Hollow Mesh on islet graft function. When evaluating the AUC for the entire 120-minute IPGTT duration, the Oxygen-Regulating Hollow Mesh group demonstrates a significantly lower AUC of 42433.93±13494.42 mg/dL·min compared to 60328.75±8188.56 mg/dL·min for the Control Non-Hollow Mesh group. The statistical analysis yields a P-value of 0.038, confirming a significantly enhanced islet graft function in the Oxygen-Regulating Hollow Mesh group over the Control Non-Hollow Mesh group.

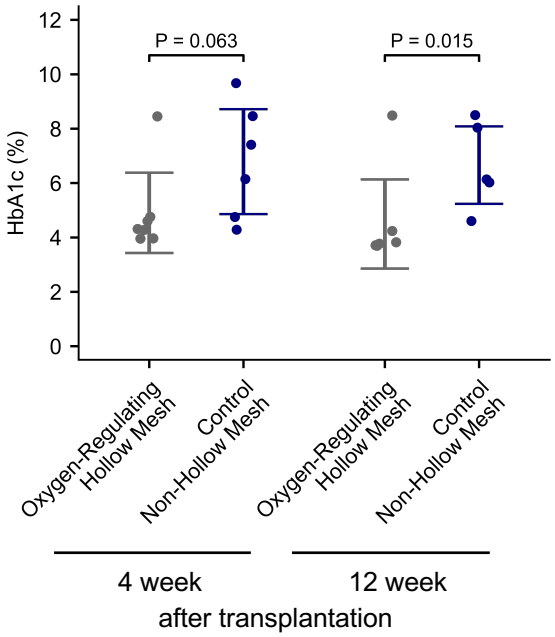

Figure 5-8. Hemoglobin A1c (HbA1c) levels in both Oxygen-Regulating Hollow Mesh and Control Non-Hollow Mesh groups, measured at 4 and 12 weeks post-transplantation. The Mann-Whitney U test alongside a Chi-square distribution is utilized to calculate the P-value. Error bar: ±SD.

The Hemoglobin A1C (HbA1c) test, a crucial measure of blood sugar management, is conducted at both 4 and 12 weeks post-transplantation. The HbA1c results provide the percentage of hemoglobin that is glycosylated, acting as a marker for average blood glucose levels over the previous two to three months and serving as an additional indicator to distinguish between normal (< 5.7%), pre-diabetic (5.7–6.4%), and diabetic (> 6.5%) states.

Figure 5-8 depicts the HbA1c percentages in mice models following islet transplantation, measured at both 4 and 12 weeks after transplantation for the Oxygen-Regulating Hollow Mesh and Control Non-Hollow Mesh groups. For the Oxygen-Regulating Hollow Mesh group, the HbA1c levels are 4.90±1.47% at 4 weeks and 4.50±1.64% at 12 weeks, with both time points indicating a non-diabetic state in the mice. In contrast, for the Control Non-Hollow Mesh group, the HbA1c levels are 6.79±1.93% at 4 weeks and 6.66±1.43% at 12 weeks, with both time points suggesting the mice remain in a diabetic state. When comparing the two groups, at week 4 the P-value is 0.063, indicating a marginally non-significant difference. However, by week 12 the P-value drops to 0.015, demonstrating a significant long-term improvement in blood glucose regulation and diabetic management in the Oxygen-Regulating Hollow Mesh group.

Figure 5-9 offers a detailed view of histological stains at 20 weeks post-transplantation. In the Oxygen-Regulating Hollow Mesh group, the mesh's structure is highlighted by a hollow appearance with a thin Parylene HT layer, maintaining the integrity and viability of the 1200 IEQ islet graft. In contrast, in the Control Non-Hollow Mesh group, where the mesh area is indicated by a solid rectangular thick Parylene C film, it shows a significant loss of islet grafts, which are largely undetectable.

Hematoxylin and Eosin (H&E) staining highlights the islets in light purple, with the nuclei appearing in a darker shade of purple, contrasting with the mesh structures. The presence of red blood cells, visible as red dots within the microvessels, indicates the penetration of the microvascular network into the mesh holes, confirming

successful revascularization. Masson's Trichrome (MT) staining reveals collagen-rich fibrotic tissues in blue. The presence of blue layers around the devices indicates a mild foreign body response, characterized by a fibrotic layer that is neither dense nor thick, as would be seen with a strong foreign body reaction. The MT stain also supports the biocompatibility of the devices and underscores their clinical potential.

In this study, we also utilize multi-color immunofluorescence staining to display the spatial relationships among different cellular components within and surrounding the islet graft, such as alpha, beta, delta, and endothelial cells. Beta cells, marked by insulin, are typically found at the core of the islets, alpha cells, indicated by glucagon, are situated peripherally, and delta cells, denoted by somatostatin, are interspersed and comprise less than 5% of the population. This distinct islet architecture is preserved in the Oxygen-Regulating Hollow Mesh group, indicating successful engraftment. Contrastingly, the Control Non-Hollow Mesh lacks discernible islet morphology. The CD31/Chromogranin panel illuminates the mesh structure with endothelial cells marked by CD31 in green, penetrating the mesh, and red-stained chromogranin, indicating islet grafts nestled within the meshwork.

These findings affirm the Oxygen-Regulating Hollow Mesh's superiority in promoting long-term graft survival. Given the primary difference between Oxygen-Regulating Hollow Mesh and Control Non-Hollow Mesh is the presence of air-containing hollow microchannels in the former, we can confirm these channels directly contribute to enhanced viability and function of the islet graft by facilitating the redistribution of oxygen, thereby autonomously regulating the microenvironment to optimize conditions for the islet graft.

To conclude, all the experimental findings presented significantly substantiate the superior performance of our Oxygen-Regulating Hollow Mesh device in effectively regulating the oxygen environment. This regulation is critical for facilitating long-term islet graft survival and the reversal of diabetes. These results underscore the potential of the Oxygen-Regulating Hollow Mesh as a viable tool in islet transplantation therapy, showcasing its oxygen-regulating ability to maintain an

optimal oxygen environment for prolonged periods, thereby enhancing the efficacy of diabetes treatment.

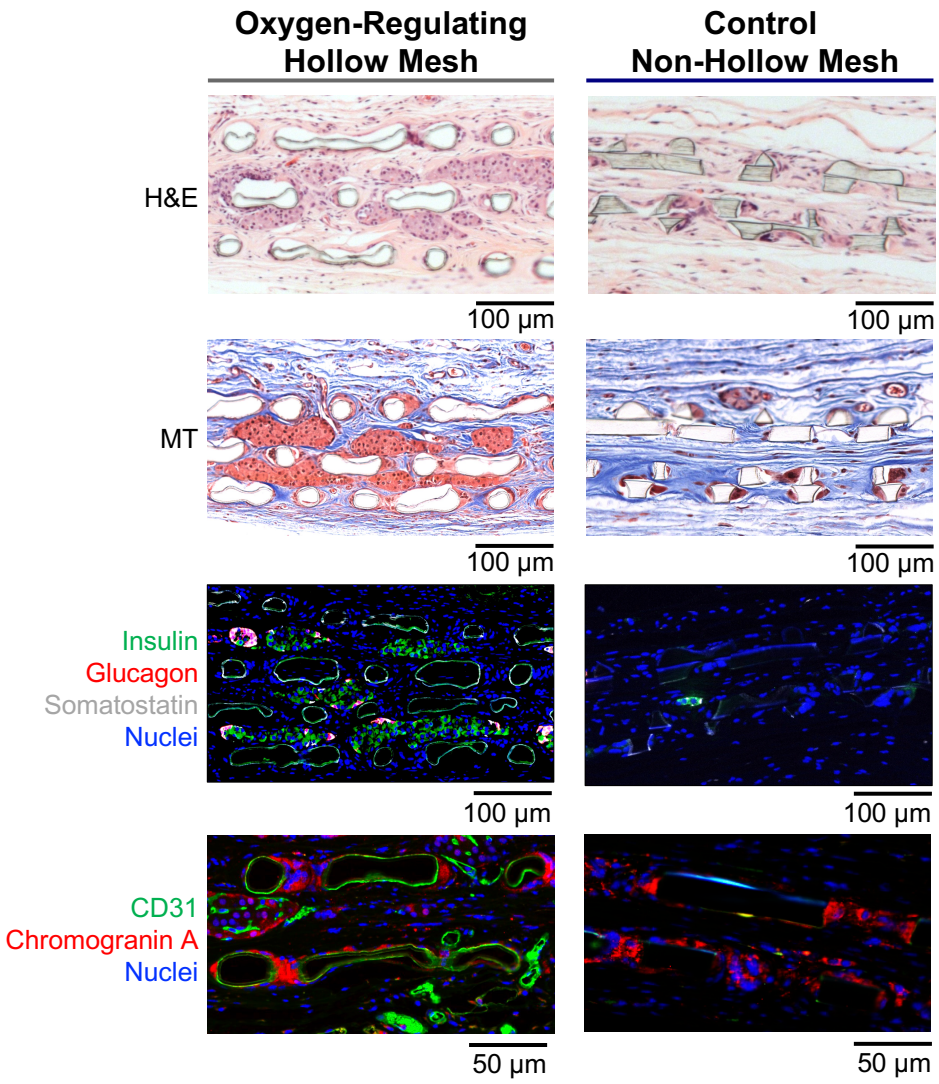

Figure 5-9. Detailed and magnified 20-week histological images of rat 1000 IEQ islet grafts integrated with Oxygen-Regulating Hollow Mesh and Control Non-Hollow Mesh in the subcutaneous space of mice. The samples are processed using various staining techniques: first row: Hematoxylin and Eosin (H&E) staining; second row: Masson's Trichrome (MT) staining; third row: immunofluorescence staining for insulin, glucagon, somatostatin, and nuclei; fourth row: and immunofluorescence staining for CD31, Chromogranin A, and nuclei.

5.3 IN VIVO OXYGEN REGULATING EFFECTS ON ISLET GRAFT SURVIVAL WITH INCREASED ISLET SEEDING DENSITY

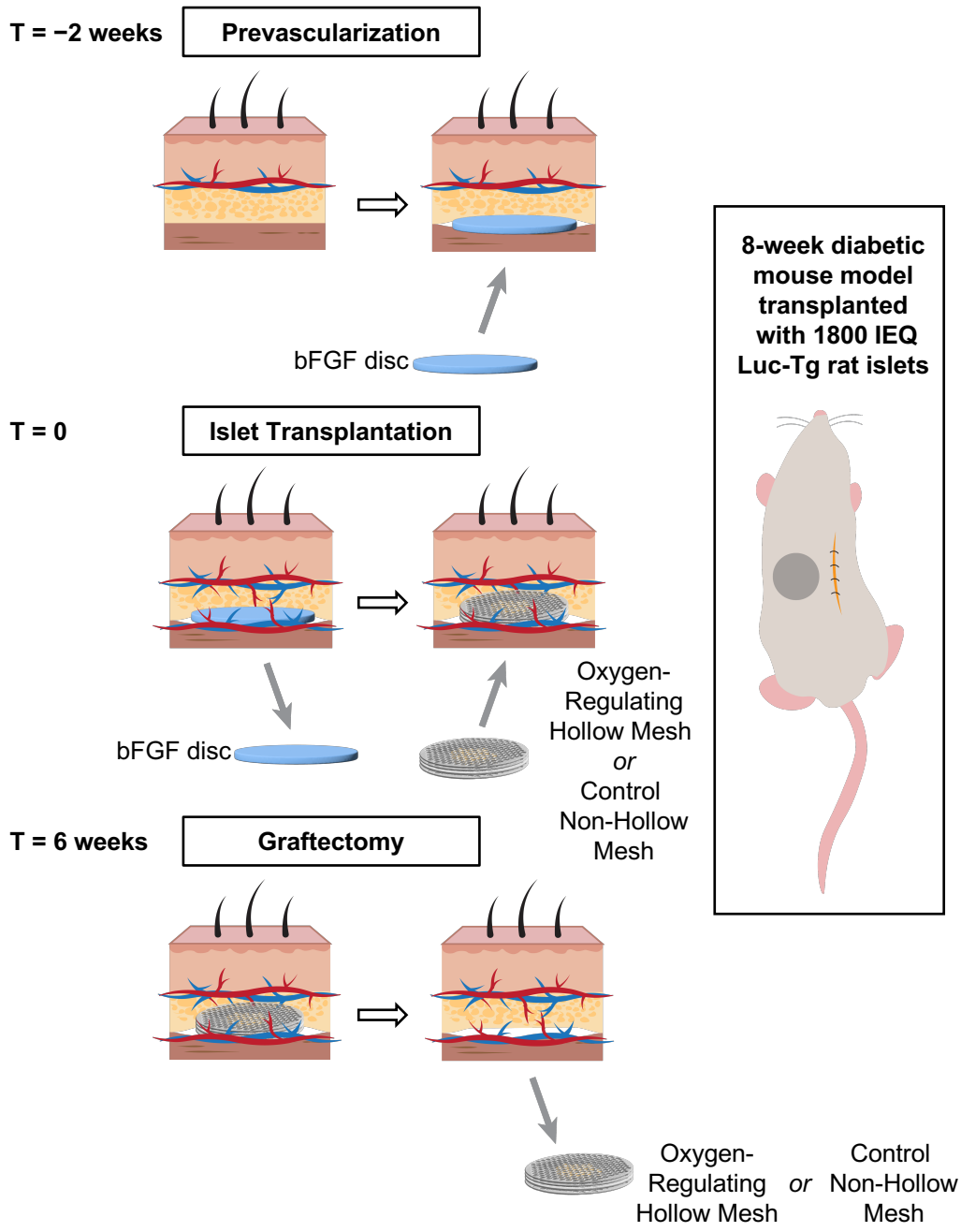

Figure 5-10. Illustration of the experimental protocol employing Oxygen-Regulating Hollow Mesh and Control Non-Hollow Mesh to evaluate oxygen-regulating effects on islet graft survival with increased islet seeding density (1800 IEQ) by in vivo bioluminescence imaging.

In this section, we aim to validate the Oxygen-Regulating Hollow Mesh's ability to support increased islet seeding density. To this end, we transplanted 1800 IEQ of Luc-Tg islets, representing a 50% increase from the 1200 IEQ referenced in Chapter 4.6.

While the transplantation of 1200 IEQ has been effective in reversing diabetes within the Oxygen-Regulating Hollow Mesh, it is advantageous to showcase the device's clinical utility at a higher islet seeding density. This is particularly relevant as larger numbers of islets may be necessary for therapies in larger animals or human subjects. As Luc-Tg LEW rat islets are utilized in this study, the in vivo bioluminescence is monitored as an indicator of islet graft viability.

Figure 5-10 illustrates the methodology employed in our study, mirroring the protocol depicted in **Figure 5-4**, with the subcutaneous site chosen for islet transplantation. Vascularity is promoted through the implantation of a bFGF-releasing disc two weeks prior to the transplantation of the islets (T = -2 weeks), as described in Chapter 4.5. To provoke diabetes, an intraperitoneal administration of STZ is carried out at a dose of 50 mg/kg body weight for three days in succession, commencing three weeks before the grafting. When transplantation commences (T = 0), the bFGF discs are first excised. Subsequently, we implant either the Oxygen-Regulating Hollow Mesh or the Control Non-Hollow Mesh, each embedded with 1800 IEQ of Luc-Tg LEW rat islets, into the dorsal subcutaneous region of immunodeficient NOD scid diabetic mice. Islets are isolated from the pancreases of Luc-Tg LEW rats using an established method [88]. The study includes 6 mice in the Oxygen-Regulating Hollow Mesh group and 7 in the Control Non-Hollow Mesh group. To ensure ethical treatment and the welfare of the animals, all procedures are performed under general anesthesia.

Our primary objective is to assess the preservation of graft mass over time. The quantity of islet cells transplanted in this study is above the threshold needed to counteract diabetes, which led us to expect improved glycemic control in both test groups. Although graft mass is traditionally monitored through histological

examination, this approach necessitates terminal surgeries that end the experiment when the graft mass is measured. To circumvent this, we adopt a non-invasive, longitudinal in vivo tracking method using bioluminescent imaging. This technique enabled us to repeatedly evaluate graft mass in the same subjects at various time points.

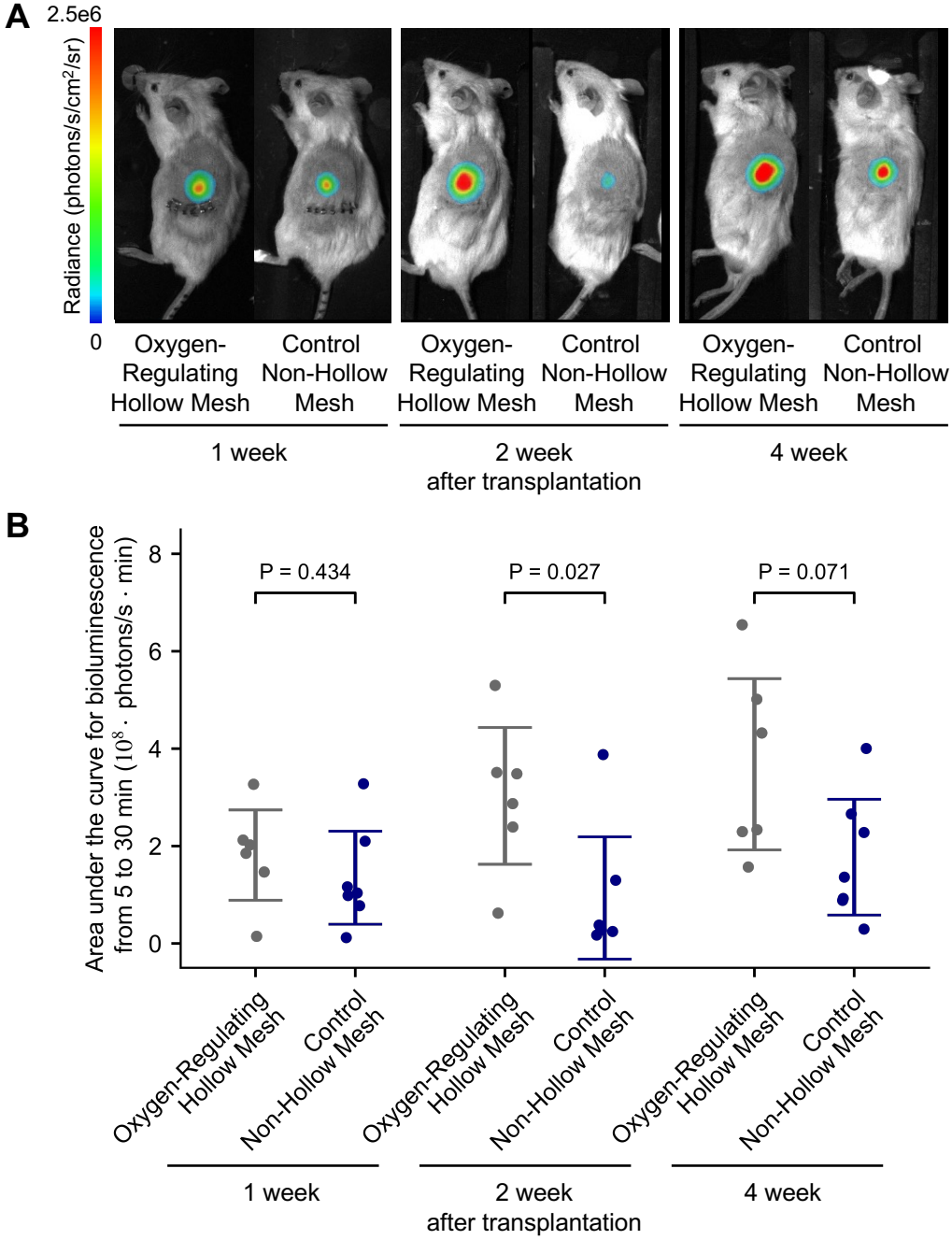

Figure 5-11. Bioluminescence imaging outcomes from the in vivo transplantation experiment at the time of 1, 2, and 4 weeks where 1800 IEQ islet graft is transplanted into the O2TR Mesh and Control Non-Hollow Mesh. (A) Representative bioluminescence images at 20 minutes after the intraperitoneal injection of luciferin showcasing luciferase-transgenic rat islets integrated within Oxygen-Regulating Hollow Mesh or Control Non-Hollow Mesh. Images are taken at 5 – 30 min after the intraperitoneal injection of luciferin under the general anesthesia. The representative images demonstrate the same animals in the different timepoints. (B) The area under the curve (AUC) of the total flux of bioluminescence, measured from 5 to 30 minutes, serving as an islet graft viability indicator under the aforementioned conditions, with sample sizes ranging from five to seven subjects per group. AUC from 5 to 30 minutes is chosen due to the delayed kinetic response following the intraperitoneal injection of luciferin to the islet graft. Welch's t-tests are used to determine P-values, with an alpha threshold of 0.05 indicating statistical significance. Error bar: ±SD.

Figure 5-11 showcases the bioluminescence imaging used to evaluate islet graft viability at 1, 2, and 4 weeks post-transplantation for both the Oxygen-Regulating Hollow Mesh and Control Non-Hollow Mesh groups. **Figure 5-11A** provides representative bioluminescent images illustrating the outcomes under four different conditions. **Figure 5-11B** quantifies the area under the curve of total bioluminescent flux, revealing the following data: for the Oxygen-Regulating Hollow Mesh, $1.81\pm0.93 \times 10^8$ photons/s·min at 1 week, $3.03\pm1.40 \times 10^8$ photons/s·min at 2 weeks, $3.68\pm1.76 \times 10^8$ photons/s·min at 4 weeks post-transplantation; for the Control Non-Hollow Mesh, $1.35\pm0.96 \times 10^8$ photons/s·min at 1 week, $0.93\pm1.25 \times 10^8$ photons/s·min at 2 weeks, $1.77\pm1.19 \times 10^8$ photons/s·min at 4 weeks post-transplantation.

A significant finding is that the Oxygen-Regulating Hollow Mesh group shows enhanced islet viability compared to the Control Non-Hollow Mesh after two weeks post-transplantation. The P-values are indicative of the differences in viability at various time points: $P = 0.434$ at 1 week, $P = 0.027$ at 2 weeks, and $P = 0.071$ at 4 weeks. These findings underscore the efficacy of the Oxygen-Regulating Hollow Mesh in maintaining islet graft viability, particularly when a higher density of islets is seeded, over the course of a month.

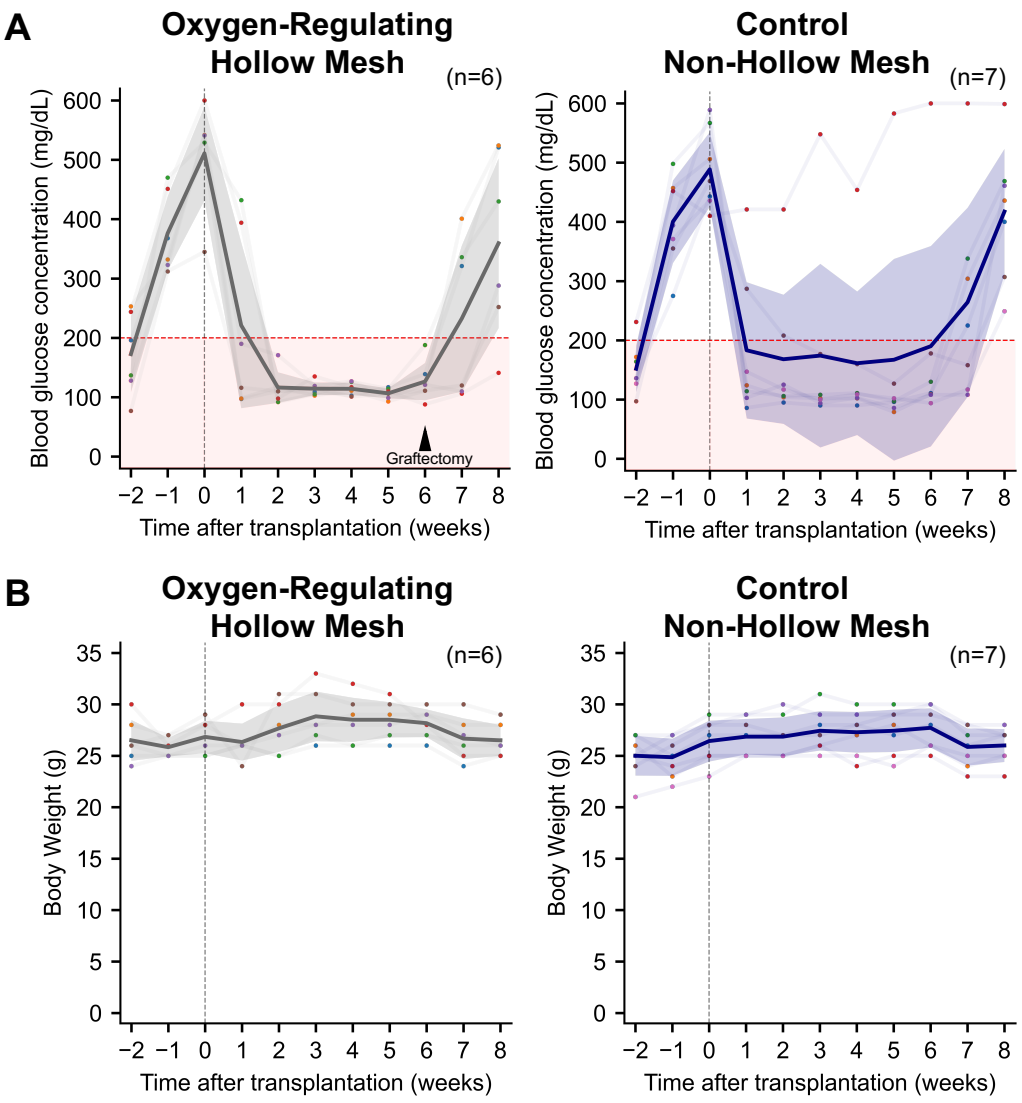

Figure 5-12. Blood glucose concentration (A) and body weight (B) measurements of STZ-induced diabetic male NODscid rat after 1800 IEQ islet transplantation into the O2TR Mesh and Control Non-Hollow Mesh. Graftectomy is performed 6 weeks after the islet transplantation. Error band: ±SD.

Blood glucose levels and body weight are carefully monitored as part of this study on diabetic mice, with results presented in **Figure 5-12A and B**. In the Oxygen-Regulating Hollow Mesh group, blood glucose levels in all six mice are regulated to below 200 mg/dL, which we define as a reversal of diabetes, within 2 weeks post-transplantation. A graftectomy is carried out at six weeks for those recipients who

have experienced a reversal of diabetes. This procedure is intended to provoke the recurrence of diabetes, thereby verifying that the euglycemia was due to the transplanted graft rather than the native islets in the pancreas.

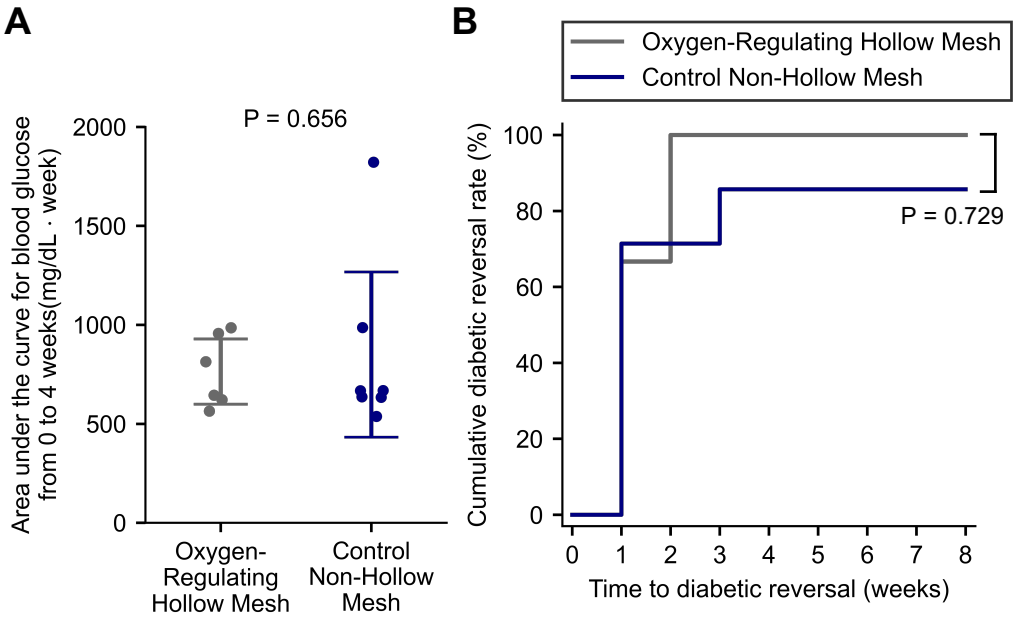

Figure 5-13. Detailed analysis of blood glucose measurements from in vivo transplantation experiments using Oxygen-Regulating Hollow Mesh and Control Non-Hollow Mesh. (A) Area under the curve (AUC) of blood glucose levels recorded from week 0 to week 4. Welch's t-test is used to determine the P-value. Error bar: ±SD. (B) Cumulative diabetes reversal rate in the diabetic mouse model treated with Oxygen-Regulating Hollow Mesh and Control Non-Hollow Mesh groups over an 8-week period. The log-rank test is used for statistical analysis to calculate the P-value.

Furthermore, detailed analyses of the blood glucose data are conducted. The AUC of the blood glucose profile is recognized as a strong indicator of long-term islet graft functionality [90]. The data presented in **Figure 5-13A** show an AUC of 764.33 ± 164.93 mg/dL·week for the Oxygen-Regulating Hollow Mesh group and 850.21 ± 417.46 mg/dL·week for the Control Non-Hollow Mesh group. The P-value between these two groups stands at 0.0656, not reaching conventional levels of statistical significance.

Using the criterion for diabetes reversal—blood glucose levels below 200 mg/dL—the cumulative diabetes reversal rate is presented in **Figure 5-13B**. The P-value derived from the log-rank test is 0.729, which suggests no statistically significant difference in the reversal rates between two mesh groups.

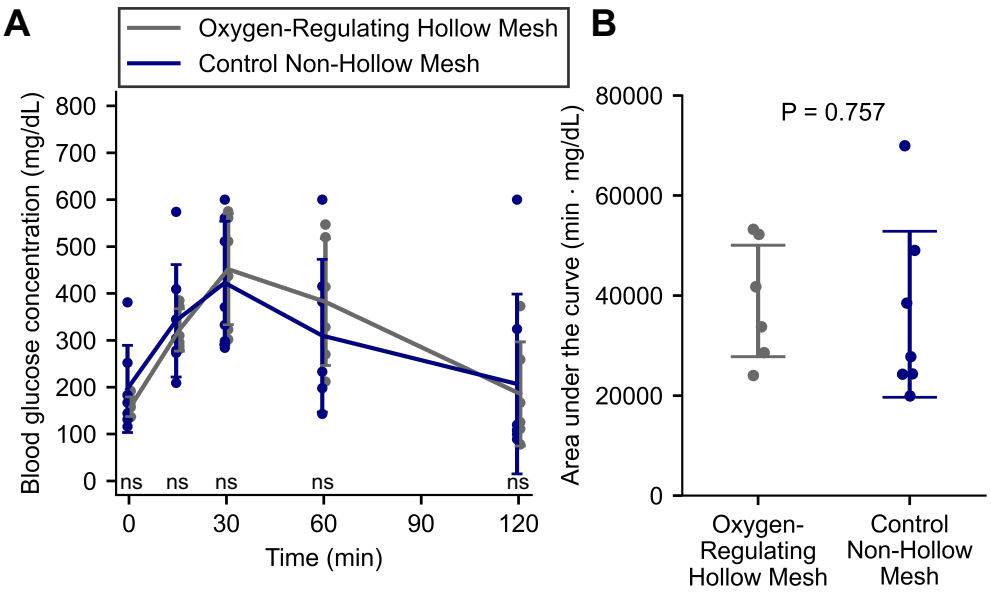

Figure 5-14. Blood glucose responses using the intraperitoneal glucose tolerance test (IPGTT) six weeks post-transplantation to assess the in vivo function of islets with the Oxygen-Regulating Hollow Mesh and Control Non-Hollow Mesh. (A) The IPGTT blood glucose concentration at time points 0, 15, and 30 minutes. Error bar: ±SD. (B) The area under the curve (AUC) analysis between Oxygen-Regulating Hollow Mesh and Control Non-Hollow Mesh. The Welch's t-test is used to determine P-values, with an alpha threshold of 0.05 indicating statistical significance and ns denotes non-significant. Error bar: ±SD.

Islet graft function, assessed via the IPGTT and represented by the time-course glucose concentration curve at week 6 post-transplantation (**Figure 5-14**). The glucose levels at 0, 15, 30, 60, and 120 minutes post-glucose injection demonstrate a non-significant difference between the time points for both Oxygen-Regulating Hollow Mesh and Control Non-Hollow Mesh groups. The AUC of blood glucose, over the 120-minute test period, is calculated as 38926±11149 mg/dL·min for the Oxygen-Regulating Hollow Mesh group and 36255±16606 mg/dL·min for the

Control Non-Hollow Mesh group. With a P-value of 0.757, this comparison indicates no statistically significant difference between the two groups in terms of islet graft function.

Across the measures of blood glucose levels, diabetes reversal rate, and IPGTT for islet functionality, the Oxygen-Regulating Hollow Mesh demonstrates marginally improved outcomes compared to the Control Non-Hollow Mesh. However, statistical analysis reveals these differences are not significant, hence no definitive conclusions can be made. This lack of significant difference can be attributed to the substantial number of rat islets (1800 IEQ) transplanted into the mouse recipients.

To conclude the above dataset, the critical observation is that bioluminescence results suggest an improved islet graft survival in the Oxygen-Regulating Hollow Mesh group compared to the Control Non-Hollow Mesh group, especially at a high islet seeding density of 1800 IEQ. It is inferred that hypoxia persists in the Control Non-Hollow Mesh group, with reduced viability due to an inadequate oxygen supply. However, the residual functional islet mass within the Control Non-Hollow Mesh group, albeit diminished, seems sufficient to regulate blood glucose levels effectively and reverse diabetes for a minimum of 8 weeks following transplantation.

Figures 5-15 and 5-16 provide histological evidence at 6 weeks post-transplantation, showcasing the sustained integration and viability of 1800 IEQ islet grafts within both the Oxygen-Regulating Hollow Mesh and Control Non-Hollow Mesh. In the Oxygen-Regulating Hollow Mesh group, the mesh area is indicated by a hollow space lined with a thin layer of parylene-HT coating. Conversely, in the Control group, the mesh area is demarcated by a solid rectangular section featuring a thick parylene-C coating. These figures display a variety of staining techniques described as follows:

H&E staining displays islets as light purple structures with darker purple nuclei, contrasting against the mesh structures. The red blood cells, visible as red dots within

microvessels, indicate microvascular network integration into the mesh openings, confirming revascularization.

MT staining reveals collagen-rich fibrotic tissue in blue hues. The blue peripheries around the devices hint at a mild foreign body reaction, as the fibrotic layer is not as dense or thick as would be seen with a robust foreign body reaction. The MT staining also identifies islet grafts with red coloring and dark red nuclei. Minimal fibroblast presence, indicated in dark blue or purple, around the device underscores the biocompatibility and potential for clinical use once again.

Immunohistochemical staining for insulin, manifesting as brown staining, corroborates the presence and engraftment of insulin-producing beta cells, the principal cells within pancreatic islets.

Immunohistochemistry for von Willebrand Factor (vWF) delineate endothelial cells in dark brown, distinct from the lighter brown of islet graft areas, furnishing further proof of successful revascularization through the opening holes of the mesh devices.

These histological staining techniques collectively demonstrate that both the Oxygen-Regulating Hollow Mesh and Control Non-Hollow Mesh devices are biocompatible, facilitate engraftment through revascularization, and can preserve the viability and function of the islet grafts over an 8-week period.

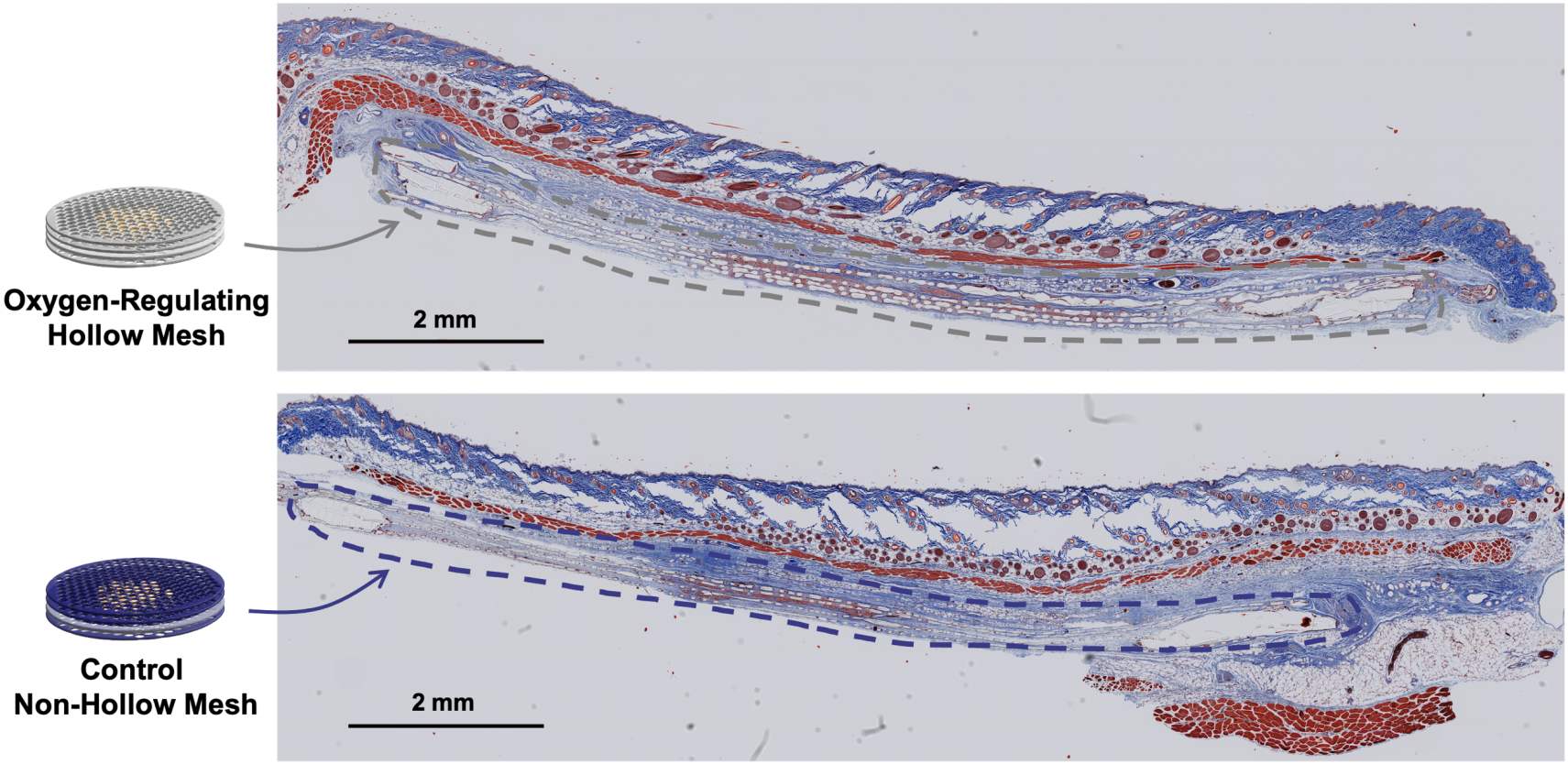

Figure 5-15. 6-week histological images of 1800 IEQ rat islet grafts integrated with Oxygen-Regulating Hollow Mesh and Control Non-Hollow Mesh in the mouse subcutaneous space. Masson's Trichrome (MT) staining has been applied to these samples. The dotted line delineates the area occupied by the mesh device.

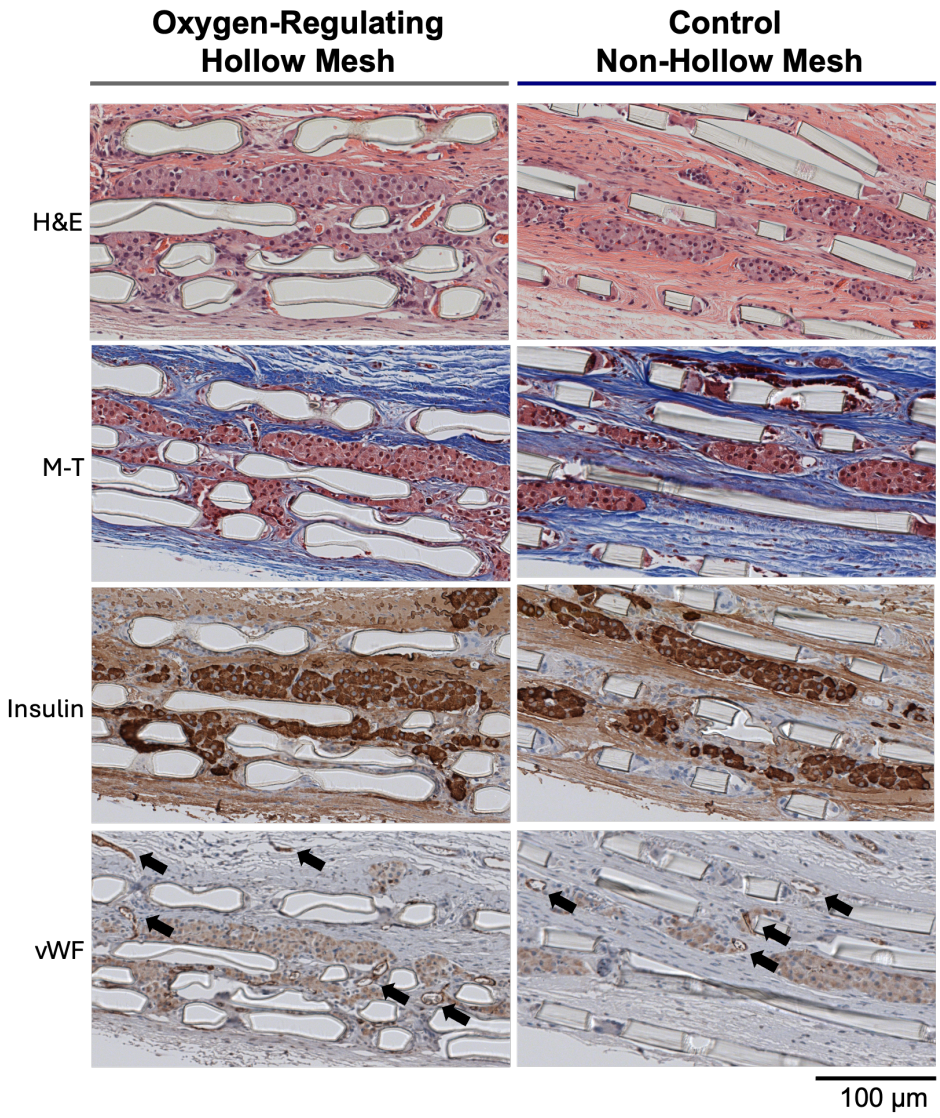

Figure 5-16. Detailed and magnified 6-week histological analysis of 1800 IEQ rat islet grafts integrated with Oxygen-Regulating Hollow Mesh and Control Non-Hollow Mesh in the subcutaneous space of mice. The samples are processed using Hematoxylin and Eosin (H&E) staining, Masson's Trichrome (M-T) staining, immunohistochemistry staining for insulin (Insulin), and immunohistochemistry staining for von Willebrand Factor (vWF) to assess tissue components, including red blood cells, fibroblasts, islet cells, and endothelial cells. The brown-colored staining indicates vWF, which is highlighted with arrows.

Chapter 6

Cannula-Connected Extended-Range Oxygen-Regulating Hollow Mesh Device

In Chapters 4 and 5, we introduce a novel oxygen-regulating hollow mesh device capable of self-regulating oxygen tension for the transplanted islet grafts. In this setup, the oxygen supply is primarily facilitated by the microvascular network. However, as an increasing number of islets are loaded onto the mesh device — a scenario more relevant to clinical applications — the oxygen supplied by the microvasculature may prove insufficient for the large volume of transplanted islets. Therefore, finding a method to adequately provide oxygen for a significant number of islets has become a critical challenge.

6.1 DESIGN OVERVIEW

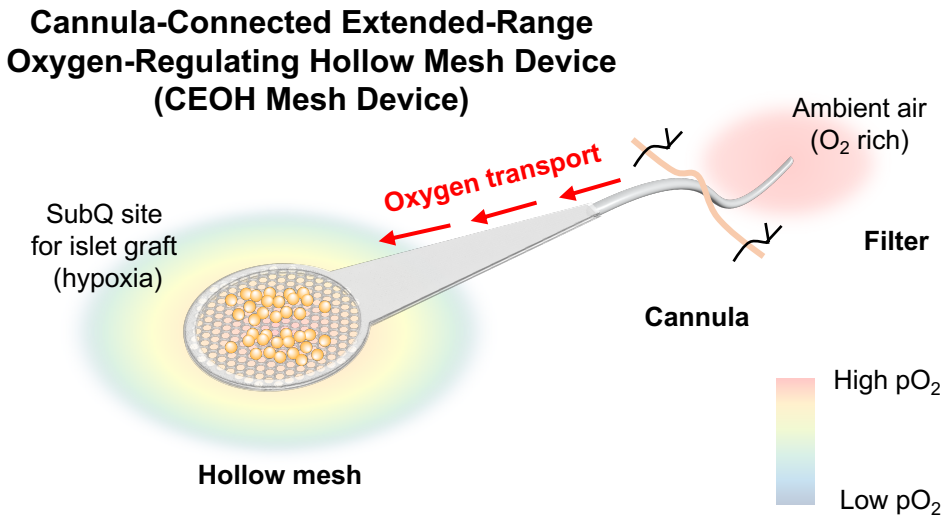

Figure 6-1. Schematic representation of the Cannula-Connected Extended-Range Oxygen-Regulating Hollow Mesh Device (CEOH Mesh Device). This illustration details the three principal components of the oxygen transport system: the hollow mesh, cannula, and filter.

We proposed a Cannula-Connected Extended-Range Oxygen-Regulating Hollow Mesh Device (**CEOH Mesh Device**) that leverages on the abundant oxygen available in the atmosphere. By utilizing this boundless source of oxygen, we could connect it to the islet graft, which often suffers from lack of oxygen (i.e., hypoxia). Due to the inherent oxygen gradient between the oxygen-rich air and the oxygen-poor transplant site, a steady and extended-ranged oxygen supply can be achieved.

To capitalize on this concept, we have designed a Cannula-Connected Extended-Range Oxygen-Regulating Hollow Mesh device illustrated in **Figure 6-1**. This device is ingeniously segmented into three main components: the air filter, the cannula, and the hollow mesh.

Beginning with the air filter, it boasts an oxygen-permeable membrane made from PDMS, connected to the external air. The air filter could also be made from a thin hydrophobic Teflon membrane with the average pore size less than 0.50 μm. This membrane permits oxygen diffusion while effectively filtering out potential contaminants such as condensed fluid and microorganisms. We can adjust the membrane thickness to regulate the volume of oxygen that flows into the device. As such, an extended-range of oxygen tension can be achieved.

Connecting the receiver to the hollow mesh is the cannula, constructed from a biocompatible silicone tube approximately 1.5 mm in diameter. Its dimensions and material composition ensure that it maintains patency against tissue pressure without inciting a significant foreign body response [159].

The pinnacle of our design is the hollow mesh, a meticulously designed mesh structure composed of microcapillary hollow channels, similar to our Oxygen-Regulating Hollow Mesh introduced in Chapter 4, allowing unhindered diffusion of oxygen. As described in Chapter 4, these hollow microchannels, only 25 μm wide, match the size of natural blood vessels and minimize foreign body reactions due to their slender and flexible design [159]. The parylene coating on the hollow channels permits oxygen transfer while blocking tissue fluids. The hexagonal lattice of the

hollow mesh, with islet-sized circular openings, supports islets and promotes vascularization, allowing insulin release and exchange of nutrients and waste, vital for islet transplant success.

6.2 ANALYSIS OF OXYGEN TRANSPORT

Let us utilize the equivalent circuit model to analyze the oxygen transport characteristics of our devices.

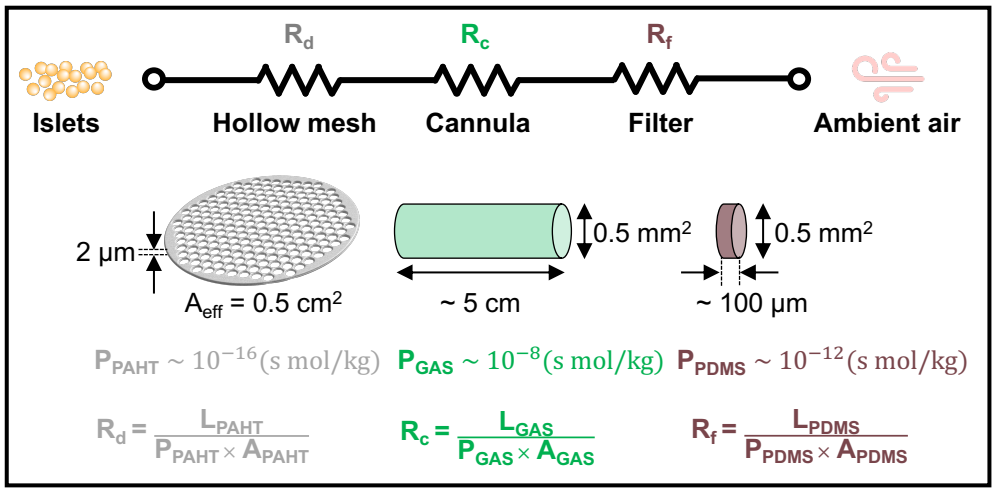

Figure 6-2. Equivalent permeation resistivity circuit model and calculation of the Cannula-Connected Extended-Range Oxygen-Regulating Hollow Mesh Device (CEOH Mesh Device).

Figure 6-2 depicts the equivalent permeation resistance circuit model for calculating the oxygen transport in our Cannula-Connected Extended-Range Oxygen-Regulating Hollow Mesh device. Assuming the thin PDMS air filter has a thickness of 100 μm, we can determine the resistivity by e**quation (3.35).** With the filter's diameter at roughly 0.5 mm^2 and PDMS permeability approximately $10^{-12}\ \frac{kg}{s \cdot mol \cdot m}$, the diffusion resistance of the air filter (R_f) is calculated in (**4.1**).

$$R_f = \frac{L_{PDMS}}{P_{PDMS} A_{PDMS}} \approx 2 \times 10^{14} \left(\frac{kg}{s \cdot mol \cdot m} \right) \tag{4.1}$$

For the air component inside the cannula, due to air's significantly higher diffusivity and solubility, we consider the resistance negligible.

$$R_c \cong 0 \tag{4.2}$$

At the hollow mesh, the total footprint is 1 cm². If the area covered by PAHT, excluding the holes, is approximately 50%, the effective area (A_{PAHT}) is 0.5 cm^2. The PAHT thickness (L_{PAHT}) is 2 μm with a permeability of roughly $10^{-16}\,\frac{kg}{s \cdot mol \cdot m}$. Consequently, we can compute the equivalent diffusion resistance (R_r) in (**4.3**).

$$R_d = \frac{L_{PAHT}}{P_{PAHT} A_{PAHT}} \approx 2 \times 10^{14} \left(\frac{kg}{s \cdot mol \cdot m}\right) \tag{4.3}$$

Here, we observe that the resistance at the hollow mesh and receiver are approximately equal. Leveraging this insight, we can advance our analysis to determine the flux and steady-state oxygen tension within the device.

Another crucial parameter is the loading capacity of our oxygen transport device, quantified as the number of islet equivalents (IEQ, n). Based on our circuit model analysis, the oxygen flux through the PDMS membrane matches the flux through the PAHT mesh hollow mesh, indicating that the pO_2 drops across both materials are the same. Mathematically, this is represented in (**4.4**).

$$\frac{pO_2(air) - pO_2(cannula)}{R_f} = \frac{pO_2(cannula) - pO_2(cells)}{R_d} \tag{4.4}$$

Therefore, the oxygen flux (J) entering the receiver end into the device can be expressed in (**4.5**).

$$J \cong -P_{PDMS} \frac{\Delta pO_2}{\Delta x} = P_{PDMS} \frac{pO_2(air) - pO_2(cells)}{2 \cdot L_{PDMS}} \left(\frac{mol}{m^2 \cdot s}\right) \tag{4.5}$$

It is reasonable to assume the oxygen traversing the device is predominantly consumed by the metabolically active transplanted islet cells. Given that the oxygen

consumption rate (R) of islet cells falls around 1 pmol/min/IEQ, and considering the typical islet diameter (d) is 150 µm, with a total islet layer thickness (T) of 500 µm (accounting for a slight gap between the hollow mesh and the actual islets and size variation), we can calculate the overall oxygen consumption rate (**4.6**).

$$J \cong n \cdot R \cdot T \cong n \cdot 10^{-6} \left(\frac{mol}{m^2 \cdot s}\right) \tag{4.6}$$

By equating the oxygen flux entering the receiver with the islet oxygen consumption, we can plot the cellular pO_2 against the IEQ loaded at the device's hollow mesh end (**Figure 6-3**). Hence, this analysis demonstrates the extended-range capabilities.

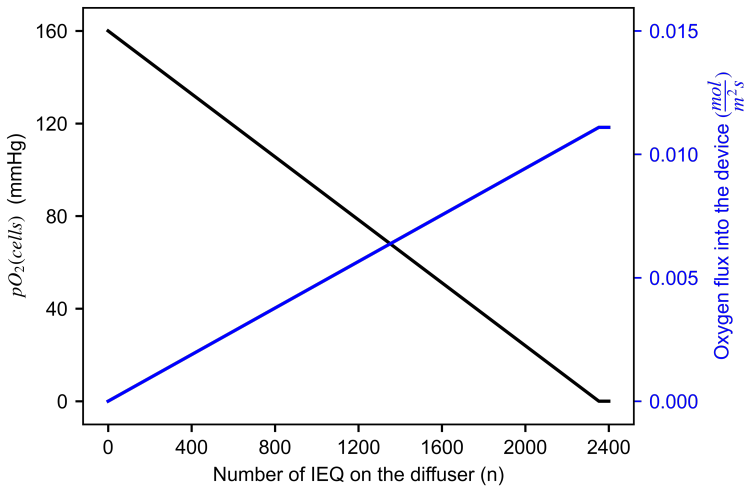

Figure 6-3. Estimation of $pO_2(cells)$ and oxygen flux entering the CEOH Mesh Device with respect to loading capacity (number of IEQ loaded).

From this analysis, we can deduce that the device possesses a loading capacity of up to approximately 1800 IEQ while maintaining a minimal oxygen partial pressure of 40 mmHg at the site of the transplanted cells. The maximum loading capacity using this calculation is around 2400 IEQ.

It is important to recognize that this calculation presumes oxygen is solely sourced from ambient air. As detailed in Chapter 4, the CEOH MESH DEVICE's hollow

mesh can also harness oxygen from the surrounding microvascular network. Despite the simplifications involved in this rough estimate, it provides a ballpark understanding of the CEOH Mesh Device's islet loading capacity.

6.3 FABRICATION PROCESSES

HOLLOW MESH COMPONENT FOR CEOH MESH DEVICE

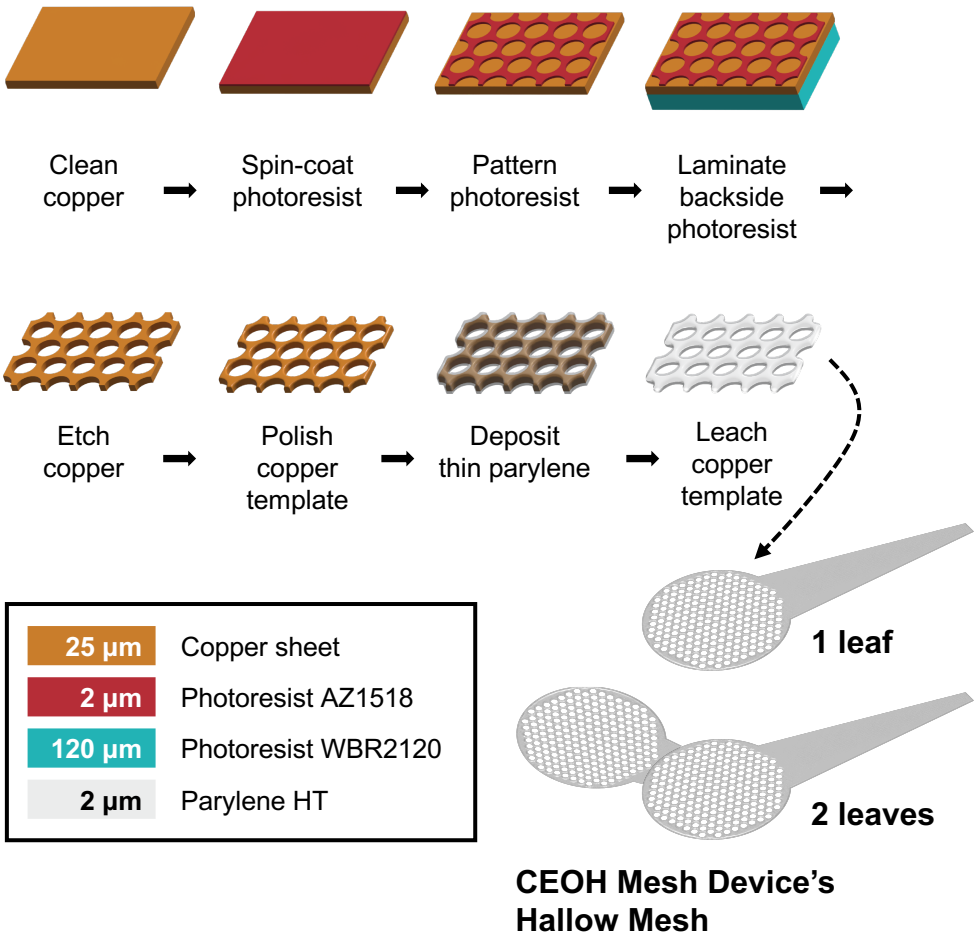

Figure 6-4. Fabrication processes of the Cannula-Connected Extended-Range Oxygen-Regulating Hollow Mesh Device (CEOH Mesh Device) hollow mesh. This figure outlines the photolithographical steps in fabrication the hollow mesh component of the CEOH MESH DEVICE, detailing the step-by-step processes and materials applied in its construction.

The CEOH MESH DEVICE's hollow mesh is crafted similarly to the Oxygen-Regulating Hollow Mesh device detailed in Chapter 4, employing microfabrication of a copper template which is then coated with parylene. Subsequently, the copper is etched away to create the microchannels. **Figure 6-4** illustrates this fabrication process, while an in-depth, step-by-step methodology is available in Section 4.2.

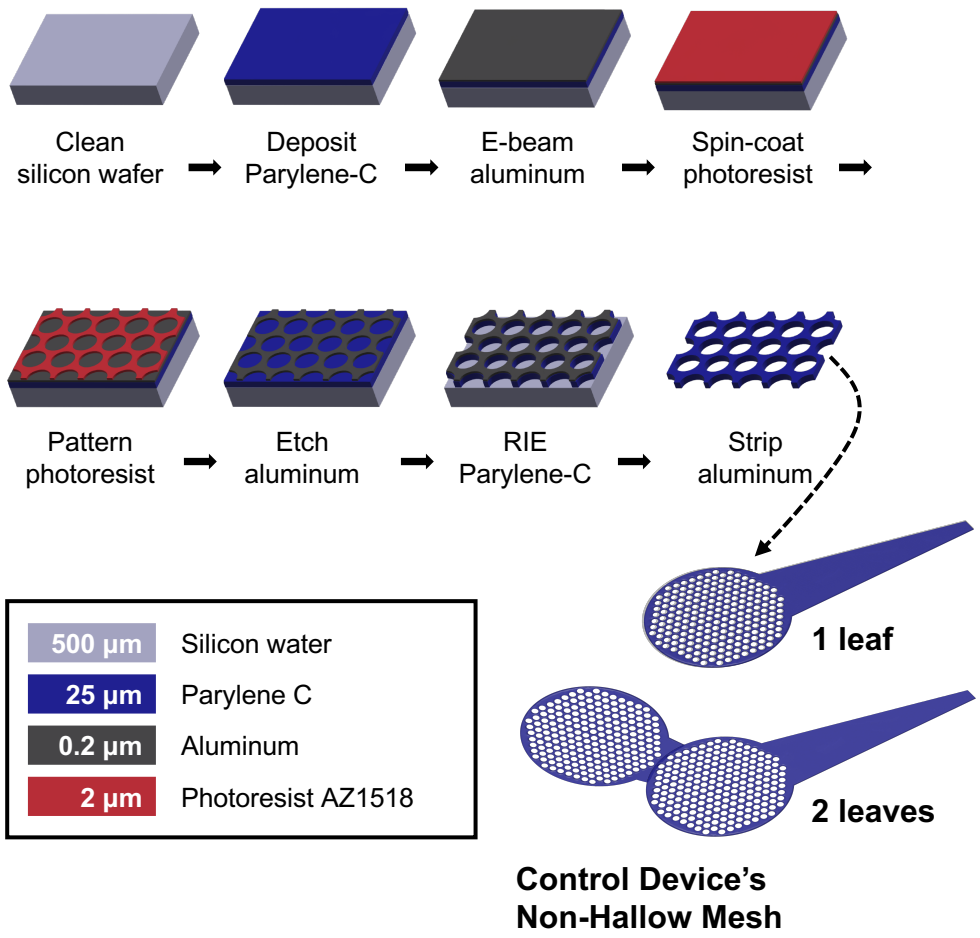

Figure 6-5. Fabrication processes of the Control Device mesh area. This figure outlines the photolithographical steps in fabrication the mesh area component of the Control Device, detailing the step-by-step processes and materials applied in its construction.

To thoroughly assess the CEOH Mesh Device's performance, we developed a custom Control Device and documented its fabrication process in **Figure 6-5**. Since the

Control Device closely mirrors the Control Mesh outlined in Chapter 4, detailed procedural steps are provided in Section 4.2.

Unlike the CEOH Mesh Device, the Control Device does not feature air-filled micro-channels but instead consists of a solid mesh structure made by thick parylene-C film. Both devices are designed with identical dimensions.

DEVICE ASSEMBLY

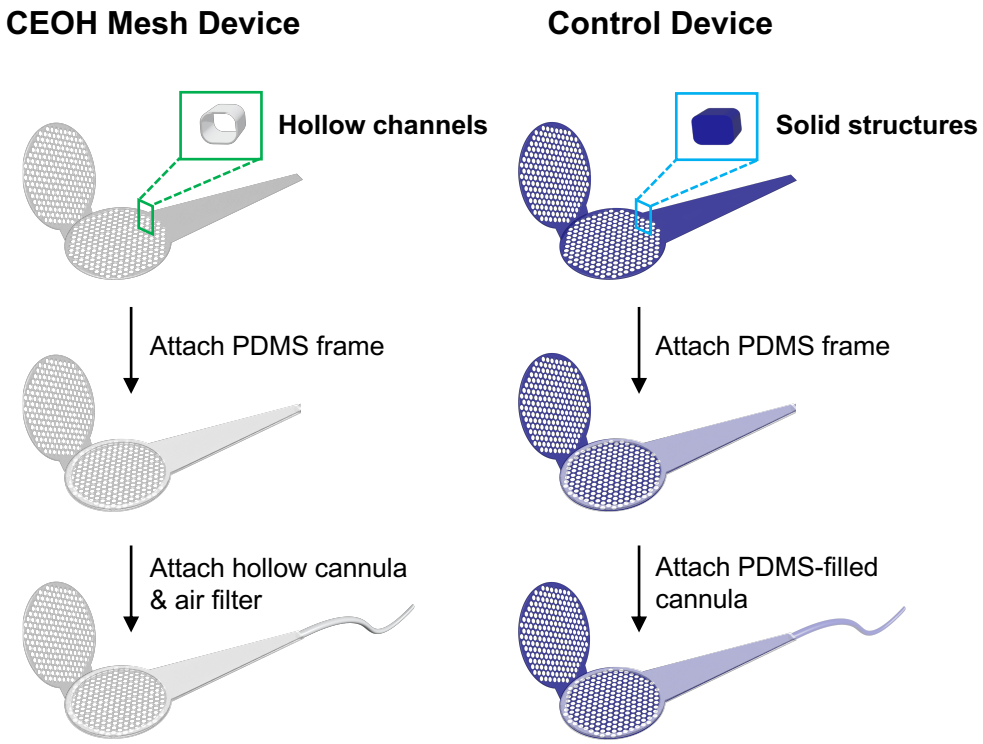

Figure 6-6. Assembly procedures of the CEOH Mesh Device and the Control Device.

After crafting the hollow mesh components, the assembly of both the CEOH Mesh Device and Control Device is delineated in **Figure 6-6**. The assembly entails the application of a thin layer of implantable-grade silicone adhesive (MED3-4213, NuSil) to securely attach the PDMS frame to the thin parylene hollow mesh. The additional double layers of 100 μm thick PDMS frame sandwiching the hollow meshes enhances the mechanical support of the devices when transplanted. Silicone

tubing (BB518-30, Scientific Commodities) is utilized as the cannula and is connected to the hollow mesh component. The medical-grade silicone adhesive is then carefully applied to ensure a sealed connection, guaranteeing air passage without leakage. For the Control Device, the silicone tubing is filled with PDMS (Sylgard 184, Dow) to obstruct oxygen transport. In the CEOH Mesh Device, a thin PDMS layer is applied at the open end, acting as an air filter. Alternatively, a hydrophobic PTFE filter (T050A013A, Thomas Scientific) with a pore size of 0.50 μm can be affixed as the air filter.

The assembled units, including both the CEOH Mesh Device and the Control Device, will undergo an overnight IPA extraction process followed by UV exposure to ensure the devices are fully sterilized. Prior to transplantation, the devices will be thoroughly dried.

PRESSURIZED TEST

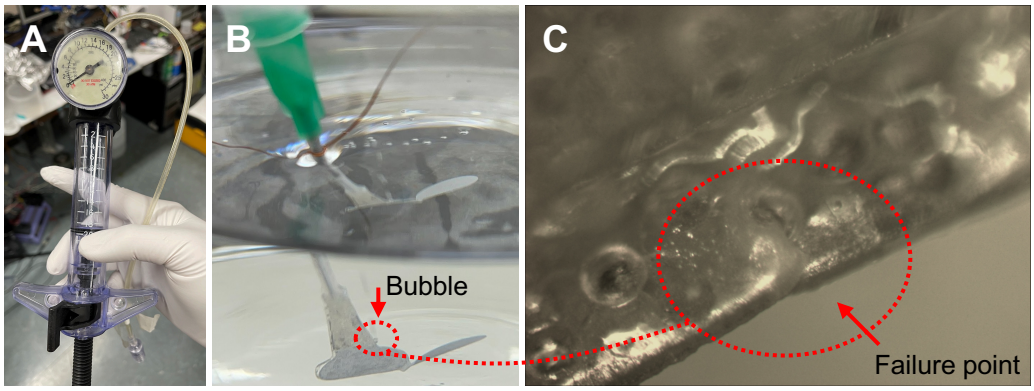

Figure 6-7. Evaluation of CEOH Mesh Device integrity under pressurization. (A) Pressurization apparatus, comprising a syringe fitted with a pressure gauge, attached to the CEOH Mesh Device, which is expected to endure pressures of up to 3 psi without failure. (B) Visual inspection of device integrity, showing bubble emergence as the pressurized CEOH Mesh Device is submerged in water, indicating areas of a compromised seal. (C) Microscopic examination of the identified failure site on the CEOH Mesh Device, correlating to the macroscopic bubble formation site, to determine the precise fracture location.

A critical aspect of the CEOH Mesh Device is to minimize water leakage into the device. To evaluate the integrity of devices, a pressurized test can be conducted (**Figure 6-7**). A syringe equipped with a pressure gauge (**Figure 6-7A**) is connected to the CEOH Mesh Device. If the device is compromised, air bubbles will appear under water (**Figure 6-7B**). The location of bubble formation allows for a visual inspection of the failure point (**Figure 6-7C**). Silicone adhesive can then be applied to this point to restore the device's integrity.

IMAGE GALLERY

Here, we illustrate the manufacturing process detailed in preceding sections through a sequence of figures. **Figures 6-8A and B** display the 4-inch copper film coated with patterned photoresist, where the lighter regions represent the copper set to be etched away, which will define the boundaries of the device. **Figures 6-8C and D** exhibit the copper template post-etching, correlating to the exposed regions in **Figures 6-8A and B**. **Figure 6-8E** depicts the setup for electropolishing, with red clips attached to the anode and black clips to the cathode—the anode links to the copper template undergoing polishing, and the cathode to a large-surface-area copper sheet. **Figure 6-8F** presents the PDMS frame. To fabricate this frame, a 4-inch silicon wafer is first cleaned with acetone, IPA, and deionized water, followed by a 3-minute hexamethyldisilazane (HMDS) surface treatment for functionalization. This dual HMDS layer acts as a de-adhesion layer. Subsequently, a 100-µm thick layer of medical-grade silicone (MED 6219, NuSil) is spin-coated onto the wafer. Post high-temperature cure, the PDMS film is laser cut under specific conditions (5W, Speed: 10%, 2 passes) using a CO_2 laser cutter (VLS3.50, Universal Laser System). Any residues are meticulously brushed off, and then the PDMS frame is detached from the wafer using an IPA extraction process before moving to the assembly phase.

Figure 6-9 displays the CEOH Mesh Device, differentiated by the inclusion of either a single leaf or two leaves in the hollow mesh. The single leaf CEOH Mesh Device is utilized for benchtop experiments, whereas the two leaves version is designed for animal studies, providing the capability to sandwich the islets between the leaves.

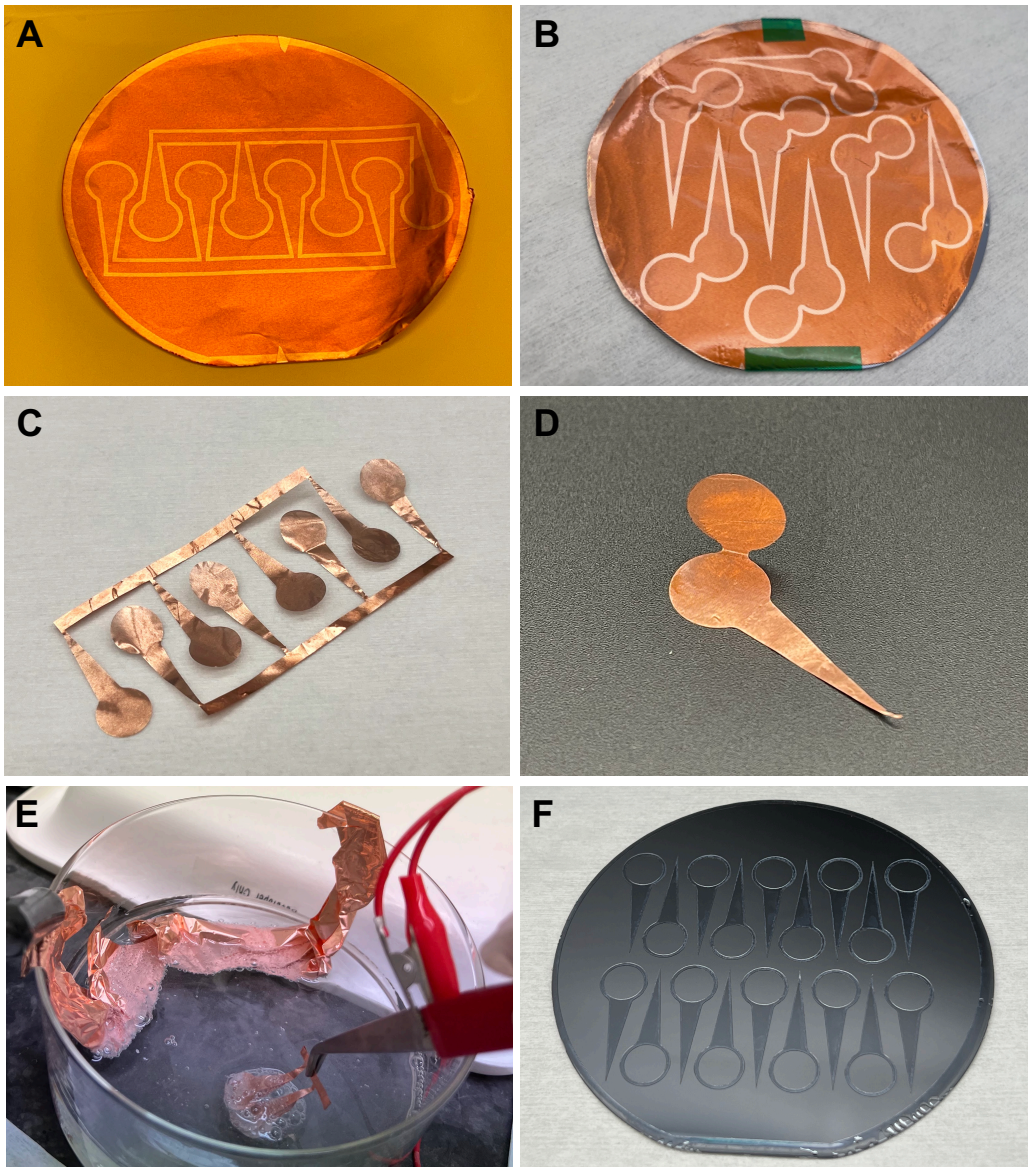

Figure 6-8. Images depicting the detailed fabrication steps of the device. (A) Copper wafer showcasing single leaf device features following photoresist development. (B) Copper wafer displaying two leaf device features after photoresist development. (C) Copper template following the etching of exposed copper from (A). (D) Copper template following the etching of exposed copper from (B). (E) Electropolishing setup. (F) PDMS frames.

We present the two-leaf CEOH Mesh Device as it encapsulates primary islets, shown in **Figure 6-10**. The image reveals how the islets are distributed across the CEOH MESH DEVICE's hollow mesh surface. The transplantation procedure may result in

varying islet densities across the area (**Figure 6-10A)**. As shown in **Figure 6-10B**, the majority of islets are larger than the hollow mesh's holes.

Figure 6-9. Images of CEOH Mesh Device. (A) One leaf CEOH Mesh Device. (B) Two leaves CEOH Mesh Devices.

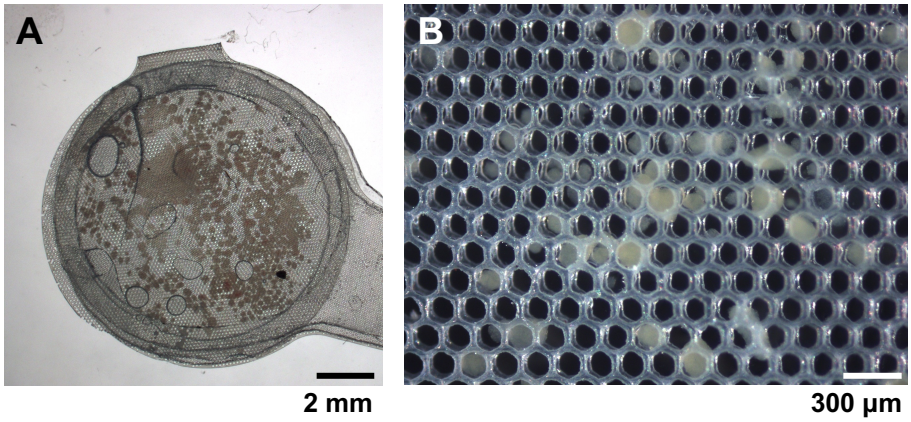

Figure 6-10. Images of two leaves CEOH Mesh Device sandwiching 600 rat islets. Approximately 600 rat islets are equivalent to 1800 IEQ islets. (A) Macroscopic view. (B) Microscopic view.

6.4 BENCHTOP CHARACTERIZATION

BENCHTOP OXYGEN TRANSPORT TEST

To substantiate the oxygen transport capabilities of the CEOH Mesh Device, we conducted a benchtop test to visualize and measure this function. The experimental setup for this test is detailed in **Figure 6-11**.

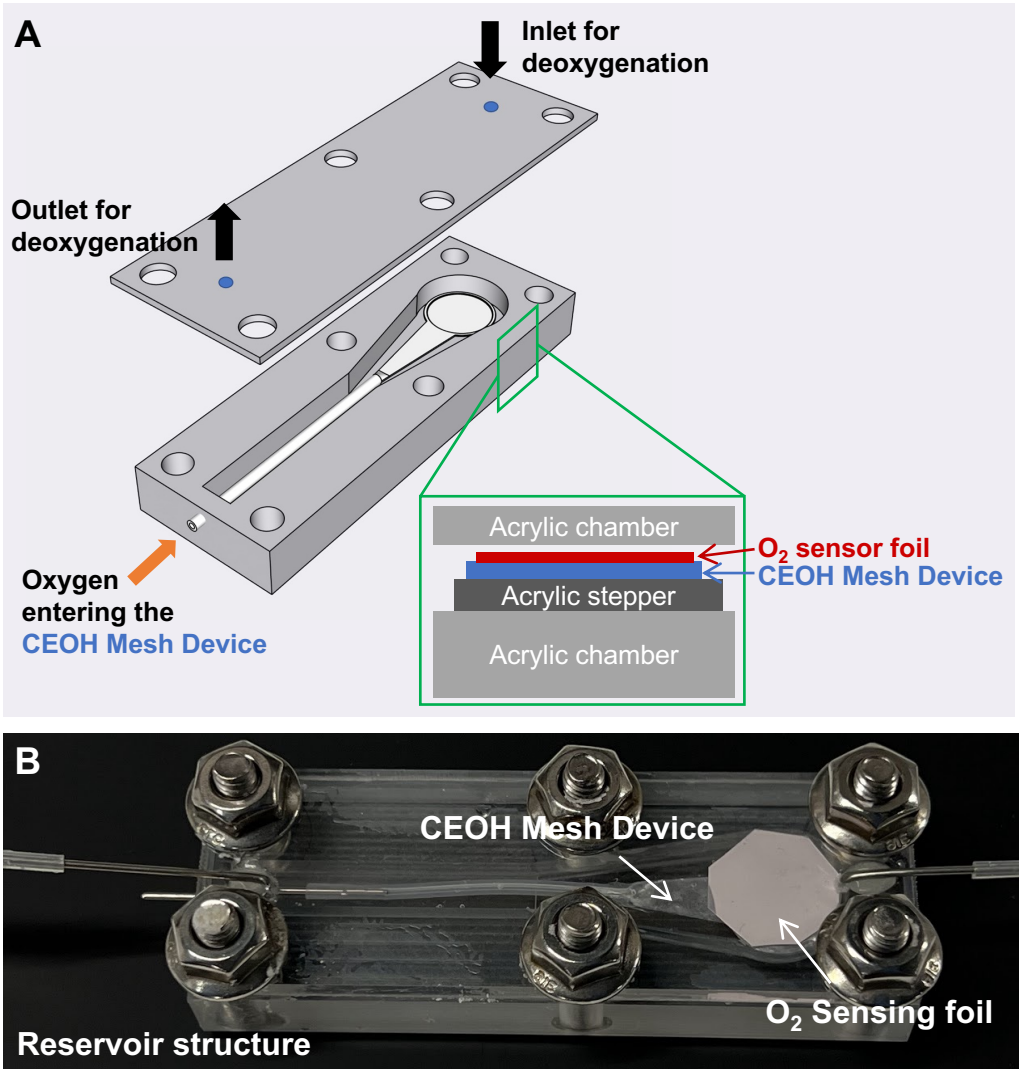

Figure 6-11. Experimental arrangement for benchtop evaluation of oxygen transport of CEOH Mesh Device. (A) Diagrammatic representation of the setup. (B) Photographic depiction.

Figure 6-11A displays a specially crafted acrylic chamber designed to encase the CEOH Mesh Device. This chamber is composed of a base and a corresponding cap, with a fine silicone layer applied between them. When fastened securely, this construction ensures a hermetic seal. It features both an inlet and an outlet to allow fluid flow. The configuration is intended to circulate deoxygenated water, establishing an initial condition where the fluid's partial oxygen pressure is essentially zero. Atop the CEOH Mesh Device, a sensitive oxygen sensor film is placed, which dims its fluorescence in response to oxygen presence, with a luminosity that correlates directly to the pO_2 within the film. Utilizing an image-based technique, we can track the changes in pO_2 as the CEOH Mesh Device actively transports oxygen into the sealed chamber. Once assembled with all elements — the CEOH Mesh Device, a spacer, and the oxygen-sensing film — the reservoir holds approximately 1 mL of liquid. **Figure 6-11B** illustrates the experimental arrangement post-assembly, ready for the evaluation of the device's oxygen transport effectiveness.

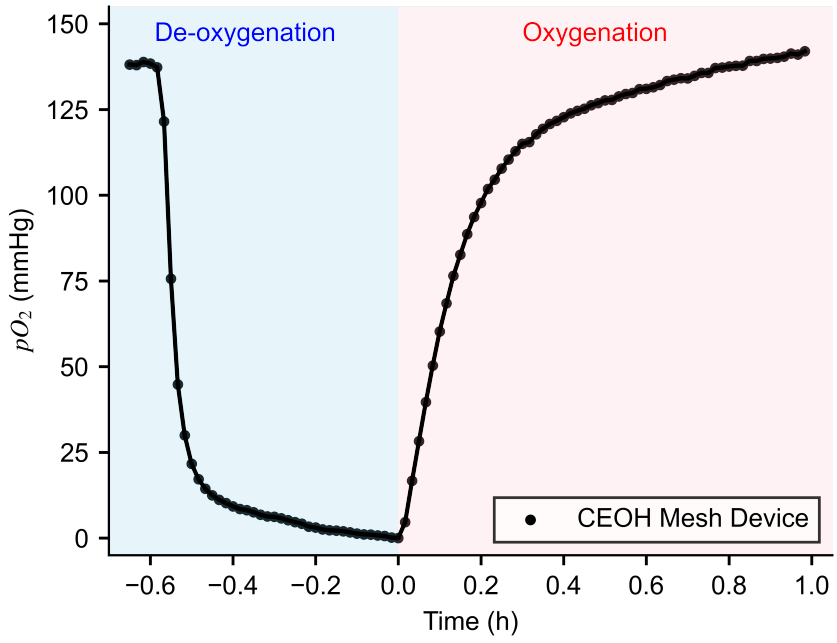

Figure 6-12. Transient analysis of oxygen transport characteristics and pO_2 response of the CEOH Mesh Device.

Figure 6-12 illustrates the dynamic pO_2 response of the CEOH Mesh Device, employing the configuration depicted in **Figure 6-11**. During the deoxygenation phase, nitrogen-saturated saline at 37°C is circulated into the reservoir. Concurrently, the open end of CEOH Mesh Device that connected to the air is hermetically sealed. Once the pO_2 within the reservoir stabilizes at zero, the valves on both sides of the inlet and outlet are closed. Subsequently, the open end of the CEOH Mesh Device is exposed, allowing oxygen to diffuse into the device and subsequently oxygenate the reservoir. The gradual rise in pO_2 is discernible, substantiating the device's capacity to transport oxygen effectively. The duration required to saturate the liquid surrounding the CEOH Mesh Device with oxygen is approximately one hour, indicating the efficiency of the oxygenation process facilitated by the device. This experiment not only showcases the functional competency of the CEOH Mesh Device but also quantifies the temporal aspects of its oxygen delivery performance.

6.5 IN SILICO OXYGEN TRANSPORT ANALYSIS

Based on the experiments depicted in **Figure 6-11**, it is evident that establishing a steady-state oxygen profile requires a relatively short amount of time, approximately an hour. We aim to characterize the steady-state pO_2 profile when the CEOH Mesh Device is integrated with the islet, which actively consumes oxygen. To accomplish this, we employ the Finite Element Method (FEM) and construct an oxygen simulation using COMSOL software. **Figure 6-13A** displays the geometric setup of our model. The entire simulation boundary is represented by a hexagonal prism, with the top and bottom planes set at 40 mmHg. This is based on the assumption that 40 mmHg is continuously maintained by the vascularized support at the subcutaneous site. The six sidewalls depict the plane of oxygen profile symmetry, correlating with the hexagonal arrangement of the holes in the oxygen hollow meshes. The model features two layers of hollow meshes sandwiching the islets, with the islets centered above and below the holes. By setting up a symmetrical plane, our model assumes that each mesh hole corresponds to an islet.

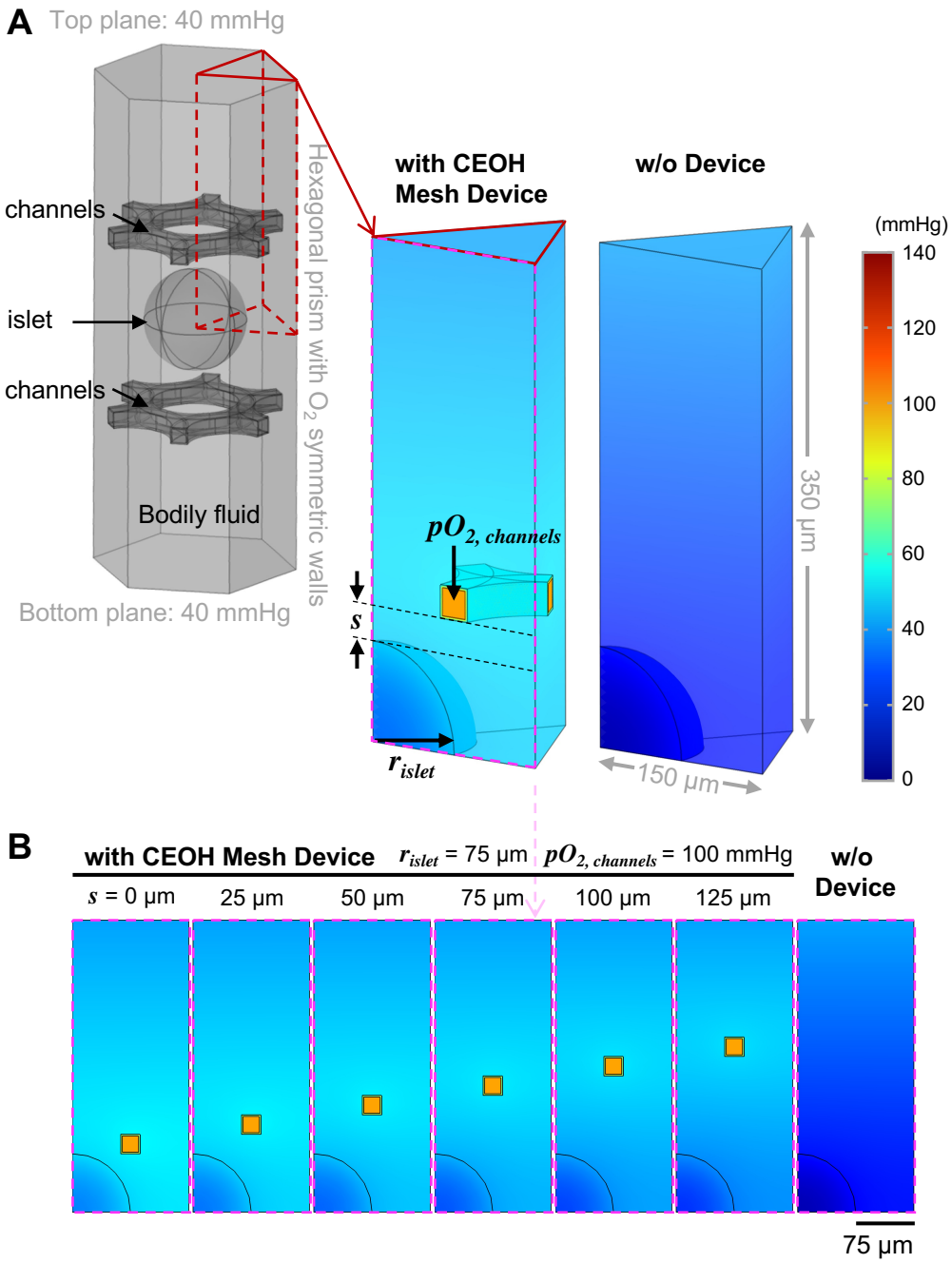

Figure 6-13. Computational simulations of oxygen profile with and without the transplantation of the CEOH Mesh Device alongside an islet at a subcutaneous site. (A) Illustrations of the geometric configuration, boundary conditions, and three variables ($pO_{2,channels}$, r_{islet}, s) of the model. (B) Presentation of 2D simulation snapshots of the pO_2 profile.

However, in reality, islets are distributed more sparsely on the hollow mesh and may not be perfectly aligned. Consequently, our simulation results may represent the

lower bound of the oxygen pO_2 profile due to the high islet seeding density and the maximum distance between the oxygen-transporting microchannels and the islets.

In this simulation, we also postulate a specific pO_2 level within the microchannels ($pO_{2,channels}$) and vary this parameter to observe changes in the oxygen profile. Previous calculations have indicated that the diffusive resistance within these channels is negligible, making this a reasonable assumption. Additionally, we consider two geometric variables: the radius of the islet (r_{islet}) and the spacing (s) between the islet and the device. Adjusting these variables provides insights into the effectiveness of the CEOH Mesh Device, especially when dealing with larger primary islets or when surgical procedures do not position the islets at the vicinity to the device, potentially reducing oxygen availability. We alter these three variables and conduct simulations to compile a comprehensive oxygen profile. Moreover, we evaluate scenarios where no device is present, and oxygen supply is solely dependent on vascularization from the subcutaneous site. This comparison serves as a benchmark to quantify the enhancement in oxygen delivery afforded by the CEOH Mesh Device. The simulation parameters are provided in Chapters 2 and 3.

Figure 6-13B illustrates a 2-D pO_2 profile across a cut plane, delineated by a pink dotted boundary. The simulation parameters include an islet radius (r_{islet}) of 75 μm and an oxygen partial pressure within the microchannels ($pO_{2,channels}$) of 100 mmHg. In this example, we manipulate the vertical distance (s) between the hollow mesh meshes and the islet. It is apparent from the results that the pO_2 value within the islet progressively decreases as this spacing is increased. These findings highlight the critical nature of the liquid interface distance; minimizing this spacing is essential for achieving optimal oxygenation of the islet. Nonetheless, in every scenario assessed, the use of the CEOH Mesh Device still offers advantages over situations where no device is employed.

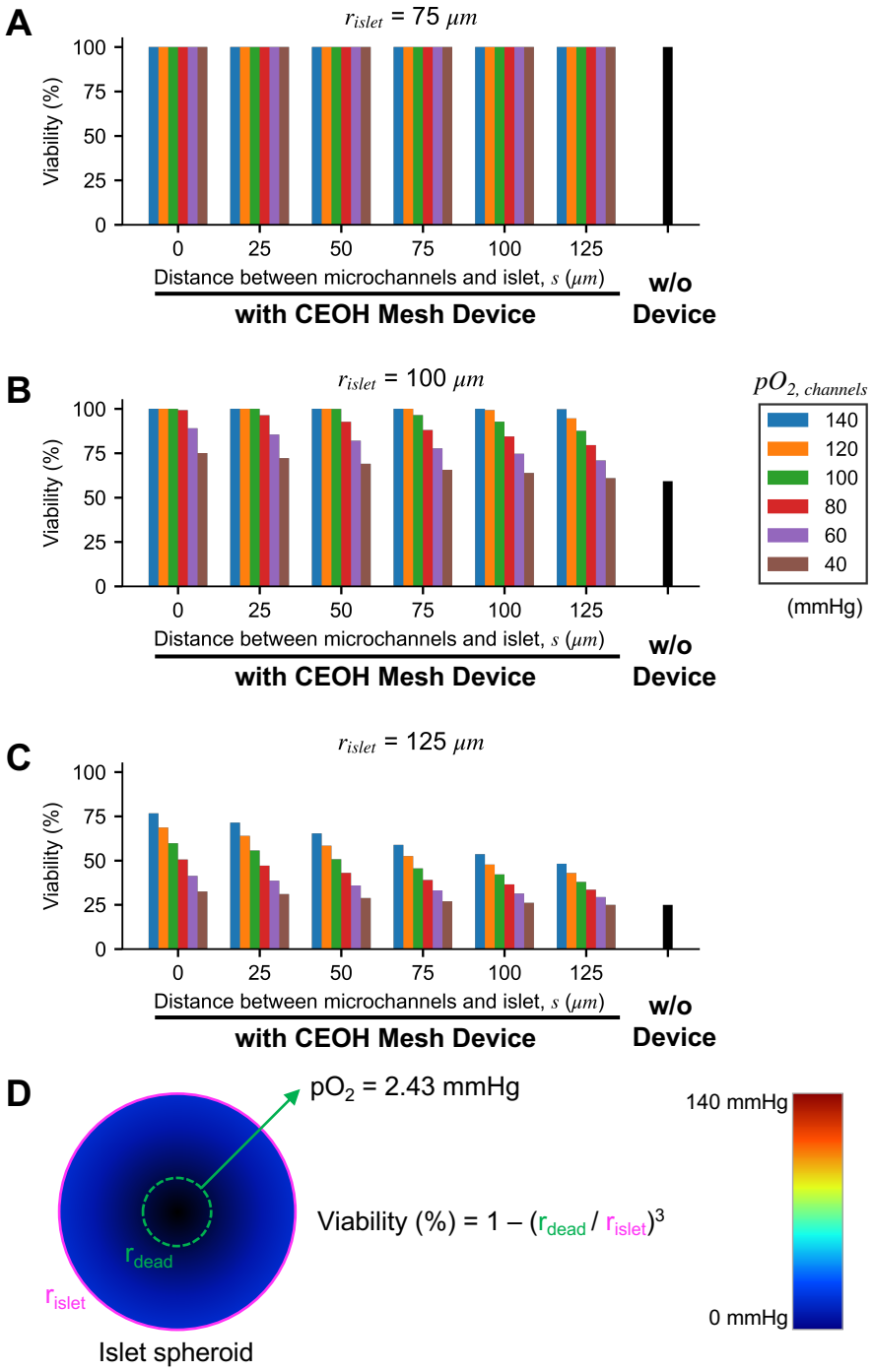

Figure 6-14. Computed islet viability with and without the CEOH Mesh Device at a subcutaneous transplantation site. Estimated islet viabilities are shown for three islet radii: 75 μm (A), 100 μm (B), and 125 μm (C). (D) Illustration of computing the estimated islet viability. Estimated Islet viability is quantified as the volumetric percentage of the islet with an pO_2 exceeding 2.43 mmHg.

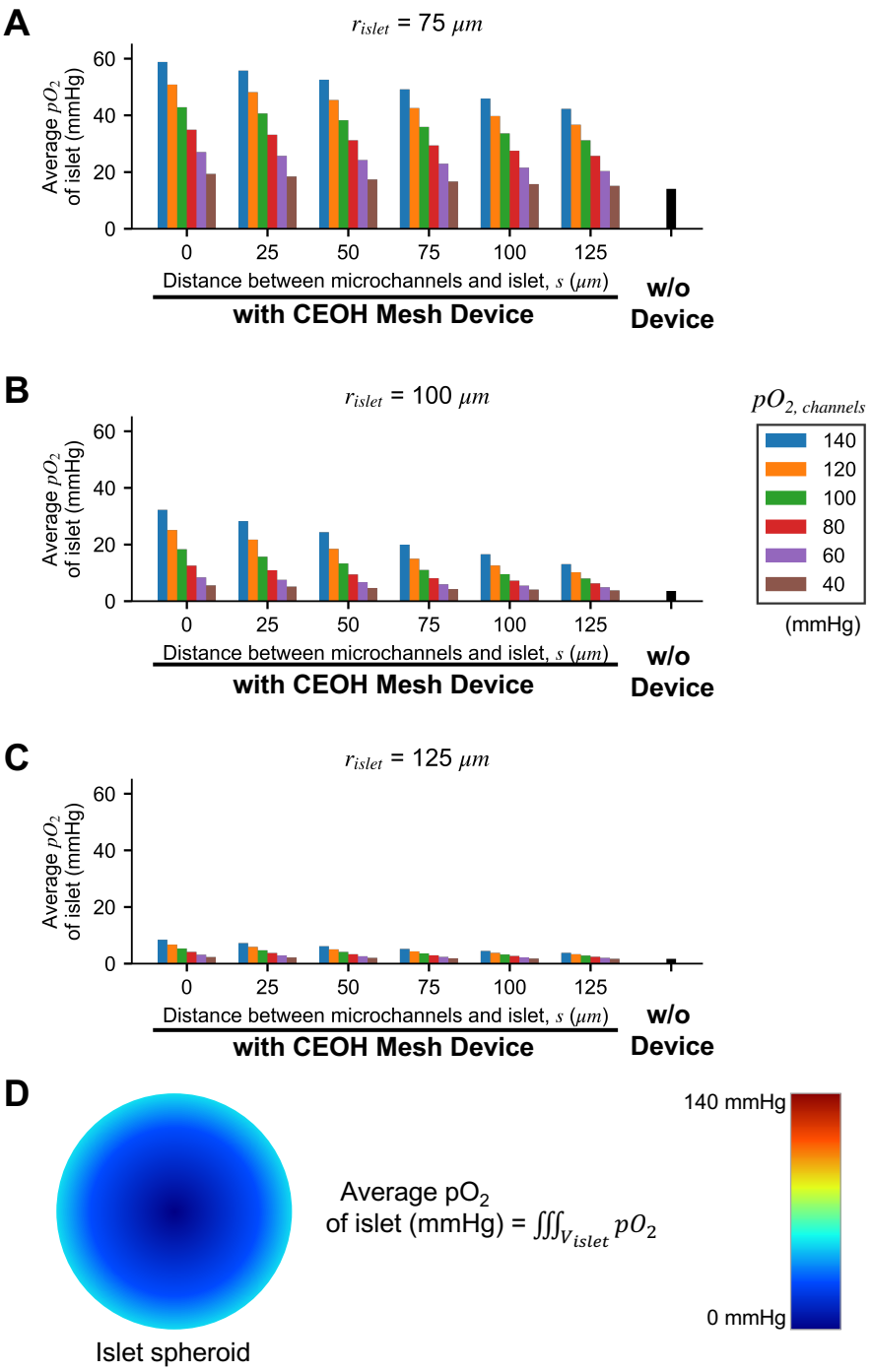

Figure 6-15. Averaged pO_2 of islet with and without the CEOH Mesh Device at a subcutaneous transplantation site. Three islet radii are shown: 75 µm (A), 100 µm (B), and 125 µm (C). (D) Illustration of computing the average pO_2 of islet.

To provide a comprehensive analysis of the impact of the CEOH Mesh Device on islet viability, we performed calculations based on the critical survival pO_2 established in Chapter 2, which is 2.43 mmHg. Estimated islet viability is estimated as the volumetric percentage of the islet with a pO_2 exceeding 2.43 mmHg. The estimated islet viability results are depicted in **Figure 6-14**. Also in **Figure 6-15**, we present the average pO_2 within an islet under varying conditions. For an islet of standard size (r_{islet} = 75 μm), as shown in **Figure 6-14A**, both scenarios—with and without the device—maintained 100% viability. It should be noted that, in the model without the device, it is assumed that islets are uniformly distributed in a two-dimensional array within the subcutaneous space. However, typically, in the absence of the device, islets tend to aggregate in a three-dimensional formation, which can result in more severe hypoxia for the transplanted tissue. Moreover, while 100% viability is preserved, the average pO_2 that the islet is exposed to is substantially elevated with the device in place, even if there is some space between the islet and the graft (**Figure 6-15A**). Given the critical role of pO_2 in the metabolic functions of the islet—particularly in glucose sensing and insulin secretion—these findings suggest that the CEOH Mesh Device provides a significant advantage for islet transplantation therapy by enhancing the oxygenation of the surrounding tissue.

To elucidate the efficacy of the CEOH Mesh Device for larger islets, it is important to recognize that despite their lower frequency, the significant biomass of larger islets means they have a substantial impact on the success of islet cell therapy. According to **Figure 6-14B**, maintaining an pO_2 within the channels at 100 mmHg allows islets with a radius of 100 μm to retain viability above 80%, even when the spacing between the device and islets is as much as 125 μm. **Figure 6-15B** reveals that an islet of 100 μm radius can sustain an average pO_2 greater than 10 mmHg. Conversely, in the absence of the device, islet viability drops to approximately 50%, and the average pO_2 plummets to merely 5 mmHg.

The oxygen delivery facilitated by the CEOH Mesh Device encounters a limitation when the islet size reaches a radius of 125 μm. Although this dimension is atypical for a primary islet, it is crucial to consider all possible variations. As illustrated in

Figures 5-14C and 5-15C, the viability for islets of a 125 μm radius falls to approximately 50%, with the average pO_2 descending to as low as 5 mmHg, which is less than 1% O_2. This decline in efficacy is attributable to the increased internal distance oxygen must diffuse within larger islets, which inherently makes oxygen delivery more challenging—even with an augmented external oxygen source is provided by CEOH Mesh Device.

6.6 IN VIVO DEVICE EFFICACY IN A RAT MODEL

Ultimately, our goal is to ascertain the effectiveness of the CEOH Mesh Device in improving the outcomes of islet transplantation to treat T1D. This section provides a detailed description of the experimental protocols implemented to demonstrate the enhanced performance of the CEOH Mesh Device when compared to a Control Device. The rate of diabetes reversal, determined by blood glucose levels, and the assessment of in vivo functionality through glucose tolerance tests are conducted and compared.

EXPERIEMENTAL ANIMALS

The syngeneic transplantation is conducted using the immunocompetent inbred Lewis (LEW) rats. For this purpose, male LEW rats (Charles River) serve as pancreas donors. Donors are specifically chosen to be male LEW rats aged between sixteen to twenty weeks. This age range is targeted because it provides a high yield of islets with consistent quality across different batches. It has been observed that a higher body weight in these rats correlates with a better yield of islets. The quality of islets tends to decline after the rats reach approximately six months of age [171]. Recipient rats are young female LEW rats, aged ten to twelve weeks, with an average weight of around 200 grams. This choice reflects the typical onset of T1D in younger patients. Female rats are preferred as recipients due to their slower rate of weight gain, approximately 20 grams per month, compared to male LEW rats, which gain about 50 grams per month. This slower weight gain in females is significant because

the ratio of transplanted islet cells to body weight is a crucial factor in the successful reversal of diabetes [103]. Maintaining this ratio is essential for the study's outcomes.

All animal use and procedures have been approved by the City of Hope/Beckman Research Institute's Institutional Animal Care and Use Committee (IACUC protocol #13036). Furthermore, all surgical procedures are carried out under general anesthesia using isoflurane, with Buprenorphine administered for post-transplant pain management.

ISLOATION OF PANCREATIC ISLETS

Islets are isolated from the pancreases of LEW rats using an established method [88]. Initially, the rats are placed under general anesthesia, and 9 mL of a cold collagenase solution (2.5 mg/mL concentration in Hanks' Balanced Salt Solution (HBSS), Sigma-Aldrich) is infused into the pancreatic duct via the common bile duct. Following this, the inflated pancreas is removed and enzymatically broken down at a temperature of 37°C for 10 minutes. After digestion, the pancreas is spun at a force of 300 ×g for 3 minutes. The resultant pellets are then separated through a density gradient centrifugation using HBSS and Histopaque-1077 (with a density of 1.077 g/mL, Sigma-Aldrich) for 25 minutes at the same centrifugal force. The islets are manually hand-picked for purity. Considering the variation in islet sizes, a standardized counting unit known as the Islet Equivalent (IEQ) is employed for a volume-normalized count, with an islet measuring 150 μm in diameter being equated to 1 IEQ [89]. Before proceeding to in vitro culture tests, the isolated islets undergo a recovery phase from the isolation process. This recovery involves an overnight incubation at a temperature of 27°C in a low-density arrangement (11–15 IEQ per cm^2, within a 95 mm Petri dish from Corning Life Sciences) using 8 ml of CMRL 1066 culture media (Corning Life Sciences). This culture media is enhanced with 0.5% human serum albumin, 0.1 μg/mL insulin-like growth factor-1 (Cell Sciences), 10 unit/mL heparin sodium (Sagent Pharmaceuticals), and Penicillin-Streptomycin-Glutamine (Gibco), all incubated in a 5% CO_2 environment at 27°C.

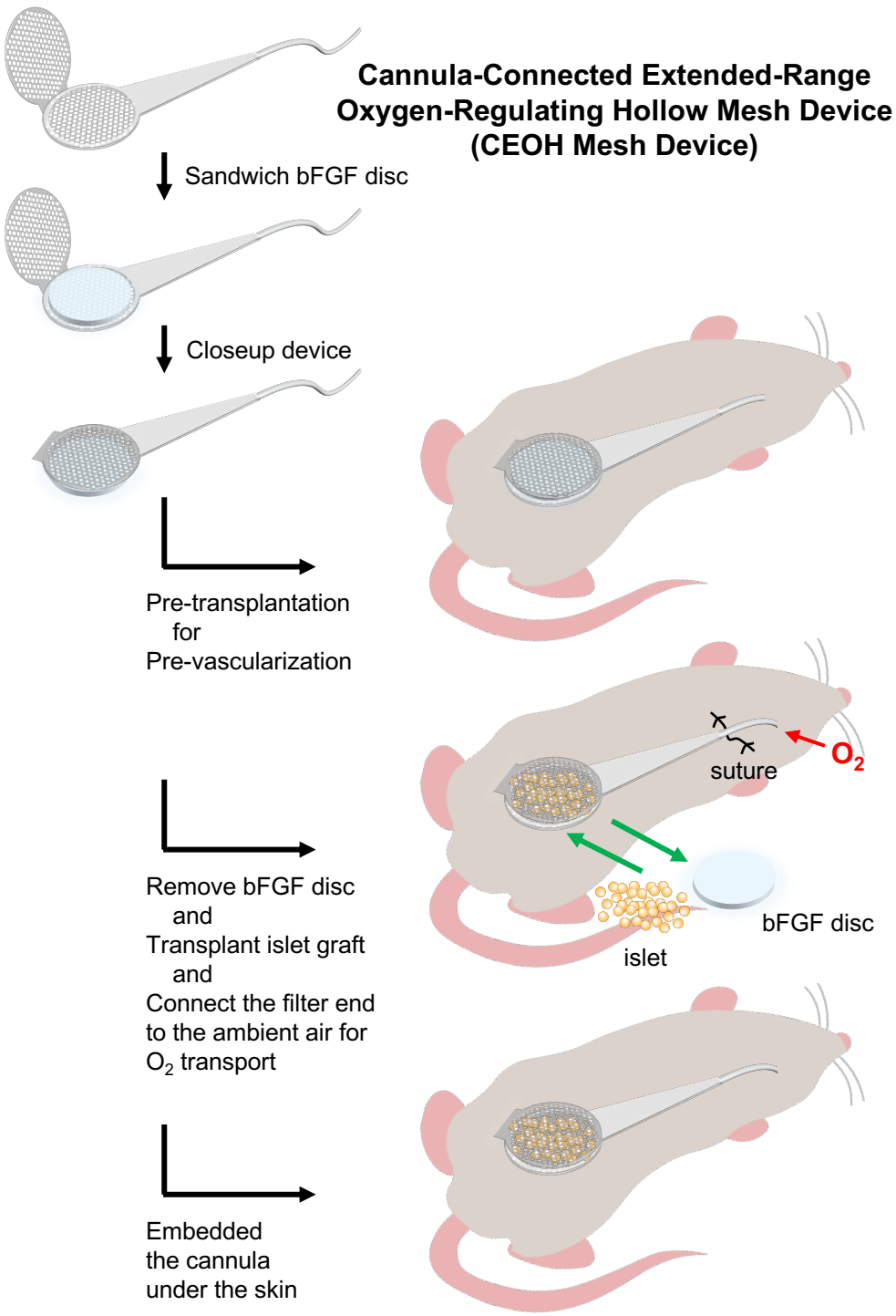

Figure 6-16. Illustration of the CEOH Mesh Device transplantation procedure with islet graft. All key components of the device are located subcutaneously, except for the cannula and air filter end, which remain exposed to the atmosphere to facilitate oxygen transport.

TRANSPLANTATION PROCEDURES

The transplantation technique for the CEOH Mesh Device is outlined in **Figure 6-16**. Although the figure only displays the CEOH Mesh Device, the Control Device is inserted using the same method.

Initially, the device is sterilized and then thoroughly dried. A lyophilized agarose disc—created from a 4.5% agarose solution containing 500 μg/mL of basic fibroblast growth factor (bFGF, Gold Biotechnology) in saline and 250 μg/mL of heparin sodium solution (Sigma-Aldrich)—is placed between the device's two leaves Once closed, the device is implanted in the recipient rat's dorsal side to promote prevascularization of the transplantation site, triggered by the bFGF disc, over a four-week duration. All surgical procedures were performed under the general anesthesia using the isoflurane and appropriate analgesics for the post-transplant pain control using Buprenorphine.

It is worth mentioning that before transplanting islets into the rat recipients, a prevascularized site within the subcutaneous tissue is prepared. The rationale behind this preparation is to create a dense vascular network at the transplantation site, facilitating a rapid connection and integration of the transplanted islets with the recipient's microvasculature. It is well-known that such prevascularization can significantly decrease the amount of islet mass needed to effectively regulate glucose levels in diabetic animals post-transplantation. In this study, we enhance this prevascularization technique by inserting a disc that releases bFGF into the subcutaneous site [103].

It is also important to note, however, that vascular connection with the islet graft does not occur immediately after the transplantation—it usually takes between one to four weeks for spontaneous vascularization towards the graft. This delay creates a critical period where the graft might suffer from hypoxia. Our study aims to evaluate the efficacy of the CEOH Mesh Device compared to a Control Device in mitigating this risk of graft hypoxia during the vascular connection engraftment period.

Recipient rats are induced with diabetes by a single intravenous dose of 60 mg/kg of streptozotocin (STZ, Sigma-Aldrich) four days before the transplantation of the islet graft, with diabetes being confirmed by non-fasting blood glucose readings exceeding 400 mg/dL.

On the transplantation day, the bFGF disc is replaced with a fresh islet graft seeded on a PLGA/collagen scaffold [172], which is then placed into the pocket formed by the device's leaves (CEOH Mesh Device: n=6, Control Device: n=5). The cannula is made opened and connected to air while other the surgical site is sutured and closed (**Figure 6-17**). A continuous oxygen supply is provided for four days, after which the cannula and air filter are embedded under the skin to stop oxygenation. All procedures are performed under general anesthesia.

IN VIVO FUNCITONAL ASSEMENT TESTS

Post-transplant, the animals are observed for six weeks, and non-fasting blood glucose levels and body weight are consistently recorded. Reversal of diabetes is defined as blood glucose below 200 mg/dL. At the six-week mark, we conduct an intraperitoneal glucose tolerance test (IPGTT) to assess the graft function. Prior to the test, recipient rats are fasted for 8 hours, followed by an intraperitoneal injection of a glucose solution dosed at 2 g of glucose per kilogram of body weight. Blood glucose levels are then measured at intervals of 0, 15-, 30-, 60-, and 120-minutes post-injection [173]. AUC of the blood glucose between 0 and 120 min is calculated and expressed in the unit of mg/dL × min to quantify the IPGTT data.

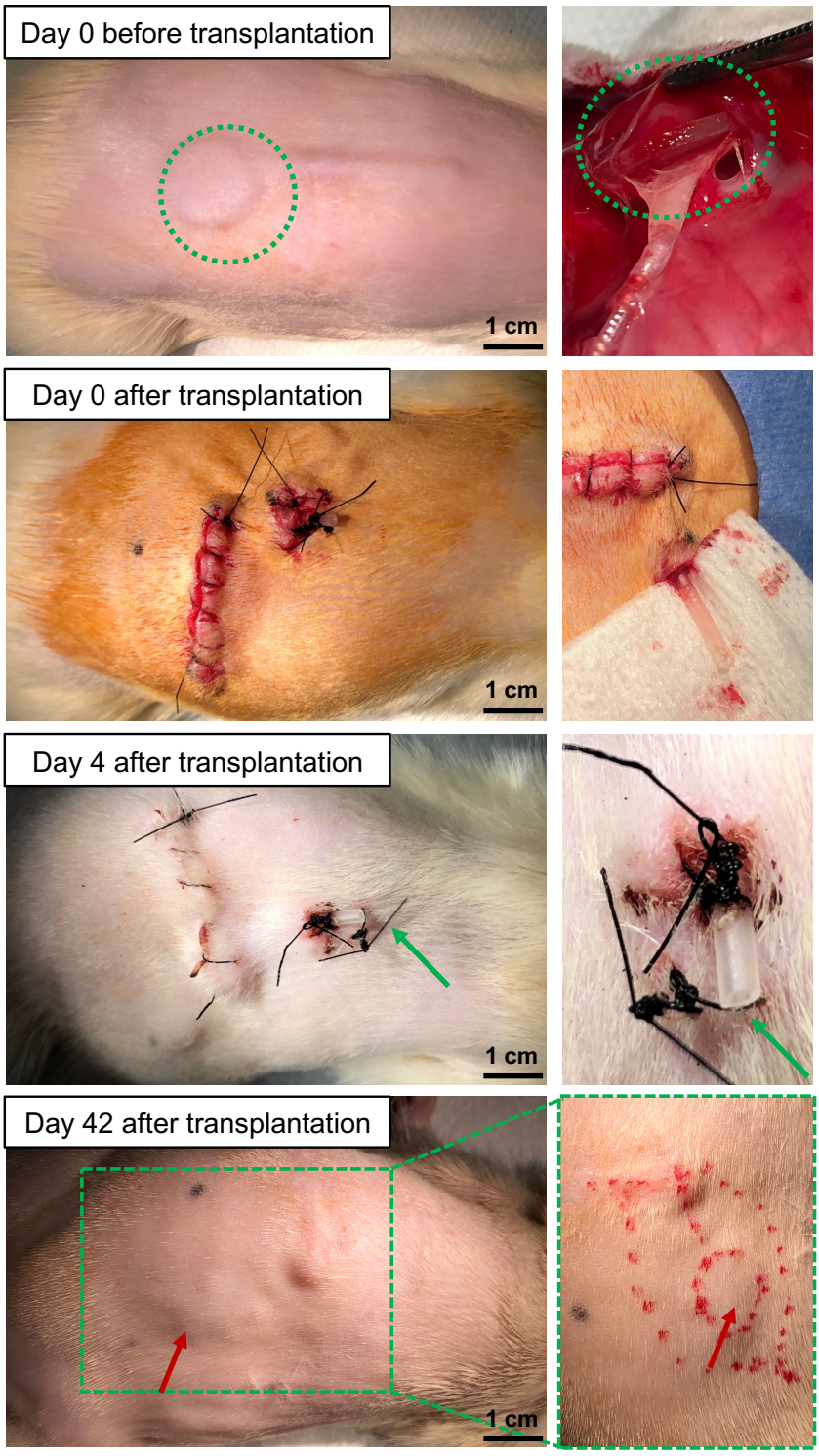

Figure 6-17. Photographs depicting critical stages of the CEOH Mesh Device surgical transplantation procedures. The green dotted circle highlights the bFGF disc. The green arrows point to the open end of the cannula. The red arrows point to the area of the Device and islet graft after the cannula is removed.

DIABETES REVERSAL

Throughout the six-week monitoring period, blood glucose levels are measured, and the data is presented in **Figure 6-18A**, with each individual rat denoted by a unique color. Diabetes reversal is characterized by blood glucose levels falling below 200 mg/dL at any point. In the CEOH Mesh Device group, two rats exhibited blood glucose levels dropping and maintaining below 200 mg/dL by the third week and throughout, while the remaining four rats continued to show elevated glucose levels. In contrast, all rats in the control group maintained high glucose levels throughout the six-week observation period. Body weight was also tracked to detect any potential abnormalities (**Figure 6-18B**). Across all groups, there is a mild and consistent increase in body weight around 200 grams, which suggests the absence of any irregularities.

The CEOH Mesh Device group demonstrated a diabetes reversal rate of 33.3% (2 out of 6), which is notably higher compared to the control device group, which had a 0% (0 out of 5) reversal rate. This difference underscores the oxygen transport effectiveness of the CEOH Mesh Device in promoting diabetes reversal when compared to the Control Device where oxygen is not adequately supplied.

It is noteworthy that the CEOH Mesh Device supplied oxygen for only four days, while diabetes reversal was observed at week three. This correlates well with the fact that revascularization, defined as the restoration of microvascular networks to the transplanted tissue, may not commence until one to three days post-device removal and might not be complete until two weeks later [174], [175], [176]. Additionally, there are concerns that excessive oxygenation might suppress the hypoxia-induced expression of pro-angiogenic factors including vascular endothelial growth factor (VEGF) [177]. Incomplete revascularization could compromise the islet graft's function in glucose sensing and insulin secretion, which may explain why diabetes reversal was not achieved in four rats within the CEOH Mesh Device group. In conclusion, for optimal islet graft functionality, a meticulously designed oxygen supply, level, and microenvironment are critical [178].

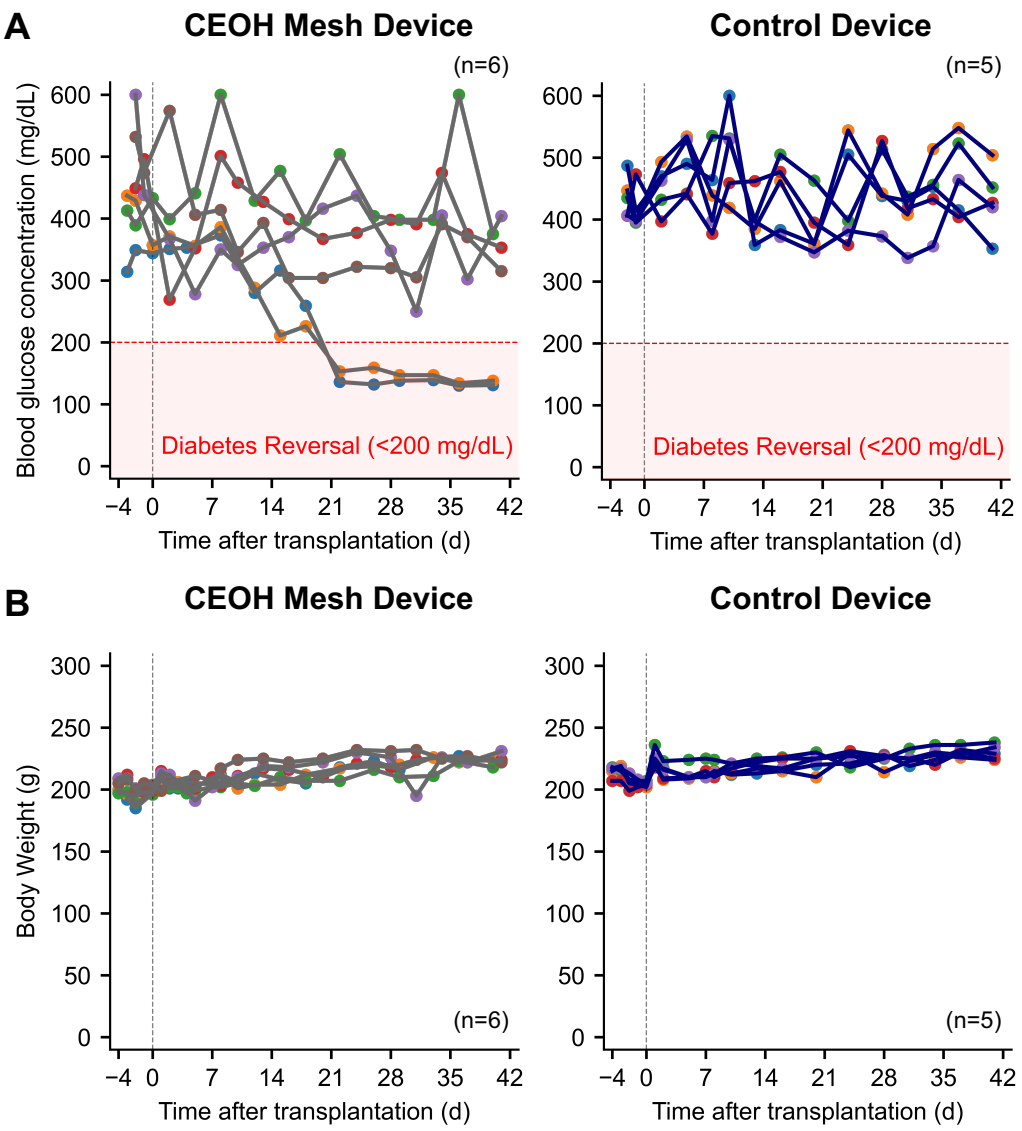

Figure 6-18. Blood glucose concentration (A) and body weight (B) measurements of STZ-induced diabetic female LEW rat after 600 islet graft transplantation into the CEOH Mesh and Control Device. STZ is injected 4 days prior to the islet graft transplantation.

GLUCOSE TOLERANCE

Beyond monitoring blood glucose, we conduct the IPGTT test at the conclusion of the observation period. **Figure 6-19A** illustrates an improved glucose tolerance in rats with the CEOH Mesh Device compared to those with the Control Device. The area under the curve (AUC), depicted in **Figure 6-19B**, further signifies a statistically

significant improvement in transient glucose tolerance facilitated by the CEOH Mesh Device. This indicates the islet graft is more functional in the CEOH Mesh Device group compared to the Control Device group. Note that the animal model employed in this study is the STZ-induced diabetic model, in which the islets in the native pancreas were destroyed, therefore the post-transplant glycemic control is solely relied on the islet graft transplanted.

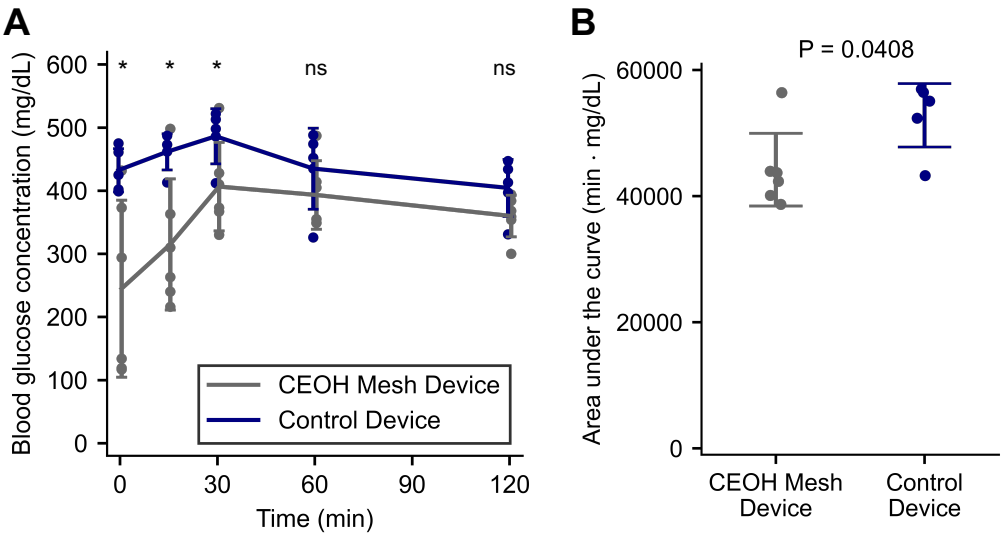

Figure 6-19. Blood glucose responses using the intraperitoneal glucose tolerance test (IPGTT) six weeks post-transplantation to assess the in vivo function of islets with the CEOH Mesh Device and Control Device. (A) The IPGTT curve shows significant differences at time points 0, 15, and 30 minutes (* denotes P < 0.05). (B) The area under the curve (AUC) analysis reveals statistical significance (P = 0.0408) between CEOH MESH DEVICE and Control Devices. Welch's t-tests are used to determine P-values, with an alpha threshold of 0.05 indicating statistical significance.

In summary, the CEOH Mesh Device's provision of sourcing oxygen from the ambient air effectively counters the problem of hypoxia-induced islet cell death. Having the capability to extend the oxygen range presents notable advantages when a larger amount of islet being transplanted. It demonstrates considerable clinical promise for sustained islet transplantation therapies aimed at treating type 1 diabetes.

Chapter 7

Discussion and Future Works

In this study, we have characterized the oxygen transport properties in pancreatic cells, emphasizing that oxygen supply is the limiting factor for transplanted islet cells in treating diabetes. By combining fundamental knowledge with a diffusion circuit model, we have designed, fabricated, and characterized oxygen-regulating hollow mesh devices to address the oxygen supply challenge. The devices, created using MEMS microfabrication techniques with biocompatible parylene material, is long-term implantable and therefore translational. More importantly, our devices leverage the fact that air has an oxygen diffusivity 10,000 times greater than in bodily fluid. By introducing micron-sized unobstructed air channels within the tissue, this device enables local oxygen regulation in a passive yet effective manner. Our hollow mesh devices effectively bridge the oxygen from the vascular network to the transplanted islet graft, enhancing oxygen delivery. Preclinical results demonstrate that these air-containing, oxygen-redistributing hollow channels are crucial in enabling long-term graft survival and diabetes reversal in a rodent model. Furthermore, the hollow mesh device can be connected to a more abundant oxygen source, ambient air, to expand the oxygen supply range and accommodate a higher islet seeding density that is clinically required. Our results also demonstrate the oxygen-regulating function of this extended-range, cannula-connected hollow mesh. Together, these two devices pave the way for an innovative solution to overcome the local hypoxia challenge for successful engraftment in cell therapy for curing type 1 diabetes.

The hollow mesh devices exhibit potential for a variety of cell transplantation applications where local oxygen regulation is critical. This is particularly relevant for cells with high metabolic demands and elevated oxygen consumption rates, such as cardiomyocytes [179], [180], hepatocytes [181], [182], neurons [183], [184], and stem cells [184], [185]. By incorporating the hollow mesh scaffold with biological tissues, a seamless integration can be achieved in cell therapies to address hypoxic

challenges. This approach promises to enhance the viability and function of transplanted cells, potentially offering a versatile solution to a common obstacle in regenerative medicine [186].

As we progress towards the clinical application of the hollow mesh devices, a critical consideration is the development of immunoisolation strategies beyond the conventional use of immunosuppressive drugs. These drugs can have side effects and negatively impact the patient's quality of life. Thus, by effectively integrating the oxygen-regulating device with immunoisolation, we could entirely eliminate the need for immunosuppressive drugs, marking a significant advancement toward actual clinical success.

The first strategy to address this challenge is through biological means, specifically genetic engineering. A promising avenue in islet transplantation is the use of stem cell-derived insulin-producing cells as an alternative to mitigate the donor shortage issue [187]. An example of such is a clinical trial of Vertex's V-880 (ClinicalTrials.gov Identifier: NCT04786262). Moreover, there are advancements in the development of immune-evasive stem cell-derived insulin-producing cells [188], [189]. This approach has the potential to minimize the immune response of the host recipient, thereby reducing the likelihood of graft rejection.

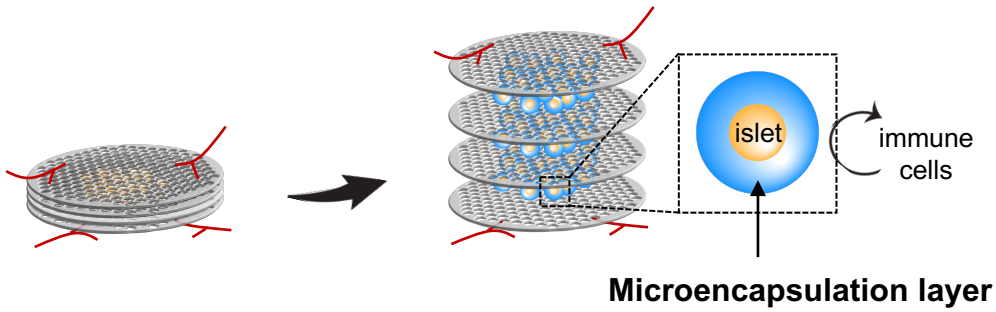

Figure 7-1. The microencapsulation strategy applied to the oxygen-regulating hollow mesh.

The second strategy involves incorporating microencapsulation into the islet graft while maintaining all other variables same to our oxygen-regulating hollow mesh.

Figure 7-1 depicts an illustrative diagram comparing the oxygen-regulating hollow mesh with islets to the hollow mesh with micro-encapsulated islets. Microencapsulation can be achieved, for instance, by applying a thin layer of non-biodegradable hydrogel around the islet cells, preventing immune cells and antigens from making contact with the islets. Yet, this layer still allows for the free passage of oxygen, nutrients, glucose, and insulin. It is important to note that the distance between each layer may need to be adjusted based on the added thickness from the microencapsulation layer. To maintain and regulate the appropriate oxygen tension for the islet graft, varying pore sizes in the mesh or different mesh dimensions may be further designed and optimized.

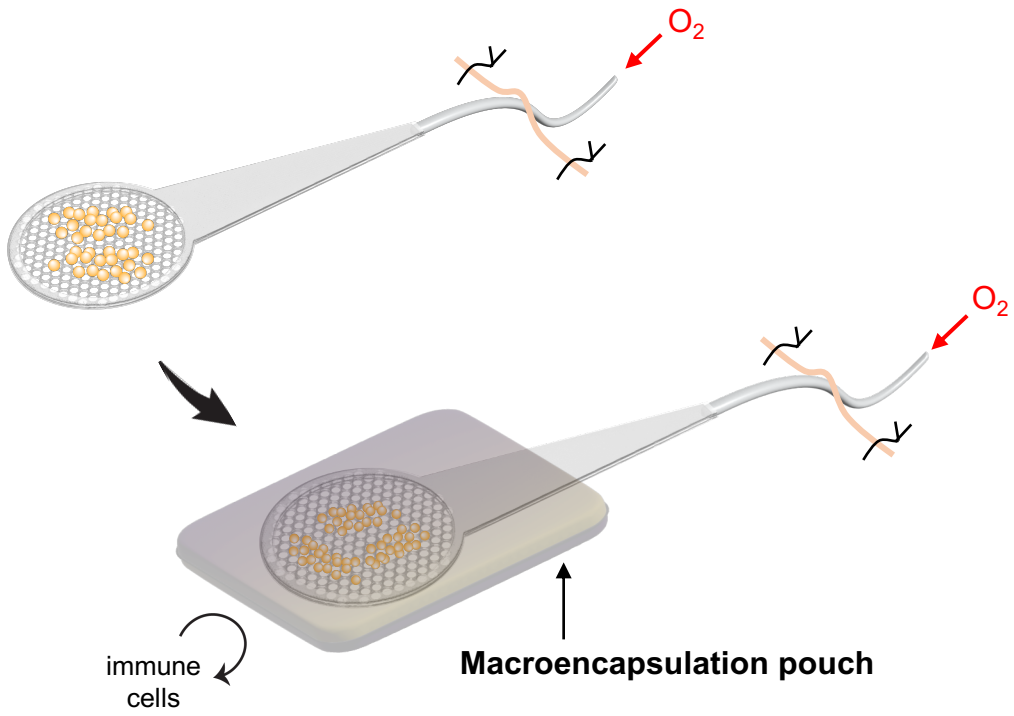

Figure 7-2. The macroencapsulation strategy applied to the cannula-connected, extend-range, oxygen-regulating hollow mesh.

The third strategy involves the integration of macroencapsulation within the islet graft, while all other parameters remain consistent with our cannula-connected, extended-range, oxygen-regulating hollow mesh. **Figure 7-2** provides a comparative

illustrative diagram, showcasing the cannula-connected, extended-range, oxygen-regulating hollow mesh with islets alongside the devices with macroencapsulation. Macroencapsulation is accomplished by enclosing the islet cells inside a pouch that acts as a barrier to immune cells and antigens, thereby preventing contact with the islets. The macroencapsulation approach has undergone clinical trials but encountered setbacks due to inadequate oxygen supply. Optimizing the macroencapsulation strategy, especially in conjunction with our device, holds significant promise for enhancing clinical outcomes.

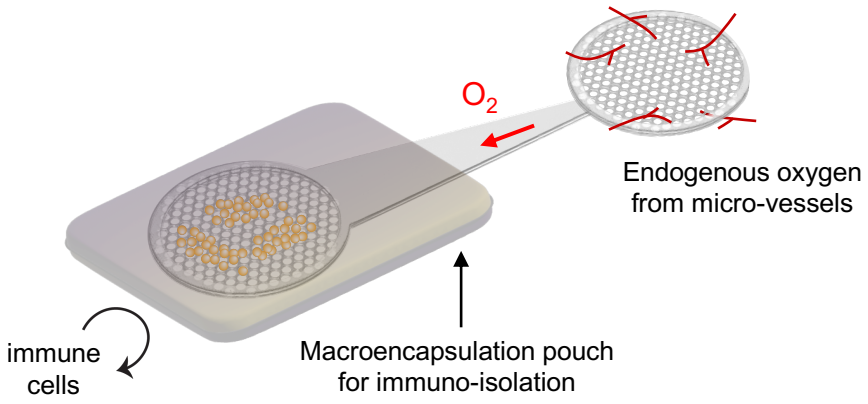

Figure 7-3. The macroencapsulation strategy applied to the cannula-connected, dual-scaffold, oxygen-regulating hollow mesh. The entire device is designed for implantation at the subcutaneous site.

Building on this concept, with meticulous design, we could merge our previously proposed mesh devices with and without cannula into a singular device that also incorporates the macroencapsulation pouch, as illustrated in **Figure 7-3**. This unified device would be implanted entirely at the subcutaneous site, consisting of dual mesh scaffolds interconnected by a cannula. One mesh would house the islets encapsulated within the immunoisolating pouch. The other mesh, devoid of islets, would be fully vascularized, allowing it to supply oxygen from the endogenous microvascular network to the other end. As demonstrated in this work, we have shown that hollow channels facilitate rapid and efficient air diffusion. Consequently, this design ensures that the islet graft receives sufficient oxygenation even after complete implantation.

Without relying on an abundant air supply as an unlimited oxygen source, the potential risks for contamination or infection through the cannula can be prevented.

By incorporating immunoisolation techniques into islet grafting, the issue of donor scarcity can be addressed, and the bioengineering burdens involved in creating immune-evasive cells can be eased. Moreover, xenotransplantation strategies might also be explored. A significant clinical hurdle of immunoisolation is that while it shields against immune cells and antigens, it also hinders oxygen diffusion. However, with the integration of our device, the critical aspect of oxygenation can be effectively resolved.

Our device has been tested in rodent models, yet it can be seamlessly upscaled for use in larger animals or human subjects. For instance, a typical human subject requires approximately 500,000 IEQ to reverse diabetes and become insulin independent [190]. In our demonstrations in rodent models, the oxygen-regulating mesh has supported between 1200-1800 IEQ within a 4 mm diameter circular area. Through a simple calculation, this translates to a device roughly 75 mm in diameter for the required islet volume. Allowing for additional non-islet-containing areas, the estimated diameter for a human-compatible device would be about 100 mm, assuming a four-layer mesh structure. Such a size is viable for human use given the ample skin surface area. Furthermore, the dimensions of the human-compatible device could be reduced by employing additional mesh layers or by distributing the islet grafts across multiple sites.

The transition from preclinical studies to clinical success represents the ultimate goal. With the discussion above, we highlight one of several potential scenarios in **Figure 7-4**. Two separate devices, both integrated with islets, are designed for transplantation under the abdominal skin. These larger-sized, human-compatible oxygen-regulating hollow mesh devices ensure adequate oxygenation supported by the vascular network. When a greater amount of IEQ is necessary to reverse diabetes and achieve insulin independence, these devices provide a clinically viable solution.

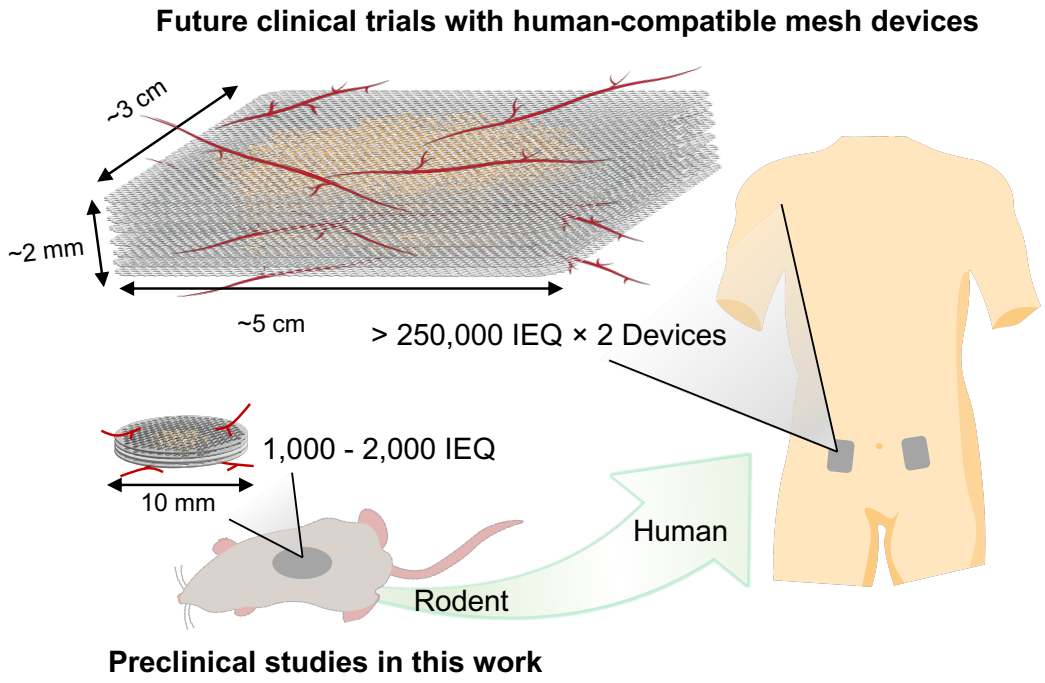

Figure 7-4. Path to clinical success. This illustration compares the size of a human-compatible device with those used in preclinical studies with rodent model discussed in this work. It exemplifies one of several potential approaches, demonstrating how devices integrated with islets can be transplanted under the abdominal skin. Immunoisolation strategic options referenced from Figures 7-1, 7-2, and 7-3 are adopted, although not explicitly depicted in this illustration.

In summary, our devices are versatile in numerous respects. It can be adapted for various cell types, subject sizes ranging from animals to humans, and diverse encapsulation strategies for immunoisolation. This adaptability is due to our capability to engineer hollow channels that facilitate rapid oxygen diffusion, ensuring adequate oxygenation for a range of applications. We believe that such a device has the potential to revolutionize the clinical outcomes of islet transplantation for the treatment and ultimate cure of type 1 diabetes.

BIBLIOGRAPHY

[1] S. J. Livingstone *et al.*, "Estimated life expectancy in a Scottish cohort with type 1 diabetes, 2008-2010," *The Journal of American Medical Association*, vol. 313, no. 1, pp. 37–44, Jan. 2015, doi: 10.1001/jama.2014.16425

[2] S. Kaptoge *et al.*, "Life expectancy associated with different ages at diagnosis of type 2 diabetes in high-income countries: 23 million person-years of observation," *The Lancet Diabetes & Endocrinology*, vol. 11, no. 10, pp. 731–742, Oct. 2023, doi: 10.1016/S2213-8587(23)00223-1

[3] W. H. Organization, "WHO Global report on diabetes," World Health Organization, Report, Apr. 2016. Available: https://apo.org.au/node/62469

[4] P. Saeedi *et al.*, "Global and regional diabetes prevalence estimates for 2019 and projections for 2030 and 2045: Results from the International Diabetes Federation Diabetes Atlas, 9th edition," *Diabetes Research and Clinical Practice*, vol. 157, p. 107843, Nov. 2019, doi: 10.1016/j.diabres.2019.107843

[5] W. R. Rowley, C. Bezold, Y. Arikan, E. Byrne, and S. Krohe, "Diabetes 2030: Insights from yesterday, today, and future trends," *Population Health Management*, vol. 20, no. 1, pp. 6–12, Feb. 2017, doi: 10.1089/pop.2015.0181

[6] American Diabetes Association, "Diagnosis and classification of diabetes mellitus," *Diabetes Care*, vol. 33, no. Supplement_1, pp. S62–S69, Jan. 2010, doi: 10.2337/dc10-S062

[7] P. E. MacDonald and P. Rorsman, "Oscillations, intercellular coupling, and insulin secretion in pancreatic β cells," *PLOS Biology*, vol. 4, no. 2, p. e49, Feb. 2006, doi: 10.1371/journal.pbio.0040049

[8] T. Kuzuya *et al.*, "Report of the committee on the classification and diagnostic criteria of diabetes mellitus," *Diabetes Research and Clinical Practice*, vol. 55, no. 1, pp. 65–85, Jan. 2002, doi: 10.1016/S0168-8227(01)00365-5

[9] M. Tominaga, "Diagnostic criteria for diabetes mellitus," *Rinsho Byori*, vol. 47, no. 10, pp. 901–908, Oct. 1999.

[10] S. F. Dinneen *et al.*, "Effects of changing diagnostic criteria on the risk of developing diabetes," *Diabetes Care*, vol. 21, no. 9, pp. 1408–1413, Sep. 1998, doi: 10.2337/diacare.21.9.1408

[11] S. Genuth *et al.*, "Follow-up report on the diagnosis of diabetes mellitus," *Diabetes Care*, vol. 26, no. 11, pp. 3160–3168, Nov. 2003.

[12] American Diabetes Association Professional Practice Committee, "2. Classification and diagnosis of diabetes: Standards of medical care in diabetes—2022," *Diabetes Care*, vol. 45, no. Supplement_1, pp. S17–S38, Dec. 2021, doi: 10.2337/dc22-S002

[13] R. M. Cohen, S. Haggerty, and W. H. Herman, "HbA1c for the diagnosis of diabetes and prediabetes: Is it time for a mid-course correction?" *The Journal*

of Clinical Endocrinology & Metabolism, vol. 95, no. 12, pp. 5203–5206, Dec. 2010, doi: 10.1210/jc.2010-2352

[14] M. A. Atkinson, G. S. Eisenbarth, and A. W. Michels, "Type 1 diabetes," *The Lancet*, vol. 383, no. 9911, pp. 69–82, Jan. 2014, doi: 10.1016/S0140-6736(13)60591-7

[15] S. James, R. Gallagher, J. Dunbabin, and L. Perry, "Prevalence of vascular complications and factors predictive of their development in young adults with type 1 diabetes: Systematic literature review," *BMC Research Notes*, vol. 7, no. 1, p. 593, Sep. 2014, doi: 10.1186/1756-0500-7-593

[16] F. G. Banting, C. H. Best, J. B. Collip, W. R. Campbell, and A. A. Fletcher, "Pancreatic extracts in the treatment of diabetes mellitus," *Canadian Medical Association Journal*, vol. 12, no. 3, pp. 141–146, Mar. 1922.

[17] A. Janež *et al.*, "Insulin therapy in adults with type 1 diabetes mellitus: A narrative review," *Diabetes Therapy*, vol. 11, no. 2, pp. 387–409, Feb. 2020, doi: 10.1007/s13300-019-00743-7

[18] M. Lind *et al.*, "Glycemic control and excess mortality in type 1 diabetes," *New England Journal of Medicine*, vol. 371, no. 21, pp. 1972–1982, Nov. 2014, doi: 10.1056/NEJMoa1408214

[19] S. K. Garg *et al.*, "Glucose outcomes with the in-home use of a hybrid closed-loop insulin delivery system in adolescents and adults with type 1 diabetes," *Diabetes Technology & Therapeutics*, vol. 19, no. 3, pp. 155–163, Mar. 2017, doi: 10.1089/dia.2016.0421

[20] Office of the Commissioner, "FDA approves first automated insulin delivery device for type 1 diabetes," *FDA*, Mar. 24, 2020. Available: https://www.fda.gov/news-events/press-announcements/fda-approves-first-automated-insulin-delivery-device-type-1-diabetes

[21] J. M. Quintana, A. L. Stinchcomb, J. H. Kostyo, B. M. Robichaud, M. A. Plunk, and R. R. Kane, "Chemical strategies for improving islet transplant outcomes," *OBM Transplantation*, vol. 2, no. 4, Art. no. 4, Dec. 2018, doi: 10.21926/obm.transplant.1804036

[22] A. M. J. Shapiro *et al.*, "Islet transplantation in seven patients with type 1 diabetes mellitus using a glucocorticoid-free immunosuppressive regimen," *New England Journal of Medicine*, vol. 343, no. 4, pp. 230–238, Jul. 2000, doi: 10.1056/NEJM200007273430401

[23] A. M. J. Shapiro *et al.*, "International trial of the Edmonton protocol for islet transplantation," *New England Journal of Medicine*, vol. 355, no. 13, pp. 1318–1330, Sep. 2006, doi: 10.1056/NEJMoa061267

[24] L. Piemonti, "Islet Transplantation," in *Endotext*, K. R. Feingold, B. Anawalt, M. R. Blackman, A. Boyce, G. Chrousos, E. Corpas, W. W. de Herder, K. Dhatariya, K. Dungan, J. Hofland, S. Kalra, G. Kaltsas, N. Kapoor, C. Koch, P. Kopp, M. Korbonits, C. S. Kovacs, W. Kuohung, B. Laferrère, M. Levy, E. A. McGee, R. McLachlan, M. New, J. Purnell, R. Sahay, A. S. Shah, F. Singer, M. A. Sperling, C. A. Stratakis, D. L. Trence, and D. P. Wilson, Eds., South Dartmouth (MA): MDText.com, Inc., 2000. Available: http://www.ncbi.nlm.nih.gov/books/NBK278966/

[25] F. B. Barton *et al.*, "Improvement in outcomes of clinical islet transplantation: 1999–2010," *Diabetes Care*, vol. 35, no. 7, pp. 1436–1445, Jun. 2012, doi: 10.2337/dc12-0063

[26] "Insulin-independence is rarely sustained after pancreatic islet transplantation," *Nature Review Endocrinology*, vol. 3, no. 1, pp. 6–6, Jan. 2007, doi: 10.1038/ncpendmet0358

[27] R. Olsson, J. Olerud, U. Pettersson, and P.-O. Carlsson, "Increased numbers of low-oxygenated pancreatic islets after intraportal islet transplantation," *Diabetes*, vol. 60, no. 9, pp. 2350–2353, Aug. 2011, doi: 10.2337/db09-0490

[28] L. Moberg *et al.*, "Production of tissue factor by pancreatic islet cells as a trigger of detrimental thrombotic reactions in clinical islet transplantation," *The Lancet*, vol. 360, no. 9350, pp. 2039–2045, Dec. 2002, doi: 10.1016/S0140-6736(02)12020-4

[29] P.-O. Carlsson, F. Palm, A. Andersson, and P. Liss, "Markedly decreased oxygen tension in transplanted rat pancreatic islets irrespective of the implantation site," *Diabetes*, vol. 50, no. 3, pp. 489–495, Mar. 2001, doi: 10.2337/diabetes.50.3.489

[30] N. M. Desai *et al.*, "Elevated portal vein drug levels of sirolimus and tacrolimus in islet transplant recipients: Local immunosuppression or islet toxicity," *Transplantation*, vol. 76, no. 11, p. 1623, Dec. 2003, doi: 10.1097/01.TP.0000081043.23751.81

[31] S. Matsumoto, "Islet cell transplantation for type 1 diabetes," *Journal of Diabetes*, vol. 2, no. 1, pp. 16–22, 2010, doi: 10.1111/j.1753-0407.2009.00048.x

[32] T. Anazawa, H. Okajima, T. Masui, and S. Uemoto, "Current state and future evolution of pancreatic islet transplantation," *Annals of Gastroenterological Surgery*, vol. 3, no. 1, pp. 34–42, 2019, doi: 10.1002/ags3.12214

[33] M. A. Lilly, M. F. Davis, J. E. Fabie, E. B. Terhune, and G. I. Gallicano, "Current stem cell-based therapies in diabetes," *American Journal of Stem Cells*, vol. 5, no. 3, pp. 87–98, Oct. 2016.

[34] D. T. Bowers, W. Song, L.-H. Wang, and M. Ma, "Engineering the vasculature for islet transplantation," *Acta Biomaterialia*, vol. 95, pp. 131–151, Sep. 2019, doi: 10.1016/j.actbio.2019.05.051

[35] H. Komatsu, F. Kandeel, and Y. Mullen, "Impact of Oxygen on Pancreatic Islet Survival," *Pancreas*, vol. 47, no. 5, p. 533, Jun. 2018, doi: 10.1097/MPA.0000000000001050

[36] H. Komatsu *et al.*, "Oxygen environment and islet size are the primary limiting factors of isolated pancreatic islet survival," *PLOS ONE*, vol. 12, no. 8, p. e0183780, Aug. 2017, doi: 10.1371/journal.pone.0183780

[37] K. K. Frame and W.-S. Hu, "Cell volume measurement as an estimation of mammalian cell biomass," *Biotechnology and Bioengineering*, vol. 36, no. 2, pp. 191–197, 1990, doi: 10.1002/bit.260360211

[38] B. A. Wagner, S. Venkataraman, and G. R. Buettner, "The rate of oxygen utilization by cells," *Free Radical Biology and Medicine*, vol. 51, no. 3, pp. 700–712, Aug. 2011, doi: 10.1016/j.freeradbiomed.2011.05.024

[39] A. U. Ernst *et al.*, "A predictive computational platform for optimizing the design of bioartificial pancreas devices," *Nature Communication*, vol. 13, no. 1, Art. no. 1, Oct. 2022, doi: 10.1038/s41467-022-33760-5

[40] G. A. Rutter, E. Georgiadou, A. Martinez-Sanchez, and T. J. Pullen, "Metabolic and functional specialisations of the pancreatic beta cell: Gene disallowance, mitochondrial metabolism and intercellular connectivity," *Diabetologia*, vol. 63, no. 10, pp. 1990–1998, Oct. 2020, doi: 10.1007/s00125-020-05205-5

[41] T. M. Suszynski, E. S. Avgoustiniatos, and K. K. Papas, "Intraportal islet oxygenation," *Journal of Diabetes Science and Technology*, vol. 8, no. 3, pp. 575–580, May 2014, doi: 10.1177/1932296814525827

[42] H. Komatsu *et al.*, "A subcutaneous pancreatic islet transplantation platform using a clinically applicable, biodegradable Vicryl mesh scaffold - an experimental study," *Transplant International*, vol. 33, no. 7, pp. 806–818, 2020, doi: 10.1111/tri.13607

[43] A. Sterkers *et al.*, "Islet survival and function following intramuscular autotransplantation in the minipig," *American Journal of Transplantation*, vol. 13, no. 4, pp. 891–898, Apr. 2013, doi: 10.1111/ajt.12136

[44] M. D. Menger, S. Jaeger, P. Walter, G. Feifel, F. Hammersen, and K. Messmer, "Angiogenesis and hemodynamics of microvasculature of transplanted islets of langerhans," *Diabetes*, vol. 38, no. Supplement_1, pp. 199–201, Jan. 1989, doi: 10.2337/diab.38.1.S199

[45] P. Vajkoczy *et al.*, "Histogenesis and ultrastructure of pancreatic islet graft microvasculature. Evidence for graft revascularization by endothelial cells of host origin.," *American Journal of Pathology*, vol. 146, no. 6, pp. 1397–1405, Jun. 1995.

[46] C. K. Colton, "Engineering challenges in cell encapsulation technology," *Trends in Biotechnology*, vol. 14, no. 5, pp. 158–162, May 1996, doi: 10.1016/0167-7799(96)10021-4

[47] T. Desai and L. D. Shea, "Advances in islet encapsulation technologies," *Nature Review Drug Discovery*, vol. 16, no. 5, pp. 338–350, May 2017, doi: 10.1038/nrd.2016.232

[48] R. R. HENRY *et al.*, "Initial clinical evaluation of VC-01™ combination product—A stem cell–derived islet replacement for type 1 diabetes (T1D)," *Diabetes*, vol. 67, no. Supplement_1, pp. 138-OR, Jul. 2018, doi: 10.2337/db18-138-OR

[49] B. Memon and E. M. Abdelalim, "Stem cell therapy for diabetes: Beta cells versus pancreatic progenitors," *Cells*, vol. 9, no. 2, Art. no. 2, Feb. 2020, doi: 10.3390/cells9020283

[50] J. Schweicher, C. Nyitray, and T. A. Desai, "Membranes to achieve immunoprotection of transplanted islets," *Frontiers in Bioscience-Landmark*, vol. 19, no. 1, Art. no. 1, Jan. 2014, doi: 10.2741/4195

[51] U. Barkai *et al.*, "Enhanced oxygen supply improves islet viability in a new bioartificial pancreas," *Cell Transplantation*, vol. 22, no. 8, pp. 1463–1476, Aug. 2013, doi: 10.3727/096368912X657341

[52] P.-O. Carlsson *et al.*, "Transplantation of macroencapsulated human islets within the bioartificial pancreas βAir to patients with type 1 diabetes mellitus," *American Journal of Transplantation*, vol. 18, no. 7, pp. 1735–1744, Jul. 2018, doi: 10.1111/ajt.14642

[53] A. R. Pepper, B. Gala-Lopez, R. Pawlick, S. Merani, T. Kin, and A. M. J. Shapiro, "A prevascularized subcutaneous device-less site for islet and cellular transplantation," *Nature Biotechnology*, vol. 33, no. 5, pp. 518–523, May 2015, doi: 10.1038/nbt.3211

[54] L.-H. Wang *et al.*, "Inflammation-induced subcutaneous neovascularization for the long-term survival of encapsulated islets without immunosuppression," *Nature Biomedical Engineering*, pp. 1–19, Dec. 2023, doi: 10.1038/s41551-023-01145-8

[55] E. Pedraza, M. M. Coronel, C. A. Fraker, C. Ricordi, and C. L. Stabler, "Preventing hypoxia-induced cell death in beta cells and islets via hydrolytically activated, oxygen-generating biomaterials," *Proceedings of the National Academy of Sciences*, vol. 109, no. 11, pp. 4245–4250, Mar. 2012, doi: 10.1073/pnas.1113560109

[56] S. R. Krishnan *et al.*, "A wireless, battery-free device enables oxygen generation and immune protection of therapeutic xenotransplants in vivo," *Proceedings of the National Academy of Sciences*, vol. 120, no. 40, p. e2311707120, Oct. 2023, doi: 10.1073/pnas.2311707120

[57] L.-H. Wang *et al.*, "A bioinspired scaffold for rapid oxygenation of cell encapsulation systems," *Nature Communication*, vol. 12, no. 1, Art. no. 1, Oct. 2021, doi: 10.1038/s41467-021-26126-w

[58] S. Goutelle *et al.*, "The Hill equation: A review of its capabilities in pharmacological modelling," *Fundamental & Clinical Pharmacology*, vol. 22, no. 6, pp. 633–648, 2008, doi: 10.1111/j.1472-8206.2008.00633.x

[59] S. Sarraute, H. Delepine, M. F. Costa Gomes, and V. Majer, "Aqueous solubility, Henry's law constants and air/water partition coefficients of *n*-octane and two halogenated octanes," *Chemosphere*, vol. 57, no. 10, pp. 1543–1551, Dec. 2004, doi: 10.1016/j.chemosphere.2004.07.046

[60] I. Anundi and H. de Groot, "Hypoxic liver cell death: critical Po2 and dependence of viability on glycolysis," *American Journal of Physiology-Gastrointestinal and Liver Physiology*, vol. 257, no. 1, pp. G58–G64, Jul. 1989, doi: 10.1152/ajpgi.1989.257.1.G58

[61] P. Buchwald, "FEM-based oxygen consumption and cell viability models for avascular pancreatic islets," *Theoretical Biology and Medical Modelling*, vol. 6, no. 1, p. 5, Apr. 2009, doi: 10.1186/1742-4682-6-5

[62] E. S. Avgoustiniatos and C. K. Colton, "Effect of external oxygen mass transfer resistances on viability of immunoisolated tissue," *Annals of the New York Academy of Sciences*, vol. 831, no. 1, pp. 145–166, 1997, doi: 10.1111/j.1749-6632.1997.tb52192.x

[63] K.-M. Shang, H. Kato, N. Gonzalez, F. Kandeel, Y.-C. Tai, and H. Komatsu, "A novel approach to determine the critical survival threshold of cellular oxygen within spheroids via integrating live/dead cell imaging with oxygen

modeling," *American Journal of Physiology-Cell Physiology*, vol. 326, no. 4, pp. C1262–C1271, Apr. 2024, doi: 10.1152/ajpcell.00024.2024
[64] P. Carmeliet *et al.*, "Role of HIF-1α in hypoxia-mediated apoptosis, cell proliferation and tumour angiogenesis," *Nature*, vol. 394, no. 6692, Art. no. 6692, Jul. 1998, doi: 10.1038/28867
[65] P. H. Maxwell *et al.*, "The tumour suppressor protein VHL targets hypoxia-inducible factors for oxygen-dependent proteolysis," *Nature*, vol. 399, no. 6733, Art. no. 6733, May 1999, doi: 10.1038/20459
[66] W. Jelkmann, "Molecular biology of erythropoietin," *Internal Medicine*, vol. 43, no. 8, pp. 649–659, 2004, doi: 10.2169/internalmedicine.43.649
[67] H. F. Bunn, "Erythropoietin," *Cold Spring Harbor Perspectives in Medicine*, vol. 3, no. 3, p. a011619, Mar. 2013, doi: 10.1101/cshperspect.a011619
[68] N. Ferrara, "Vascular endothelial growth factor: basic science and clinical progress," *Endocrine Reviews*, vol. 25, no. 4, pp. 581–611, Aug. 2004, doi: 10.1210/er.2003-0027
[69] F. Rosetti and T. N. Mayadas, "The many faces of Mac-1 in autoimmune disease," *Immunological Reviews*, vol. 269, no. 1, pp. 175–193, 2016, doi: 10.1111/imr.12373
[70] P. Vaupel, A. Mayer, and M. Höckel, "Tumor hypoxia and malignant progression," in *Methods in Enzymology*, in Oxygen Sensing, vol. 381. Academic Press, 2004, pp. 335–354. doi: 10.1016/S0076-6879(04)81023-1.
[71] A. L. Harris, "Hypoxia — a key regulatory factor in tumour growth," *Nature Review Cancer*, vol. 2, no. 1, Art. no. 1, Jan. 2002, doi: 10.1038/nrc704
[72] R. A. Stokes *et al.*, "Hypoxia-inducible factor-1α (HIF-1α) Potentiates β-Cell Survival after Islet Transplantation of Human and Mouse Islets," *Cell Transplantation*, vol. 22, no. 2, pp. 253–266, Feb. 2013, doi: 10.3727/096368912X647180
[73] M. Garcia-Contreras *et al.*, "metabolomics study of the effects of inflammation, hypoxia, and high glucose on isolated human pancreatic islets," *Journal of Proteome Research*, vol. 16, no. 6, pp. 2294–2306, Jun. 2017, doi: 10.1021/acs.jproteome.7b00160
[74] P. A. Gerber and G. A. Rutter, "The role of oxidative stress and hypoxia in pancreatic beta-cell dysfunction in diabetes mellitus," *Antioxidants & Redox Signaling*, vol. 26, no. 10, pp. 501–518, Apr. 2017, doi: 10.1089/ars.2016.6755
[75] K. K. Papas, H. De Leon, T. M. Suszynski, and R. C. Johnson, "Oxygenation strategies for encapsulated islet and beta cell transplants," *Advanced Drug Delivery Reviews*, vol. 139, pp. 139–156, Jan. 2019, doi: 10.1016/j.addr.2019.05.002
[76] U. Barkai *et al.*, "Enhanced oxygen supply improves islet viability in a new bioartificial pancreas," *Cell Transplantation*, vol. 22, no. 8, pp. 1463–1476, Aug. 2013, doi: 10.3727/096368912X657341
[77] B. Ludwig *et al.*, "Improvement of islet function in a bioartificial pancreas by enhanced oxygen supply and growth hormone releasing hormone agonist," *Proceedings of the National Academy of Sciences*, vol. 109, no. 13, pp. 5022–5027, Mar. 2012, doi: 10.1073/pnas.1201868109

[78] B. Ludwig *et al.*, "Transplantation of human islets without immunosuppression," *Proceedings of the National Academy of Sciences*, vol. 110, no. 47, pp. 19054–19058, Nov. 2013, doi: 10.1073/pnas.1317561110
[79] S. H. Oh, C. L. Ward, A. Atala, J. J. Yoo, and B. S. Harrison, "Oxygen generating scaffolds for enhancing engineered tissue survival," *Biomaterials*, vol. 30, no. 5, pp. 757–762, Feb. 2009, doi: 10.1016/j.biomaterials.2008.09.065
[80] P. O. Carlsson, P. Liss, A. Andersson, and L. Jansson, "Measurements of oxygen tension in native and transplanted rat pancreatic islets.," *Diabetes*, vol. 47, no. 7, pp. 1027–1032, Jul. 1998, doi: 10.2337/diabetes.47.7.1027
[81] K. C. Murphy *et al.*, "Measurement of oxygen tension within mesenchymal stem cell spheroids," *Journal of The Royal Society Interface*, vol. 14, no. 127, p. 20160851, Feb. 2017, doi: 10.1098/rsif.2016.0851
[82] M. Quaranta, S. M. Borisov, and I. Klimant, "Indicators for optical oxygen sensors," *Bioanalytical Review*, vol. 4, no. 2, pp. 115–157, Dec. 2012, doi: 10.1007/s12566-012-0032-y
[83] M. Kotecha *et al.*, "In vitro oxygen imaging of acellular and cell-loaded beta cell replacement devices," *Scientific Reports*, vol. 13, no. 1, Art. no. 1, Sep. 2023, doi: 10.1038/s41598-023-42099-w
[84] S. Cai Lesher-Pérez *et al.*, "Dispersible oxygen microsensors map oxygen gradients in three-dimensional cell cultures," *Biomaterials Science*, vol. 5, no. 10, pp. 2106–2113, 2017, doi: 10.1039/C7BM00119C
[85] M. Kotecha, B. Epel, S. Ravindran, D. Dorcemus, S. Nukavarapu, and H. Halpern, "noninvasive absolute electron paramagnetic resonance oxygen imaging for the assessment of tissue graft oxygenation," *Tissue Engineering Part C: Methods*, vol. 24, no. 1, pp. 14–19, Jan. 2018, doi: 10.1089/ten.tec.2017.0236
[86] R. J. Myrick *et al.*, "Micropyramid-patterned, oxygen-permeable bottomed dish for high density culture of pancreatic islets," *Biofabrication*, vol. 15, no. 1, p. 015018, Dec. 2022, doi: 10.1088/1758-5090/aca79a
[87] M. Salgado *et al.*, "Semi-automated assessment of human islet viability predicts transplantation outcomes in a diabetic mouse model," *Cell Transplantation*, vol. 29, p. 0963689720919444, Jan. 2020, doi: 10.1177/0963689720919444
[88] T. Ito *et al.*, "mesenchymal stem cell and islet co-transplantation promotes graft revascularization and function," *Transplantation*, vol. 89, no. 12, p. 1438, Jun. 2010, doi: 10.1097/TP.0b013e3181db09c4
[89] C. Ricordi, "Quantitative and qualitative standards for islet isolation assessment in humans and large mammals," *Pancreas*, vol. 6, no. 2, p. 242, Mar. 1991.
[90] H. Komatsu *et al.*, "A Multiparametric Assessment of Human Islets Predicts Transplant Outcomes in Diabetic Mice," *Cell Transplantation*, vol. 30, p. 09636897211052291, Jan. 2021, doi: 10.1177/09636897211052291
[91] H. Komatsu *et al.*, "Isolated human islets require hyperoxia to maintain islet mass, metabolism, and function," *Biochemical and Biophysical Research*

Communications, vol. 470, no. 3, pp. 534–538, Feb. 2016, doi: 10.1016/j.bbrc.2016.01.110

[92] H. Komatsu, K. Omori, M. Parimi, J. Rawson, F. Kandeel, and Y. Mullen, "Determination of islet viability using a zinc-specific fluorescent dye and a semiautomated assessment method," *Cell Transplantation*, vol. 25, no. 10, pp. 1777–1786, Oct. 2016, doi: 10.3727/096368915X689721

[93] F. Podczeck and J. M. Newton, "A shape factor to characterize the quality of spheroids," *Journal of Pharmacy and Pharmacology*, vol. 46, no. 2, pp. 82–85, Feb. 1994, doi: 10.1111/j.2042-7158.1994.tb03745.x

[94] N. Gonzalez, M. Salgado, L. Medrano, Y. Mullen, and H. Komatsu, "Isolated pancreatic islet yield and quality is inversely related to organ donor age in rats," *Experimental Gerontology*, vol. 128, p. 110739, Dec. 2019, doi: 10.1016/j.exger.2019.110739

[95] P. Virtanen *et al.*, "SciPy 1.0: Fundamental algorithms for scientific computing in Python," *Nature Methods*, vol. 17, no. 3, Art. no. 3, Mar. 2020, doi: 10.1038/s41592-019-0686-2

[96] Y. Ntamo, E. Samodien, J. Burger, N. Muller, C. J. F. Muller, and N. Chellan, "In vitro characterization of insulin−producing β-Cell spheroids," *Frontiers in Cell and Developmental Biology*, vol. 8, p. 623889, 2021, doi: 10.3389/fcell.2020.623889

[97] T. M. Suszynski, E. S. Avgoustiniatos, and K. K. Papas, "Oxygenation of the intraportally transplanted pancreatic islet," *Journal of Diabetes Research*, vol. 2016, p. e7625947, Oct. 2016, doi: 10.1155/2016/7625947

[98] W. Xing, M. Yin, Q. Lv, Y. Hu, C. Liu, and J. Zhang, "1 - Oxygen solubility, diffusion coefficient, and solution viscosity," in *Rotating Electrode Methods and Oxygen Reduction Electrocatalysts*, W. Xing, G. Yin, and J. Zhang, Eds., Amsterdam: Elsevier, 2014, pp. 1–31. doi: 10.1016/B978-0-444-63278-4.00001-X

[99] M.-C. Kim, R. H. W. Lam, T. Thorsen, and H. H. Asada, "Mathematical analysis of oxygen transfer through polydimethylsiloxane membrane between double layers of cell culture channel and gas chamber in microfluidic oxygenator," *Microfluid Nanofluid*, vol. 15, no. 3, pp. 285–296, Sep. 2013, doi: 10.1007/s10404-013-1142-8

[100] T. C. Merkel, V. I. Bondar, K. Nagai, B. D. Freeman, and I. Pinnau, "Gas sorption, diffusion, and permeation in poly(dimethylsiloxane)," *Journal of Polymer Science Part B: Polymer Physics*, vol. 38, no. 3, pp. 415–434, 2000, doi: 10.1002/(SICI)1099-0488(20000201)38:3<415::AID-POLB8>3.0.CO;2-Z

[101] D. Espes, J. Lau, M. Quach, U. Banerjee, A. F. Palmer, and P.-O. Carlsson, "Cotransplantation of polymerized hemoglobin reduces β-cell hypoxia and improves β-cell function in intramuscular islet grafts," *Transplantation*, vol. 99, no. 10, p. 2077, Oct. 2015, doi: 10.1097/TP.0000000000000815

[102] R. P. Accolla *et al.*, "Engineering modular, oxygen-generating microbeads for the in situ mitigation of cellular hypoxia," *Advanced Healthcare Materials*, vol. 12, no. 19, p. 2300239, 2023, doi: 10.1002/adhm.202300239

[103] H. Komatsu *et al.*, "Posttransplant oxygen inhalation improves the outcome of subcutaneous islet transplantation: A promising clinical alternative to the conventional intrahepatic site," *American Journal of Transplantation*, vol. 18, no. 4, pp. 832–842, Apr. 2018, doi: 10.1111/ajt.14497
[104] O. Warburg, "On the origin of cancer cells," *Science*, vol. 123, no. 3191, pp. 309–314, Feb. 1956, doi: 10.1126/science.123.3191.309
[105] M. Ma *et al.*, "Core–shell hydrogel microcapsules for improved islets encapsulation," *Advanced Healthcare Materials*, vol. 2, no. 5, pp. 667–672, 2013, doi: 10.1002/adhm.201200341
[106] M. Kumagai-Braesch *et al.*, "The TheraCyte™ device protects against islet allograft rejection in immunized hosts," *Cell Transplantation*, vol. 22, no. 7, pp. 1137–1146, Jul. 2013, doi: 10.3727/096368912X657486
[107] T. Noll, H. de Groot, and P. Wissemann, "A computer-supported oxystat system maintaining steady-state O2 partial pressures and simultaneously monitoring O2 uptake in biological systems," *Biochemical Journal*, vol. 236, no. 3, pp. 765–769, Jun. 1986, doi: 10.1042/bj2360765
[108] M. A. Miranda, J. F. Macias-Velasco, and H. A. Lawson, "Pancreatic β-cell heterogeneity in health and diabetes: Classes, sources, and subtypes," *American Journal of Physiology-Endocrinology and Metabolism*, vol. 320, no. 4, pp. E716–E731, Apr. 2021, doi: 10.1152/ajpendo.00649.2020
[109] H. Kato *et al.*, "Microwell culture platform maintains viability and mass of human pancreatic islets," *Frontiers in Endocrinology*, vol. 13, 2022, doi: 10.3389/fendo.2022.1015063.
[110] A. Pisania *et al.*, "Enumeration of islets by nuclei counting and light microscopic analysis," *Laboratory Investigation*, vol. 90, no. 11, pp. 1676–1686, Nov. 2010, doi: 10.1038/labinvest.2010.125
[111] A. Pisania *et al.*, "Quantitative analysis of cell composition and purity of human pancreatic islet preparations," *Laboratory Investigation*, vol. 90, no. 11, pp. 1661–1675, Nov. 2010, doi: 10.1038/labinvest.2010.124
[112] C. Ricordi *et al.*, "Islet isolation assessment in man and large animals," *Acta diabet. lat*, vol. 27, no. 3, pp. 185–195, Jul. 1990, doi: 10.1007/BF02581331
[113] K. Papas *et al.*, "Human islet oxygen consumption rate and DNA measurements predict diabetes reversal in nude mice," *American Journal of Transplantation*, vol. 7, no. 3, pp. 707–713, Mar. 2007, doi: 10.1111/j.1600-6143.2006.01655.x
[114] D. Balboa *et al.*, "Functional, metabolic and transcriptional maturation of human pancreatic islets derived from stem cells," *Nature Biotechnology*, vol. 40, no. 7, pp. 1042–1055, Jul. 2022, doi: 10.1038/s41587-022-01219-z
[115] H. Shiku *et al.*, "Oxygen permeability of surface-modified poly(dimethylsiloxane) characterized by scanning electrochemical microscopy," *Chemistry Letter*, vol. 35, no. 2, pp. 234–235, Feb. 2006, doi: 10.1246/cl.2006.234
[116] S.-T. Hwang, T. E. S. Tang, and K. Kammermeyer, "Transport of dissolved oxygen through silicone rubber membrane," *Journal of Macromolecular Science, Part B*, vol. 5, no. 1, pp. 1–10, Mar. 1971, doi: 10.1080/00222347108212517

[117] D. A. Markov, E. M. Lillie, S. P. Garbett, and L. J. McCawley, "Variation in diffusion of gases through PDMS due to plasma surface treatment and storage conditions," *Biomedical Microdevices*, vol. 16, no. 1, pp. 91–96, Feb. 2014, doi: 10.1007/s10544-013-9808-2

[118] M. E. Cox and B. Dunn, "Oxygen diffusion in poly(dimethyl siloxane) using fluorescence quenching. I. Measurement technique and analysis," *Journal of Polymer Science Part A: Polymer Chemistry*, vol. 24, no. 4, pp. 621–636, 1986, doi: 10.1002/pola.1986.080240405

[119] M. W. Toepke and D. J. Beebe, "PDMS absorption of small molecules and consequences in microfluidic applications," *Lab on a Chip*, vol. 6, no. 12, pp. 1484–1486, Nov. 2006, doi: 10.1039/B612140C

[120] J. Padmanabhan *et al.*, "Allometrically scaling tissue forces drive pathological foreign-body responses to implants via Rac2-activated myeloid cells," *Nat. Biomed. Eng*, vol. 7, no. 11, pp. 1419–1436, Nov. 2023, doi: 10.1038/s41551-023-01091-5

[121] W.-C. Kuo, T.-C. Wu, C.-F. Wu, and W.-C. Wang, "Bioperformance analysis of parylene C coating for implanted nickel titanium alloy," *Materials Today Communications*, vol. 27, p. 102306, Jun. 2021, doi: 10.1016/j.mtcomm.2021.102306

[122] T. Stieglitz, "Considerations on surface and structural biocompatibility as prerequisite for long-term stability of neural prostheses," *Journal of Nanoscience and Nanotechnology*, vol. 4, no. 5, pp. 496–503, May 2004, doi: 10.1166/jnn.2004.075

[123] "SCS ParyFree® meets ISO 10993 biocompatibility testing requirements," *Specialty Coating Systems*, Feb. 22, 2021. Available: https://scscoatings.com/newsroom/scs-paryfree-meets-iso-10993-biocompatibility-testing-requirements/

[124] C.-Y. Lin *et al.*, "Bio-compatibility and bio-insulation of implantable electrode prosthesis ameliorated by A-174 silane primed parylene-C deposited embedment," *Micromachines*, vol. 11, no. 12, Art. no. 12, Dec. 2020, doi: 10.3390/mi11121064

[125] M. Golda-Cepa, K. Engvall, M. Hakkarainen, and A. Kotarba, "Recent progress on parylene C polymer for biomedical applications: A review," *Progress in Organic Coatings*, vol. 140, p. 105493, Mar. 2020, doi: 10.1016/j.porgcoat.2019.105493

[126] "Parylene History," *Specialty Coating Systems*. Available: https://scscoatings.com/parylene-coatings/parylene-history/

[127] J. B. Fortin and T.-M. Lu, *Chemical Vapor Deposition Polymerization: The Growth and Properties of Parylene Thin Films*. Springer Science & Business Media, 2003.

[128] D. Kang, A. Standley, J. H.-C. Chang, Y. Liu, and Y.-C. Tai, "Effects of deposition temperature on Parylene-C properties," in *2013 IEEE 26th International Conference on Micro Electro Mechanical Systems (MEMS)*, Jan. 2013, pp. 389–390. doi: 10.1109/MEMSYS.2013.6474260

[129] A. Kahouli, “Effect of film thickness on structural, morphology, dielectric and electrical properties of parylene C films,” *Journal of Applied Physics*, vol. 112, no. 6, p. 064103, Sep. 2012, doi: 10.1063/1.4752022
[130] N. Jackson, F. Stam, J. O’Brien, L. Kailas, A. Mathewson, and C. O’Murchu, “Crystallinity and mechanical effects from annealing Parylene thin films,” *Thin Solid Films*, vol. 603, pp. 371–376, Mar. 2016, doi: 10.1016/j.tsf.2016.02.047
[131] W. Li, “Integrated retinal implants,” PhD, California Institute of Technology, 2009. doi: 10.7907/AMK6-TA42.
[132] A. Kachroudi, C. Lagomarsini, V. H. Mareau, and A. Sylvestre, “Annealing for the improvement of the capabilities of parylene C as electret,” *Journal of Applied Polymer Science*, vol. 136, no. 1, p. 46908, 2019, doi: 10.1002/app.46908
[133] R. P. von Metzen and T. Stieglitz, “The effects of annealing on mechanical, chemical, and physical properties and structural stability of parylene C,” *Biomedical Microdevices*, vol. 15, no. 5, pp. 727–735, Oct. 2013, doi: 10.1007/s10544-013-9758-8
[134] J. M. Zielinski and J. L. Duda, “Predicting polymer/solvent diffusion coefficients using free-volume theory,” *AIChE Journal*, vol. 38, no. 3, pp. 405–415, 1992, doi: 10.1002/aic.690380309
[135] L. Bian *et al.*, “MD simulation and cluster analyses of the gas permeability of parylene AF4 membranes,” *Journal of Molecular Structure*, vol. 1105, pp. 142–151, Feb. 2016, doi: 10.1016/j.molstruc.2015.10.027
[136] A. Gieldon, C. Czaplewski, K. Smalara, and M. Bobrowski, “Molecular dynamics simulations of the growth of poly(chloro-para-xylylene) films,” *Journal of Molecular Modeling*, vol. 17, no. 11, pp. 2725–2733, Nov. 2011, doi: 10.1007/s00894-011-1050-3
[137] L. Bian, Y. Shu, J. Xu, and L. Wang, “Theoretical calculation on permeation of gas molecules through crystalline poly (p-xylylene) (PPX) films,” *Science China Technology Sciences*, vol. 56, no. 1, pp. 40–47, Jan. 2013, doi: 10.1007/s11431-012-5068-2
[138] L. Bian, Y. Shu, J. Xu, and L. Wang, “Molecular dynamics study on permeability of gas molecules through amorphous PPX polymers,” *International Polymer Processing*, vol. 28, no. 1, pp. 24–33, Mar. 2013, doi: 10.3139/217.2610
[139] A. Kahouli *et al.*, “Structural and dielectric study of parylene C thin films,” *Applied Physics Letters*, vol. 94, no. 15, p. 152901, Apr. 2009, doi: 10.1063/1.3114404
[140] A. Kahouli *et al.*, “Dielectric properties of parylene AF4 as low-*k* material for microelectronic applications,” *Thin Solid Films*, vol. 520, no. 7, pp. 2493–2497, Jan. 2012, doi: 10.1016/j.tsf.2011.10.025
[141] A. Tanioka, N. Fukushima, K. Hasegawa, K. Miyasaka, and N. Takahashi, “Permeation of gases across the poly(chloro-p-xylylene) membrane,” *Journal of Applied Polymer Science*, vol. 54, no. 2, pp. 219–229, 1994, doi: 10.1002/app.1994.070540208

[142] “SCS parylene properties.” Specialty Coating Systems, 2018. Available: https://rsc.aux.eng.ufl.edu/_files/documents/176.pdf
[143] C. Chindam, A. Lakhtakia, and O. O. Awadelkarim, “Surface energy of Parylene C,” *Materials Letters*, vol. 153, pp. 18–19, Aug. 2015, doi: 10.1016/j.matlet.2015.04.009
[144] C. Qu *et al.*, “Bio-inspired antimicrobial surfaces fabricated by glancing angle deposition,” *Scientific Reports*, vol. 13, no. 1, p. 207, Jan. 2023, doi: 10.1038/s41598-022-27225-4
[145] M. Akhtar, S. van den Driesche, A. Bödecker, and M. J. Vellekoop, “Long-term storage of droplets on a chip by parylene AF4 coating of channels,” *Sensors and Actuators B: Chemical*, vol. 255, pp. 3576–3584, 2018.
[146] C. Desai and N. Laube, “Development of a technical approach to modify the internal surface of biomedical tubes and other elongated small lumen macrodevices with parylene coating,” *Journal of Coatings Technology and Research*, vol. 16, no. 1, pp. 103–111, Jan. 2019, doi: 10.1007/s11998-018-0104-1
[147] J. Crank, *The Mathematics of Diffusion*. Clarendon Press, 1979.
[148] Y. Wei, Y. Jiao, D. An, D. Li, W. Li, and Q. Wei, “Review of dissolved oxygen detection technology: From laboratory analysis to online intelligent detection,” *Sensors*, vol. 19, no. 18, Art. no. 18, Jan. 2019, doi: 10.3390/s19183995
[149] H. Tai, Y. Yang, S. Liu, and D. Li, “A review of measurement methods of dissolved oxygen in water,” in *Computer and Computing Technologies in Agriculture V*, D. Li and Y. Chen, Eds., Berlin, Heidelberg: Springer, 2012, pp. 569–576. doi: 10.1007/978-3-642-27278-3_58
[150] R. Ramamoorthy, P. K. Dutta, and S. A. Akbar, “Oxygen sensors: Materials, methods, designs and applications,” *Journal of Materials Science*, vol. 38, no. 21, pp. 4271–4282, Nov. 2003, doi: 10.1023/A:1026370729205
[151] J. H. Carpenter, “The accuracy of the winkler method for dissolved oxygen analysis,” *Limnology and Oceanography*, vol. 10, no. 1, pp. 135–140, 1965, doi: 10.4319/lo.1965.10.1.0135
[152] J. W. Severinghaus and P. B. Astrup, “History of blood gas analysis. IV. Leland Clark’s oxygen electrode,” *Journal of Clinical Monitoring and Computing*, vol. 2, no. 2, pp. 125–139, Apr. 1986, doi: 10.1007/BF01637680
[153] Y. Rharbi, A. Yekta, and M. A. Winnik, “A method for measuring oxygen diffusion and oxygen permeation in polymer films based on fluorescence quenching,” *Analytical Chemistry*, vol. 71, no. 22, pp. 5045–5053, Nov. 1999, doi: 10.1021/ac990193c
[154] K. A. Kneas, J. N. Demas, B. Nguyen, A. Lockhart, W. Xu, and B. A. DeGraff, “Method for measuring oxygen diffusion coefficients of polymer films by luminescence quenching,” *Analytical Chemistry*, vol. 74, no. 5, pp. 1111–1118, Mar. 2002, doi: 10.1021/ac010867v
[155] “OxygensSystems.” Available: https://www.oceaninsight.com/products/systems/sensors/oxygen-systems/.
[156] “Product: VisiSens TD.” Available: https://www.presens.de/products/detail/visisens-td.

[157] O. S. Wolfbeis, “Luminescent sensing and imaging of oxygen: Fierce competition to the Clark electrode,” *BioEssays*, vol. 37, no. 8, pp. 921–928, 2015, doi: 10.1002/bies.201500002

[158] B. Ludwig, C. Heller, V. Sarangova, and P. B. Welzel, “Islet macroencapsulation: strategies to boost islet graft oxygenation,” in *Pluripotent Stem Cell Therapy for Diabetes*, L. Piemonti, J. Odorico, T. J. . . Kieffer, V. Sordi, and E. de Koning, Eds., Cham: Springer International Publishing, 2023, pp. 251–280. doi: 10.1007/978-3-031-41943-0_12.

[159] G. Theocharidis and A. Veves, “Greater foreign-body responses to big implants,” *Nature Biomedical Engineering*, pp. 1–3, Nov. 2023, doi: 10.1038/s41551-023-01118-x

[160] H. H. Billett, “Hemoglobin and hematocrit,” in *Clinical Methods: The History, Physical, and Laboratory Examinations*, H. K. Walker, W. D. Hall, and J. W. Hurst, Eds., 3rd ed. Boston: Butterworths, 1990. Available: http://www.ncbi.nlm.nih.gov/books/NBK259/.

[161] M. C. P. Van Beekvelt, W. N. J. M. Colier, R. A. Wevers, and B. G. M. Van Engelen, “Performance of near-infrared spectroscopy in measuring local O_2 consumption and blood flow in skeletal muscle,” *Journal of Applied Physiology*, vol. 90, no. 2, pp. 511–519, Feb. 2001, doi: 10.1152/jappl.2001.90.2.511

[162] E. D. De villota, M. T. G. Carmona, J. J. Rubio, and S. R. De andrés, “Equality of the *in vivo* and *in vitro* oxygen-binding capacity of hemoglobin in patients with severe respiratory disease,” *British Journal of Anaesthesia*, vol. 53, no. 12, pp. 1325–1328, Dec. 1981, doi: 10.1093/bja/53.12.1325

[163] J. Barcroft and A. V. Hill, “The nature of oxyhaemoglobin, with a note on its molecular weight,” *The Journal of Physiology*, vol. 39, no. 6, pp. 411–428, 1910, doi: 10.1113/jphysiol.1910.sp001350

[164] K.-M. Shang, H. Komatsu, and Y.-C. Tai, “Oxygen-transporting parylene-HT mesh for cell transplantation to reduce hypoxia,” in *2021 IEEE 34th International Conference on Micro Electro Mechanical Systems (MEMS)*, Jan. 2021, pp. 458–461. doi: 10.1109/MEMS51782.2021.9375215.

[165] Y.-C. Tai, K.-M. Shang, and H. Komatsu, “Microcapillary mesh oxygen transporter for cell transplantations,” US20230166004A1, Jun. 01, 2023 Available: https://patents.google.com/patent/US20230166004A1/en.

[166] R. Chen, R. Kang, and D. Tang, “The mechanism of HMGB1 secretion and release,” *Experimental & Molecular Medicine*, vol. 54, no. 2, pp. 91–102, Feb. 2022, doi: 10.1038/s12276-022-00736-w

[167] Y. Hakamata, T. Murakami, and E. Kobayashi, “‘Firefly rats’ as an organ/cellular source for long-term in vivo bioluminescent imaging,” *Transplantation*, vol. 81, no. 8, p. 1179, Apr. 2006, doi: 10.1097/01.tp.0000203137.06587.4a

[168] E. Kobayashi, Y. Hakamata, S. Enosawa, K.-M. Shang, and H. Komatsu, “Firefly rats: Illuminating the scientific community in transplantation research,” *Cell Transplantation*, vol. 33, p. 09636897231224174, Jan. 2024, doi: 10.1177/09636897231224174

[169] N. M. Luan and H. Iwata, “Long-term allogeneic islet graft survival in prevascularized subcutaneous sites without immunosuppressive treatment,” *American Journal of Transplantation*, vol. 14, no. 7, pp. 1533–1542, Jul. 2014, doi: 10.1111/ajt.12739

[170] H. Komatsu *et al.*, “Early-phase luciferase signals of islet grafts predicts successful subcutaneous site transplantation in rats,” *Molecular Imaging and Biology*, vol. 23, no. 2, pp. 173–179, Apr. 2021, doi: 10.1007/s11307-020-01560-2

[171] J. Östman *et al.*, “Gender differences and temporal variation in the incidence of type 1 diabetes: results of 8012 cases in the nationwide Diabetes Incidence Study in Sweden 1983–2002,” *Journal of Internal Medicine*, vol. 263, no. 4, pp. 386–394, 2008, doi: 10.1111/j.1365-2796.2007.01896.x

[172] Y.-G. Ko, N. Kawazoe, T. Tateishi, and G. Chen, “Preparation of novel collagen sponges using an ice particulate template,” *Journal of Bioactive and Compatible Polymers*, vol. 25, no. 4, pp. 360–373, Jul. 2010, doi: 10.1177/0883911510370002

[173] G. Yoshimatsu *et al.*, “Pancreatic β-cell–derived IP-10/CXCL10 isletokine mediates early loss of graft function in islet cell transplantation,” *Diabetes*, vol. 66, no. 11, pp. 2857–2867, Aug. 2017, doi: 10.2337/db17-0578

[174] A. R. Pepper, B. Gala-Lopez, O. Ziff, and A. M. J. Shapiro, “Revascularization of transplanted pancreatic islets and role of the transplantation site,” *Journal of Immunology Research*, vol. 2013, p. e352315, Sep. 2013, doi: 10.1155/2013/352315

[175] D. Nyqvist *et al.*, “Donor islet endothelial cells in pancreatic islet revascularization,” *Diabetes*, vol. 60, no. 10, pp. 2571–2577, Sep. 2011, doi: 10.2337/db10-1711

[176] M. Brissova *et al.*, “Intraislet endothelial cells contribute to revascularization of transplanted pancreatic islets,” *Diabetes*, vol. 53, no. 5, pp. 1318–1325, May 2004, doi: 10.2337/diabetes.53.5.1318

[177] Y. Liu, S. R. Cox, T. Morita, and S. Kourembanas, “Hypoxia regulates vascular endothelial growth factor gene expression in endothelial cells,” *Circulation Research*, vol. 77, no. 3, pp. 638–643, Sep. 1995, doi: 10.1161/01.RES.77.3.638

[178] D. Goswami *et al.*, “Design considerations for macroencapsulation devices for stem cell derived islets for the treatment of type 1 diabetes,” *Advanced Science*, vol. 8, no. 16, p. 2100820, 2021, doi: 10.1002/advs.202100820

[179] A. D. McDougal and C. F. Dewey, “Modeling oxygen requirements in ischemic cardiomyocytes,” *Journal of Biological Chemistry*, vol. 292, no. 28, pp. 11760–11776, Jul. 2017, doi: 10.1074/jbc.M116.751826

[180] K. Sekine *et al.*, “Oxygen consumption of human heart cells in monolayer culture,” *Biochemical and Biophysical Research Communications*, vol. 452, no. 3, pp. 834–839, Sep. 2014, doi: 10.1016/j.bbrc.2014.09.018

[181] U. J. Balis *et al.*, “Oxygen consumption characteristics of porcine hepatocytes,” *Metabolic Engineering*, vol. 1, no. 1, pp. 49–62, Jan. 1999, doi: 10.1006/mben.1998.0105

[182] A. Ghosh, C. Onsager, A. Mason, L. Arriola, W. Lee, and A. Mubayi, "The role of oxygen intake and liver enzyme on the dynamics of damaged hepatocytes: Implications to ischaemic liver injury via a mathematical model," *PLOS ONE*, vol. 16, no. 4, p. e0230833, Apr. 2021, doi: 10.1371/journal.pone.0230833

[183] S. R. L. Stacpoole, D. J. Webber, B. Bilican, A. Compston, S. Chandran, and R. J. M. Franklin, "Neural precursor cells cultured at physiologically relevant oxygen tensions have a survival advantage following transplantation," *Stem Cells Translational Medicine*, vol. 2, no. 6, pp. 464–472, Jun. 2013, doi: 10.5966/sctm.2012-0144

[184] L. De Filippis and D. Delia, "Hypoxia in the regulation of neural stem cells," *Cellular and Molecular Life Sciences*, vol. 68, no. 17, pp. 2831–2844, Sep. 2011, doi: 10.1007/s00018-011-0723-5

[185] A. Taguchi *et al.*, "Intravenous autologous bone marrow mononuclear cell transplantation for stroke: phase1/2a clinical trial in a homogeneous group of stroke patients," *Stem Cells and Development*, vol. 24, no. 19, pp. 2207–2218, Oct. 2015, doi: 10.1089/scd.2015.0160

[186] T. P. Keeley and G. E. Mann, "Defining physiological normoxia for improved translation of cell physiology to animal models and humans," *Physiological Reviews*, vol. 99, no. 1, pp. 161–234, Jan. 2019, doi: 10.1152/physrev.00041.2017

[187] J. Siehler, A. K. Blöchinger, M. Meier, and H. Lickert, "Engineering islets from stem cells for advanced therapies of diabetes," *Nature Review Drug Discovery*, vol. 20, no. 12, pp. 920–940, Dec. 2021, doi: 10.1038/s41573-021-00262-w

[188] F. Cuozzo, V. Sordi, and L. Piemonti, "Immune evasive stem cell islets," in *Pluripotent Stem Cell Therapy for Diabetes*, L. Piemonti, J. Odorico, T. J. . . Kieffer, V. Sordi, and E. de Koning, Eds., Cham: Springer International Publishing, 2023, pp. 299–316. doi: 10.1007/978-3-031-41943-0_14

[189] E. Yoshihara *et al.*, "Immune-evasive human islet-like organoids ameliorate diabetes," *Nature*, vol. 586, no. 7830, pp. 606–611, Oct. 2020, doi: 10.1038/s41586-020-2631-z

[190] O. Korsgren *et al.*, "Current status of clinical islet transplantation," *Transplantation*, vol. 79, no. 10, p. 1289, May 2005, doi: 10.1097/01.TP.0000157273.60147.7C